Transcritical Combustion
Scalable High-Fidelity Simulations of Reacting Multiphase Flows at Transcritical Pressure

Fathi, Mohamad

DOI
10.4233/uuid:ddb0b4b3-5cbf-4537-bccc-c00204e25378

Publication date
2026

Document Version
Final published version

Citation (APA)
Fathi, M. (2026). *Transcritical Combustion: Scalable High-Fidelity Simulations of Reacting Multiphase Flows at Transcritical Pressure*. [Dissertation (TU Delft), Delft University of Technology]. https://doi.org/10.4233/uuid:ddb0b4b3-5cbf-4537-bccc-c00204e25378

scalable high-fidelity simulations of reacting multiphase flows at TRANSCRITICAL pressure

MOHAMAD
FATHI

خورشید او را ذره‌ایم این رقص را آموختیم

Molana
by salahaddincalligraphy

Transcritical Combustion

SCALABLE HIGH-FIDELITY SIMULATIONS OF REACTING MULTIPHASE FLOWS AT TRANSCRITICAL PRESSURE

Dissertation

for the purpose of obtaining the degree of doctor
at Delft University of Technology
by the authority of the Rector Magnificus, prof. dr. ir. T.H.J.J. van der Hagen,
chair of the Board for Doctorates
to be defended publicly on
Wednesday 7, January 2026 at 10:00 o'clock

by

Mohamad FATHI AZARKHAVARANI

Master of Science in Mechanical Engineering,
Amirkabir University of Technology (Tehran Polytechnic), Iran,
born in Tehran, Iran.

This dissertation has been approved by the promotors:

Prof. Dr.-Ing. habil. S. Hickel
Em.Prof.dr. D.J.E.M. Roekaerts.

Composition of the doctoral committee:

Rector Magnificus,	Chairperson
Prof. Dr.-Ing. habil. S. Hickel,	TU Delft, *promotor*
Em.Prof.dr. D.J.E.M. Roekaerts,	TU Delft, *promotor*

Independent members:

Prof.dr. J.A. van Oijen,	TU Eindhoven, Netherlands
Prof.dr. M. Papalexandris,	UCLouvain, Belgium
Prof.dr. R. Pecnik,	TU Delft, Netherlands
Prof.dr. G. Ribert,	INSA Rouen, France
Dr. A. Wehrfritz,	UTU, Finland

Reserve member:

Prof.dr. A. Gangoli Rao,	TU Delft, Netherlands

Keywords: Multiphase thermodynamics; Real-fluid properties; Transcritical flamelets; Multiphase reacting flows; Turbulent spray flames
Cover by: M. Fathi Azarkhavarani

ISBN 978-94-6384-889-3

An electronic copy of this dissertation is available at
`https://repository.tudelft.nl/`.

To my life-giving Sun, dreaming Moon, and little Mercury

Narges, Nilda, and Anida

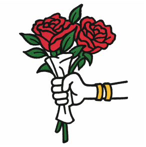

Contents

Summary

We address a fundamental challenge in modern propulsion and energy systems: accurately modeling combustion under transcritical conditions, where operating pressures exceed the critical pressure of the fuel but still lower than cricondenbar values of the air-fuel mixture, leading to a complicated thermophysical mixture behavior. Transcritical regimes are characterized by strong non-idealities and the possible coexistence of vapor and liquid phases. The main objective of this work is to develop a high-fidelity, physically consistent, and computationally efficient simulation framework that captures these phenomena within a Large Eddy Simulation (LES) context, enabled by a Multiphase Thermodynamics (MT) approach. This work has been organized into chapters, each focusing on a key component of the study:

Chapter 1 introduces the motivation and scope of the research. It highlights the limitations of existing modeling strategies in capturing phase transitions and non-ideal thermodynamics in transcritical fuel sprays. The chapter outlines the primary contributions of the dissertation: the development of robust phase equilibrium algorithms, the extension of LES-MT to chemically reacting flows, the formulation of a real-fluid multiphase flamelet model, and the integration of this framework with tabulated chemistry techniques. Foundational thermodynamic concepts and the relevance of these phenomena to practical combustion systems are also presented.

In Chapter 2, attention is directed toward a critical computational bottleneck: Vapor-Liquid Equilibrium (VLE) calculations, which must be solved reliably and rapidly at every grid point and time step in a simulation. This chapter presents a new family of flash algorithms (spanning PT, VT, HP, and UV formulations) constructed using a volume function based on the Helmholtz free energy. This approach significantly reduces the dimensionality of the problem, yielding robust convergence and substantial computational acceleration, especially in near-critical and two-phase regions.

Building on this foundation, Chapter 3 develops the core LES-MT simulation framework for modeling inert and reacting transcritical sprays. Real-fluid behavior is captured using a cubic equation of state, coupled with the VLE solvers from Chapter 2. The turbulence is modeled via the ALDM LES framework, and combustion is described using fugacity-based finite-rate chemistry. The framework is validated against the ECN Spray-A benchmark, with simulations demonstrating excellent agreement with experimental data for key metrics such as liquid/vapor penetration, ignition delay, and flame lift-off. The results underscore the need of incorporating accurate thermophysical models in transcritical spray simulations.

Chapter 4 shifts focus to transcritical counterflow diffusion flames (CDFs), which serve as canonical flamelet configurations for turbulent combustion modeling. This chapter extends the MT framework to laminar reacting flows, with a detailed treatment of molecular diffusion using the Dixon-Lewis formulation and a thermodynamic correction to account for real-fluid effects. The combustion modeling remains grounded in fugacity-based finite-rate kinetics. Applications include simulations of OxyMethylene Ether-3 OME_3 and OME_3/n-dodecane blends, illustrating how transport and chemical effects influence flame structure and ignition. The results form the basis for generating accurate flamelet libraries under transcritical conditions.

In Chapter 5, the full LES-MT framework is coupled with a tabulated chemistry approach using flamelet libraries created by application of the methods of Chapter 4. This chapter introduces a Flamelet-Progress Variable (FPV) model for simulating turbulent, reacting, transcritical sprays. The formulation includes compressible transport, real-fluid thermodynamics, and on-the-fly UV-flash calculations. The framework is applied to various OME-based fuels, offering new insights into ignition behavior, fuel evaporation dynamics, and soot precursor formation. Comparison with ECN Spray-A data confirms the model's predictive capabilities, while analysis of differential evaporation rates highlights the sensitivity of transcritical combustion to fuel composition.

Chapter 6 concludes the dissertation by synthesizing the scientific and technical contributions. The work establishes a comprehensive and validated modeling framework for transcritical combustion, spanning from detailed thermodynamics to turbulent reactive flow simulation. It provides a path forward for the predictive simulation of high-pressure combustion systems and lays a foundation for the exploration of alternative fuels and advanced engine concepts.

Preface

Automobiles, aircraft, vessels, and rockets have one thing in common: they are powered by internal combustion engines. Despite their successful and widespread use, this technology is facing significant pressure to become more efficient and environmentally friendly. In response, sustainable synthetic e-fuels are gaining attention as promising carbon-neutral alternatives for fossil fuels. For any fuel powering the engine, the operating pressure of the combustion chamber should be kept at the highest possible level in order to maximize the engine's thermal and fuel efficiencies. The operating pressure of modern engines usually exceeds the critical pressure of the injectant and is within the *transcritical* regime, where the behavior of the fuel and oxidizer deviates significantly from ideal-gas assumptions. Under these extreme conditions, a complex interplay of turbulent mixing, phase change, and chemical reactions occurs. These phenomena, while holding immense potential for improving engine performance, remain poorly understood.

To unlock the potential of these high-pressure operating conditions, a deeper understanding of transcritical combustion is crucial. This necessitates the development of advanced physical and numerical models capable of accurately accounting for the non-ideal behavior of fluid mixtures and the inherent challenges associated with transcritical vaporization, turbulent mixing, and combustion. This dissertation aims to address these challenges by developing high-fidelity simulation frameworks capable of accurately modeling these complex phenomena.

Mohamad Fathi
Delft, June 2025

1

Introduction

A theory is more impressive the greater the simplicity of its premises, the more different kinds of things it relates, and the more extended its area of applicability.

Albert Einstein

This chapter provides the necessary background on transcritical combustion, explains the challenges in simulating such complex flows, reviews existing modeling approaches and their limitations, and clearly states the research objectives and the structure of the dissertation

---

Parts of this chapter have been published as *Transcritical real-fluid effects on dual-fuel combustion of methane and n-dodecane* in Appl. Energy Combust. Sci. Journal **24** (2025) [1].

1.1. MOTIVATION

At subcritical pressures, atomization devices in propulsion systems rupture the liquid fuel volume using aerodynamic shearing to ensure uniform droplet dispersion in the combustion chamber. The hot environment of the chamber provides the required enthalpy to evaporate fuel droplets, and the vaporized fuel then mixes and burns with the surrounding gas. Many studies have investigated the combustion dynamics of fuel sprays and the flame structures at low pressure, see Ref. [2] and the references cited within, for example. In contrast, there is limited knowledge about high-pressure reacting and non-reacting sprays. This gap in understanding is partly due to the difficulties associated with experimental diagnostics [3] and the complexities of analytical modeling [4].

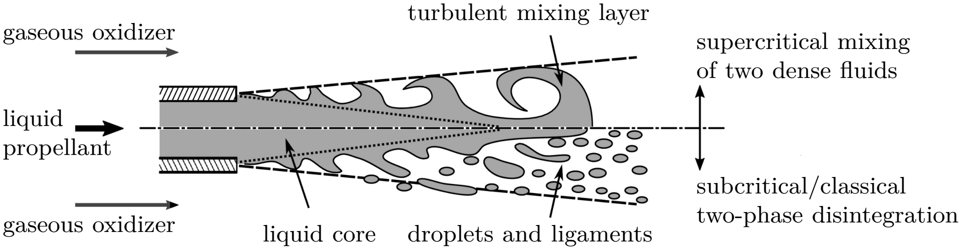

Figure 1.1.: Schematic illustration of fuel evaporation pathways without phase separation (top) and with phase separation (bottom), modified from Ma *et al.* [5]. Transcritical injections exhibit a hybrid behavior involving both mechanisms.

Combustion of liquid propellants under high pressure is crucial for various propulsion systems, but injection configurations are typically tailored to the specific application. For example, in liquid rocket engines, a cryogenic liquid oxidizer is usually injected alongside high-pressure gaseous fuel. The fuel coflow is already supercritical, and the liquid oxidizer quickly reaches supercritical states after a brief warming phase, where its temperature rises slightly over the critical point. At supercritical pressures, the liquid-gas boundary vanishes, eliminating surface tension and the need for latent heat of vaporization. Hence, the oxidizer and fuel diffusively mix like two dense gases downstream of the injector [6]. Although supercritical injection has been extensively studied in the context of rocketry, relatively little is known about the transcritical fuel spray flames in high-power modern propulsion systems, where the liquid fuel injectant can locally cross the two-phase region during mixing with air at pressures that are nominally supercritical with respect to the fuel itself. Transcritical fuel sprays resemble a combination of the classical two-phase disintegration with breakup and evaporation of droplets and the supercritical turbulent mixing of two dense fluids, see Fig. 1.1. This hybrid behavior complicates their numerical simulation; despite comprehensive experimental campaigns, it is not well understood which type of the jet disintegration dominates under exactly which conditions. Recent studies questioned the established paradigms for high-pressure fuel injection, showing that the physical understanding is still severely limited and detailed simulations are required [4]. Before examining the high-pressure transcritical injection, it is essential to understand the Gibbsian thermodynamics of monocomponent and multicomponent real fluids.

1.2. GIBBSIAN THERMODYNAMICS

In the Gibbsian version of equilibrium thermodynamics [7], the concepts of internal energy and entropy are assumed to be known and are used to provide a detailed description of the subsystems in equilibrium. Equilibrium thermodynamics consists essentially of the first, second, and third laws. However, in order to obtain useful results, these laws should be combined with an equation of state (EOS) to provide knowledge of the fluid properties at any point in the system.

1.2.1. PURE-FLUID STATE OF MATTER

As shown in Fig. 1.2, the PT-state diagram is typically divided into four quadrants (I-IV) for pure substances using the critical isobar and isotherm lines. Various researchers have used different labels for these regions based on the transition or phase change between them. Bellan [8] considers all states with temperatures or pressures beyond the critical point as supercritical, including quadrants II, III, and IV, as the coexistence of two phases is not possible in those regions. Tucker [9], however, identifies only quadrants II and III as supercritical and excludes quadrant IV due to its liquid-like properties. Oefelein [10] and Candel *et al.* [11] named quadrant IV as transcritical to highlight the difference between the evaporation of liquid and transcritical fluids .

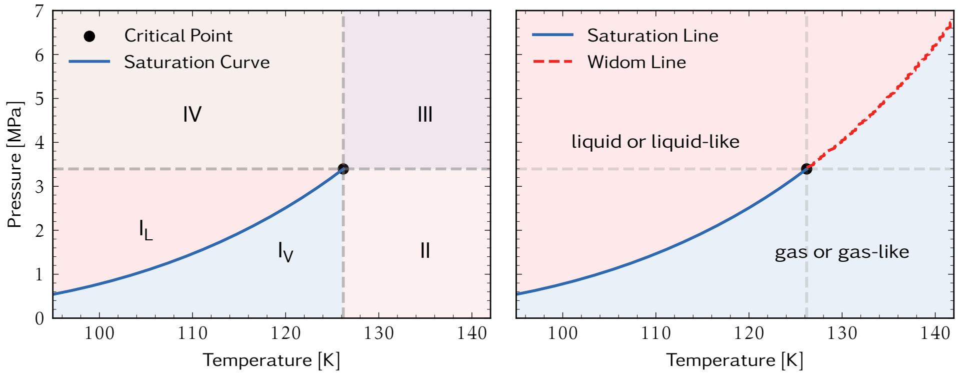

Figure 1.2.: Classical state of matter labeling (left) and its extention version (right) shown in the PT-phase diagram of nitrogen computed using the open-source library CoolProp [12].

Whereas there is no physical phase boundary separating subcritical liquid from transcritical states due to the smooth and continuous nature of the transition, experimental evidence shows there is a liquid-gas structure in the supercritical state space. This structure, marked by the Widom or pseudo-boiling line identified through maxima in specific heat capacity at constant pressure, extends the saturation or coexistence line into the supercritical domain. This line separates liquid-like and gas-like regions as shown in the right side of Fig. 1.2. Experimental observations, such as sound dispersion (i.e., the frequency-dependent increase in sound speed) measured by Gorelli *et al.* [13] and Simeoni *et al.* [14], confirm this division, as sound dispersion (a property often found in liquids) was observed at supercritical pressures. Thus, the quadrant III is not homogeneous and should be viewed as comprising distinct liquid-like and gas-like supercritical states, see Fig. 1.2.

REAL FLUID VS IDEAL GAS

Gases mimic the behavior of an ideal gas at dilute conditions with relatively low pressures or high temperatures. At low pressures or large volumes, the volume of the particles would be negligible compared to the volume of the container. At high temperatures, the interaction between molecules becomes insignificant due to the high speed of the particle movements and little time to interact. Banuti *et al.* [15] showed that the ideal gas regime is not only limited to the subcritical gases, and supercritical fluids can be modeled as ideal gas, especially when their temperature is higher than twice the critical point as shown in Fig. 1.3. Note that the compressibility factor Z measures the amount of deviation of fluid behavior from ideal gas one. It is defined as ratio of the actual pressure to the ideal-gas prediction for a given temperature and density.

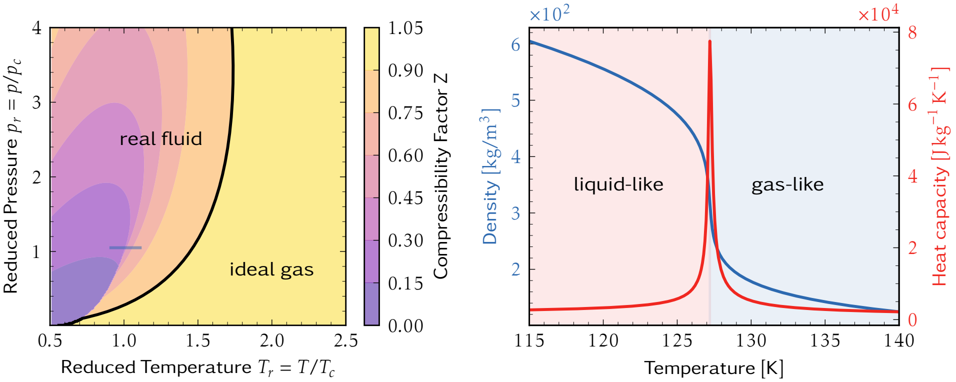

Figure 1.3.: Left shows compressibility factor for various reduced conditions. The black line shows the boundary between the ideal gas and real fluid regions. Right shows variations of heat capacity and density at reduced pressure of 1.05 for pure nitrogen. Thermodynamic properties are computed using the open-source library CoolProp [12].

However, dilute conditions do not exist in transcritical processes, especially when blending of liquid fuel and gaseous oxidizer is happening. As shown in Fig. 1.3, the fluid properties (e.g., density, heat capacity) undergo rapid changes within a narrow range of a few degrees around the pseudo-boiling point when subjected to pressures slightly above the critical point. The area beneath the sharp peak of heat capacity is indicative of the enthalpy required for pseudo-boiling [16]. Increasing the pressure results in a decrease in the peak of heat capacity, Banuti, Raju, and Ihme [17] shown that above reduced pressure of 10, the Frenkel rather than the Widom line should be used for the distinction between the liquid-like and gas-like supercritical state of matter. This line marks a transition in microscopic dynamics: the liquid-like regime is characterized by collective, caged particle motion dominated by potential-energy interactions, while the gas-like regime exhibits uncorrelated, nearly ballistic motion governed mainly by kinetic energy [18].

1.2.2. PURE NITROGEN INJECTIONS

The behavior of cryogenic liquid nitrogen jets injected into a gaseous nitrogen environment at a supercritical temperature (300 K) has been demonstrated by the experimental images shown in Fig. 1.4, see Chehroudi, Talley, and Coy [19] for the details. The injected liquid nitrogen, with initial temperatures ranging from 99 K to 110 K (subcritical), exhibits distinct structural changes depending on the chamber pressure, reported here in terms of reduced pressure (p_r), defined to be the chamber pressure divided by the critical pressure of the pure nitrogen.

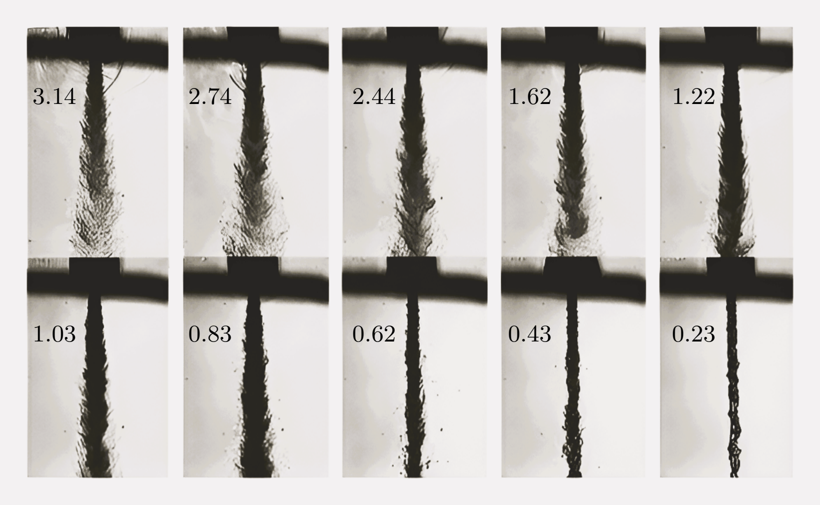

Figure 1.4.: Back-illuminated images of a cryogenic liquid nitrogen jet injected into a chamber filled with nitrogen at a fixed supercritical temperature of 300 K but varying sub to supercritical pressures. The numbers show the reduced pressure values. Images from Chehroudi, Talley, and Coy [19].

CLASSICAL ATOMIZATION

At subcritical chamber pressures ($p_r < 1$), the nitrogen jet displays conventional liquid spray characteristics. Surface instabilities develop downstream of the injector, leading to the formation of fine ligaments and droplets similar to the second wind-induced breakup regime described by Reitz and Bracco [20]. This regime is marked by clear droplet ejection and interfacial instabilities, typical of low-pressure liquid jet atomization.

TRANSITION NEAR CRITICAL POINT

A significant morphological shift occurs near the critical pressure ($p_r \simeq 1$). Beyond this threshold, droplet formation disapears, and the interface develops irregular "finger-like" structures instead of discrete droplets (see Chehroudi [21]). The mixing layer transitions to a dissolution-like process, attributed to the sharp decline in surface tension and reduced vaporization energy requirements as the fluid approaches supercritical conditions.

GAS-LIKE TURBULENT MIXING

At supercritical pressures ($p_r > 1$), the dense core of the jet shortens and thins, resembling a turbulent gaseous jet. Classical atomization mechanisms are entirely suppressed, with no observable droplet generation. These findings align with the other experimental observations of Mayer *et al.* [6], and Roy and Segal [22], confirming the dominance of diffusion-driven mixing over surface-tension-driven breakup in supercritical regimes.

1.2.3. REAL-FLUID MIXTURE EFFECTS

Woodward and Talley [23] examined nitrogen jet structure evolution under various pressures and environmental conditions. The experimental setup involved injecting liquid nitrogen through a 0.25 mm injector into two environments: pure nitrogen at 2.8 MPa and 6.9 MPa, and a nitrogen-helium mix at 6.9 MPa. The critical pressure of nitrogen is 3.4 MPa. Figure 1.5 presents their shadowgraph images at three axial points downstream from the injector: near-field (0.0 to 1.9 mm), mid-field (7.4 to 9.5 mm), and far-field (15.0 to 17.1 mm).

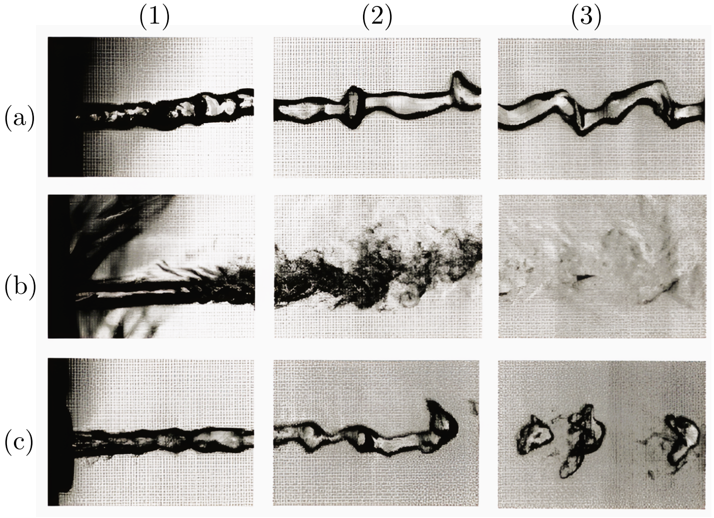

Figure 1.5.: Shadowgraph images of transcritical nitrogen injection, injector diameter 0.25 mm. (a) and (b) into pure nitrogen at a sub and supercritical pressure; (c) into mixture of nitrogen and helium at the same supercritical pressure. Taken at axial locations downstream of injector exit, modified from Woodward and Talley [23].

In Fig. 1.5, injecting the nitrogen jet into pure nitrogen at subcritical pressure of 2.8 MPa showed the classical atomization with clear interfaces. At supercritical pressure of 6.9 MPa, the jet thickened but stayed in a single-phase gas-like turbulent mixing regime. However, when the nitrogen is injected into a nitrogen-helium mixture at the same pressure of 6.9 MPa, surface tension effects appeared again. The jet broke up into ligaments and droplets, despite the pressure exceeding nitrogen's critical point.

The observed difference roots in real-fluid mixture effects. While pure nitrogen at 6.9 MPa remains in a supercritical state, the nitrogen-helium mixture exhibits a higher effective critical pressure due to non-ideal mixing behavior. This causes local regions near the jet interface to temporarily enter a two-phase state, reintroducing surface tension effects. The exprimental results demonstrate that ambient composition can significantly alter jet breakup behavior, even under nominally supercritical conditions relative to the injectant itself.

HYDROCARBON-NITROGEN MIXTURES

The increase in critical pressure for hydrocarbon fuels mixed with nitrogen, as expected in most air-breating power systems, follows the Type III phase behavior of Van Konynenburg and Scott [24]. This differs significantly from Type I mixtures, which is expected for any two species with a similar molecular structure.

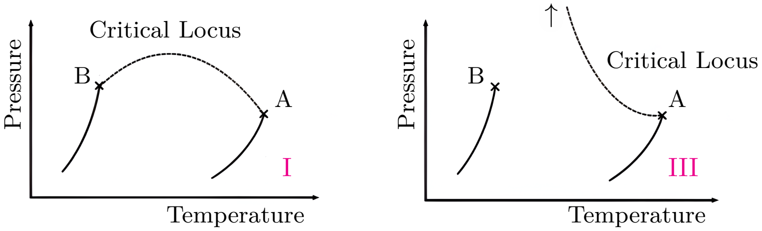

Figure 1.6.: PT-phase diagrams of two mixture types: Type I for hydrocarbon mixtures and Type III for binary mixtures of n-alkane and nitrogen. In contrast to the continuous critical locus line for Type I, the critical line for Type III mixtures starts from the critical point of the pure alkane (B) and ends at extremely high pressures.

The critical point of a mixture varies with its composition. Consequently, for binary systems, evaluating the critical point over the entire composition range and connecting these points yields the so-called critical locus. For Type I mixtures, such as hydrocarbon-hydrocarbon systems, the critical locus forms a continuous line connecting the critical points (CP) of the two components. The critical pressure typically peaks at intermediate compositions before decreasing toward the CP of the second component. In contrast, for Type III mixtures (e.g., hydrocarbons with nitrogen), the critical locus begins at the CP of the hydrocarbon but diverges to extremely high pressures as nitrogen is added, never reaching the CP of nitrogen. The significantly different properties of molecules creates a telescopic effect where the mixture's critical pressure rises sharply with small additions of nitrogen.

For example, Qiu and Reitz [25] showed such phase behaviour for normal-alkanes with 12 to 14 carbons mixed with nitrogen. They used equilibrium thermodynamics and confirmed that the critical pressure of the hydrocarbon-nitrogen system rapidly exceeds the chamber pressure, forcing local regions of the fluid into a two-phase state despite globally supercritical conditions.

VOLUMETRIC PHASE DIAGRAM

Last but not least, the pressure-volume (PV-state) diagrams of pure substances and mixtures exhibit fundamental differences in phase behavior, particularly near critical conditions. Figure 1.7 highlights some of these different features.

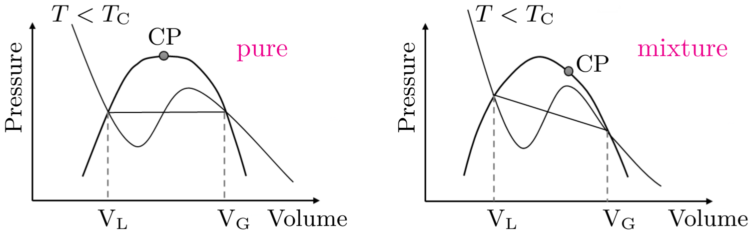

Figure 1.7.: Representation of VT-phase diagrams with an isothermal curve at subcritical temperature for pure substances and a mixture with a fixed compositon. The sketches are abstract. CP denotes the critical point.

In pure substances, the PV-state diagram shows a distinct CP where the liquid and gas phases become identical. Below the CP, isotherms (constant temperature lines) have a flat section where pressure stays constant during phase change, connecting the liquid (V_L) and gas (V_G) volumes. At the CP itself, the constant-temperature curve has a stationary inflection point, meaning both the first and second derivatives of pressure with respect to volume are zero. The compressibility factor (Z) always satisfies $Z_L < Z_G$ for equilibrium states, and liquid density remains higher than gas density ($\rho_L > \rho_G$).

For mixtures, the PV behavior is more complex. Unlike pure substances, mixtures do not have a single CP and it varies with composition. Isotherms in the two-phase region are not flat but curved, and the points V_L and V_G do not represent the equilibrium states anymore. At what appears to be the critical point, the mathematical conditions of the stationary inflection point do not hold. The compressibility factor Z_L can be either smaller or larger than Z_G at equilibrium, though the liquid phase always remains denser ($\rho_L > \rho_G$). This complex behavior makes modeling mixtures, especially near critical conditions, significantly more challenging than for pure substances.

For mixtures, the critical point no longer represents the limit for liquid-vapor coexistence, see the phase diagrams of the Y8 and MY10 mixtures in Fig. 2.2. Instead, two key boundaries emerge: the cricondenbar (maximum pressure allowing phase equilibrium) and cricondentherm (maximum temperature allowing phase equilibrium). Unlike pure substances, mixtures can maintain liquid-vapor equilibrium above their critical temperature or pressure, as long as conditions remain below the limits set by cricondenbar and cricondentherm. This explains why surface tension effects may unexpectedly appear in supercritical injections. Local composition variations can create two-phase regions even when system pressure and temperature exceed the pure component's or even mixture's critical point as shown in Fig. 1.5.

1.3. TRANSCRITICAL FUEL SPRAYS

We consider cases where combustion is initiated by auto-ignition during or after the injection of a cold liquid fuel in a pressurized chamber filled with a hot gas oxidizer. The chamber pressure is greater than the critical pressure of the fuel but less than the cricondenbar pressure of the fuel-oxidizer mixture. This operating pressure causes the injectant to cross the two-phase region due to mixing with the environment. Such turbulent reacting sprays at transcritical pressures have drawn significant attention due to the complexity of the physical and numerical modeling. Besides real fluid effects due to the high pressure, the possibility of coexisting saturated liquid and vapor phases further complicates the modeling of transcritical fuel sprays.

1.3.1. MULTIPHASE FLOW MODELING

The atomization of the liquid jet in a surrounding gas phase and phase change from liquid to gas involve the transfer of momentum, heat, and mass. In subcritical conditions, there is a clear separation between liquid and gas. Thermodynamic and physical properties of the individual phases, together with latent heat and surface tension at the interface, play a role in the fluid mechanical equations. Transfer phenomena at the interface in fully resolved simulations are explicitly computed, but in statistical modeling approaches are modeled according to standard correlations. In transcritical conditions, a transition to a supercritical state without sharp interfaces can occur; however, states in the subcritical two-phase region may also be possible.

Different numerical methods have been developed to track the interface location and to capture its dynamics accurately. These methods are broadly classified as Lagrangian and Eulerian methods. The former method monitors the interface based on moving meshes, while the latter captures the interface on a fixed grid. Modeling the discontinuities or jump conditions across the interface leads to two approaches. In the first approach, the discontinuities of the fluid properties and jump conditions are smoothened across the interface; the governing equations are solved in the whole domain. In contrast, the other approach uses the interfacial jump-condition formulation, where the discontinuities or jump conditions are treated without smoothening across the interface. The governing equations are solved in each phase (or sub-domain) where the interfacial location at the sub-cell level is used for sharply considering the discontinuities.

Previous state-of-the-art LES of the high-speed transcritical injection have either modeled the transcritical multiphase flows by Lagrangian particle tracking (LPT) methods with sharp vapor–liquid interfaces [26–28] or later by Eulerian single-phase dense-gas (DG) approaches with diffuse vapor–liquid interfaces [29–32]. LPT methods represent the interface through discrete particles (droplets, bubbles, or solid particles depending on the application) whose dynamics are governed by interfacial transfer rates, particle size, and relative velocity, making them particularly suitable for capturing discrete-phase effects in spray-dominated flows. In contrast, DG methods treat the entire system as a single-phase flow using real-fluid equations of state, which naturally captures thermodynamic non-idealities and smooth property transitions across pseudo-boiling regions but lacks the ability to resolve sharp interfacial features or discrete-phase physics. Both approaches are efficient for many flows, but their inherent model assumptions impose significant limitations at transcritical conditions. The standard LPT method is susceptible to empirical tuning parameters and was developed for dilute mixtures, neglecting the nonideal-fluid effects [33]. On the other hand, the DG approach excludes transcritical phase separation. This may lead to nonphysical or ill-defined states when a part of the flow passes the metastable boundaries, particularly at lower transcritical pressures [5]. Furthermore, some important transcritical effects, such as the high solubility of the saturated liquids or the different evaporation rates of the components of the fuel, are not captured by these models; see also the discussion in Refs. [25, 34–37], for example.

One effective remedy for breaking these limitations is to employ a consistent multicomponent two-phase model for high-pressure flows using vapor-liquid equilibrium (VLE) calculations [35]. The idea of adding VLE to real-fluid thermodynamic calculations was initiated in the group of Rolf Reitz, University of Wisconsin and initially used as post-processing of fluid dynamics simulations due to the high computational cost. The model, which we refer to as multiphase thermodynamics (MT), can represent multicomponent supercritical states and coexisting multicomponent subcritical two-phase states. It also includes the effect of dissolved ambient gases in the liquid fuel phase, which can become substantial at high pressures [25, 33]. Note that the MT model does not include any ad-hoc tuning parameters and is hence genuinely predictive. It provides detailed phase information that can be directly and non-ambiguously linked to experimental measurements [38].

MT-based high-fidelity studies show excellent agreement with experimental data for the non-reacting transcritical sprays [39–43]; however, the applicability of this method for reacting and non-reacting cases with many species, is limited due to the surging the computational cost of classic VLE solvers, which exponentially increases with the number of components in the mixture.

1.3.2. REACTING FLOW MODELING

High-fidelity simulations of transcritical reacting multiphase flows are computationally impractical unless utilizing a dynamic two-step reaction mechanism. In practice, such reduced mechanisms may be insufficient due to their limited validity range for which they are optimized. Hence, to include all the intricate details of the combustion, identifying a very low-dimensional subspace (manifold) that can effectively represent the reacting behavior of the whole system is inevitable.

Flamelet models can effectively identify the required manifold when the flame thickness is smaller than the flow's smallest energy-containing length scale. There is evidence that such conditions exist in high-pressure combustion engines [44]. According to the flamelet method, turbulent eddies corrugate or wrinkle the turbulent flame on large scales, of which the laminar-like structure remains unchanged on small scales. Therefore, it is possible to solve a set of laminar counterflow flames separately with detailed chemistry at conditions close to the target flame. Then the required thermo-chemistry data of the main (turbulent) reacting flow are retrievable via a tabulation method using a few controlling parameters representing the simulated laminar flame behavior. The minimal set of controlling parameters, which construct the manifold, are usually a mixture fraction indicating how much fuel is mixed with the oxidizer and a progress variable representing the reaction progress rate between the fuel and oxidizer.

In LES-LPT methods, igniting flamelet models are typically considered due to the fact that the main combustion mode in transcritical engines is non-premixed and autoignition is inherently transient [45–47]. On the other hand, in LES-DG methods, highly-reduced reaction mechanisms are typically used to accurately examine the impact of the real-fluid environment and low-temperature chemistry [48–50]. Nevertheless, the application of such combustion models in the context of the LES-MT approach remains unexplored.

1.4. OBJECTIVES AND ACHIEVEMENTS

The main objective of this thesis is to significantly advance our understanding of reacting transcritical multiphase flows in modern energy conversion systems. To achieve this, we will develop numerical frameworks capable of solving the governing equations of reacting flows using a multiphase thermodynamic approach within a diffuse-interface method. The research is structured around four key sub-objectives, each addressing critical challenges in the complex puzzle of modeling transcritical reacting flows:

1. **Developing a Robust and Rapid VLE Solver**
   Computationally efficient phase-splitting or flash calculations are essential in any LES-MT of realistic multicomponent vapor–liquid fluid flows that need millions of VLE calculations at each time step of simulations. At the same time, such flash algorithms must be fault tolerant and robust because even a method that fails to converge only once in a billion will eventually spoil the entire simulation

2. **Extending LES-MT method to Reacting Flows**
   Building upon the robust VLE solver, our second objective focuses on extending multiphase real-fluid thermodynamics from inert to reacting high-pressure flows. This will involve utilizing a highly-reduced reaction mechanism and effectively capture real-gas effects on chemical kinetics.

3. **Developing a real-fluid multiphase flamelet solver**
   A detailed analysis of transcritical fuel sprays necessitates accurate

simulations of flamelets under relevant conditions. Such simulations demand precise modeling of transport phenomena, particularly molecular diffusion, in addition to accurate equilibrium thermodynamics and chemical properties. Hence, the third objective is set to generalize the MT approach to compute transport properties and the diffusion driving force for transcritical real-fluid mixtures. The combination of these innovations provides a transcritical flamelet solver with unprecedented accuracy.

4. **Using the LES-MT method with Tabulated Chemistry**
   To precisely predict transcritical flame behavior and emissions, it is essential to include detailed reaction mechanisms of fuel cracking and radical formation, which initiate upon contact between the cold fuel and the hot environment. We incorporate more chemical detail by employing the real-fluid multiphase flamelet model developed for transcritical pressures, as our final objective. This calibration-free approach can significantly improve our understanding of the transcritical combustion of emerging fuels such as OME_3 or their combination with traditional fuels such as n-dodecane.

1.5. DISSERTATION LAYOUT

The dissertation is organized into four main chapters, along with an introduction and conclusion, each answering one of the aformentioned four sub-objectives through innovative methodologies and frameworks for simulating complex real-fluid behaviors under transcritical conditions.

Chapter 2 introduces a new family of fast and robust methods for phase-splitting calculations under both isothermal and nonisothermal conditions. The foundation of the new approach lies in the formulation of phase-equilibrium conditions for multicomponent mixtures, which are expressed in an effectively reduced space based on the molar-specific value of the volume function, a new thermodynamic function derived from the Helmholtz free energy.

Chapter 3 presents a novel numerical framework designed for high-fidelity simulations of inert and reacting sprays at transcritical conditions. The modeling of high-pressure jet disintegration is accomplished through a diffuse interface method that incorporates multiphase thermodynamics. This framework integrates multicomponent real-fluid volumetric and caloric state equations with the newly introduced VLE calculations of Chapter 2 to accurately compute the thermodynamic properties of mixtures at transcritical pressures. Additionally, combustion source terms are evaluated using a finite-rate chemistry model that accounts for real-gas effects based on the fugacity of the species involved.

Chapter 4 points out a comprehensive numerical framework for the unsteady flamelet calculations at transcritical pressures using real-fluid thermo-transport and chemical properties. The transport properties of the working fluid are modeled using high-pressure correction methods with a proper structural mixing rule in the coexistence area. The real-fluid effect on diffusion driving force has been quantified via the thermodynamic correction factor with a proposed extension to the multiphase transcritical regions. The impact of high pressure on reaction source terms is also included via the fugacity of species in the mixture.

While Chapter 4 established the foundation for unsteady real-fluid multiphase flamelets by solving low-Mach counterflow flame equations, **Chapter 5** extends this framework to turbulent high-speed (compressible) spray combustion described by the fully conservative Navier-Stokes equations. As our final objetive, this chapter presents the integration of such an advanced flamelet approach with compressible, multiphase LES of the transcritical fuel sprays, explaining the two-way coupling between the flamelet library and online multiphase thermodynamics. Beyond methodology, this chapter provides novel physical insights for transcritical injection and combustion of pure OME_3 and n-dodecane fuels and their blends.

2

Rapid and Robust Phase Equilibrium Calculations

This chapter lays the foundation by introducing a new family of algorithms for vapor–liquid equilibrium (VLE) calculations as the core of the MT model. These algorithms work under various thermodynamic conditions and use a new formulation that significantly reduces the computational cost. By reformulating the VLE problem in a reduced space independent of the number of species, and using a Newton-based method with an exact Jacobian, the approach achieves high speed, robustness, and accuracy—even near challenging regions like phase boundaries or spinodal curves.

The content of this chapter has been published as *Rapid Multi-Component Phase-Split Calculations Using Volume Functions and Reduction Methods* in AIChE Journal **67** (2021) [51].

2.1. INTRODUCTION

In simulations of realistic multi-component vapor-liquid fluid flows, millions of phase-equilibrium calculations are required every time step in the various forms, depending on the chosen formulation of the governing equations. Methods similar to what we used in the next chapter, that solve the compressible Navier-Stokes equations based on the conservation laws for mass, linear momentum and total energy, require a UV-flash, where the input is the overall specific internal energy and volume, and composition. The calculation of thermodynamic equilibrium properties of multi-component multi-phase mixtures typically consumes more than three quarters of the total computational time [52] and thus imposes severe limitation on the tractable space-time resolution or even the computational feasibility of such numerical simulations. At the same time, flash algorithms have to be fault tolerant and robust, because even a method that fails to converge only once in a billion will eventually spoil the entire simulation.

The simplest case and workhorse of most phase-equilibrium calculations is the so-called PT-flash, where the equilibrium pressure and temperature of the mixture are already given. Most methods for calculating the isobaric-isothermal equilibrium volume fractions and compositions follow the approach proposed by Michelsen [53]. For solving flash problems at conditions other than constant pressure and temperature, Michelsen [54] introduced an indirect method based on nesting PT-flash calculations. For VT-flashes, for example, Michelsen's method aims to find the pressure at which the PT-flash results in the given total specific volume. This results in an optimization algorithm, in which the pressure is adjusted in the outer loop and a PT-flash is solved in the inner loop. Accordingly, UV-flashes are solved by a bivariant optimization of temperature and pressure corresponding to the given internal energy and volume.

Nested algorithms based on the PT-flash are also attractive for mixtures with many components, because they offer the possibility of adopting reduction methods [55], which provide a considerable speedup and, in addition, improve the robustness of the algorithm [56]. The first reduction method was introduced by Michelsen [55], who found that the phase-splitting problem can be fully defined by only three reduced parameters regardless of the number of components when all Binary Interaction Coefficients (BICs) are zero. Hendriks and van Bergen [57] successfully generalized the method for cases with some non-zero BICs through an eigenvalue analysis of the binary interaction matrix. Nichita and Graciaa [58] found a new set of reduced parameters for PT-flash calculations, for which they demonstrated a notable decrease in the number of iterations relative to previous reduction methods specifically near the phase boundary and the critical point.

Employing a direct VT-flash, on the other hand, could considerably reduce the computational time by eliminating the outer pressure iteration loop, provided that the method itself would be fast and robust enough. To this end, Mikyska and Firoozabadi [59] introduced an alternative formulation of the VT-flash problem based on a new thermodynamic function, the so-called volume function. They solved the problem directly by a successive-substitution iteration (SSI) algorithm with nearly the same number of iterations as a conventional PT-flash based solver requires for one inner iteration loop. Recently, Jindrova and Mikyska [60] and Nichita [61] presented methods for solving the VT-flash problem via direct minimization of the total Helmholtz free energy. Cismondi, Ndiaye, and Tavares [62] directly included the pressure equality and volume constraint in a new algorithm very similar to the PT-flash, and showed about 20 % reduction in the computational time compared to Michelsen's nested optimization technique. However, for working fluids with a large number of components, these methods lead to a significantly stronger increase of the computational time compared to the nested approach that benefits from the quadratic Newton-Raphson convergence rate in the reduced space.

In this chapter, by extending the work of Mikyska and Firoozabadi [59] and Nichita and Graciaa [58], we present a very fast and robust method for direct vapor-liquid phase-split calculations based on formulating phase equilibrium conditions in terms of the molar specific value of the volume function (instead of fugacity coefficients) and a corresponding reduction method. This new formulation allows us to solve isothermal flashes (both PT and VT) directly and with the exact analytical Jacobian matrix, which results in optimum quadratic convergence of the Newton-Raphson method. Non-isothermal cases, such as UV and HP flashes, are solved through nested univariate optimization with the corresponding isothermal flash (PT for HP and VT for UV) and the readily available specific heat capacity at constant pressure (for HP-flash) or at constant volume (for UV-flash) as exact Jacobian.

2.2. GENERAL FORMULATION

According to the Gibbsian thermodynamics [63], a multi-component system consisting of vapor and liquid phases is in equilibrium when the temperatures, pressures, and chemical potentials of phases are equal, that is,

$$T^{\mathrm{L}} = T^{\mathrm{V}}, \quad p^{\mathrm{L}} = p^{\mathrm{V}}, \quad \mu_i^{\mathrm{L}} = \mu_i^{\mathrm{V}}, \tag{2.1}$$

where T, p, and μ_i are the temperature, pressure, and chemical potential of the component $i = \{1 \dots n\}$ in a mixture with n components, and the superscripts L and V refer to the values of the liquid and vapor phases.

The pressures can be computed as a function of temperature, molar specific volume, and composition of each phase using the general form of the cubic equation of states (EOS):

$$p = \frac{RT}{(v-b)} - \frac{a}{(v+\delta_1 b)(v+\delta_2 b)}, \tag{2.2}$$

where δ_1 and δ_2 are the two volumetric EOS parameters (see below), R is the universal gas constant, and v is the molar specific volume of the mixture. Here, the energy and co-volume parameters a and b are computed using the van der Waals mixing rules:

$$a = \sum_{i=1}^{n}\sum_{j=1}^{n} z_i z_j \left(1-\kappa_{ij}\right)\sqrt{\hat{a}_i \hat{a}_j}, \tag{2.3}$$

and

$$b = \sum_{i=1}^{n} z_i \hat{b}_i, \tag{2.4}$$

in which z_i is the mole fraction of the component i, and κ_{ij} is the binary interaction coefficient between the component i and j in the mixture. $\hat{a}_i$ and $\hat{b}_i$ are energy and co-volume parameters of the pure component i, which are obtained through

$$\hat{a}_i = \Omega_a R^2 T_{ci}^2 p_{ci}^{-1} \left[1 + c(\omega_i)\left(1 - \sqrt{T/T_{ci}}\right)\right]^2, \tag{2.5}$$

and

$$\hat{b}_i = \Omega_b R T_{ci} p_{ci}^{-1}, \tag{2.6}$$

where T_{ci}, p_{ci} are critical temperature and pressure of the component i. The two constants Ω_a and Ω_b as well as the form of the function of $c(\omega_i)$, in which ω_i is the acentric factor, depend of the selected cubic EOS: for instance, in the Peng-Robinson (PR) EOS: $\delta_1 = 1 + \sqrt{2}$ and $\delta_2 = 1 - \sqrt{2}$, which result in $\Omega_a = 0.45724$, $\Omega_b = 0.0778$, and

$$c(\omega_i) = \begin{cases} 0.37464 + 1.54226\omega_i - 0.26992\omega_i^2 & \omega_i < 0.5 \\ 0.3796 + 1.485\omega_i - 0.1644\omega_i^2 + 0.01667\omega_i^3 & \omega_i \geq 0.5 \end{cases}$$

In the Soave-Redlich-Kwong (SRK) EOS, with $\delta_1 = 0$ and $\delta_2 = 1$, they are $\Omega_a = 0.42748$, $\Omega_b = 0.08664$, and

$$c(\omega_i) = 0.48508 + 1.55171\omega_i - 0.15613\omega_i^2.$$

The equality of chemical potentials is typically expressed in terms of the K-factor (also named K-value or equilibrium ratio, which is the ratio of the mole fractions in the vapor (y) and liquid (x) phases), and the fugacity coefficient derived from the Gibbs free energy. The logarithmic form of this relation for a two-phase vapor-liquid mixture is

$$\ln K_i = \ln \varphi_i^L - \ln \varphi_i^V, \quad \text{for} \quad i = 1 \ldots n, \tag{2.7}$$

with φ as the fugacity coefficient and K as the K-factor. Mikyska and Firoozabadi [59] derived a new thermodynamic function for the evaluation of the equilibrium ratio via minimization of the Helmholtz free energy that uses the specific volume, temperature, and mole fractions as its primary variables and eliminates the need for knowing the equilibrium pressure and for solving the state equation for the stable volume. They proved that the following relationship exists between the K-factor and the volume function coefficient for the liquid and vapor phases:

$$K_i = \frac{v^V \Phi_i(v^V, T, y_1, ..., y_n)}{v^L \Phi_i(v^L, T, x_1, ..., x_n)}, \tag{2.8}$$

in which Φ_i is the volume function coefficient of the component i and can be computed analytically as a function of temperature, specific volume, and mole fractions via

$$\ln \Phi_i = \int_v^{+\infty} \left[\frac{1}{v} - \frac{1}{RT} \left(\frac{\partial p}{\partial z_i} \right)_{T,v,z_{j\neq i}} \right] dv. \tag{2.9}$$

We define

$$\psi_i \equiv v\Phi_i \tag{2.10}$$

as the molar specific value of the volume function, such that, instead of using Eq. (2.7), the natural logarithm of K-factors can be calculated by

$$\ln K_i = \ln \psi_i^V - \ln \psi_i^L, \quad \text{for} \quad i = 1 \ldots n. \tag{2.11}$$

It can be shown that this (molar) specific volume function is related to the fugacity coefficient via $\psi_i = RT/p\varphi_i$. By substituting the general cubic EOS (2.2) for the evaluation of the partial pressure term in the integral (2.9), the following expression is obtained for this new thermodynamic function:

$$\ln \psi_i = \ln (v - b) - \frac{\hat{b}_i}{v - b} + \frac{av\hat{b}_i / (bRT)}{(v + \delta_1 b)(v + \delta_2 b)} - \frac{a\hat{b}_i - 2bg_i}{(\delta_1 - \delta_2) b^2 RT} \ln \left(\frac{v + \delta_1 b}{v + \delta_2 b} \right), \tag{2.12}$$

where g_i is

$$g_i = \sum_{j=1}^{n} z_j (1 - \kappa_{ij}) \sqrt{\hat{a}_i \hat{a}_j}, \quad \text{for} \quad i = 1 \ldots n. \tag{2.13}$$

The equality of chemical potentials and component material balances can be systematically expressed by means of K-factors in such a way that the vapor mole fraction θ is determined by the classic Rachford-Rice equation

$$\sum_{i=1}^{n} \frac{\hat{z}_i (K_i - 1)}{1 + \theta (K_i - 1)} = 0, \tag{2.14}$$

where $\hat{z}_i$ is the overall mole fractions of component i in the feed. Then, molar compositions of the liquid and vapor phases are obtained:

$$x_i = \frac{\hat{z}_i}{1 + \theta (K_i - 1)} \quad \text{and} \quad y_i = x_i K_i \tag{2.15}$$

for $i = 1 \ldots n$. This formulation leads to a notable reduction in the number of variables in isothermal flash calculations; we know the overall composition of the feed, therefore, knowing the n K-factors, we can compute the molar compositions of the vapor and liquid. The molar specific volumes of the phases can then be calculated by evaluating the state equations separately for vapor and liquid based on the given pressure in PT-flash calculations [64], or by solving the pressure equality equation along with a volume constraint based on the given volume in VT-flash calculations [62]. The procedure is shown in Fig. 2.1.

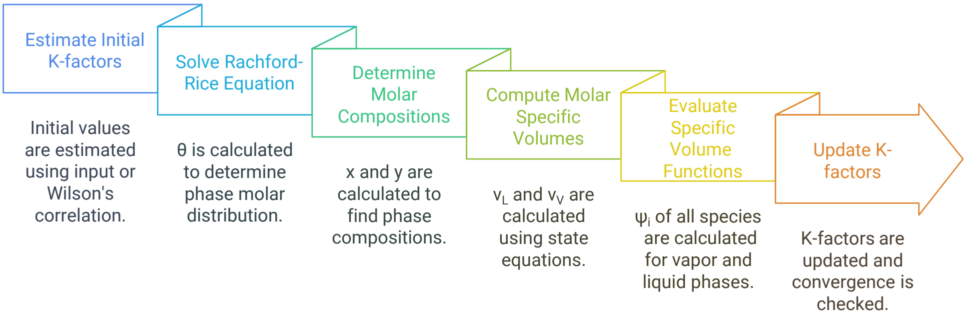

Figure 2.1.: Procedure for evaluating K-factors in multicomponent vapor–liquid equilibrium during isothermal flash calculations.

2.3. REDUCTION METHOD

The basic idea of all reduction methods is to calculate the K-factors in a lower-dimensional hyperspace spanned by parameters that are independent of the number of components in the mixture. According to the classical theory of reduction [63], such reduced parameters can be obtained by decomposing the symmetric matrix $\beta_{ij} = 1 - \kappa_{ij}$ that represents the binary interactions into matrices composed of its eigenvectors and eigenvalues, that is,

$$\beta = SDS^{-1} = SDS^{T}, \tag{2.16}$$

in which the diagonal matrix $D = diag\,(\lambda_1, ..., \lambda_n)$ represents the eigenvalues $\lambda_i (i = 1 \ldots n)$ of the matrix β, and the orthogonal matrix $S = (\vec{s}_1, ..., \vec{s}_n)$ includes the corresponding eigenvectors $\vec{s}_i (i = 1 \ldots n) = (s_{i1}, ..., s_{in})^T$. For most mixtures with a large number of components, only a few $(m < n)$ eigenvalues are significant as a result of negligible binary interactions between many components; we can hence use the following approximation for the evaluation of the entries of the matrix β:

$$\beta_{ij} = \sum_{k=1}^{n} \lambda_k s_{ki} s_{kj} \approx \sum_{k=1}^{m} \lambda_k s_{ki} s_{kj}. \tag{2.17}$$

Defining $\hat{s}_{ki} \equiv s_{ki}\sqrt{\hat{a}_i}$ as entries of the reduction matrix with size of $m \times n$, we can express $g_i (i = 1 \ldots n)$ in Eq. (2.13) as

$$g_i = \sum_{j=1}^{n} z_j (\sum_{k=1}^{m} \lambda_k s_{ki} s_{kj}) \sqrt{\hat{a}_i \hat{a}_j} = \sum_{k=1}^{m} \lambda_k \hat{s}_{ki} (\sum_{j=1}^{n} z_j \hat{s}_{kj}) = \sum_{k=1}^{m} \lambda_k \hat{s}_{ki} q_k, \tag{2.18}$$

as a function of the reduced parameters

$$q_k = \sum_{i=1}^{n} z_i \hat{s}_{ki}, \quad \text{for} \quad k = 1 \ldots m. \tag{2.19}$$

Similarly, the energy parameter a of the mixture in Eq. (2.3) can be calculated from these reduced parameters via

$$a = \sum_{i=1}^{n}\sum_{j=1}^{n} z_i z_j (\sum_{k=1}^{m} \lambda_k s_{ki} s_{kj}) \sqrt{\hat{a}_i \hat{a}_j} = \sum_{k=1}^{m} \lambda_k (\sum_{i=1}^{n} z_i \hat{s}_{ki})^2 = \sum_{k=1}^{m} \lambda_k q_k^2. \tag{2.20}$$

Then, an equation for evaluation of the molar specific value of the volume functions, ψ_i, can be derived by substituting $g_i (i = 1 \dots n)$ and a into Eq. (2.12) using Eqs. (2.18) and (2.20):

$$\ln \psi_i = \sum_{k=1}^{m} h_k \hat{s}_{ki} + h_{m+1} \hat{b}_i + h_{m+2}, \quad \text{for} \quad i = 1 \dots n, \tag{2.21}$$

where coefficients h are functions of $q_k (k = 1 \dots m)$, b, and v:

$$\begin{aligned} h_k &= 2\lambda_k q_k \ln\left[(v+\delta_1 b)(v+\delta_2 b)^{-1}\right]\left([\delta_1-\delta_2]bRT\right)^{-1};\ k = 1\dots m \\ h_{m+1} &= -(v-b)^{-1} + (RTb^2)^{-1} \sum_{k=1}^{m} \lambda_k q_k^2 \{vb(v+\delta_1 b)^{-1}(v+\delta_2 b)^{-1} \dots \\ &\quad - \ln\left[(v+\delta_1 b)(v+\delta_2 b)^{-1}\right](\delta_1-\delta_2)^{-1}\}, \\ h_{m+2} &= \ln(v-b). \end{aligned} \tag{2.22}$$

Because the entries of reduction matrix $\hat{s}_{ki}$ and $\hat{b}_i$ are equal in the liquid and vapor phases, all K-factors can be computed from:

$$\ln K_i = \sum_{k=1}^{m} h_k^{\Delta} \hat{s}_{ki} + h_{m+1}^{\Delta} \hat{b}_i + h_{m+2}^{\Delta}, \tag{2.23}$$

with $h_\alpha^\Delta \equiv h_\alpha^V - h_\alpha^L$ $(\alpha = 1, \dots, m+2)$. Performing the calculations in the h-space with size $m+2$ leads to another remarkable reduction in the number of variables in the multi-component flash calculation, i.e., to dimension $m+2$ instead of n regardless of the number of components in the mixture.

We note that these h-based reduced parameters are Lagrange multipliers of the classical reduced parameters, similar to the reduced parameters introduced by Nichita and Graciaa [58]. Hence, the reduced-space iteration has a better condition number and will converge faster than other methods [65].

For non-isothermal flash calculations, it is necessary to compute additional thermodynamic quantities such as the specific molar enthalpy, internal energy, and heat capacities at constant volume and pressure. They are typically calculated as a summation of the ideal part, which is here evaluated as a function of temperature using the 9-coefficient NASA polynomials [66], and the excess part obtained from the state equation using the reduced parameters. Overall mixture quantities are computed through

$$\eta^{mix} = (1-\theta)\,\eta^L + \theta\eta^V, \tag{2.24}$$

where $\eta \in \{u, h, c_v, c_p\}$ are specific internal energy, enthalpy, and heat capacities at constant volume and pressure. The molar specific internal energy of the liquid or vapor (superscripts L and V are not repeated for brevity) is computed by means of

$$u = \sum_{i=1}^{n} z_i u_i^{ig}(T) + \frac{a - T\left(\partial a/\partial T\right)}{\left(\delta_2 - \delta_1\right) b} \ln\left(\frac{v + \delta_1 b}{v + \delta_2 b}\right), \tag{2.25}$$

where u_i^{ig} is the ideal gas (NASA polynomial) molar specific internal energy of pure component i; a is obtained from Eq. (2.20) and its first temperature derivative is

$$\frac{\partial a}{\partial T} = 2 \sum_{k=1}^{m} \lambda_k q_k \frac{\partial q_k}{\partial T}, \tag{2.26}$$

with

$$\frac{\partial q_k}{\partial T} = -\frac{R}{2}\sqrt{\frac{\Omega_a}{T}} \sum_{i=1}^{n} \frac{z_i c(\omega_i) s_{ki}}{\operatorname{sgn}(\vartheta_i)} \sqrt{\frac{T_{ci}}{p_{ci}}}, \tag{2.27}$$

where $\operatorname{sgn}(\vartheta_i)$ is the sign function of variable $\vartheta_i = 1 + c(\omega_i)(1 - \sqrt{T/T_{ci}})$ and its value is equal to plus one for $\vartheta_i > 0$ and equal to minus one otherwise. The molar specific enthalpy of the mixture is defined as

$$h = u + pv, \tag{2.28}$$

where p is either known or computed via Eq. (2.2). The molar specific heat capacity at constant volume for a multi-component mixture can be computed via

$$c_v = \sum_{i=1}^{n} z_i c_{v,i}^{ig}(T) + \frac{T\left(\partial^2 a/\partial T^2\right)}{\left(\delta_1 - \delta_2\right) b} \ln\left(\frac{v + \delta_1 b}{v + \delta_2 b}\right). \tag{2.29}$$

Here, $c_{v,i}^{ig}$ is the molar specific heat capacity of the ideal gas at constant volume for the component i, which is computed as a function of temperature using NASA polynomials, and the second derivative $\partial^2 a/\partial T^2$ is

$$\frac{\partial^2 a}{\partial T^2} = 2 \sum_{k=1}^{m} \lambda_k \left[\left(\frac{\partial q_k}{\partial T}\right)^2 + q_k \frac{\partial^2 q_k}{\partial T^2}\right], \tag{2.30}$$

with

$$\frac{\partial^2 q_k}{\partial T^2} = \frac{R}{4T}\sqrt{\frac{\Omega_a}{T}} \sum_{i=1}^{n} \frac{z_i c(\omega_i) s_{ki}}{\operatorname{sgn}(\vartheta_i)} \sqrt{\frac{T_{ci}}{p_{ci}}}. \tag{2.31}$$

The molar specific heat capacity at constant pressure of the mixture is computed from the thermodynamic relation:

$$c_p = c_v - T \frac{\left(\partial p/\partial T\right)^2}{\partial p/\partial v}, \tag{2.32}$$

where the derivatives of pressure with respect to the specific volume and temperature are

$$\frac{\partial p}{\partial v} = -\frac{RT}{(v-b)^2} + \frac{a\left[2v + (\delta_1 + \delta_2)\, b\right]}{(v+\delta_1 b)^2 (v+\delta_2 b)^2}, \tag{2.33}$$

and

$$\frac{\partial p}{\partial T} = \frac{R}{v-b} - \frac{\partial a/\partial T}{(v+\delta_1 b)\,(v+\delta_2 b)}. \tag{2.34}$$

2.4. NUMERICAL ALGORITHMS

2.4.1. ISOTHERMAL FLASHES

In this section, numerical solution procedures for two important isothermal phase splitting cases, PT and VT-flashes, are presented. In Algorithm 1, we need to estimate the initial K-factors at Step 0: if there is no promising data available (blind flash), Wilson's correlation

$$K_i = (p_{ci}/p)\exp\left[5.373\,(1+\omega_i)\,(1 - T_{ci}/T)\right], \quad \text{for} \quad i = 1\dots n \tag{2.35}$$

is commonly employed for the initialization of the iteration. This is straightforward if the pressure and temperature are known as in the PT-flash; in the case of a blind VT-flash, however, the pressure is unknown. In this case, one could estimate the pressure from the state equation of the mixture by using the total specific volume $\hat{v}$, temperature T, and overall mole fractions $\hat{z}_i$ as an input, but this will result in negative pressures in many cases. A simple remedy is to set a minimum value in pressure estimation [62], or to employ the initialization method based on the vapor pressures of the components [67]. We propose to use the geometric average of the

Algorithm 1: VT and PT flash calculations

```
Result: K-factors of a multi-component vapor-liquid equilibrium
Step 0: Estimate initial values of K-factors using the input values or via the Wilson's
  correlation (Eq. 2.35) in case of blind flashes;
while convergence criteria not met do
    Step 1: Calculate $\theta$ by solving the Rachford-Rice equation (Eq. 2.14);
    Step 2: Determine molar compositions $x$ and $y$ (Eq. 2.15) and then compute
      parameters $q_k$ and $b$ for both phases (Eqs. 2.19 and 2.4);
    Step 3: Compute molar specific volumes $v^L$ and $v^V$ using pressure equality and
      volume constraint equations in case of VT-flash and two state equations of liquid
      and vapor in case of PT-flash;
    Step 4: Evaluate Jacobian matrix and update the reduced principal variables for the
      Newton-Raphson iteration or update the principal variables via their definitions in
      case of the successive substitution method;
    Step 5: Update K-factors (Eq. 2.23) and check the convergence criteria (Eq. 2.71).
end
```

pressures of the dew and bubble points estimated as

$$p \approx \sqrt{\sum_{i=1}^{n} \hat{z}_i p_i^{sat} / \sum_{i=1}^{n} \frac{\hat{z}_i}{p_i^{sat}}}, \tag{2.36}$$

where p_i^{sat} is the vapor pressure of the pure component i, which can be estimated from Raoult's law and Wilson's correlation, instead of using other excess experimental data in the form of Antoine equation.

In Step 1, we need to solve the Rachford-Rice Eq. (2.14) to determine the vapor mole fraction. Usually, a Newton method is coupled with a bisection method for reasons explained by Michelsen and Mollerup [64]. In order to preserve the fully quadratic convergence rate of the Newton method, we rather use the convex transformation technique of Nichita and Leibovici [68]. In the convex transformation technique, the first and last indexes are assigned to the components with maximum and minimum K-factors, and vectors $c_i = 1/(1 - K_i)$ and $d_i = (c_1 - c_i)/(c_n - c_1)$ are obtained for all components. Two convex functions of the variable $\sigma = (\theta - c_1)/(c_n - \theta)$, can be then computed:

$$G(\sigma) = (1 + \sigma)S(\sigma), \tag{2.37a}$$
$$H(\sigma) = -\sigma(1 + \sigma)S(\sigma), \tag{2.37b}$$

where

$$S(\sigma) = \sum_{i=1}^{n} \frac{z_i}{d_i + \sigma(1 + d_i)}. \tag{2.38}$$

For any starting value σ_0 in the range of $(0, +\infty)$, monotonic convergence of the Newton iteration is guaranteed for one of these two functions. The estimated value of σ is updated via

$$\sigma_{new} = \begin{cases} \sigma - G(\sigma)/G'(\sigma), & G(\sigma) > 0 \\ \sigma - H(\sigma)/H'(\sigma), & G(\sigma) < 0 \end{cases} \tag{2.39}$$

where G' and H' are derivatives of G and H with respect to σ:

$$G'(\sigma) = S(\sigma) + (1 + \sigma)S'(\sigma), \tag{2.40a}$$
$$H'(\sigma) = -(1 + 2\sigma)S(\sigma) - \sigma(1 + \sigma)S'(\sigma), \tag{2.40b}$$

and

$$S'(\sigma) = \sum_{i=1}^{n} \frac{-z_i(1 + d_i)}{(d_i + \sigma(1 + d_i))^2}. \tag{2.41}$$

The Newton iteration is repeated with σ_{new} until the convergence criteria are met. The vapor mole fraction is then obtained via $\theta = (c_1 + \sigma c_n)/(1 + \sigma)$.

In Step 2, the molar compositions of the liquid x_i and the vapor y_i for $(i = 1 \ldots n)$ are calculated using Eq. (2.15). Then m reduced parameters q_k and the mixture co-volume parameter b are obtained using Eqs. (2.19) and (2.4)for both phases.

In Step 3, the energy parameter a is computed for the liquid and vapor phases using their m reduced parameters via Eq. (2.20). For the case of PT flash, in which the value of the equilibrium pressure p is given, the specific volume is then calculated for the vapor and liquid phases separately. For the general cubic EOS Eq. (2.2) this means finding the roots of the cubic equation that is written below for the liquid phase:

$$v_L^3 + \varrho_2 v_L^2 + \varrho_1 v_L + \varrho_0 = 0, \tag{2.42}$$

where

$$\begin{aligned}
\varrho_0 &= -a_L b_L/p - (b_L + RT/p)\,\delta_1\delta_2 b_L^2, \\
\varrho_1 &= \delta_1\delta_2 b_L^2 + a_L/p - (\delta_1 + \delta_2)\, b_L\,(b_L + RT/p)\,, \\
\varrho_2 &= (\delta_1 + \delta_2 - 1)\, b_L - RT/p.
\end{aligned}$$

The same equation holds for the vapor phase. We use Cardino's algorithm to determine all roots of Eq. (2.42). If more than one real root is found, the root associated with the lowest Gibbs free energy is selected [64].

For the VT-flash, in which the value of the total molar specific volume $\hat{v}$ is given, we first compute the molar specific volume of one phase from the volume constraint $(1-\theta)v_L + \theta v_V = \hat{v}$ and then substitute it into the pressure equality equation. The resulting equation is a quintic function of the other phase specific volume that is given below for the liquid phase:

$$\varsigma_5 v_L^5 + \varsigma_4 v_L^4 + \varsigma_3 v_L^3 + \varsigma_2 v_L^2 + \varsigma_1 v_L + \varsigma_0 = 0, \tag{2.43}$$

where

$$\begin{aligned}
\varsigma_0 = {} & (\alpha_2^L\alpha_5^V - \alpha_2^V\alpha_5^L)\theta^3 - (\alpha_5^L\alpha_1^V - \alpha_4^V\alpha_2^L)\hat{v}\theta^2 + (\alpha_2^L\alpha_3^V - \alpha_5^L)\theta\hat{v}^2 + \alpha_2^L\hat{v}^3, \\
\varsigma_1 = {} & \left(\alpha_1^L\alpha_5^V - \alpha_5^L\alpha_1^V + \alpha_4^V\alpha_2^L - \alpha_2^V\alpha_4^L\right)\theta^3 + \left(\alpha_1^L\alpha_3^V + 3\alpha_2^L - \alpha_4^L\right)\hat{v}^2\theta + (\hat{v}\alpha_1^L - 3\alpha_2^L)\hat{v}^2 \ldots \\
& + 2(\alpha_5^L - \alpha_2^L\alpha_3^V)\hat{v}\theta + (\alpha_1^L\alpha_4^V - \alpha_1^V\alpha_4^L + 2\alpha_2^L\alpha_3^V - 2\alpha_5^L)\hat{v}\theta^2 + (\alpha_5^L\alpha_1^V - \alpha_4^V\alpha_2^L)\theta^2, \\
\varsigma_2 = {} & (\alpha_1^L\alpha_4^V - \alpha_1^V\alpha_4^L + \alpha_2^L\alpha_3^V - \alpha_2^V\alpha_3^L - \alpha_5^L + \alpha_5^V)\theta^3 + (\hat{v}^2 - 3\hat{v}\alpha_1^L + 3\alpha_2^L)\hat{v} \ldots \\
& + (2\alpha_1^L\alpha_3^V - \alpha_1^V\alpha_3^L + 3\alpha_2^L - 2\alpha_4^L + \alpha_4^V)\hat{v}\theta^2 + (\alpha_1^V\alpha_4^L - \alpha_1^L\alpha_4^V - 2\alpha_2^L\alpha_3^V + 2\alpha_5^L)\theta^2 \ldots \\
& + (3\alpha_1^L - \alpha_3^L + \alpha_3^V)\hat{v}^2\theta + 2(\alpha_4^L - \alpha_1^L\alpha_3^V - 3\alpha_2^L)\hat{v}\theta + (\alpha_2^L\alpha_3^V - \alpha_5^L)\theta, \\
\varsigma_3 = {} & (\alpha_1^L\alpha_3^V - \alpha_1^V\alpha_3^L + \alpha_2^L - \alpha_2^V - \alpha_4^L + \alpha_4^V)\theta^3 + (3\alpha_1^L - \alpha_1^V - 2\alpha_3^L + 2\alpha_3^V)\hat{v}\theta^2 \ldots \\
& + (\alpha_1^V\alpha_3^L - 2\alpha_1^L\alpha_3^V - \alpha_4^V - 3\alpha_2^L + 2\alpha_4^L)\theta^2 + (-6\alpha_1^L + 2\alpha_3^L - 2\alpha_3^V)\hat{v}\theta \ldots \\
& + (2\hat{v}^2 + \alpha_1^L\alpha_3^V + 3\alpha_2^L - \alpha_4^L)\theta - 3\hat{v}^2 + 3\hat{v}\alpha_1^L - \alpha_2^L, \\
\varsigma_4 = {} & [(\alpha_1^L - \alpha_1^V - \alpha_3^L + \alpha_3^V)\theta^2 + (\hat{v} - 2\alpha_1^L + \alpha_3^L - \alpha_3^V)\theta - 3\hat{v} + \alpha_1^L](\theta - 1), \\
\varsigma_5 = {} & -(\theta - 1)^2\ .
\end{aligned}$$

Here, parameters $\alpha_i (i = 1 \ldots 5)$ are computed via the following expressions using the liquid and vapor co-volume and energy parameters:

$$\begin{aligned} &\alpha_1 = b(\delta_1+\delta_2) - a/RT,\ \ \alpha_2 = b\left(b\delta_1\delta_2 + a/RT\right),\ \ \alpha_3 = b\left(\delta_1\delta_2 - 1\right), \\ &\alpha_4 = b^2\left(\delta_1+\delta_2-\delta_1\delta_2\right),\ \ \alpha_5 = -b^3\delta_1\delta_2. \end{aligned} \tag{2.44}$$

Since there is no analytical solution, Eq. (2.43) has to be solved by iterative methods to obtain v_L. We use a Newton method with a starting point very close to the co-volume of the mixture in this study. Afterwards, the vapor's specific volume is obtained through the volume constraint $v_V = \left[\hat{v} - (1-\theta)v_L\right]/\theta$.

In Step 4, we update the principal variables via their definitions in the first iteration (corresponding to a successive substitution iteration (SSI)) or evaluate Jacobian matrix and update the reduced principal variables for the Newton-Raphson iteration (NRI). In the case of the SSI, the new values of the reduced principal variables are obtained as the difference between the h values of the vapor and liquid phase calculated via Eq. (2.22). In the case of the NRI, first the error functions

$$e_\alpha = h_\alpha^V - h_\alpha^L - h_\alpha^\Delta,\quad \text{for}\ \ \alpha = 1\ldots m+2 \tag{2.45}$$

and the associated Jacobian matrix:

$$J_{\alpha\beta} = \frac{\partial e_\alpha}{\partial h_\beta^\Delta} = \frac{\partial h_\alpha^V}{\partial h_\beta^\Delta} - \frac{\partial h_\alpha^L}{\partial h_\beta^\Delta} - \delta_{\alpha\beta},\quad \text{for}\ \ \alpha,\beta = 1\ldots m+2 \tag{2.46}$$

are calculated, in which $\delta_{\alpha\beta}$ is the Kronecker delta function. Next, the resulting set of linear equations $J\Delta\vec{h}^\Delta = \vec{e}$, can be solved by using the Gauss elimination method with partial pivoting to compute $\Delta\vec{h}^\Delta = \vec{h}^\Delta_{new} - \vec{h}^\Delta_{old}$ and the new values of the reduced principal variables

$$\vec{h}^\Delta_{new} = \vec{h}^\Delta_{old} + \Delta\vec{h}^\Delta. \tag{2.47}$$

In order to find the analytical expressions of the entries in the Jacobian matrix (2.46), we used the classical $m+2$ reduced parameters including $q_k (k = 1\ldots m)$, b, and θ as the helping variables in the derivative chain rule for the required partial derivatives

$$\frac{\partial h_\alpha^j}{\partial h_\beta^\Delta} = \sum_{k=1}^{m}\left(\frac{\partial h_\alpha^j}{\partial q_k^j} + \frac{\partial h_\alpha^j}{\partial v^j}\frac{\partial v^j}{\partial q_k^j}\right)\frac{\partial q_k^j}{\partial h_\beta^\Delta} + \left(\frac{\partial h_\alpha^j}{\partial b^j} + \frac{\partial h_\alpha^j}{\partial v^j}\frac{\partial v^j}{\partial b^j}\right)\frac{\partial b^j}{\partial h_\beta^\Delta} + \frac{\partial h_\alpha^j}{\partial v^j}\frac{\partial v^j}{\partial \theta}\frac{\partial \theta}{\partial h_\beta^\Delta}, \tag{2.48}$$

for j being L and V. The required partial derivatives of the coefficients h are obtained by Eq. (2.22). The derivatives with respect to the reduced variable q_k are

$$\begin{aligned}
\partial h_\alpha/\partial q_k &= 2\delta_{\alpha k}\lambda_k \ln[(v+\delta_1 b)(v+\delta_2 b)^{-1}]/[(\delta_1-\delta_2)bRT];\ \ \alpha = 1:m\\
\partial h_{m+1}/\partial q_k &= 2\lambda_k q_k\{vb/\left[(v+\delta_1 b)(v+\delta_2 b)\right]\ldots\\
&\quad -\ln\left[(v+\delta_1 b)/(v+\delta_2 b)\right]/(\delta_1-\delta_2)\}/(RTb^2),\\
\partial h_{m+2}/\partial q_k &= 0.
\end{aligned}\tag{2.49}$$

In addition, the derivatives with respect to the co-volume of the phase are

$$\begin{aligned}
\partial h_\alpha/\partial b &= 2\lambda_\alpha q_\alpha\{vb/\left[(v+\delta_1 b)(v+\delta_2 b)\right]\ldots\\
&\quad -\ln\left[(v+\delta_1 b)/(v+\delta_2 b)\right]/(\delta_1-\delta_2)\}/(RTb^2);\ \ \alpha = 1:m\\
\partial h_{m+1}/\partial b &= -1/(v-b) + av\{2\ln[(v+\delta_1 b)/(v+\delta_2 b)]/[bv(\delta_1-\delta_2)]\ldots\\
&\quad -[4\,\delta_1\delta_2\,b^2 + 3\,vb(\delta_1+\delta_2) + 2\,v^2]/[(v+\delta_1 b)(v+\delta_2 b)]^2\}/(RTb^2),\\
\partial h_{m+2}/\partial b &= -1/(v-b),
\end{aligned}\tag{2.50}$$

where a is computed via Eq. (2.20) as a function of reduced parameters The derivatives respect to the specific volume of the phase are

$$\begin{aligned}
\partial h_\alpha/\partial v &= -2\lambda_\alpha q_\alpha/[RT(v+\delta_1 b)(v+\delta_2 b)];\ \ \alpha = 1:m\\
\partial h_{m+1}/\partial v &= a[2\,b\delta_1\delta_2 + v(\delta_1+\delta_2)]/[RT\,(v+\delta_1 b)^2(v+\delta_2 b)^2] + 1/(v-b),\\
\partial h_{m+2}/\partial v &= 1/(v-b).
\end{aligned}\tag{2.51}$$

Next, the partial derivatives of the specific volume in Eq. (2.48) are obtained through the implicit function theorem. For PT-flashes, we directly utilize the general cubic EOS (2.2) for each phase as follows:

$$\partial v^j/\partial q_k^j = -(\partial p/\partial q_k)^j/(\partial p/\partial v)^j,\quad \text{for}\ \ j = L, V \tag{2.52}$$

with $\partial p/\partial v$ from Eq. (2.33). Using the relationship between a and q_k, we can compute $\partial p/\partial q_k$ as

$$\partial p/\partial q_k = -2\lambda_k q_k/[(v+\delta_1 b)(v+\delta_2 b)]. \tag{2.53}$$

Moreover, the derivatives with respect to the co-volume of the mixture are

$$\partial v^j/\partial b^j = -(\partial p/\partial b)^j/(\partial p/\partial v)^j,\quad \text{for}\ \ j = L, V \tag{2.54}$$

with

$$\partial p/\partial b = RT/(v-b)^2 + a[2\,\delta_1\delta_2 b + v(\delta_1+\delta_2)]/[(v+\delta_1 b)(v+\delta_2 b)]^2. \tag{2.55}$$

It is obvious that in PT-flashes, the partial derivatives of the specific volumes with respect to the vapor mole fraction are zero, i.e.

$$\partial v^j/\partial\theta = 0,\quad \text{for}\ \ j = L, V. \tag{2.56}$$

Using the implicit function theorem for VT-flashes, we define the function $f \equiv p^L - p^V$ and then compute the required derivatives as

$$\partial v^j/\partial q_k^j = -(\partial f/\partial q_k^j)/(\partial f/\partial v^j), \quad \text{for} \quad j = L, V, \tag{2.57}$$

$$\partial v^j/\partial b^j = -(\partial f/\partial b^j)/(\partial f/\partial v^j), \quad \text{for} \quad j = L, V, \tag{2.58}$$

where partial derivatives of f can be computed using the chain rule. For example, when $j = L$, we obtain

$$\partial f/\partial v^L = (\partial p/\partial v)^L - (\partial p/\partial v)^V (\partial v^V/\partial v^L), \tag{2.59}$$

$$\partial f/\partial q_k^L = (\partial p/\partial q_k)^L - (\partial p/\partial q_k)^V (\partial q_k^V/\partial q_k^L), \tag{2.60}$$

$$\partial f/\partial b^L = (\partial p/\partial b)^L - (\partial p/\partial b)^V (\partial b^V/\partial b^L), \tag{2.61}$$

along with $\partial v^V/\partial v^L = \partial q_k^V/\partial q_k^L = \partial b^V/\partial b^L = (\theta - 1)/\theta$. Subsequently, the partial derivatives of specific volumes with respect to the vapor mole fraction are computed through

$$\partial v^j/\partial \theta = -(\partial f/\partial \theta)^j/(\partial f/\partial v^j), \quad \text{for} \quad j = L, V, \tag{2.62}$$

where $\partial f/\partial \theta$ for the liquid and vapor phases can be calculated as follows:

$$\begin{aligned}(\partial f/\partial \theta)^L = {} & \theta^{-1} \sum_{k=1}^{m} (q_k^L - q_k^V)(\partial f/\partial q_k^V) \\ & + (b^L - b^V)(\partial f/\partial b^V) + (v^L - v^V)(\partial f/\partial v^V),\end{aligned} \tag{2.63}$$

$$\begin{aligned}(\partial f/\partial \theta)^V = {} & (1-\theta)^{-1} \sum_{k=1}^{m} (q_k^V - q_k^L)(\partial f/\partial q_k^L) \\ & + (b^V - b^L)(\partial f/\partial b^L) + (v^V - v^L)(\partial f/\partial v^L).\end{aligned} \tag{2.64}$$

Finally, partial derivatives of the reduced parameters $q_k (k = 1 \ldots m)$ as well as b with respect to principal variables $h_\beta^\Delta (\beta = 1 \ldots m+2)$ can be obtained via their definitions: for all m reduced parameters

$$\partial q_k/\partial h_\beta^\Delta = \sum_{i=1}^{n} \left(\partial z_i/\partial h_\beta^\Delta\right) \hat{s}_{ki}, \tag{2.65}$$

and for the co-volume parameter

$$\partial b/\partial h_\beta^\Delta = \sum_{i=1}^{n} \left(\partial z_i/\partial h_\beta^\Delta\right) \hat{b}_i. \tag{2.66}$$

In both equations, we need the derivatives of the phase mole fractions z_i, which are equal to x_i and y_i for liquid and vapor phases, with respect to the principal variables. Using the Rachford-Rice equation and the definition of the equilibrium ratio, we obtain

$$\partial x_i/\partial h_\beta^\Delta = d_i\left[\theta\partial K_i/\partial h_\beta^\Delta + (K_i-1)\partial\theta/\partial h_\beta^\Delta\right], \tag{2.67}$$

and

$$\partial y_i/\partial h_\beta^\Delta = d_i\left[(1-\theta)\partial K_i/\partial h_\beta^\Delta + K_i(K_i-1)\partial\theta/\partial h_\beta^\Delta\right], \tag{2.68}$$

where $d_i = -z_i/[1+\theta(K_i-1)]^2$. The partial derivative with respect to the principal variables is expressed as follows for all K-values:

$$\begin{aligned} \partial K_i/\partial h_\beta^\Delta &= K_i\hat{s}_{\beta i}, \text{ for } \beta = 1\ldots m \\ \partial K_i/\partial h_{m+1}^\Delta &= K_i\hat{b}_i, \\ \partial K_i/\partial h_{m+2}^\Delta &= K_i, \end{aligned} \tag{2.69}$$

and for the vapor mole fraction and the index in the range from $\beta = 1$ to $m+2$:

$$\partial\theta/\partial h_\beta^\Delta = \sum_{i=1}^{n} d_i(\partial K_i/\partial h_\beta^\Delta)/\sum_{i=1}^{n} d_i(K_i-1)^2. \tag{2.70}$$

In Step 5, the logarithm of the equilibrium ratios is computed from the updated principal variables via Eq. (2.23) and the following convergence criterion is checked:

$$\left\|\ln K_i^{new} - \ln K_i^{old}\right\| \le \varepsilon_k. \tag{2.71}$$

We propose and use $\varepsilon_k = 10^{-2}$ for the initial SSI and $\varepsilon_k = 10^{-10}$ for the NRI, but one SSI step is usually enough for most cases. If the solution does not converge, we jump back to step 1 with the new K-values.

2.4.2. NON-ISOTHERMAL FLASHES

This section explains the numerical solution method for the HP- and UV-flashes. The main idea is to use the most appropriate isothermal flash (that is, PT for HP and VT for UV) and iterate its input temperature in such a way that the

Algorithm 2: UV and HP flash calculations

```
Result: Equilibrium temperature

Step 0: Estimate the initial value of temperature;
while convergence criteria not met do
    Step 1: Execute one VT-flash or PT-flash according to the availability of the specific
      volume or pressure and the latest available temperature;

    Step 2: In case of UV-flash, compute the specific internal energy and $c_v$ of the
      mixture, or in case of HP-flash, compute the specific enthalpy and $c_p$ of the
      mixture;

    Step 3: Update the temperature and check the convergence criteria;
end
```

specific internal energy (UV) or enthalpy (HP) converges to the given value. The numerical procedure is summarized in Algorithm 2 and explained more in detail in the following:

In Step 0, the temperature of the mixture is estimated. To provide an initial guess at regions close to the critical point or near phase boundaries, one can estimate the temperature by considering the mixture as a single-phase mixture and then iterate the EOS for the given specific internal energy or enthalpy.

In Step 1, we perform an isothermal flash calculation using the method that most closely corresponds to the targeted non-isothermal problem, that is, we perform a PT-flash in the case of the HP problem and a VT-flash for the case of the UV-flash. It is clear that for the first iteration these iso-thermal flashes require an estimate of the K-factors (it might exist from previous data otherwise those can be estimated via Wilson's correlation as discussed above) whereas for the subsequent iterations, the previously computed values of K-factors can be used to accelerate computations.

In Step 2, the internal energy of the mixture u^{mix} and its derivatives with respect to the temperature, i.e. c_v^{mix}, for the case of UV-flash and the specific enthalpy of the mixture h^{mix} and its derivative with respect to the temperature, i.e. c_p^{mix}, for the case of HP-flash are computed. All derivatives are computed from the reduced variables as explained in the previous section.

In Step 3, the estimated temperature is updated by a Newton iteration with line search $\mathscr{L}$ in the range of $[0,1]$ for the case of UV-flashes:

$$T^{new} = T - \mathscr{L}(\hat{u} - u^{mix})/c_v^{mix} \tag{2.72}$$

and for the case of HP-flashes:

$$T^{new} = T - \mathscr{L}(\hat{h} - h^{mix})/c_p^{mix} \tag{2.73}$$

Using the line search $\mathscr{L}$ ensures global convergence of the algorithm and renders the temperature initial guess less important. Subsequently, the relative error is computed, i.e. $\varepsilon_r = |(\hat{h} - h^{mix})/\hat{h}|$ or $\varepsilon_r = |(\hat{u} - u^{mix})/\hat{u}|$ for HP or UV-flashes, respectively. Steps 1 to 3 are repeated until the convergence criterion is satisfied, for the calculations presented in this chapter until $\varepsilon_r < 10^{-10}$.

2.5. Numerical Results

We have developed a Fortran implementation of the proposed flash algorithms for the four discussed isothermal and non-isothermal flash calculations, and tested it for a large number of different multi-component mixtures and different cubic EOS. The representative selected cases that we will discuss in the following use PR EOS, and the values for the critical temperatures, critical pressures, and acentric factors are listed in Table 2.1.

Table 2.1.: Species critical properties and acentric factors.

Name	T_c [K]	p_c [bar]	ω [-]	Name	T_c [K]	p_c [bar]	ω [-]
C_1	190.6	45.4	0.008	nC_6	507.5	30.1	0.305
C_2	305.4	48.2	0.098	nC_7	540.3	27.4	0.305
C_3	369.8	41.9	0.152	nC_8	568.8	24.9	0.396
nC_4	425.2	37.5	0.193	nC_{10}	617.9	21.0	0.484
nC_5	469.6	33.3	0.251	nC_{14}	691.9	15.2	0.747

2.5.1. Convergence Behavior and Robustness

Two mixtures with specified compositions including a synthetic condensate gas and synthetic oil are selected in order to validate and evaluate the performance of the proposed flash algorithms. In each test case, we first generated the phase diagram for a wide range of temperatures and pressures using the PT-flash. Next, VT-flashes have been conducted along isochores drawn on the phase diagram. For each case, we will discuss in detail the vapor-liquid equilibrium result and the convergence graphs for three algorithmically challenging points that are selected close to the critical point and near the phase envelope boundaries. The first fluid is the Y8 mixture introduced by Yarborough [69]. It is a six-component synthetic gas condensate of normal alkanes including 80.97 C_1, 5.66 C_2, 3.06 C_3, 4.57 nC_5, 3.30 nC_7, and 2.44 nC_{10} mole percents with a zero binary interaction matrix. With our reduction method, the latter results in only three governing equations for the reduced variables. The second fluid is the MY10 mixture introduced by Metcalfe and Yarborough [70]. It is a ten-component mixture with overall molar fractions of 0.35 C_1, 0.03 C_2, 0.04 C_3, 0.06 nC_4, 0.04 nC_5, 0.03 nC_6, 0.05 nC_7, 0.05 nC_8, 0.30 nC_{10}, and 0.05 nC_{14}. For this mixture, all binary interaction coefficients are zero except those between the methane and the other components as reported by Firoozabadi and Pan [71]. This sparse binary interaction matrix results in three non-zero eigenvalues $\lambda_1 = 9.9574$, $\lambda_2 = 0.0707$ and $\lambda_3 = -0.0280$.

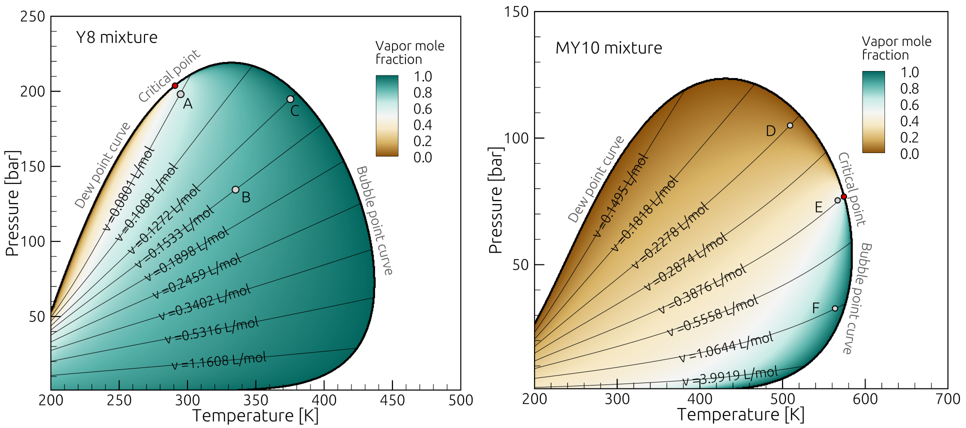

Figure 2.2.: Phase diagrams for the Y8 and MY10 mixtures including isochores and the states selected for the detailed analysis of the convergence of the flash algorithms.

In Fig. 2.2, the phase diagrams for the two mixtures with contours of vapor mole fractions are shown. These diagrams are generated without any convergence problems of the blind PT-flashes over a fine Cartesian grid with 800 × 800 nodes for the pressure-temperature range shown in the figure. This very fine grid is selected to check the applicability of the PT-flash algorithm at many different conditions that are very close to the phase boundaries and the critical point, where other methods may converge either very slowly or not at all.

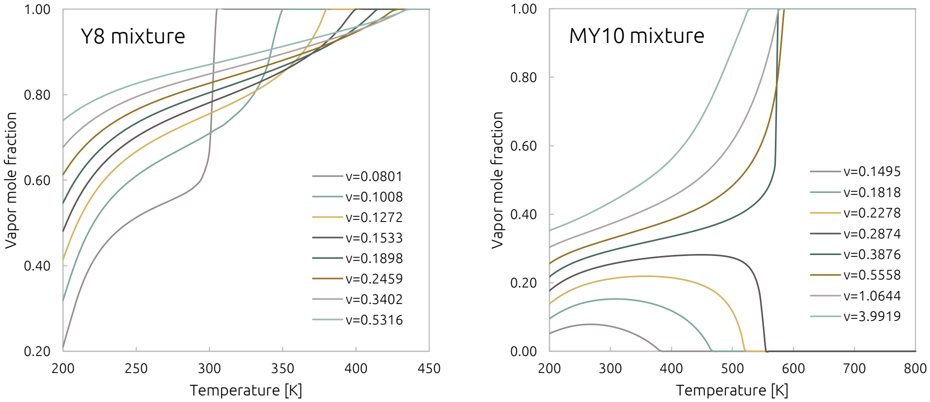

Figure 2.3.: Vapor mole fraction curves as a function of temperature generated by the VT-flash algorithm corresponding to the lines shown in Fig. 2.2.

Next, VT-flashes have been conducted along isochores drawn on the phase diagram. Selected isochoric lines are drawn in Fig. 2.2 to show the pressure evolution during constant volume heating or cooling of a typical condensate gas or synthetic oil. The corresponding vapor mole fraction curves shown in Fig. 2.3 were computed using the proposed VT-flash algorithm with a starting temperature of 200 K and a step size of 1 K up to the saturation point. The retrograde behavior of MY10 for specific volumes lower than or equal to 0.2874 L/mol is an interesting phenomenon: by increasing the temperature from 200 K the vapor mole fraction first increases with temperature and then decreases to zero. We verified that the results agree with the previous implementation of Michelson's methods [72] and that the results of the VT-flashes are the same as those obtained with the PT-flashes up to machine round-off precision.

Table 2.2.: Total mixture properties of the test fluids.

	Y8 mixture			MY10 mixture		
	Point A	Point B	Point C	Point D	Point E	Point F
T [K]	295.40000	335.20000	375.30000	509.10000	566.60000	563.50000
p [bar]	198.10000	134.50000	194.80000	104.90000	75.400000	32.700000
v [L/mol]	0.0805680	0.1533446	0.1273056	0.2280903	0.3846589	1.0596464
h [KJ/mol]	-94.704181	-90.636841	-87.895981	-142.74142	-124.94053	-120.73426
u [KJ/mol]	-96.300235	-92.699326	-90.375895	-145.13409	-127.84086	-124.19930

Table 2.3.: Molar composition of vapor and liquid in equilibrium at the states selected for the analysis of the convergence of the flash algorithms.

Y8	Point A		Point B		Point C	
	Liquid	Vapor	Liquid	Vapor	Liquid	Vapor
C_1	0.74744792	0.84906008	0.47658529	0.87746005	0.60400388	0.81762325
C_2	0.06057858	0.05408446	0.06296756	0.05530475	0.05844115	0.05652908
C_3	0.03589832	0.02725004	0.05092726	0.02646516	0.03965730	0.03025112
nC_5	0.06266242	0.03497518	0.13974651	0.02656967	0.09067889	0.04396745
nC_7	0.05032462	0.02204618	0.13898012	0.01144221	0.09260111	0.03070421
nC_{10}	0.04308814	0.01258406	0.13079327	0.00275817	0.11461768	0.02092489

MY10	Point D		Point E		Point F	
	Liquid	Vapor	Liquid	Vapor	Liquid	Vapor
C_1	0.32277170	0.65714256	0.27245022	0.42483512	0.07783597	0.38155198
C_2	0.02889804	0.04243037	0.02539431	0.03444446	0.00953245	0.03237280
C_3	0.03944780	0.04622895	0.03581565	0.04403788	0.01633421	0.04274357
nC_4	0.06033169	0.05625849	0.05673424	0.06315144	0.03147630	0.06330675
nC_5	0.04080501	0.03091922	0.03964769	0.04033998	0.02627885	0.04159069
nC_6	0.03095915	0.01918057	0.03106314	0.02897407	0.02441470	0.03064750
nC_7	0.05206707	0.02668295	0.05397352	0.04616557	0.05015849	0.04998163
nC_8	0.05247517	0.02207942	0.05603950	0.04417191	0.06088237	0.04873841
nC_{10}	0.31843114	0.09209178	0.36069877	0.24142602	0.52938744	0.27340711
nC_{14}	0.05381324	0.00698568	0.06818296	0.03245354	0.17369922	0.03565955

The performance of the isothermal and non-isothermal flash algorithms is investigated for six algorithmically challenging points (A-F) marked in the phase diagrams of the mixtures, see Fig. 2.2. The overall thermodynamic properties at these points are listed in Table 2.2 and results for the molar composition of the vapor and liquid in equilibrium are shown in Table 2.3. These values are the same for all types of flash calculations.

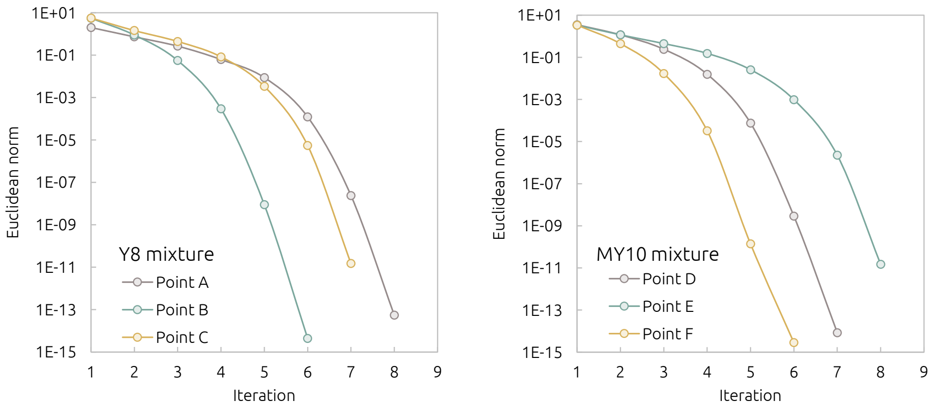

Figure 2.4.: PT-flash convergence for the Y8 and MY10 mixtures at the points marked in Fig. 2.2.

The evolution of the Euclidean residual norm for the PT-flash calculations at points A (198.1 bar, 295.4 K), B (134.5 bar, 335.2 K), and C (194.8 bar, 375.3 K) for the Y8 mixture, and at points D (104.9 bar, 509.1 K), E (75.4 bar, 566.6 K), and F (32.7 bar, 566.6 K) for the MY10 mixture are plotted in Fig. 2.4. For all points, one SSI has been carried out on the initial K-factors obtained from Wilson's correlation before switching to the NRI. The results indicate that the PT-flash algorithm requires about $6-8$ iterations for the points at the heart of the two-phase dome, near the phase boundaries, and close to the critical point.

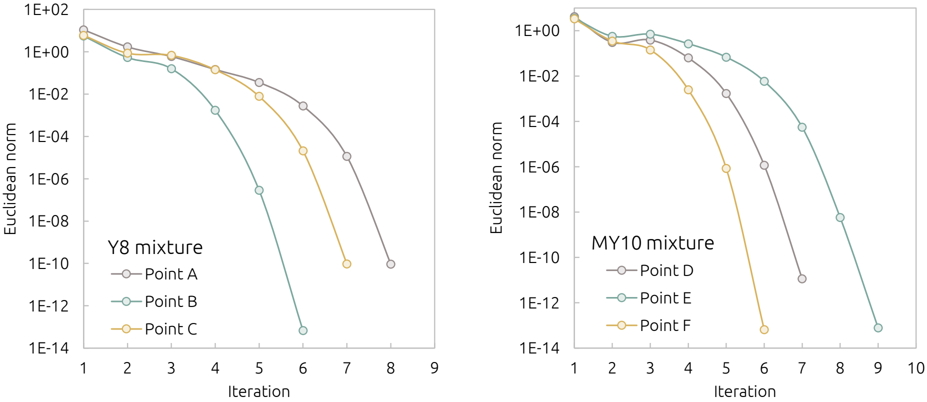

Figure 2.5.: VT-flash convergence for the Y8 and MY10 mixtures at the points marked in Fig. 2.2.

The convergence of the residuals of VT-flash calculations are shown in Fig. 2.5 for the points A (0.0806 L/mol, 295.4 K), B (0.1533 L/mol, 335.2 K), and C (0.1273 L/mol, 375.3 K) corresponding to the marked points on the phase diagram of the Y8 mixture, and for the points D (0.2281 L/mol, 509.1 K), E (0.3847 L/mol, 566.6 K), and F (1.0596 L/mol, 563.5 K) corresponding to the tagged points on the phase diagram of the MY10 mixture. Initial values for the K-factors were obtained from Wilson's correlation using a pressure obtained from the state equation by the overall composition and given temperature and volumes, i.e. $p = \{188.8, 119.3, 193.2, 95.5, 74.1, 33.2\}$ bar for points { A to F }. As for the PT-flashes, one initial SSI was executed before switching to NRI. The VT-flash results show the same excellent convergence behavior as observed for the PT-flashes, that is, both algorithms have optimum quadratic convergence and require only very few iterations, with only two iterations difference between points close to and far from the extreme conditions.

Figure 2.6 shows the convergence of the relative errors for the blind HP-flash at points A (−94.704 kJ/mol, 198.1 bar), B (−90.637 kJ/mol, 134.5 bar), and C (−87.896 kJ/mol, 194.8 bar) for the the condensate gas and at points D (−142.741 kJ/mol, 104.9 bar), E (−124.941 kJ/mol, 75.4 bar), and F (−120.734 kJ/mol, 32.7 bar) for the synthetic oil. We initialize the iteration with a temperature of 250 K for Y8 and 400 K for MY10, far away from the true solution, in order to test the robustness of the non-isothermal flashes at extreme

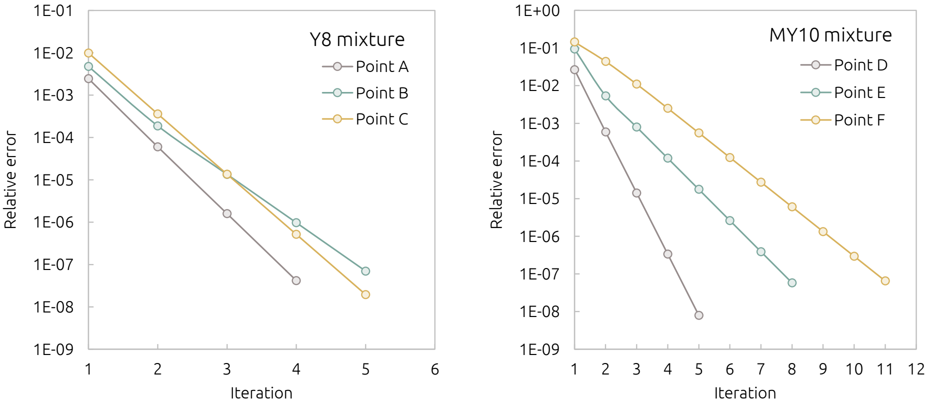

Figure 2.6.: HP-flash convergence for the Y8 and MY10 mixtures at the points marked in Fig. 2.2.

conditions. As the convergence plots show, they rapidly converge within very few iterations even with a poor inital temperature guess.

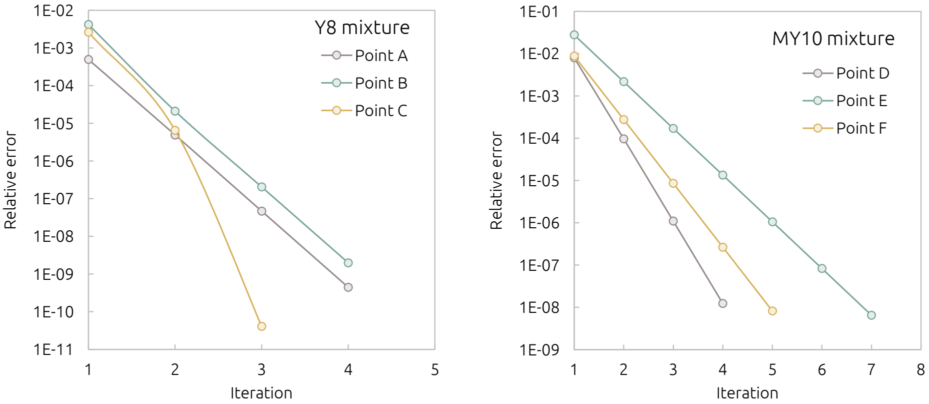

Figure 2.7.: UV-flash convergence for the Y8 and MY10 mixtures at the points marked in Fig. 2.2.

Figure 2.7 shows results for the blind UV-flash at the points A (−96.300 kJ/mol, 0.0805 L/mol), B (−92.699 kJ/mol, 0.1533 L/mol), and C (−90.376 kJ/mol, 0.1273 L/mol) for Y8 and at the points D (−145.134 kJ/mol, 0.2281 L/mol), E (−127.841 kJ/mol, 0.3847 L/mol), and F (−124.199 kJ/mol, 1.0596 L/mol) for the MY10 mixture. As before, the initial temperature guess is 250 K for the Y8 gas condensate and 400 K for the MY10 oil mixture. The initial values for the pressure are the same as used for the VT-flash at these points, see above. We observe rapid convergence within 4 to 7 iterations to within a relative error of 10^{-8}. For the most of engineering applications, it is, however, not necessary to know the temperature with such a high precision and a much larger error, say 0.1 K can be tolerated. The algorithms for both non-isothermal flashes yield temperature differences of less than 0.1 K in just 3 iterations.

2.5.2. COMPUTATIONAL TIME

In this section, we analyze the computational performance of the proposed flash algorithms for different mixtures and demonstrate the improved efficiency resulting from using a reduction method and direct VT-flashes instead of PT-flashes in the inner iteration loop of UV-flashes. For a fair quantitative evaluation, the computational time required for the new flash algorithms is compared with the highly optimized implementation of a conventional method that was developed in [30] for large-scale turbulence-resolving CFD simulations of transcritical fuel injection. Both algorithms use the Newton method to achieve fast convergence. The calculations were performed on an Intel Xeon W-2123 CPU at 3.60 GHz using the Intel Fortran compiler.

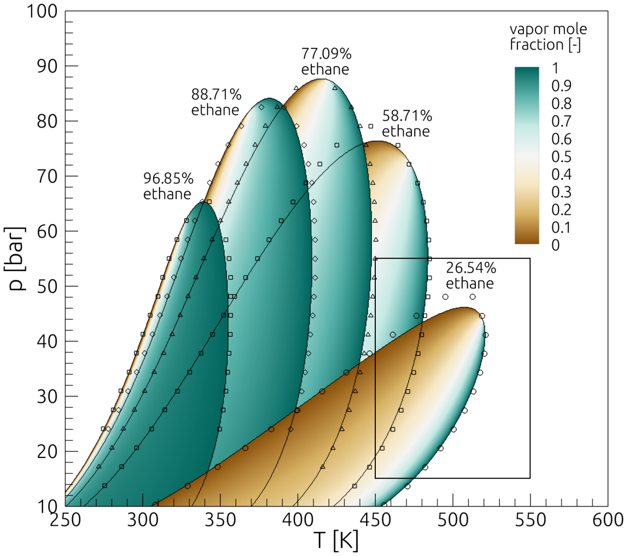

Figure 2.8.: Phase diagram of binary mixtures of n-heptane and ethane at various molar compositions computed by the proposed algorithm. The symbols denote experimental reference data for the dew-point and bubble-point lines [73, 74]. The black box encloses the pressure-temperature domain that was used for measuring the computational performance of the flash algorithms.

The test fluid is a mixture of ethane and normal heptane. The phase diagrams of this binary mixture for various molar compositions are shown in Fig. 2.8. To study the effect of the number of components in the mixture, we have added pseudo-components with properties identical to those of ethane and normal heptane and adjusted the mole fractions in a way that the total composition remains constant. First, PT-flash calculations were carried out for a mixture with 26.54% ethane and we record the total computational time required for the computation of 100 × 100 states in the pressure-temperature range enclosed by the black box in Fig. 2.8. Then, the mixture's internal energy and specific volume computed by the PT-flashes are used for executing the corresponding UV-flashes. In order to assess the performance of the proposed UV-flash at conditions that are similar to what we typically encounter in CFD simulations, initial guesses of pressure and temperature were computed by adding random perturbations to the true values:

$$T_{\text{guess}} = T_{\text{true}} + r\Delta T, \tag{2.74a}$$

$$p_{\text{guess}} = p_{\text{true}} + r\Delta p, \tag{2.74b}$$

where r is a random number generated in the range $[-0.5, 0.5]$. The perturbation amplitudes ΔT and Δp are set to 20 K and 20 kPa, which corresponds to the maximum change that we can expect between two subsequent time steps in CFD simulations.

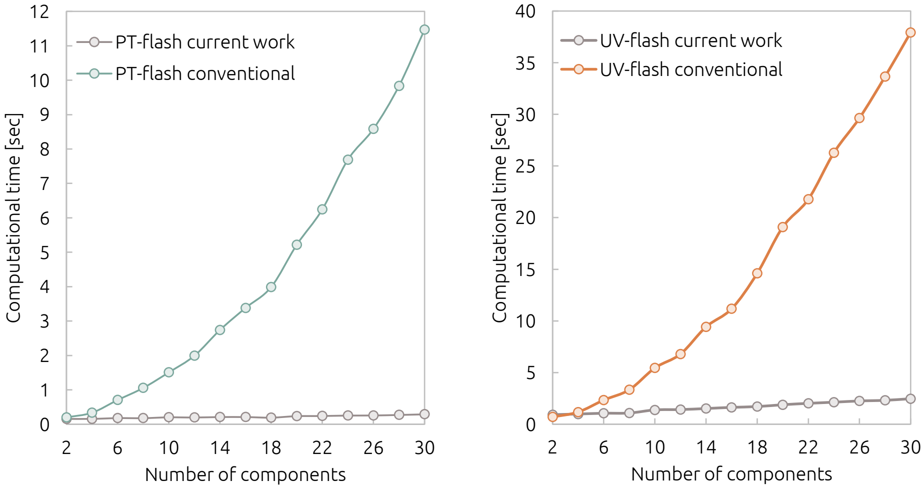

Figure 2.9.: Computational time for PT-flashes and UV-flashes vs. number of mixture components. Shown is the total CPU time for 100 × 100 flash calculations in the part of the phase diagram highlighted in Fig. 2.8.

The results are shown in Fig. 2.9. The computational time for the current PT-flash algorithm is always lower than the highly optimized reference method. The difference becomes more significant as the number of components is increased, which shows the importance of reduction methods for both iso-thermal and non-isothermal flashes. Surprisingly, we also measure a performance gain for the two-component mixture, where the number of variables is not reduced by the new method. In this case, the reduction method acts as a preconditioner and reduces the number of required iterations for the PT-flash. Furthermore, it should be noted that the computational performance the UV-flash based on the VT-flash is much less sensitive to the amplitude of the imposed pressure perturbation Δp than the conventional method based on the PT-flash. For instance, the conventional method becomes more than five times slower for $\Delta p = 400$ kPa, whereas the total time required for the new method remains unchanged.

2.6. Conclusions

This chapter was motivated by the need for computationally efficient and very robust vapor-liquid phase-split calculations in turbulence-resolving CFD simulations of high-pressure liquid-fuel injection and reacting transcritical multiphase flows in modern energy conversion systems, such as rocket engines, gas turbines, and jet engines. Such simulations typically require 10^{10} to 10^{16} flash calculations for given overall specific internal energy, volume, and composition and unknown pressure, temperature, volume fractions, and phase compositions (isoenergetic-isochoric flash – UV-flash). The standard methods for such applications that we have used in the past [72] are based on a nested PT-flash and suffer from poor conditioning near the spinodal[1] and coexistence curves and polynomial growth of the computational cost in terms of the number of mixture components. To this end, and building upon and extending the work in [59] and [58], we have developed a new multi-component reduction method for direct PT-flash and VT-flash calculations based on the formulation of phase equilibrium conditions in terms of the molar specific value of Mikyska and Firoozabadi [59]'s volume function and a corresponding adaptation of Nichita and Graciaa [58]'s reduction method. The computational cost of solving the PT-flash and VT-flash in terms of the new reduced set of variables is almost independent of the number of components and the point in the phase diagram. The reduced-space Newton-Raphson iteration, using the exact analytical Jacobian matrix, results in optimum quadratic convergence in very few iterations. We further showed that the non-isothermal UV and HP flashes are efficiently solved through univariate residual minimization with the naturally corresponding isothermal flash (PT-flash for HP-flash and VT-flash for UV-flash) and the specific heat capacity at constant pressure (for HP-flash) or at constant volume (for UV-flash) as exact Jacobian. We have thoroughly verified the reliability and efficiency of the algorithmic implementation. The computational results show a considerable speed-up compared to conventional methods, as well as improved robustness and better convergence behavior near the spinodal and coexistence curves of multi-component mixtures, where the preconditioning by the reduction method is most effective.

---

[1] The *spinodal* is a boundary defining the absolute limit of metastability, beyond which a phase becomes intrinsically unstable and undergoes spontaneous phase separation.

3

High-Fidelity Simulations of Transcritical Sprays

Building on Chapter 2, this chapter presents a new simulation framework for transcritical fuel sprays, where the MT model is coupled with a finite-rate chemistry (FRC) formulation. The approach removes the need for empirical spray breakup models by resolving transcritical vaporization directly through diffuse-interface methods. Combined with the RKPR equation of state and fugacity-based chemistry, the model accurately captures real-fluid effects in both inert and reacting sprays. Validation against experimental data from the Engine Combustion Network (ECN) Spray-A shows excellent agreement in key metrics like ignition delay, spray penetration, and flame lift-off.

This chapter's content has been published as *Large Eddy Simulations of Reacting and Non-Reacting Transcritical Fuel Sprays Using Multiphase Thermodynamics* in Physics of Fluids **34** (2022) [75].

3.1. INTRODUCTION

Aligned with Gibbsian thermodynamics and experimental reports [76–79], a transcritical mixture can locally enter the two-phase regime and interfaces between liquid-like and gas-like phases may form. Transcritical jets and sprays, therefore, resemble a combination of the classical two-phase disintegration with breakup and evaporation of droplets and the supercritical turbulent mixing of two dense fluids. This hybrid behavior complicates their numerical simulation.

Traditional large-eddy simulation (LES) of the high-speed transcritical injection have either modeled the transcritical multiphase fluid flows by Lagrangian particle tracking (LPT) methods with sharp vapor-liquid interfaces [80–82], or by Eulerian single-phase dense-gas (DG) approaches with diffuse vapor-liquid interfaces [4, 29, 83]. LES-LPT and LES-DG approaches are efficient for many flows, but their inherent model assumptions impose significant limitations at transcritical conditions. The standard LPT method is very sensitive to empirical tuning parameters and was developed for dilute mixtures, neglecting real-fluid effects. The LES-DG approach, on the other hand, excludes transcritical phase separation and may lead to nonphysical or ill-defined states when a part of the flow passes the meta-stable boundaries, specially at lower transcritical pressures [5]. Furthermore, some important transcritical effects such as the high solubility of the saturated liquids or the different evaporation rates of the components of the fuel are not captured by these models [25].

Using multiphase thermodynamics (MT) in the context of a diffuse-interface method has been demonstrated recently to be a promising technique to overcome the aforementioned limitations [30, 35]. In this formulation, the fully conservative Navier-Stokes equations (NSE) are solved for a hypothetical multi-component fluid mixture with thermo-transport properties computed using a suitable equation of state (EOS) coupled with vapor-liquid equilibrium (VLE) calculations. Although the weak surface tension force is neglected, the method can accurately capture the flow physics including the subcritical region of coexisting multi-component vapor and liquid as well as the non-ideal fluid behavior such as dissolution of the ambient gas in the compressed liquid.

LES-MT studies show excellent agreement with experimental data for the non-reacting transcritical sprays [39, 41, 72]; however the applicability of the method to reacting flows remained as an open question mainly due to the high computational cost of the VLE calculations, which increases with the number of components in the mixture, and due to the need for chemistry models that can capture the departure from ideal-gas behavior in regions with high pressures and low temperatures. The latter can be solved using an appropriate reduced reaction mechanism [84] and utilizing the fugacity values of species in the mixture for the evaluations of real fluid effects on the reaction rates [85].

The non-ideal fluid behavior becomes apparent when using an appropriate EOS. Two-parameter cubic EOS, such as the Soave-Redlich-Kwong (SRK) [86] and Peng-Robinson (PR) [87] models, are very popular because of their computational efficiency [38, 88–91]. The intrinsic drawback of these two-parameter cubic EOS is the use of a universal critical compressibility factor, which can severely limit their accuracy close to the critical point. To overcome this limitation, volume translation methods can be employed to improve the density predictions, but the calculation of consistent caloric properties is computationally very expensive and, thus, simplified approximations are typically used in practice [30] . Another option is utilizing a cubic EOS with three parameters. The Redlich-Kwong-Peng-Robinson (RKPR) model of Cismondi and Mollerup [92] calibrates the cubic EOS using the actual value of the compressibility at the critical point, and provides a consistent framework for real-fluid thermodynamic modeling at tractable computational cost [93].

In this chapter, we present several novel physical and numerical models that improve the accuracy and computational efficiency of high-fidelity simulation of turbulent reacting and non-reacting multiphase flows at transcritical pressures. The framework is provided by a fully conservative formulation of the multi-component compressible Navier-Stokes equations with multiphase thermodynamics models and the adaptive local deconvolution method (ALDM) for LES turbulence modelling [94]. Improved accuracy compared to previous LES-MT simulations is provided by the RKPR EOS [92] for transcritical vaporization and real-fluid properties, and by fugacity-based finite rate chemistry for combustion modeling. The computational cost is significantly reduced by the rapid VLE solver of Chapter 2 and by utilizing a highly-optimized reaction mechanism [84], which reduces the required number of transported species. The proposed LES-MT method is validated by comparing computational results with experimental data reported for the transcritical reacting and non-reacting Engine Combustion Network (ECN) Spray-A benchmark test cases.

3.2. PHYSICAL AND NUMERICAL MODELS

We use the LES-MT method for solving reacting multiphase compressible Navier-Stokes equations in a fully conservative form with real-fluid thermo-transport properties and fugacity-based finite-rate chemistry. In this section, the required physical and numerical models for the MT-based simulations are presented.

3.2.1. GOVERNING EQUATIONS

The three-dimensional compressible reacting Navier-Stokes equations (NSE) describe the conservation of mass, species, momentum, and total (absolute) internal energy:

$$\partial_t \rho + \boldsymbol{\nabla} \cdot (\rho \mathbf{u}) = 0, \tag{3.1}$$

$$\partial_t \rho Y_i + \boldsymbol{\nabla} \cdot (\rho Y_i \mathbf{u}) = \boldsymbol{\nabla} \cdot \mathbf{j}_i + \dot{\omega}_i, \tag{3.2}$$

$$\partial_t \rho \mathbf{u} + \boldsymbol{\nabla} \cdot (\rho \mathbf{u}\mathbf{u} + p\mathbf{I}) = \boldsymbol{\nabla} \cdot \boldsymbol{\tau}, \tag{3.3}$$

$$\partial_t \rho e_t + \boldsymbol{\nabla} \cdot [(\rho e_t + p)\mathbf{u}] = \boldsymbol{\nabla} \cdot (\mathbf{u} \cdot \boldsymbol{\tau} - \mathbf{q}), \tag{3.4}$$

where ρ is the mass density of the mixture, $\mathbf{u}$ is the velocity vector, p is the thermodynamic pressure of the mixture, and $e_t = e + |\mathbf{u}|^2/2$ is the total absolute specific internal energy of the mixture and e is the corresponding absolute specific internal energy. For species $i = 1, 2, \ldots, N$ with N being the total number of components comprising the mixture, Y_i is the mass fraction, $\mathbf{j}_i$ is the diffusive mass-flux vector, and $\dot{\omega}_i$ is the net mass production rate. $\boldsymbol{\tau}$ and $\mathbf{q}$ denote the viscous stress tensor and the vector of heat fluxes. $\mathbf{I}$ is the unit tensor and $\boldsymbol{\nabla}$ is the nabla operator.

The viscous stress tensor is modeled by assuming a Newtonian fluid and Stokes' hypothesis

$$\boldsymbol{\tau} = \mu \left(\boldsymbol{\nabla} \mathbf{u} + (\boldsymbol{\nabla} \mathbf{u})^T \right) - 2/3\mu(\boldsymbol{\nabla} \cdot \mathbf{u})\mathbf{I}. \tag{3.5}$$

The molecular viscosity coefficient μ of the multi-component mixture is estimated using Chung's correlations [95]. We neglect bulk-viscosity effects in our computations because accurate models to be used at pressures close to the critical point are unavailable.

For multi-component fluid flows, the total heat flux vector

$$\mathbf{q} = -\lambda \nabla T - \textstyle\sum_{i=1}^{N} h_i \mathbf{j}_i \tag{3.6}$$

consists of heat conduction and interspecies enthalpy diffusion, and is a function of the thermal conductivity of the mixture λ, temperature T, and the partial mass absolute enthalpy h_i of component i. Similar to the viscosity, the thermal conductivity of the mixture is modeled by Chung's correlations [95].

By neglecting Soret and Dufour effects, the mass diffusion $\mathbf{j}_i$ is modeled using Fick's law through a simplified correlation based on the mixture-averaged diffusion approximation along with an extra term to ensure zero total mass diffusion

$$\mathbf{j}_i = \rho D_i \nabla Y_i - Y_i \textstyle\sum_{j=1}^{N} \rho D_j \nabla Y_j. \tag{3.7}$$

The effective binary diffusion coefficient between species i and the bulk mixture is approximated by

$$\rho D_i = (1 - X_i) \, / \textstyle\sum_{j \neq i}^{N} X_j / (\rho D_{ij}), \tag{3.8}$$

where X_i is the mole fraction of species i, which can be computed via $X_i = Y_i M / M_i$ from the mass fractions and the mean molecular weight $M = 1/(\sum_i^N Y_i/M_i)$ of the mixture, with M_i being the molar mass of the species i. The product of density and the binary mass diffusion coefficient of species i and j, ρD_{ij}, can be approximated accurately with Chapman and Enskog theory [95] without high-pressure corrections if the system pressure is under 100 bar [96].

3.2.2. MULTIPHASE THERMODYNAMICS

Simulations of multi-component fluid flows at elevated pressure require proper volumetric and caloric EOS that account for the volume of molecules and interactive forces between them in order to accurately calculate pressure and temperature from the density, internal energy, and mass composition of the mixture. The partial mass enthalpies of all components in the mixture are additionally required for the evaluation of the interspecies enthalpy diffusion flux. At transcritical pressures, additional phase-splitting calculations should be carried out to account for the coexistence of vapor and liquid phases. In this section, we present the equations required for the computation of temperature, pressure, and partial mass enthalpies of a general fluid in a single phase or two phases in equilibrium.

VOLUMETRIC EQUATION OF STATE

A volumetric EOS represents the thermodynamic relation between the pressure, specific volume (inverse of the density), and temperature of a single-phase substance that can be pure or a multi-component mixture. The most popular volumetric EOS is the ideal gas (IG); however, its applicability is limited to gaseous media with a compressibility factor close to unity, that is, it is only appropriate at relatively high temperatures and low pressures. For the typical pressures and temperatures of transcritical fuel sprays, cubic EOSs are an attractive compromise between accuracy, model complexity, and computational cost.

The most widely used cubic EOS are SRK [86] and PR [87]. Both are formulated based on two model parameters. They have the intrinsic limitation of predicting a unique and universal compressibility factor at the critical point, which therefore results in a systematic error for the specific volume (or density) at conditions close to the critical point. To overcome this limitation, Cismondi and Mollerup [92] proposed a three-parameter cubic EOS. This so-called RKPR EOS considers the effect of the actual critical compressibility factor as the third EOS parameter. In Fig. 3.1, we compare the accuracy of various cubic EOS against the highly accurate reference EOS of Lemmon and Huber [97] for pure n-dodecane at the ECN Spray A operating pressure 60 bar. The data shows that RKPR EOS significantly improves on the known deficiencies of two-parameter EOS (SRK and PR). The RKPR EOS can also yield more accurate predictions of caloric properties than the perturbed chain-statistical associating fluid theory (PC-SAFT) EOS [98], such as shown for the heat capacity in the temperature range $450\,\mathrm{K} \leq T \leq 750\,\mathrm{K}$ in Fig. 3.1. The advantages of using the RKPR EOS for predicting fluid properties at transcritical and supercritical pressures have also been previously highlighted [72, 93, 99].

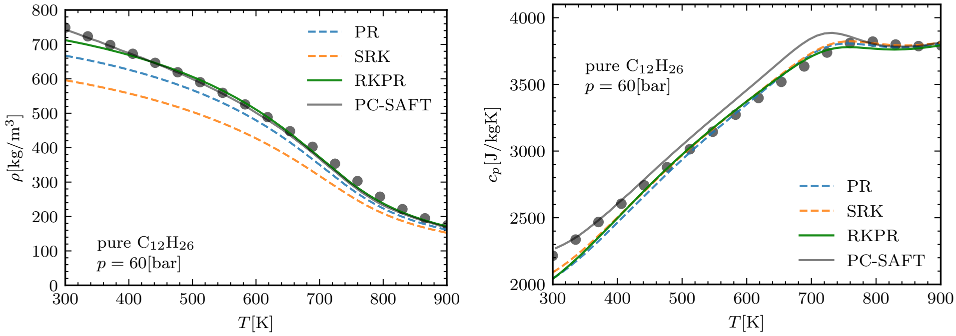

Figure 3.1.: Density (left) and constant-pressure heat capacity (right) of pure n-dodecane predicted by PC-SAFT [98], PR [87], SRK [86], and RKPR [92] compared with the reference EOS of Lemmon and Huber [97] denoted by circles.

The RKPR EOS is employed for all application examples discussed in the present work. However, as for the general cubic EOS,

$$p = RT/(\overline{\vartheta} - b) - a/[(\overline{\vartheta} + \delta_1 b)(\overline{\vartheta} + \delta_2 b)], \tag{3.9}$$

includes IG, SRK, PR, RKPR, and other EOS as special cases, all thermodynamic model relations are presented in form of this general cubic EOS, in which R is the universal gas constant, $\overline{\vartheta} = M/\rho$ is the molar specific volume, a is the attractive energy parameter, and b is the co-volume parameter. δ_1 and δ_2 are two constant parameters in the case of two-parameter cubic EOS, whereas they are variables computed from one extra constraint in the case of three-parameter cubic EOS. With the RKPR EOS, the energy parameter is

$$a = (3\xi^2 + 3\xi d + d^2 + d - 1)/(3\xi + d - 1)^2 (R^2 T_c^2/p_c)[3/(2 + T/T_c)]^m, \tag{3.10}$$

where $d = (1 + \delta_1^2)/(1 + \delta_1)$, $\xi = 1 + [2(1 + \delta_1)]^{\frac{1}{3}} + [4/(1 + \delta_1)]^{\frac{1}{3}}$, and

$$m = (-2.4407\mathcal{Z}_c + 0.0017)\omega^2 + (7.4513\mathcal{Z}_c + 1.9681)\omega + (12.5040\mathcal{Z}_c - 2.7238), \tag{3.11}$$

with $\mathcal{Z}_c = 1.168 Z_c$ being the tuned critical compressibility factor. The co-volume parameter of the RKPR EOS is

$$b = (RT_c/p_c)/(3\xi + d - 1). \tag{3.12}$$

The third parameter

$$\delta_1 = 0.428 + 18.496(0.338 - \mathcal{Z}_c)^{0.66} + 789.723(0.338 - \mathcal{Z}_c)^{2.512} \tag{3.13}$$

is an empirical function of $\mathcal{Z}_c$, and δ_2 follows from the constraint

$$\delta_2 = (1 - \delta_1)/(1 + \delta_1). \tag{3.14}$$

In these equations, p_c, T_c, Z_c, and ω are the critical pressure, critical temperature, critical compressibility factor, and acentric factor of the pure fluid.

The conventional approach to extend this pure-fluid cubic EOS to multi-component mixtures is based on considering the mixture as a pure hypothetical substance and estimating the EOS parameters via the van der Waals mixing rule:

$$\begin{aligned} a &= \textstyle\sum_{i=1}^{N} \sum_{j=1}^{N} X_i X_j a_{ij}, \\ b &= \textstyle\sum_{i=1}^{N} X_i b_i, \\ \delta_1 &= \textstyle\sum_{i=1}^{N} X_i \delta_{1,i}, \\ \delta_2 &= \textstyle\sum_{i=1}^{N} X_i \delta_{2,i}, \end{aligned} \tag{3.15}$$

where a_{ij} is obtained through a combination rule that can include any possible binary interaction effects among the components. We use the classical combination rule

$$a_{ij} = (1 - \varrho_{ij})(a_i a_j)^{\frac{1}{2}}, \tag{3.16}$$

with ϱ_{ij} being the binary interaction coefficient between components i and j in the mixture. In contrast to the pseudo-critical combination rule, in which a_{ij} is estimated by the pure-fluid formula of the energy parameter with critical quantities estimated based on those for components i and j, the classical combination rule (3.16) provides the possibility of applying reduction methods for the phase equilibrium calculations, which can significantly reduce the computational costs for mixtures with many components. Using the reduction theory as explained in Chapter 2, the energy parameter of the mixture can be computed through

$$a = \sum_{k=1}^{N_m} \lambda_k q_k^2 \quad \text{where } q_k \equiv \sum_{i=1}^{N} X_i s_{ki} a_i^{\frac{1}{2}}. \tag{3.17}$$

Here, λ_k and s_{ki} are significant (non-zero) eigenvalues and their corresponding eigenvectors for a symmetric matrix with entries $\varrho'_{ij} = 1 - \varrho_{ij}$. N_m is the number of significant eigenvalues. More often than not, binary interaction coefficients are set to zero due to lack of accurate data or just to simplify the computations. In that case, the matrix of ϱ'_{ij} becomes a diagonal matrix, and $N_m = 1$ regardless of the number of components in the mixture.

Single-Phase Pressure: The RKPR EOS explicitly provides the thermodynamic pressure of a thermodynamically stable mixture whose molar composition, specific volume, and temperature are specified. The required temperature is computed via the caloric EOS, which is explained in the next subsection for non-ideal multi-component fluids.

Caloric Equation of State

A caloric EOS provides a thermodynamic relation between a caloric property like specific internal energy, and two other properties such as temperature and specific volume for a mixture with specified molar or mass composition. Real-fluid caloric EOS can be derived by the departure function formalism using the volumetric EOS. For the general cubic EOS (3.9), the molar specific internal energy $\overline{e} = Me$ of a multi-component real fluid is obtained as

$$\overline{e} = \sum_{i=1}^{N} X_i \overline{h}_i^{\circ}(T) - RT + (a - T\partial a/\partial T)/[(\delta_2 - \delta_1)\, b] \ln[(\overline{\vartheta} + \delta_1 b)/(\overline{\vartheta} + \delta_2 b)], \tag{3.18}$$

where the first two terms account for the absolute internal energy of the mixture at the actual temperature but at the standard pressure, and the last term accounts for the internal energy change via an isothermal thermodynamic path from the standard reference pressure to the actual value.

The molar specific enthalpy at standard pressure is usually computed using polynomials [100]

$$\overline{h}_i^{\circ}(T)/R = -A_{i,1}/T + A_{i,2} \ln T + \sum_{j=1}^{5} A_{i,j+2} T^j / j + A_{i,8}, \tag{3.19}$$

where $A_{i,1\ldots8}$ are the calibrated polynomial coefficients for each component i, which include the formation enthalpy.

Single-Phase Temperature: The temperature of a stable mixture with specified molar composition, molar specific volume, and molar specific internal energy is determined implicitly via the caloric Eq. (3.18). It can be computed numerically by an initial guess and Newton iterations:

$$T = T^* - \mathcal{L}(\overline{e} - \overline{e}^*)/\overline{c}_V^*, \tag{3.20}$$

where $\mathcal{L}$ is the line search parameter in order to ensure global convergence, $\overline{e}$ is the target energy, and $\overline{e}^*$ is computed via Eq. (3.18) using T^*. Here, $\overline{c}_V^*$ is the molar specific heat capacity at constant volume and computed at temperature T^*. The thermodynamic relation required for the evaluation of $\overline{c}_V$ using the departure function formalism for a general cubic EOS is

$$\overline{c}_V = \textstyle\sum_{i=1}^{N} X_i \overline{c}_{P,i}^{\circ}(T) - R + T\partial^2 a/\partial T^2 [(\delta_1 - \delta_2)b] \ln[(\overline{\vartheta} + \delta_1 b)/(\overline{\vartheta} + \delta_2 b)]. \tag{3.21}$$

The specific molar heat capacity of the component i at the standard pressure is computed by taking the derivative of the polynomial (3.19) with respect to the temperature, which yields

$$\overline{c}_{P,i}^{\circ}(T)/R = \textstyle\sum_{j=1}^{7} A_{i,j} T^{j-3}. \tag{3.22}$$

VAPOR-LIQUID EQUILIBRIUM

When vapor and liquid phases coexist, phase-splitting calculations are necessary in order to correctly determine the thermodynamic properties of the multi-component mixture, of which overall values of molar specific internal energy $\overline{e}$, molar specific volume $\overline{\vartheta}$, and molar composition X_i are known. The required phase-splitting or flash calculations are briefly explained in this section.

The two-phase equilibrium state of a fluid with N components is described by N equations for species mass conservation and $2+N$ equations for temperature, pressure, and species chemical potentials of the two phases. This set of $2N+2$ equations must be supplemented with two more constraints in order to uniquely determine the molar specific volume, temperature, and molar composition of the multi-component liquid and vapor phases. These two constraints define the type of the flash problem. As we solve the conservative form of the governing Navier-Stokes equations, that is, transport equations for the mixture energy and density, isoenergetic-isochoric phase-splitting calculations also known as UV-flash calculations must be carried out. The two additional constraints for UV-flash calculations are

$$\overline{\vartheta} = (1-\alpha)\overline{\vartheta}_l + \alpha\overline{\vartheta}_v, \tag{3.23}$$

and

$$\overline{e} = (1-\alpha)\overline{e}_l + \alpha\overline{e}_v. \tag{3.24}$$

Subscripts l and v refer to liquid and vapor values, and α is the vapor mole fraction, defined as the ratio of the moles of the vapor phase to the total mole of all phases. In order to evaluate the required specific internal energies of the liquid and vapor phases, we use Eq. (3.18) for each phase separately, and to compute α, we use total mass balance rewritten as

$$\alpha = (M - M_l)/(M_v - M_l), \tag{3.25}$$

with M as overall average molecular weight computed using overall mole fractions X_i. M_l and M_v are average molecular weights for the liquid and vapor mixtures that are computed from the liquid mole fractions $X_{l,i}$ and vapor mole fractions $X_{v,i}$, respectively. The molar compositions of liquid and vapor phases represent the solution of the phase-splitting calculations.

In order to solve flash equations efficiently, we use the new method from the previous chapter that performs UV-flash calculations very fast and robust via Newton iterations with the exact Jacobian of the equilibrium temperature used for VT-flash calculations. The VT-flash here refers to isochoric-isothermal phase-splitting calculations, which this method formulates in an effectively reduced space in terms of the molar specific value of the volume function of Mikyska and Firoozabadi [59] and reduced parameters similar to those used by Nichita and Graciaa [58]. In the following, we briefly explain how this method can be used to determine the equilibrium temperature and pressure in a general cubic EOS framework. For a comprehensive review and practical implementation guidelines, interested readers are referred to the original article [51].

Equilibrium Temperature: The temperature in the two-phase region is obtained through an iterative method similar to that used for the single-phase case, but using specific vapor and liquid internal energies and heat capacities to determine the overall values.

$$\begin{aligned} \bar{e}^* &= (1-\alpha)\bar{e}_l^* + \alpha \bar{e}_v^*, \\ \bar{c}_V^* &= (1-\alpha)\bar{c}_{V,l}^* + \alpha \bar{c}_{V,v}^*. \end{aligned} \tag{3.26}$$

Vapor and liquid quantities require the molar composition and specific volume of that phase, which are the results of rapid VT-flash calculations together with the vapor mole fraction. The iterative method can be terminated when $|\bar{e} - \bar{e}^*|/|\bar{e}| < 10^{-6}$.

According to Fathi and Hickel [51], the VT-flash problem can be formulated based on effectively reduced parameters $\overrightarrow{\mathcal{H}} = (\mathcal{H}_1^\Delta, \ldots, \mathcal{H}_{N_m+2}^\Delta)$ derived from Helmholtz free energy using species molar specific volume functions. The reduced parameters are determined iteratively by applying the Newton-Raphson method for $N_m + 2$ error equations

$$\mathcal{E}_k \equiv \mathcal{H}_{k,v}(\overrightarrow{\mathcal{H}}) - \mathcal{H}_{k,l}(\overrightarrow{\mathcal{H}}) - \mathcal{H}_k^\Delta = 0, \tag{3.27}$$

for $k = 1, \ldots, N_m + 2$ with the Jacobian matrix

$$\mathcal{J}_{kj} \equiv \frac{\partial \mathcal{E}_k}{\partial \mathcal{H}_j^\Delta} = \frac{\partial \mathcal{H}_{k,v}}{\partial \mathcal{H}_j^\Delta} - \frac{\partial \mathcal{H}_{k,l}}{\partial \mathcal{H}_j^\Delta} - \delta_{kj}, \tag{3.28}$$

for $k, j = 1, \dots, N_m + 2$. In order to compute $\overrightarrow{\mathcal{H}}_v$ and $\overrightarrow{\mathcal{H}}_l$ as well as the required partial derivatives analytically, we first compute the K-factors

$$\ln \mathcal{K}_i = \textstyle\sum_{k=1}^{N_m} \mathcal{H}_k^{\Delta} s_{ki} + \mathcal{H}_{N_m+1}^{\Delta} b_i + \mathcal{H}_{N_m+2}^{\Delta} \;, \tag{3.29}$$

with $\mathcal{K}_i \equiv y_i/x_i$ being the K-factor of the component i in the mixture. Afterwards, the vapor mole fraction is initially obtained by the solving the classic Rachford–Rice equation

$$\textstyle\sum_{i=1}^{N} [X_i(\mathcal{K}_i - 1)]/[1 + \alpha(\mathcal{K}_i - 1)] = 0. \tag{3.30}$$

Next, the vapor and liquid molar compositions are obtained from the material balances and the K-factors through

$$\begin{aligned} X_{i,l} &= X_i/[1 + \alpha(\mathcal{K}_i - 1)], \\ X_{i,v} &= X_{i,l}\mathcal{K}_i, \end{aligned} \tag{3.31}$$

for $i = 1, 2 \dots N$. From the molar compositions for both phases, we compute the required parameters of the RKPR EOS, including $a, q, b, \delta_1, \delta_2$ through the relations given in the previous section for a stable single-phase mixture. The specific molar volume of the vapor is then evaluated using the isochoric constraint.

$$\overline{\vartheta}_v = [\overline{\vartheta} - (1 - \alpha)\overline{\vartheta}_l]/\alpha. \tag{3.32}$$

Requiring equality of pressures between two phases, the liquid specific molar volume for the general cubic EOS is the solution of a fifth-order polynomial

$$\varsigma_5 \overline{\vartheta}_l^5 + s_4 \overline{\vartheta}_l^4 + \varsigma_3 \overline{\vartheta}_l^3 + \varsigma_2 \overline{\vartheta}_l^2 + \varsigma_1 \overline{\vartheta}_l + \varsigma_0 = 0. \tag{3.33}$$

The polynomial coefficients $\varsigma_{0..5}$ are listed in Ref. [51]. They are functions of the parameters that we computed in the previous steps. Finally, $\mathcal{H}_{k,l}$ or $\mathcal{H}_{k,v}$ is computed from

$$\mathcal{H}_k = 2\lambda_k q_k \ln\left[(\overline{\vartheta} + \delta_1 b)/(\overline{\vartheta} + \delta_2 b)\right]/[(\delta_1 - \delta_2)bRT], \tag{3.34}$$

for $k \leq N_m$,

$$\begin{aligned} &\mathcal{H}_k = a/(RTb^2)\{\overline{\vartheta}b/[(\overline{\vartheta} + \delta_1 b)(\overline{\vartheta} + \delta_2 b)] \dots \\ &-\ln\left[(\overline{\vartheta} + \delta_1 b)/(\overline{\vartheta} + \delta_2 b)\right]/(\delta_1 - \delta_2)\} - (v - b)^{-1}, \end{aligned} \tag{3.35}$$

for $k = N_m + 1$, and

$$\mathcal{H}_k = \ln(\overline{\vartheta} - b), \tag{3.36}$$

for $k = N_m + 2$. Note that the subscripts l and v are dropped for simplicity as these equations apply to both phases. The required equations are listed in Ref. [51] including the analytical expression of the components of the Jacobian matrix.

Starting the procedure requires an initial guess for the vector $\overrightarrow{\mathcal{H}} = (\mathcal{H}_1^{\Delta}, \dots, \mathcal{H}_{N_m+2}^{\Delta})$. This can by calculated from K-factor values by following the steps from the solution of the Rachford-Rice until the evaluation of $\mathcal{H}_{k,l}$ and $\mathcal{H}_{k,v}$.

Then, the vector of reduced parameters can be computed using its definition via

$$\mathcal{H}_k^{\Delta} = \mathcal{H}_{k,v} - \mathcal{H}_{k,l}, \tag{3.37}$$

for $k = 1, \ldots, N_m + 2$. Typically, the K-factors are available from previous time steps in computational fluid dynamics simulations. In case of blind flashes, where no previous equilibrium information is available, one can use Wilson's correlation as an initial guess.

Equilibrium Pressure Neglecting the surface tension force, the pressure is equal for both phases in equilibrium. As we used this equality for the determination of specific volumes, the equilibrium pressure is the saturation pressure of vapor or liquid obtained by the flash calculations at the equilibrium temperature.

PARTIAL ENTHALPY

By definition, the partial derivative of a quantity with respect to the mole fraction of a species while keeping temperature, pressure, and mole fractions of the other species unchanged is called the partial molar value of that quantity. It can be shown that thermodynamic relations between extensive quantities are also valid for corresponding partial values. In this section, the calculation of the partial (mass) enthalpy in the multiphase thermodynamics framework is briefly explained, as it is required for the heat flux (3.6) and for some discretization schemes.

The (mass-basis) partial enthalpies can be computed easily from the mole-basis ones: $h_i = \overline{h}_i / M_i$. The partial molar enthalpy for a single-phase mixture with known temperature, specific volume and molar composition can be computed via the thermodynamic relation

$$\overline{h}_i = \overline{e}_i + p\overline{\vartheta}_i, \tag{3.38}$$

where $\overline{\vartheta}_i \equiv (\partial\overline{\vartheta}/\partial X_i)|_{T,P,X_{j\neq i}}$ is the partial molar volume, which can be obtained from its definition for the considered volumetric EOS (3.9) as

$$\begin{aligned} &\overline{\vartheta}_i = -\{RT/(\overline{\vartheta}-b) + RTb_i/(\overline{\vartheta}-b)^2 \ldots \\ &+ab_i[2b\delta_1\delta_2 + \overline{\vartheta}(\delta_1+\delta_2)]/[(\overline{\vartheta}+\delta_1 b)(\overline{\vartheta}+\delta_2 b)]^2 \ldots \\ &-a_i/[(\overline{\vartheta}+\delta_1 b)(\overline{\vartheta}+\delta_2 b)]\}/(\partial p/\partial\overline{\vartheta})|_{T,X_j} \end{aligned} \tag{3.39}$$

where $a_i \equiv (\partial a/\partial X_i)|_{T,P,X_{j\neq i}}$ can be computed using reduced parameters [51]:

$$a_i = -2(\textstyle\sum_{k=1}^{N_m} \lambda_k q_k s_{ki} a_i^{1/2}), \tag{3.40}$$

and

$$(\partial p/\partial\overline{\vartheta})|_{T,X_j} = -RT/(\overline{\vartheta}-b)^2 + a\left[2\overline{\vartheta} + (\delta_1+\delta_2)\,b\right]/[(\overline{\vartheta}+\delta_1 b)(\overline{\vartheta}+\delta_2 b)]^2. \tag{3.41}$$

The partial molar internal energy $\overline{e}_i \equiv (\partial\overline{e}/\partial X_i)|_{T,P,X_{j\neq i}}$ can be computed from the caloric EOS as

$$\begin{aligned}\bar{e}_i = \bar{h}_i^\circ(T) - RT + (\bar{\vartheta}_i - \bar{\vartheta} b_i/b)(a - T\partial a/\partial T)/[(\bar{\vartheta}+\delta_1 b)(\bar{\vartheta}+\delta_2 b)]\dots\\ +[T(b_i\partial a/\partial T - b\partial a_i/\partial T) + ba_i - ab_i]\ln\left[(\bar{\vartheta}+\delta_1 b)/(\bar{\vartheta}+\delta_2 b)\right]/[(\delta_2-\delta_1)\,b^2].\end{aligned} \tag{3.42}$$

Note that we have neglected the dependence of δ_1 and δ_2 on the molar composition in the above-proposed equations following the approach used by Gmehling *et al.* [101] for SRK and PR EOS.

Equilibrium Partial Enthalpy: If the mixture is unstable in a single phase, then phase-equilibrium calculations are necessary to determine the thermodynamic properties of a stable mixture of saturated vapor and liquid phases. The overall partial enthalpy of the component i can then be estimated as

$$X_i\bar{h}_i \simeq (1-\alpha)X_{i,l}\bar{h}_{i,l} + \alpha X_{i,v}\bar{h}_{i,v}. \tag{3.43}$$

3.2.3. Real Finite-Rate Chemistry

Chemical reactions change the composition of a fluid mixture via the formation and destruction of species, which is expressed in the species mass balance equations by net mass production rates $\dot{\omega}_i$. At elevated pressures, finite-rate chemistry models have to account for the non-ideal thermodynamic state. Differences from the usually used ideal-gas definitions are addressed in this section.

Similar to the mass action law of the elementary reactions, the species net mass production rates of reactions with non-integer stoichiometric coefficients can also be expressed as

$$\dot{\omega}_i = M_i \textstyle\sum_{r=1}^{N_r}(\nu_{ir}^{\mathcal{P}} - \nu_{ir}^{R})\mathcal{Q}_r, \tag{3.44}$$

where N_r is the total number of reactions, and $\nu_{ir}^{\mathcal{P}}$ and ν_{ir}^{R} are the positive molar stoichiometric coefficients of species i on the right (product) and left (reactant) side of the reaction r, which might be non-integer numbers in general. The reaction rate $\mathcal{Q}_r$ of the reaction r depends on the concentrations of the reactants through

$$\mathcal{Q}_r = k_{f,r}\textstyle\prod_{j=1}^{N}\mathcal{C}_j^{n'_{jr}} - k_{b,r}\prod_{j=1}^{N}\mathcal{C}_j^{n''_{jr}}. \tag{3.45}$$

The forward and backward rate coefficients k_{fr} and k_{br} are usually expressed by the Arrhenius law

$$k(T) = \mathcal{A}\exp[-E_a/(RT)], \tag{3.46}$$

as an exponential function of the temperature, with $\mathcal{A}$ being the pre-exponential factor and E_a the reaction activation energy. In addition, n'_{jr} and n''_{jr} are reaction orders with respect to species j in the forward and backward reactions. Reaction orders might be listed separately for global reactions, otherwise they are considered equal to the molar stoichiometric coefficients of that species in the reactants and products.

It is important to note that the concentrations $\mathcal{C}_j$ of the species j in Eq. (3.45) should be computed in a thermodynamically consistent way for dense gaseous mixtures at high pressure. We propose to use the species' fugacity for this purpose, that is,

$$\mathcal{C}_j \simeq f_j/(RT), \tag{3.47}$$

with f_j being the fugacity of species j in the mixture. The fugacity is computed from the fugacity coefficient $\varphi_j = f_j/(X_j p)$, which can be obtained using the molar specific volume function

$$\varphi_j = RT/(p\psi_j), \tag{3.48}$$

with ψ_j being the molar specific value of volume function for species j, see Ref. [51]. Using the definition of the fugacity coefficient and the molar specific volume function, the required concentration can therefore be computed via the following simple relation for non-ideal multi-component gases

$$\mathcal{C}_j = X_j/\psi_j \tag{3.49}$$

where ψ_j can be computed using the effective reduced parameters

$$\ln \psi_j = \textstyle\sum_{k=1}^{N_m} \mathcal{H}_k s_{kj} + \mathcal{H}_{N_m+1} b_j + \mathcal{H}_{N_m+2}, \tag{3.50}$$

with $\mathcal{H}_1, \ldots, \mathcal{H}_{N_m+2}$ computed using the gas or supercritical mixture temperature, composition and specific volume via Eqs. (3.34-3.36). Note that in the limit of very high temperature, the fugacity coefficient tends towards unity and the ideal-gas mixture formula $\mathcal{C}_j = X_j p/(RT)$ is recovered consistently.

The fugacity-based evaluation of concentrations via Eq. (3.47) simplifies the computation of the backward reaction coefficient whenever it is not explicitly provided. In such cases, the backward rate coefficient should be computed using the equilibrium constant $K_\mathrm{c} = k_f/k_b$. If the reaction rates are expressed as proposed in terms of the fugacity, the equilibrium constant can be computed similarly to the ideal-gas formula in [102] from

$$K_{\mathrm{c},r} = [p^\circ/(RT)]^{\nu_r} \exp[\Delta S_r^\circ/R - \Delta H_r^\circ/(RT)], \tag{3.51}$$

with $\nu_r = \sum_{i=1}^{N} (\nu_{ir}^{\mathcal{P}} - \nu_{ir}^{R})$ being the net change in the number of species in the reaction, and ΔH_r° and ΔS_r° being the reaction enthalpy and entropy net change at the standard pressure $p^\circ = 1\,\mathrm{atm}$.

3.2.4. LARGE EDDY SIMULATION

In this work, LES is utilized for turbulence modeling. LES provides the time-accurate evolution of the large scales of fluid flows that encompass almost all of the mechanical energy of the turbulent fluid motion. The evolution of the large scales is governed by a coarse-grained or low-pass filtered form of the Navier-Stokes equations. The effect of nonlinear interactions between the large resolved scales and the small truncated ones is taken into account via an appropriate modeling of the subgrid-scale (SGS) stress tensor.

In explicit LES, the SGS tensor is approximated based on the continuous filtered differential equations and model expression depending on, e.g., the filtered strain rate and possibly other quantities for which additional transport equations are needed, and the discretization of the continuous filtered transport and model equations in space and time is carried out afterwards using standard approximation theory. For implicit LES, however, the coarse-grained discrete numerical model is directly derived in a single approximation step that includes models for the effects of unresolved interactions consistent with a specifically tailored high-order numerical discretization [103].

The LES presented in this chapter have been performed with the adaptive local deconvolution method (ALDM) of Hickel, Egerer, and Larsson [94], which is a physically consistent implicit LES method based on a nonlinear, solution adaptive finite-volume discretization scheme and spectral turbulence theory. ALDM is appropriate for LES of the full Mach number range without any user-defined model parameters. Its performance in comparison to common explicit LES models has been reported by Muller *et al.* [32] for several transcritical and supercritical nitrogen jets. As discussed by Matheis and Hickel [35], ALDM does not account for all additional SGS quantities that appear after low-pass filtering the non-linear equations used for the evaluation of the thermo-transport properties and chemistry sources in transcritical flows. Although novel ideas towards modelling some of these terms have been proposed, their performance for transcritical conditions at high Reynolds numbers remains unclear due to a lack of experimental data for high-order statistics and spatial details. ALDM has been extensively verified and validated for transcritical injector flows; for example, by Matheis *et al.* [89] for Tani's cryogenic coaxial injector, by Muller *et al.* [31] for Oschwald's coaxial injector, and by Matheis and Hickel [35] for the non-reacting ECN Spray-A.

3.2.5. Numerical Implementation

Real-fluid multiphase thermodynamics and the fugacity-based finite rate chemistry model are implemented in our fluid flow solver INCA (https://inca.cfd). We employ the same discretization schemes for the transport equations as Matheis and Hickel [35]. In this subsection, these schemes are briefly reviewed.

The governing equations are discretized in space by a conservative finite-volume scheme that uses a second-order central difference method for the diffusion terms, and ALDM for the inviscid fluxes. The van Albada limiter [104] is utilized for the mass and energy flux reconstruction to avoid spurious oscillations with possible under- or overshoots at sharp density gradients.

A second-order Strang-splitting scheme is utilized to separate the stiff chemical reactions from the advection and diffusion mechanisms. The method consists of three major steps: First, the solution is updated by considering only the reaction source terms in half a time step by means of a stiff ODE solver. We used VODE [105] for this purpose, which is a variable-coefficient implicit solver based on 5th-order backward differentiation formulas. Second, the obtained solution is set as the initial condition for a full advection and diffusion time step with the explicit third-order strong stability preserving Runge-Kutta scheme of Gottlieb and Shu [106]. Finally, the solution is updated with the second half reaction step. The time step size is dynamically adapted according to the Courant–Friedrichs–Lewy stability condition with CFL=1.

3.3. TRANSCRITICAL ECN SPRAY-A

3.3.1. EXPERIMENTAL SETUPS

The standard reacting and non-reacting test cases of ECN Spray-A [107] are selected for validation and demonstration. The fuel is pure n-dodecane ($C_{12}H_{26}$) with a low temperature of 363 K, and is injected into a chamber with a pressure of 60 bar and a temperature of 900 K. At these conditions, the cold liquid n-dodecane undergoes a transcritical vaporization process, since the chamber pressure is much higher than the critical pressure (18.2 bar) of n-dodecane. The injection rail pressure is 1500 bar and the injector consists of a hydro-eroded single-hole nozzle with the nominal diameter of $D = 0.09\,\mathrm{mm}$ leading to the injection of about 3.5 mg of n-dodecane fuel with a relatively constant jet velocity of about $600\,\mathrm{m\,s^{-1}}$ during the injection time of about 1.5 ms. The chamber gas is mostly nitrogen, to which oxygen is added for the reacting case. Elevated concentrations of carbon dioxide and water vapor result from burning acetylene along with hydrogen in the preparation stage. Table 3.1 summarized the initial molar composition of the gas in the chamber.

Table 3.1.: Mole percentage of species in the chamber of reacting and non-reacting cases.

	O_2	N_2	CO_2	H_2O
Non-reacting	0.00	89.71	6.52	3.77
Reacting	15.00	75.15	6.23	3.62

3.3.2. COMPUTATIONAL SETUP

GRID SPECIFICATIONS

All simulations have been carried out using a mesh generated for a three-dimensional rectangular domain with a length of 934 D in the axial direction and 467 D in the lateral directions, with $D = 0.09\,\mathrm{mm}$ being the nominal diameter of the injector nozzle.

To minimize the total number of computational cells, we instruct the flow solver INCA to perform static zonal mesh refinement within a user-defined region of interest. This region of interest is defined as a 10° cone that encloses the injected jet. The target level of refinement inside the cone is defined based on the distance from the injector nozzle, with resolution steps at axial locations 665, 411, 254, 157, 97 and 60 D from the injector nozzle. The resulting mesh is shown in Fig. 3.2. The multi-block structured grid consists of 2864 blocks and 12.7×10^6 cells with seven resolution levels, which are marked by L1 to L7 in Fig. 3.2. Around 40 % of the cells belong to the finest level with $\Delta y_{\min} = \Delta z_{\min} \simeq 10.25\,\mu\mathrm{m}$ and $\Delta x_{\min} = 2\Delta y_{\min}$ located in the near-nozzle region ($x/D < 60$), see the zoomed area on the left side in the figure.

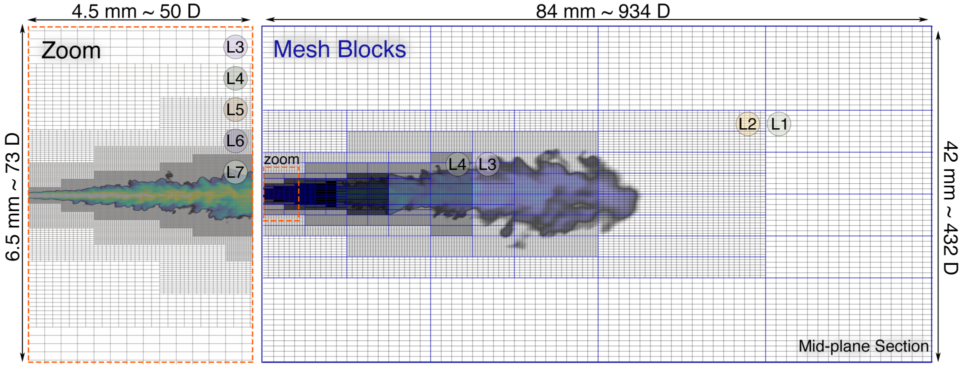

Figure 3.2.: A mid-plane section of the 3D multi-block structured grid with 7 levels of mesh refinements generated for LES-MT of reacting and non-reacting ECN Spray-A.

Boundary Conditions

The injector nozzle is not resolved; instead, a suitable transient inflow condition is used at the injector's nozzle exit plane. This inflow is pure n-dodecane at a temperature of 363 K and a pressure of 60 bar with a transient axial velocity that provides the same amount of momentum as the experiment. We calculated the mass flow rate with the CMT virtual injection rate generator (http://www.cmt.upv.es) with input parameters according to the experimental conditions and a fuel density of 687.24 kg m^{-3} consistent with the RKPR EOS at the given pressure and temperature. Fig. 3.3 shows the generated transient injection velocity. Subsonic inlet conditions are used as the Mach number of the pure liquid is approximately 0.5 at the nozzle exit. Mass densities and the velocity vector are imposed as Dirichlet boundary conditions, and a homogeneous Neumann condition is used for the static pressure. The transient profile is directly used as a boundary condition without adding any artificial turbulent fluctuations at the boundary. The induced shear and hydrodynamic pressure fluctuations at 600 m s^{-1} are expected to be strong enough to create turbulence almost instantaneously.

Subsonic pressure outflow conditions are imposed at the exit face, with a constant static pressure of 60 bar as a Dirichlet condition and extrapolation of the other independent flow variables from the domain inside. Adiabatic no-slip conditions are applied for all other boundaries of the rectangular domain.

Reaction Mechanism

The finite-rate chemistry model formulated for the real-fluid effects in Section 3.2.3 is used for the calculation of chemical source terms in the species mass conservation equations. To alleviate the already high computational load of the LES-MT method, the highly-reduced global two-step reaction mechanism of Hakim *et al.* [84] is selected. This mechanism was calibrated using Bayesian inference for the precise prediction of the ignition delay time of n-dodecane combustion at the experimental condition of the ECN Spray-A test case. The reduced mechanism has 6 species.

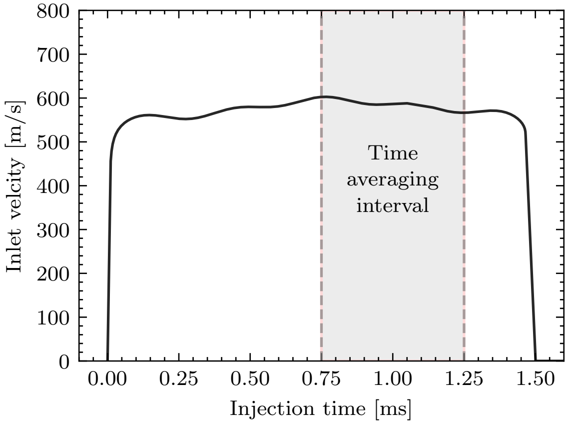

Figure 3.3.: Transient injection velocity profile used for the simulation of reacting and non-reacting ECN Spray-A test cases, computed for using RKPR EOS.

Similar to the approach of Westbrook and Dryer for the oxidation of paraffins, the incomplete oxidation of n-dodecane is accounted for by two-step reactions as given below:

$$\mathrm{C_{12}H_{26}} + 12.5\mathrm{O_2} \;\rightarrow\; 12\mathrm{CO} + 13\mathrm{H_2O}, \tag{3.52}$$

$$\mathrm{CO} + 0.5\mathrm{O_2} \;\rightleftharpoons\; \mathrm{CO_2}. \tag{3.53}$$

The forward reaction rates (in cgs units) are expressed in Arrhenius form

$$\mathcal{Q}_1 = \mathcal{A}_1 \exp[-31944/(RT)]\mathcal{C}_{\mathrm{C_{12}H_{26}}}^{0.25}\mathcal{C}_{\mathrm{O_2}}^{1.25} \tag{3.54}$$

$$\begin{aligned}\mathcal{Q}_2 = 3.98\times10^{14}\exp[-40000/(RT)]\mathcal{C}_{\mathrm{CO}}\mathcal{C}_{\mathrm{H_2O}}^{0.5}\mathcal{C}_{\mathrm{O_2}}^{0.25}\ldots\\ -5\times10^{8}\exp[-40000/(RT)]\mathcal{C}_{\mathrm{CO_2}}\end{aligned} \tag{3.55}$$

The logarithm of the Arrhenius pre-exponential factor of the first reaction varies according to the local fresh-gas condition dynamically through

$$\ln\mathcal{A}_1 = \theta_0 + \theta_1\exp(\theta_2\phi_0) + \theta_3\tanh[(\theta_4+\theta_5\phi_0)T_0+\theta_6]. \tag{3.56}$$

The best possible values of θ_0 to θ_6 found by matching the ignition delay time

Table 3.2.: The optimal parameters for evaluation of the pre-exponential factor of n-dodecane reaction in the reduced mechanism of Hakim *et al.* [48].

θ_0	θ_1	θ_2	θ_3	θ_4	θ_5	θ_6
27.38	-2.13	-2.05	1.89	-0.01	2.87e-4	8.43

with the skeletal mechanism of Narayanaswamy, Pepiot, and Pitsch [108] are listed in Table 3.2. The local fresh gas temperature T_0 and equivalence ratio ϕ_0 can be estimated using the local value of mixture fraction [48]. The mixture fraction is computed here by tracking the inert nitrogen mass fraction:

$$f = (Y^{\mathrm{ox}}_{\mathrm{N_2}} - Y_{\mathrm{N_2}})/Y^{\mathrm{ox}}_{\mathrm{N_2}}, \tag{3.57}$$

with $Y^{\mathrm{ox}}_{\mathrm{N_2}} = 0.72$ in the oxidizer stream of reacting case.

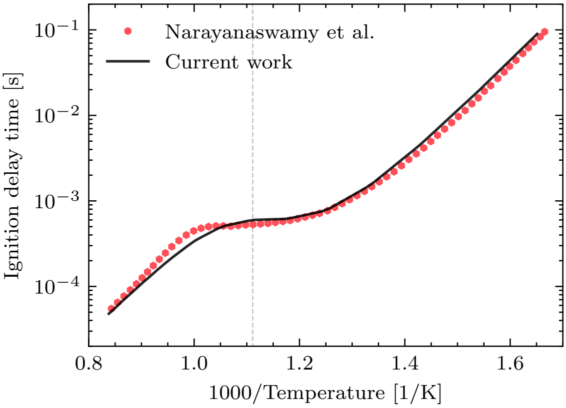

Figure 3.4.: Ignition delay time for the skeletal mechanism of Narayanaswamy, Pepiot, and Pitsch [108] and the current work using the reduced mechanism of Hakim *et al.* [84] for the stoichiometric mixture of the fuel and oxidizer of ECN Spray-A.

We evaluate the performance of the reduced two-step 6-species reaction mechanism of Hakim *et al.* [84] by calculating the ignition delay time in a homogeneous constant-volume reactor for a stoichiometric mixture of the fuel and oxidizer of the reacting Spray-A case. The volume of the reactor is set according to the initial temperature, stoichiometric composition, and pressure of 60 bar using the RKPR EOS. Table 3.3 lists the critical values and the acentric factor of the species required for the simulations of ECN Spray-A with this reduced reaction mechanism. Figure 3.4 shows the time elapsed until the temperature of the reactor has increased by 400 K above its initial value. We observe an excellent agreement between the ignition delay time predicted by the reduced two-step mechanism used in this study and the skeletal mechanism of Narayanaswamy, Pepiot, and Pitsch [108] with 876 reactions and 164 species.

Table 3.3.: Critical properties and acentric factor of the species.

Species	T_c [K]	p_c [bar]	Z_c [-]	ω [-]
$C_{12}H_{26}$	658.0	18.20	0.251	0.576
O_2	154.6	50.43	0.288	0.022
N_2	126.2	34.00	0.289	0.038
CO_2	304.2	73.83	0.274	0.224
H_2O	647.1	220.6	0.229	0.345
CO	132.9	34.99	0.299	0.048

3.4. NUMERICAL RESULTS

In this section, we use experimental reference data of the reacting and non-reacting ECN Spray-A in order to evaluate and validate the proposed multiphase thermodynamics and real-fluid finite rate chemistry model for transcritical fuel sprays.

3.4.1. NON-REACTING CASE

We compare experimental and numerical flow visualizations of the inert Spray-A at 7 specific instants after the start of injection (ASOI) in Fig. 3.5. The left column shows experimental schlieren images [109] and the right column shows predictions of our LES-MT model. The non-reacting jet first penetrates in the axial direction and spreads in the radial direction while evaporating and mixing with the hot chamber gas, and then maintains an approximately constant radius after some downstream distance from the injector nozzle. In the experimental schlieren images, the saturated dark regions represent the liquid phase. For LES-MT snapshots, we show colored contours of the liquid volume fraction (LVF), which also indicate the amount of the liquid phase, and density gradients in the single-phase gaseous regions, where LVF=0. The liquid penetration length is reported to be about 10 mm in the experiment, which is in excellent agreement with our numerical results, see also Fig. 3.6.

Figure 3.6 shows the temporal evolution of the liquid penetration length (LPL) and the vapor penetration length (VPL) for the LES-MT numerical simulation and experimental measurements [110, 111]. For the LES-MT, LPL and VPL are defined as the maximum axial locations with a LVF of 15 % and a mixture fraction of 0.01 %, respectively, similar to previous studies [30]. The LPL signals of LES and experiment are in excellent agreement. For the VPL, we observe excellent match up to about 0.6 ms. At later times, the simulation predicts slightly larger values than those measured in the experiment. This could be due to the coarsened mesh at those locations far from the nozzle, or due to measurement uncertainties. The estimated uncertainty of the experimental measurements is indicated by the gray-shaded area and significantly increases with time. On the right side of the same figure, we also compare an experimental snapshot with highlighted liquid and vapor boundaries with a numerical visualization. The agreement is good, considering that both snapshots are instantaneous samples of independent realizations of highly turbulent flows.

We present ensemble-averaged profiles of the mixture fraction on the center line and at two downstream locations in Fig. 3.7. The statistics have been computed by ensemble averaging LES data collected at 8 circumferential sections every 0.5 µs during the time interval highlighted in Fig. 3.3. LES-MT results follow the measured axial profiles very well. At the first station, $x =$18 mm, the n-dodecane mass fraction on the jet axis is overestimated by the LES compared to the experiment; however, the LES data fully agree with the experimental data further downstream, which can also be seen from the radial profiles at $x =$36 mm.

Figure 3.8 shows global scatter plots of the temperature and the mole fractions of the major species n-dodecane and nitrogen as a function of the mixture fraction.

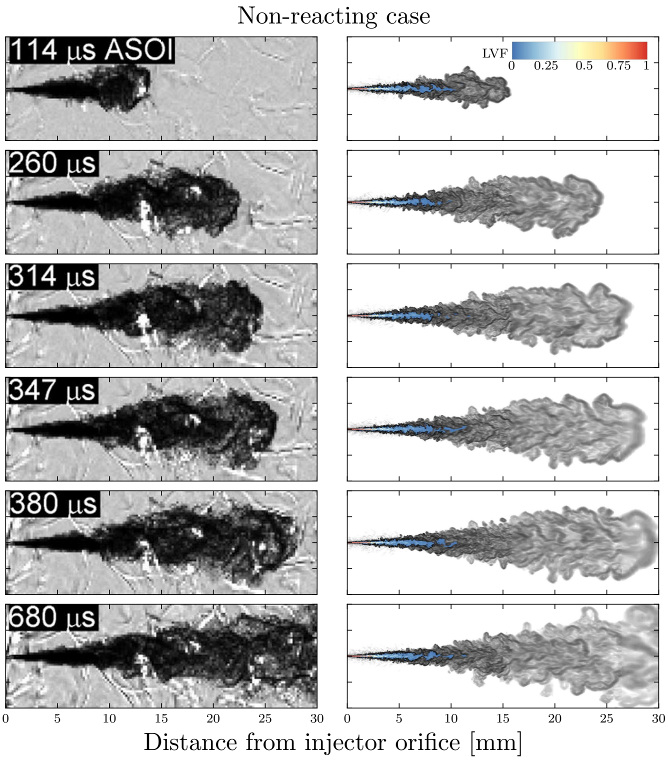

Figure 3.5.: Schlieren images of the non-reacting Spray-A (left: experiment [109]) and density gradient contours of LES-MT solution, overprinted in the two-phase region by liquid volume fraction contours (right).

Each point represents an instantaneous local state of the resolved LES-MT flow field for the non-reacting case at 680 µs. The data points are colored with the molar vapor fraction in a way that green is completely vapor and purple is completely liquid. The two-phase region at the nominal operating pressure of 60 bar is indicated in the temperature/mixture-fraction diagram. A hypothetical temperature profile predicted by multiphase thermodynamics assuming isenthalpic mixing at 60 bar is also shown. Two-phase boundary and isenthalpic curve cross each other at a mixture fraction of about 0.34 for this case using RKPR EOS. The LES data points follow the isenthalpic line strikingly well. This is explained in more detail in Refs. [30, 35]. In the two-phase region, liquid and vapor phases have different molar compositions, as determined by phase-equilibrium computations. The vapor and liquid compositions are shown for the two major species, n-dodecane and nitrogen, in the mole-fraction/mixture-fraction diagrams in Fig. 3.8. The diagrams indicate that the saturated liquid contains only about 90 % n-dodecane and the rest is mostly nitrogen. This is a consequence of the high solubility of nitrogen in n-dodecane at transcritical pressures, and questions the standard pure-fuel assumption made for liquid droplets in traditional LPT methods.

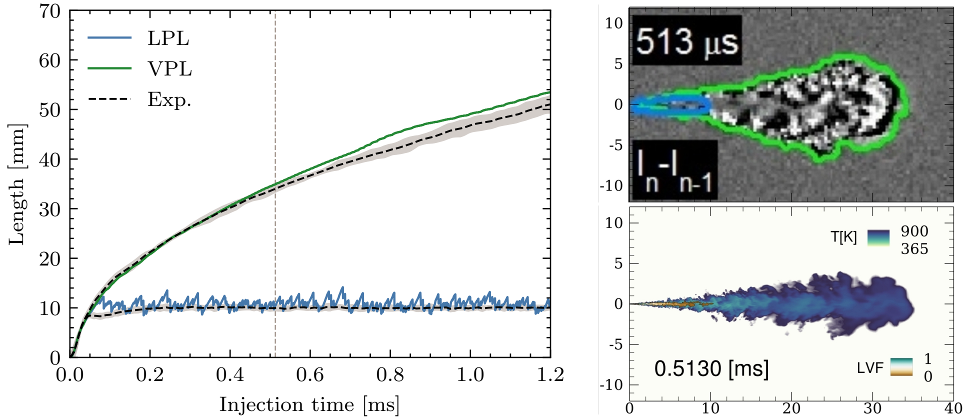

Figure 3.6.: Vapor and liquid penetration trajectories for LES-MT and experiment [110, 111] for the non-reacting ECN Spray-A on the left, and an experimental schlieren image with highlighted vapor and liquid boundaries compared with an LES-MT temperature contour overprinted with LVF in the liquid and two-phase region at the same instance on the right.

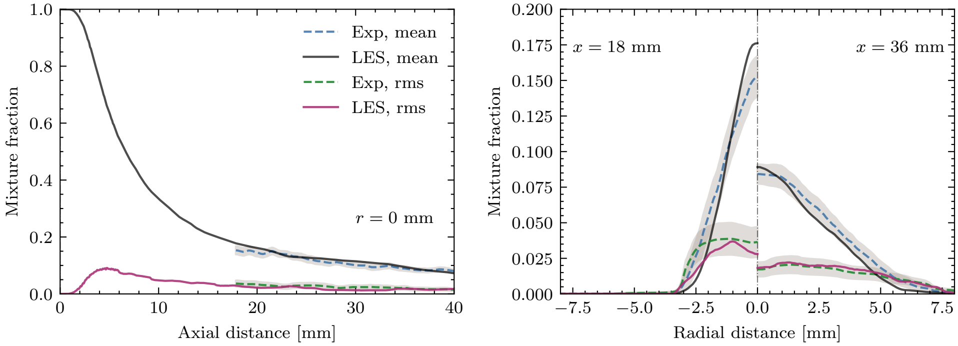

Figure 3.7.: Axial (left) and radial (right) profiles of mean and RMS fluctuations of the mixture fraction computed using LES-MT method in comparison with Rayleigh scattering measurements [111] for the non-reacting Spray-A.

Figure 3.9 shows the contours of the molar composition of the overall mixture as well as the compositions of the liquid and vapor phases for all species. Here, the *overall* refers to the total mixture within the two-phase region, i.e., the mole fraction in each cell is computed based on the total number of moles of each species present in both the saturated liquid and saturated vapor phases. The figure indicates the spatial evolution of mixing process controlled by multiphase thermodynamics. While the heavy n-dodecane molecules represent about 90 % of the total moles of the liquid core, they are in the minority in the vapor phase, which consists mainly of light nitrogen molecules corresponding to the initial composition of the chamber gas. The fuel-rich liquid core extends up to about 3 mm from the injector nozzle. Far from the nozzle and close to the tip of the liquid core,

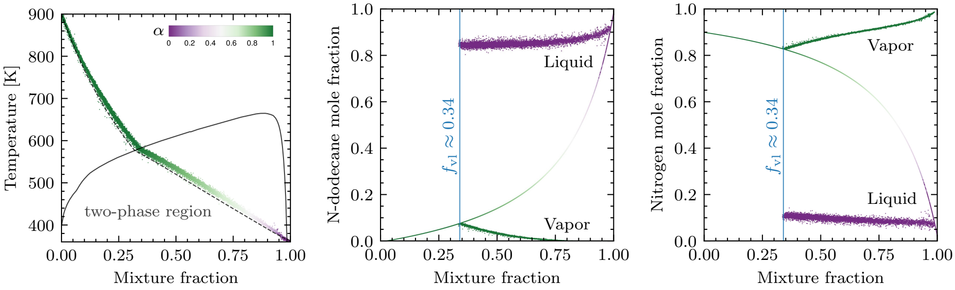

Figure 3.8.: Scatter plots of the LES results for the non-reacting Spray-A at 680 µs colored by vapor mole fraction values. The temperature / mixture-fraction diagram (left) shows also the temperature variation during an isenthalpic process (dashed line) and two-phase region boundaries at 60 bar. The n-dodecane (middle) and nitrogen (right) mole fraction diagrams show the overall as well as the saturated liquid and vapor phases.

where the vapor mole fraction is close to unity, the mixture composition is close to the saturated vapor phase and, accordingly, the mixture fraction is close to 0.34. Water has roughly the same concentration in the liquid and vapor phases, which is in contrast to nitrogen, n-dodecane, and carbon dioxide. This means that water in contact with the cold n-dodecane dissolves quickly into the liquid phase, while the other species in the environment mostly stay in the saturated vapor phase.

3.4.2. Reacting case

The temporal evolution of the reacting ECN Spray-A is shown in Fig. 3.10. This figure shows experimental schlieren images [109] on the left side and corresponding snapshots of the LES-MT solution on the right side. Similar to the inert test case, the liquid phase appears as a saturated black region in the experimental schlieren images and contours of the LVF show the predicted amount of liquid for the LES-MT. There is a very good agreement between the experiment and simulation, and the jet develops very similar to inert spray up to the auto-ignition. The ignition delay time is approximately 400 µs for both experiment and simulation. Around the ignition time, low-temperature reactions are activated in a significant portion of the vaporized fuel. This is detectable between 20 and 25 mm after 314 µs via brighter regions in the schlieren images, and visualized by blue iso-temperature surfaces at 920 K for the LES-MT results. The high-temperature ignition occurs after the low-temperature reactions created a sufficient concentration of radicals and intermediate species. The highly reacting region is highlighted by the red iso-temperature surface at 2000 K for the LES results in the last snapshot at 680 µs. The high-temperature ignition is a rapid volumetric process. An abrupt radial expansion of the reacting jet, compared to the inert case, is observed near the location of the flame front. We observe good agreement of the experimental flame lift-off length (LOL) with our LES-MT result which is about 15 mm as shown in the last snapshot.

The reacting transcritical jet can be characterized by three important lengths

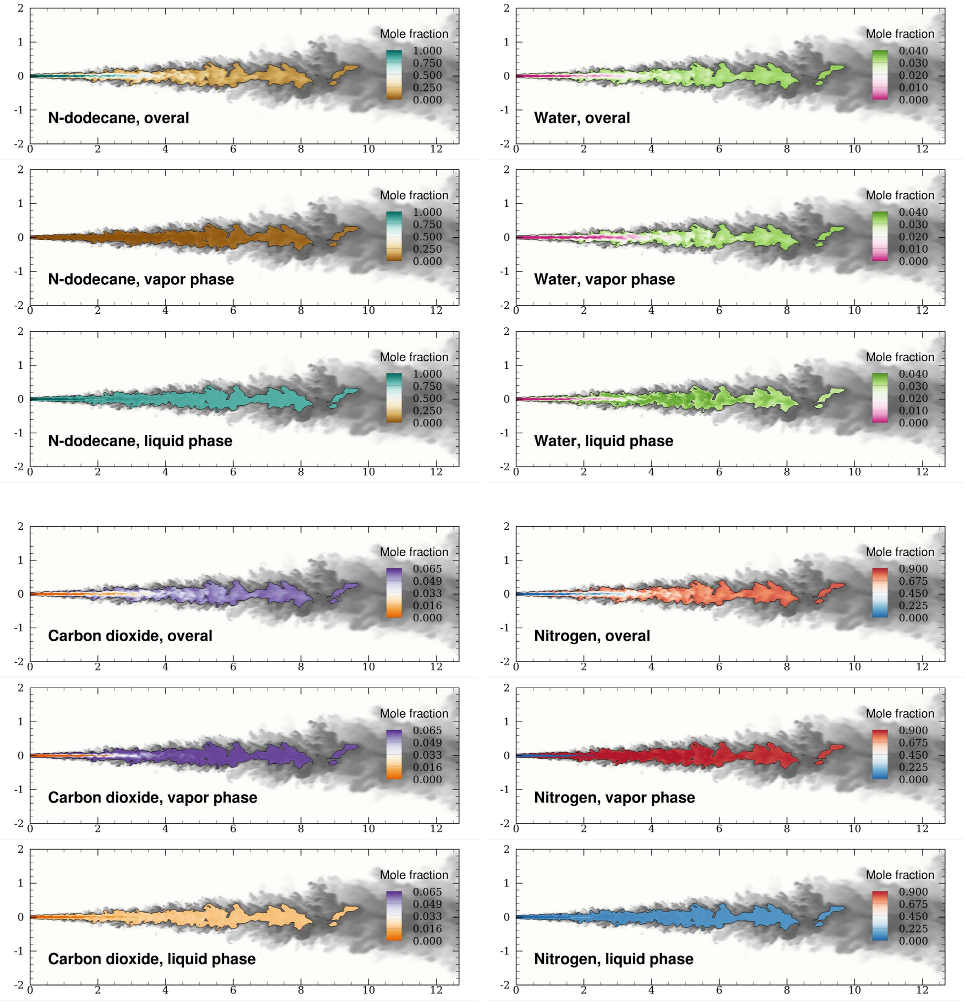

Figure 3.9.: Instantaneous molar composition of the overall fluid, as well as the composition of the vapor and liquid phases. The background contour represents the temperature field from dark to light shades. In the two-phase region, contours of the species mole fraction of saturated liquid, saturated vapor and overall mixture are presented.

scales: LPL, VPL, and LOL. Figure 3.11 shows the time evolution of these lengths for our LES-MT results and the experimental measurements [110, 111]. For the LES-MT, LPL and VPL are computed by the method explained above for the non-reacting case. The LOL is computed as the minimum axial location where the temperature exceeds 1800 K. The uncertainty of the experimental measurements is indicated by the grey area around the dotted lines in Fig. 3.11. The numerically predicted and experimentally measured LPL evolution is in excellent agreement. The VPL evolution is in very good agreement up to about 40 mm and afterwards

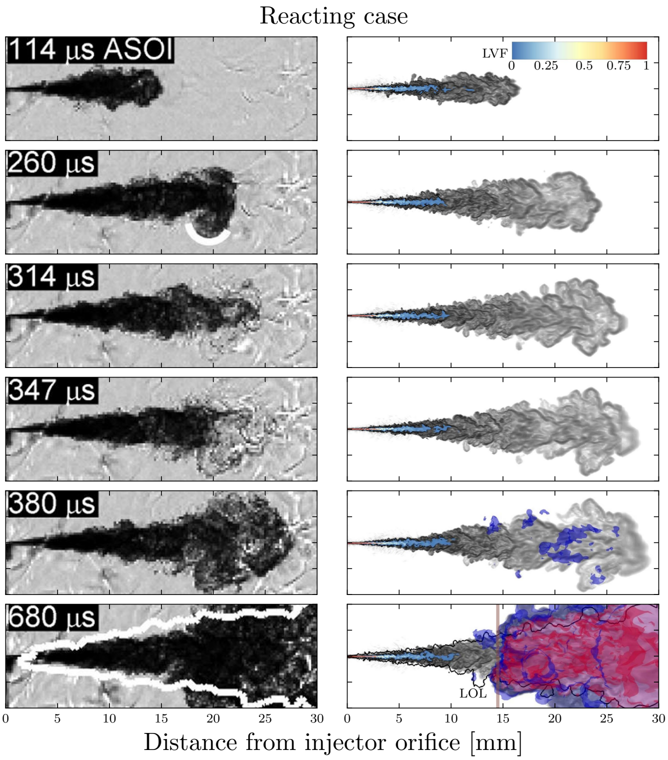

Figure 3.10.: Time sequence snapshots of reacting Spray-A for experiment (schlieren images on the left [109]) and LES-MT (right). The white border in the last snapshot of the experiment shows the non-reacting vapor boundary at the same timing. For the LES-MT, background contours of the density gradient are overprinted by liquid volume fraction contours in the two-phase region, and blue and red iso-surfaces for temperatures of 920 K and 2000 K enclose the regions of low and high temperature reactions. The flame lift-off length (LOL) is indicated in the last snapshot.

the values predicted by the simulation are slightly higher than the experimental data. This is consistent with the results for the non-reacting case. The evolution of the flame LOL is again in excellent agreement with the experiment, even though we use a highly reduced reaction mechanism for the simulation. In order to visualize the flame shape and volume, an experimental snapshot with highlighted high temperature boundaries is compared with the temperature contour plot for an LES-MT snapshot at the same time instant on the right side of Fig. 3.11. The numerical and experimental flame snapshots are in good qualitative agreement.

Figure 3.12 shows species mole fraction contours on a plane normal to the axial direction at $x = 18\,\mathrm{mm}$ and $t = 590\,\mu\mathrm{s}$, that is, at a distance larger than LOL of the developed flame. Accordingly, there exists no liquid phase at this location. The molar composition indicates partially premixed conditions of the fuel and environment even in the core of the reacting jet. The molar composition at the core is more close to the saturated vapor phase.

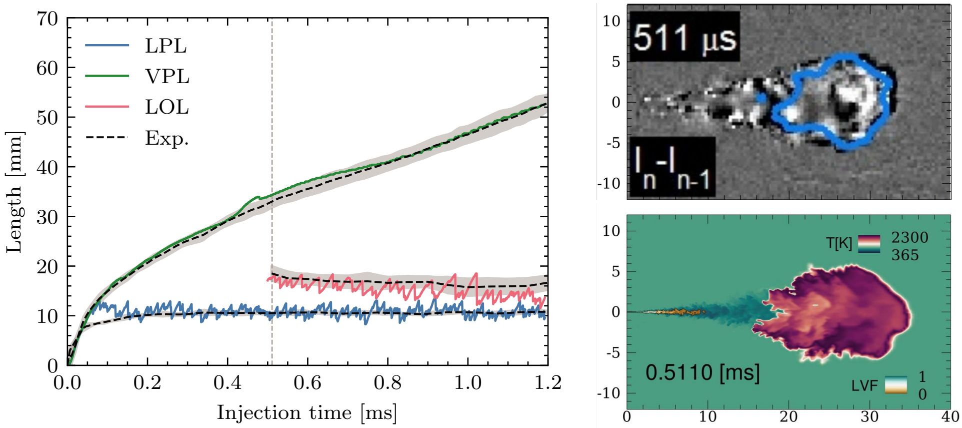

Figure 3.11.: Vapor and liquid penetration trajectories predicted by the LES-MT method and measured experimentally [110, 111] for the reacting Spray-A (left). The two right panels show an experimental schlieren image with highlighted flame boundaries along with an LES-MT temperature contour overprinted with the LVF at the same nominal time.

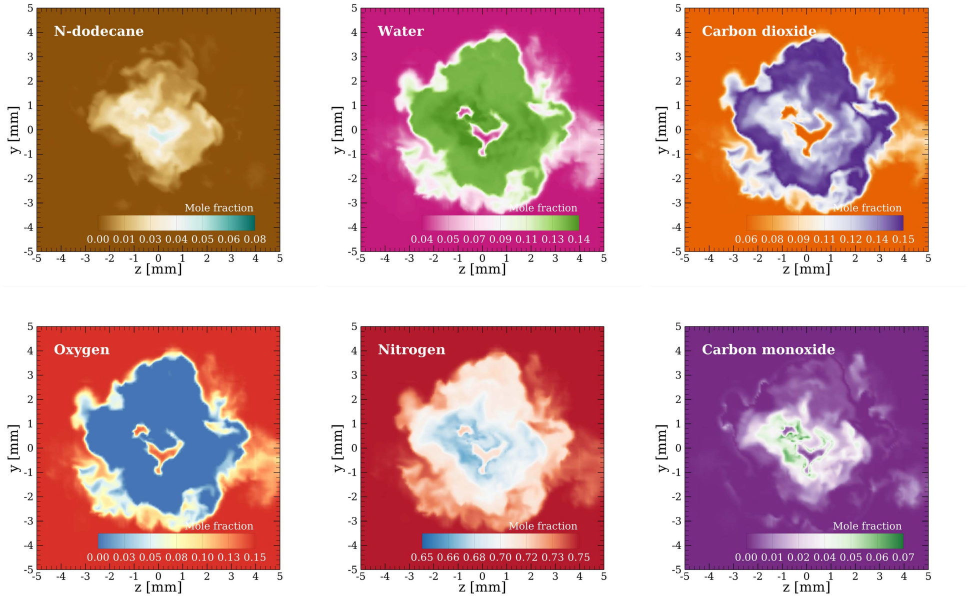

Figure 3.12.: Instantaneous snapshots of species mole fractions located at plane $x = 18\,\mathrm{mm}$ at $590\,\mu\mathrm{s}$ ASOI in the reacting case.

The auto-ignition process is illustrated in Fig. 3.13, where we show global scatter plots of the temperature in mixture fraction space at three different time instants. The first snapshot taken at $380\,\mu\mathrm{s}$ is representative for the very late pre-ignition state, where significant low-temperature reactions are occurring and the temperature is slowly increasing around the stoichiometric mixture fraction. The spatial distribution of these low-temperature kernels is shown in Fig. 3.10. The second snapshot is taken at 420 µs, that is, shortly after the auto-ignition time ($t \approx 400$ µs). Several high-temperature flame kernels have been formed in regions with a stoichiometric mixture fraction, where enough radicals and intermediate species coexist. In the third snapshot at 590 µs, the ignition process is completed and has provided enough thermal energy for the propagation of the flame. We see that the high-temperature reactions are spreading into the fuel-rich regime.

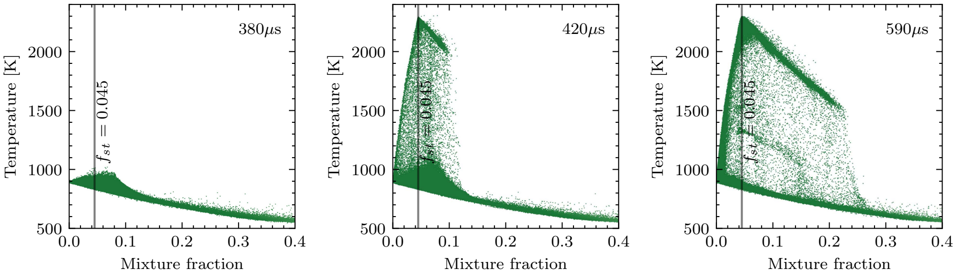

Figure 3.13.: Scatter plot of the temperature in mixture fraction space close to and after the ignition time.

3.5. Discussion

The above presented results of ECN Spray-A simulations demonstrate the potential of LES-MT modelling for the accurate prediction of reacting and non-reacting turbulent multiphase fluid flows at transcritical pressures. The proposed LES-MT method is free from the main limitations of classical Lagrangian methods, which do not account for the solubility of real-fluid mixtures at elevated pressures and additionally may suffer from inaccurate density predictions if ideal-gas models are used, and Eulerian dense-gas (DG) models, which can become arbitrarily inaccurate in the two-phase region (where they may predict negative pressures, e.g.). Moreover, high-pressure combustion typically initiates in low-temperature reacting zones in which the fluid state and transport properties deviate strongly from ideal-gas laws. Making ideal-gas assumptions, which is very common in combustion simulations, or the assumption of a dense-gas without accounting for local two-phase regions, can lead to large errors and uncertainties in transcritical combustion simulations. Furthermore, the LES-MT method provides the possibility of applying different reaction mechanisms in the liquid and vapor phases. Classical DG methods cannot make this distinction and have to apply the reaction mechanism on the overall composition, including possible condensates. For these reasons, we emphasize that real-fluid and phase-equilibrium effects should be considered in transcritical jets and flames. Doing so can yield very accurate predictions for the spreading angle, liquid penetration lengths, vapor penetration lengths, ignition delay time, and flame lift-off length, such as shown in Fig. 3.14 and discussed in the previous sections.

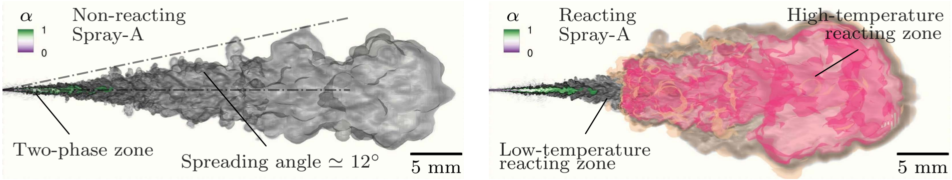

Figure 3.14.: Volume renderings at 800 µs after the start of transcritical injection of n-dodecane ($C_{12}H_{26}$ at 363 K) into a preheated chamber at 900 K without oxygen (left) and with oxygen (right) using a real-fluid finite-rate chemistry and multiphase thermodynamics models. The operating pressure is 60 bar which exceeds the critical pressure of n-dodecane.

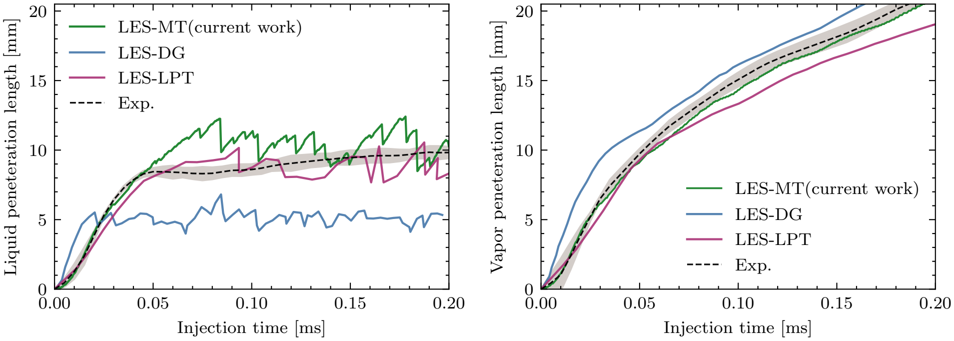

Figure 3.15.: Liquid- and vapor-penetration lengths for the LES-MT of the present work, LES-DG of Hakim, Lacaze, and Oefelein [83], and highly-calibrated LES-LPT of Gadalla *et al.* [82] against the ECN Spray-A experiment [110, 111].

The LES-MT method is accurate and calibration-free. To put its performance into perspective, we compare results for the vapor and liquid penetration trajectories of Spray-A computed with the present LES-MT method, LES-DG results of Hakim, Lacaze, and Oefelein [83], results of the highly-calibrated LES-LPT method of Gadalla *et al.* [82] and the reference experiments [110, 111] in Fig. 3.15. The figure shows the initial 0.2 ms of the transient start-up during which we expect a similar behavior for the reacting and inert cases. Predictions of the current method are very close to the measurements for both liquid and vapor length. Gadalla *et al.* [82] have calibrated the initial droplet size for their LES-LPT method in such a way that the liquid length is close to the experimental data. This calibration, however, apparently affected the vapor length prediction unfavorably. The single-phase DG method yields the least accurate prediction for this case. As the liquid phase boundaries are not directly predicted by the single-phase method, Hakim, Lacaze, and Oefelein [83] defined the boundary of the liquid regions via the mixture fraction value at which the density gradient peaks.

The major drawback of the LES-MT method might be the highly non-uniform computation costs, which limits the parallel scalability of flow solvers with domain decomposition methods. The wall-clock time for simulating 10 µs of the reacting spray, including the time needed for writing snapshots every 0.5 µs, is approximately 8.5 h on 16 nodes with two Intel Xeon Gold 6248R CPU (24 cores at 3.00 GHz), which corresponds to approximately 6500 CPUh. On average, about 40 % of the CPU time is used for evaluating the EOS and transport properties, and the majority of the rest is used for evaluating the reaction rates, the spatial derivatives of the Navier-Stokes equations, communication, and snapshot output.

Last but not least, it should also be mentioned that we have applied LES in a rather straightforward way without specifically addressing turbulence-combustion interactions other than by providing reasonable spatial and temporal resolution. The unresolved thermodynamic microstructure (SGS variations of pressure, temperature, and composition) has without doubt nonlinear effects on the resolved-scale solution [112], and it seems reasonable to assume that transcritical multiphase flows are much stronger affected than ideal-gas or single-phase real-gas flows. Hence, the quantification of uncertainties resulting from the unresolved microstructure on the resolved pressure, temperature, and subgrid-scale terms is the subject of our future studies.

3.6. CONCLUSIONS

We have presented a real-fluid finite-rate chemistry multiphase thermodynamics model for the numerical simulation of transcritical vaporization, auto-ignition, and combustion of a cold or cryogenic fuel injected into a hot high-pressure environment. The methodology is based on solving the fully conservative form of the compressible multi-species Navier-Stokes equations along with real-fluid volumetric and caloric state equations. These state equations provide accurate real-fluid thermodynamic properties for multi-component fluids that can exist either in a single phase or undergo phase transitions during vaporization and condensation. Multiphase and real-gas effects are also considered in the finite-rate chemistry model, which we propose based on the fugacity or molar specific volume function of the species.

The methodology has been demonstrated and validated for the transcritical reacting and non-reacting ECN Spray-A. LES results obtained with the proposed thermodynamic models are in excellent agreement with the experimental reference data for both cases. The time evolution of temperature in the mixture fraction space proves the existence of the low-temperature and high-temperature combustion stages in the autoignition process of Spray-A, which have been reported experimentally.

The very good agreement of auto-ignition time, flame lift-off length, and flame structure might be surprising because only a simple two-step reaction mechanism has been applied. However, one should note that Hakim's mechanism has been specifically calibrated for the considered flow conditions including low- and high-temperature ignition stages. In our LES, real-gas vapor-liquid equilibrium calculations accurately determine the saturated vapor composition, and this composition and the rate with which it mixes with the oxidizer determines when and where auto-ignition takes place.

4

Transcritical Multiphase CounterFlow Diffusion Flames

In Chapter 4, the focus shifts to counterflow diffusion flames to better understand the microscale physics of transcritical combustion. Here, advanced models are developed to simulate the nonideal transport and chemical behavior of transcritical mixtures. The chapter also introduces models for calculating fugacity-based diffusion driving force, and extends these to the multiphase regime. For completeness, this chapter includes a brief outline of material that has been presented previously. Simulations show how real-fluid effects alter flame dynamics and ignition behavior, and demonstrate that common assumptions like ideal-gas behavior or unity Lewis number can lead to large errors.

The content of this chapter has been published as *Numerical Simulation of Transcritical Multiphase Combustion Using Real-Fluid Thermochemical and Transport Properties* in Combustion and Flame **275** (2024) [113].

4.1. INTRODUCTION

Experimental studies showed that transcritical fuel injection is a mixing-controlled process depending on the amount of oxidizer dissolved in the liquid fuel stream [114, e.g.]. Consistent with these experiments, many numerical studies have modeled transcritical jets using diffuse-interface methods. In this formulation, the working fluid is modeled as a single-phase dense gas (DG), and the thermo-transport properties of the working fluid are computed via a suitable equation of state (EOS) with high-pressure correction schemes for transport coefficients. However, the applicability of the DG approach in transcritical conditions is limited to very high pressures close to the cricondenbar. This is because neglecting the effect of transcritical phase separation at lower pressures can lead to non-physical or ill-defined states when the flow locally passes one of the mechanical, thermal, and diffusional stability limits [4].

To overcome these limitations, we use the LES-MT model as explained in Chapter 3. In the MT method, rapid phase splitting (flash) calculations as explained in Chapter 2, provide information on the composition and amount of saturated vapor and liquid phases, based on which the thermo-transport properties can be determined with suitable mixing rules in the coexisting regions. Considering VLE in real-fluid thermodynamics effectively eliminates the drawbacks of DG-based approaches for describing the two-phase region [72]. For example, as shown in Fig. 4.1, problems such as negative pressure values with non-physical compression during volume expansion as reported by Ma *et al.* [5], or non-physical anti-diffusion due to the negative derivative of fugacity of species relative to its mole fraction as reported by Jofre and Urzay [4], disappear via the phase-splitting calculations with the MT method.

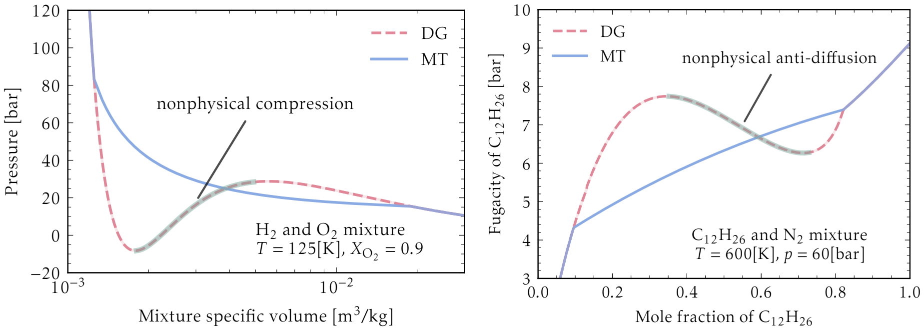

Figure 4.1.: Mixture properties computed by RKPR EOS [92] without VLE (DG) and with VLE (MT). Variation in pressure of a binary mixture of hydrogen and oxygen as a function of the specific volume (left). Composition functionality of the fugacity of n-dodecane in a binary mixture with nitrogen (right).

Due to the high pressure in the combustion chamber, the thickness of a transcritical flame is much smaller than the size of turbulent eddies in practice [44]. In other words, while turbulent eddies bring the fuel and oxidizer together on a macroscopic scale, molecular diffusion completes the mixing process on the mesoscopic scale of the flamelet thickness so that combustion can occur. Hence, a classical counterflow diffusion flame (CDF) setup under the relevant conditions can be effectively utilized for the detailed study of transcritical flames.

Accurate simulations of transcritical CDF require precise modeling of the transport phenomena, specifically molecular diffusion. In pressurized environments, the diffusion driving force deviates from that of dilute conditions on the basis of the mole fraction of species. These deviations are neglected in most studies because of the complexity of the calculations. Guven and Ribert [115] showed the importance of including the chemical potential as the actual driving force in supercritical flames; however, its implementation for transcritical multiphase effects remains an open question.

In addition to molecular diffusion, modeling the dynamic viscosity and thermal conductivity requires transcritical two-phase treatment as well. One might conduct a separate evaluation of those properties for the saturated vapor and liquid mixtures and combine both values with a suitable mixing rule; however, it is unclear how different mixing rules would affect the simulation results.

This chapter represents a comprehensive numerical framework developed based on the multiphase thermo-transport models for studying transcritical counterflow flames. The RKPR EOS of Cismondi and Mollerup [92] coupled with the rapid VLE solver of Fathi and Hickel [51] is used to efficiently model the non-ideal behavior of the working fluid. Dynamic viscosity and thermal conductivity are modeled with the Chung [116] method combined with a new mixing formula in the two-phase region. The diffusion mass flux is computed using the Dixon-Lewis formula with the thermodynamic correction factor to account for the species' actual diffusion driving force. The correction factor is computed consistently with the applied EOS and extended for two-phase conditions. To cover the whole range of real fluid effects on high-pressure combustion, a real finite-rate chemistry model based on the fugacity of species in the mixture is utilized.

To ensure completeness and maintain a coherent narrative, this chapter also provides a summary of selected material introduced in earlier sections, allowing the reader to follow the discussion without needing to refer back to previous chapters.

4.2. GOVERNING EQUATIONS

In a transcritical counterflow setup, the liquid or liquid-like supercritical fuel and the gaseous or gaseous-like supercritical oxidizer come from opposite directions and mix by diffusing across the stagnation plane. The combustible mixture ignites and generates a stable flame close to the stoichiometric region. The working pressure is higher than the critical pressure of the pure components in the fuel stream and lower than the cricondenbar pressure of the mixtures in-between. The problem configuration is shown schematically in Fig. 4.2.

The low-Mach variable-density form of reacting Navier-Stokes equations (NSE) can be utilized directly as the governing equations for the transcritical reacting counterflow problem. The governing equations can be reduced to a quasi-one-dimensional form along the axis of symmetry. Similar to Zambon and

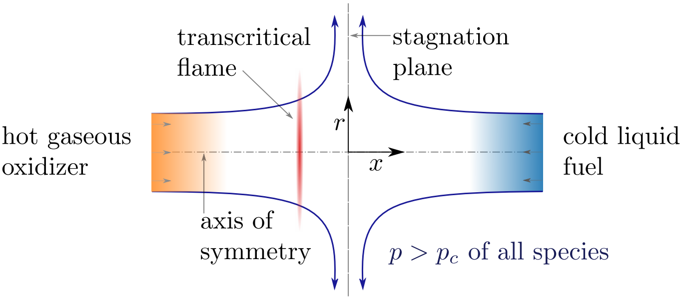

Figure 4.2.: Schematic of a transcritical counterflow diffusion flame with an operating pressure above the critical pressure of the liquid stream.

Chelliah [117], this dimensional reduction can be carried out by writing the Taylor series expansion of the variables in the radial direction about the symmetry axis:

$$\varphi(x,r,t) \approx \varphi_0(x,t) + r\frac{\partial \varphi}{\partial r}|_{r=0} + \frac{r^2}{2!}\frac{\partial^2 \varphi}{\partial r^2}|_{r=0} \;, \tag{4.1}$$

with $\varphi(x,r,t)$ denoting any variable of interest, x and r are the axial and radial coordinates, and t is time. The zero subscript indicates the value along the symmetry axis.

Along the axis of symmetry, the values of the radial velocity v and the first-order derivatives of all other variables are zero. Moreover, the second-order derivatives of all variables can be neglected except for the dynamic pressure, p_1, of which the radial dependency must be kept because of its role in the radial-momentum equation. The non-zero first derivative of the radial velocity is referred to as the stretch rate $\mathcal{K}(x,t) \equiv (\partial v/\partial r)\,|_{r=0}$, and the non-zero second derivative of the dynamic pressure is called the pressure curvature $\Lambda(t) \equiv \left(\partial^2 p_1/\partial r^2\right)|_{r=0}$. Note that by applying a radial derivative to the axial momentum equation, it can be shown that Λ is not a function of the axial direction and can be a constant or a function of time only.

The resulting equations along the symmetry axis at $r=0$ are:

$$\frac{\partial \rho}{\partial t} + \frac{\partial \rho u}{\partial x} = -2\rho\mathcal{K} \;, \tag{4.2}$$

$$\rho\frac{\partial Y_k}{\partial t} + \rho u\frac{\partial Y_k}{\partial x} = -\frac{\partial \mathcal{J}_k}{\partial x} + \dot{\omega}_k \;, \tag{4.3}$$

$$\rho\frac{\partial \mathcal{K}}{\partial t} + \rho u\frac{\partial \mathcal{K}}{\partial x} = \frac{\partial}{\partial x}\left(\mu\frac{\partial \mathcal{K}}{\partial x}\right) - \rho\mathcal{K}^2 - \Lambda \;, \tag{4.4}$$

$$\rho c_p\frac{\partial T}{\partial t} + \rho c_p u\frac{\partial T}{\partial x} = \frac{\partial}{\partial x}\left(\lambda\frac{\partial T}{\partial x}\right) - \sum_{k=1}^{N}\mathcal{J}_k\frac{\partial h_k}{\partial x} - \sum_{k=1}^{N}h_k\dot{\omega}_k \;, \tag{4.5}$$

where u is the axial velocity, ρ is the density, T is the temperature, and c_p, λ and

μ are heat capacity, thermal conductivity, and dynamic viscosity of the working fluid. Y_k, h_k, $\mathcal{J}_k$, and $\dot{\omega}_k$ are the mass fraction, partial enthalpy, diffusion flux, and net production rate of the species $k = 1, 2, \ldots, N$ with N being the total number of species.

Since the pressure curvature is not a function of the axial location, it can be computed employing the density and the strain rate at one of the boundaries via

$$\Lambda = -\rho_\infty a_\infty^2 \ , \tag{4.6}$$

where the subscript ∞ denotes the reference boundary and a is the applied strain rate at the boundary.

The axial momentum equation is implicitly included in this low-Mach model because the effect of the axial gradient of the dynamic pressure on the energy change was neglected. The axial velocity can be computed via the continuity equation after the density variation has been determined from the primary variables like temperature and species mass fractions. This can be done by replacing the density with the specific volume $\rho = 1/\vartheta$, and through thermodynamic relations under the assumption of constant thermodynamic pressure:

$$\frac{\partial \rho}{\partial t} = -\rho^2 \left(\frac{\alpha_p}{\rho} \frac{\partial T}{\partial t} + \sum_{k=1}^{N} \vartheta_k \frac{\partial Y_k}{\partial t} \right) , \tag{4.7}$$

where α_p is the volumetric thermal expansion coefficient at constant pressure and composition, which is defined as $\alpha_p \equiv (1/\vartheta)\,(\partial\vartheta/\partial T)\,|_{P,Y_k}$, and ϑ_k is the partial volume of species k, which is defined mathematically as $\vartheta_k \equiv (\partial\vartheta/\partial Y_k)\,|_{T,P,Y_{j\neq k}}$. Substitution of the temporal variation of density in the continuity equation (4.2), yields an equation for the variation of the mass flux ρu throughout the computational domain reads as:

$$\begin{aligned} \frac{\partial \rho u}{\partial x} + \left(\alpha_p \frac{\partial T}{\partial x} + \rho \sum_{k=1}^{N} \vartheta_k \frac{\partial Y_k}{\partial x} \right) \rho u = \frac{\alpha_p}{c_p} \left[\frac{\partial}{\partial x} \left(\lambda \frac{\partial T}{\partial x} \right) - \sum_{k=1}^{N} \mathcal{J}_k \frac{\partial h_k}{\partial x} - \sum_{k=1}^{N} h_k \dot{\omega}_k \right] \\ + \rho \sum_{k=1}^{N} \vartheta_k \left(-\frac{\partial \mathcal{J}_k}{\partial x} + \dot{\omega}_k \right) - 2\rho\mathcal{K}. \end{aligned} \tag{4.8}$$

That is, the axial mass flux can be computed at any time from the primary variables.

In summary, the governing equations for transcritical counterflow flames in the context of the multiphase single-fluid mixture formalism are Eqs. (4.2)-(4.5) with the constraint Eq. (4.8). The required thermo-transport properties are presented in the next section.

Flamelet models or tabulated chemistry methods typically use the mixture fraction $\mathcal{Z}$ and the progress variable $\mathcal{C}$ to universally represent the flame structure (independent of spatial coordinates). They can be defined algebraically as functions of the species and/or energy variables. In the present study, we do not address the construction of lookup tables; however, the structure of the flame is discussed as a function of the mixture fraction $\mathcal{Z}$. For this purpose, the following transport equation is added to the governing equations:

$$\rho\frac{\partial\mathcal{Z}}{\partial t}+\rho u\frac{\partial\mathcal{Z}}{\partial x}=\frac{\partial}{\partial x}\left(\frac{1}{\mathrm{Le}_{\mathcal{Z}}}\frac{\lambda}{c_p}\frac{\partial\mathcal{Z}}{\partial x}\right)\ , \tag{4.9}$$

The Lewis number $Le_{\mathcal{Z}}$ for this (and only this) auxiliary variable is set to unity. In the presence of preferential diffusion, the mixture fraction obtained from this equation is not identical to the mixture fraction obtained from the species transport equations and generalization is needed, but it is sufficient to represent the flame structure, which is the purpose here. See Ref. [118] for a discussion of the differential equations for $\mathcal{Z}$ and $\mathcal{C}$ in the case of preferential diffusion.

4.3. REAL-FLUID TRANSCRITICAL PROPERTIES

At high-pressure conditions, the fluid properties deviate strongly from ideal-gas or ideal-liquid models. In addition, the fluid mixture can locally enter into a subcritical two-phase regime, in which interfaces between liquid-like and gas-like phases may form, and the mixture properties do not directly follow from the EOS. In this section, we present a suitable volumetric and caloric EOS coupled with a VLE model that properly describes these effects.

4.3.1. THERMODYNAMIC PROPERTIES

The general cubic EOS is used as the volumetric EOS to express the relations between the molar-specific volume, pressure, and temperature of the real-fluid mixture:

$$p=\mathcal{R}T/(\bar{\vartheta}-b)-a/\left[\left(\bar{\vartheta}+\delta_1 b\right)\left(\bar{\vartheta}+\delta_2 b\right)\right]\ . \tag{4.10}$$

The symbol $\mathcal{R}$ denotes the universal gas constant, $\bar{\vartheta}=W/\rho$ is the molar specific volume with W being the mean molar mass of the mixture, a and b are the attractive energy and co-volume parameters, and δ_1 and δ_2 are two extra calibration parameters. The parameters are determined via a suitable mixing rule on the basis of the molar composition and individual species properties. For instance, energy and co-volume parameters are computed using the van der Waals mixing rule as follows:

$$\begin{aligned} a &= \textstyle\sum_{i=1}^{N}\sum_{j=1}^{N} X_i X_j\left(1-k_{ij}\right)\sqrt{\hat{a}_i\hat{a}_j}\ ,\\ b &= \textstyle\sum_{i=1}^{N} X_i\hat{b}_i\ , \end{aligned} \tag{4.11}$$

where k_{ij} is the binary interaction coefficient between species i and j. $\hat{a}_i$ and $\hat{b}_i$ refer to the values of pure species of these parameters, which can be obtained using the acentric factor and the critical temperature and pressure. Cubic EOS is generally known as an appropriate compromise between complexity and accuracy; the modeling framework described in the following is, however, not limited to this choice and is also applicable to other EOS.

The general cubic EOS can be cast into a specific cubic EOS by choosing a functional form for the model parameters in Eqs. (4.10) and (4.11) [51, e.g.]. SRK [86] and PR [87] are traditionally the most popular cubic EOS. However, as suggested by [35], the RKPR EOS of Cismondi and Mollerup [92] should be selected for transcritical conditions. RKPR yields better predictions close to the critical point by including a calibrated critical compressibility factor in its formulations. Figure 4.3 compares the performance of these cubic EOSs against the highly accurate EOS of Lemmon and Huber [97] for pure n-dodecane, and against experimental data of Regueira *et al.* [119] for a ternary mixture of methane, n-butane, and n-dodecane. We clearly see that the RKPR EOS predicts the density more accurately than SRK and PR at high pressures, and also that errors of the ideal-gas EOS are unacceptably large.

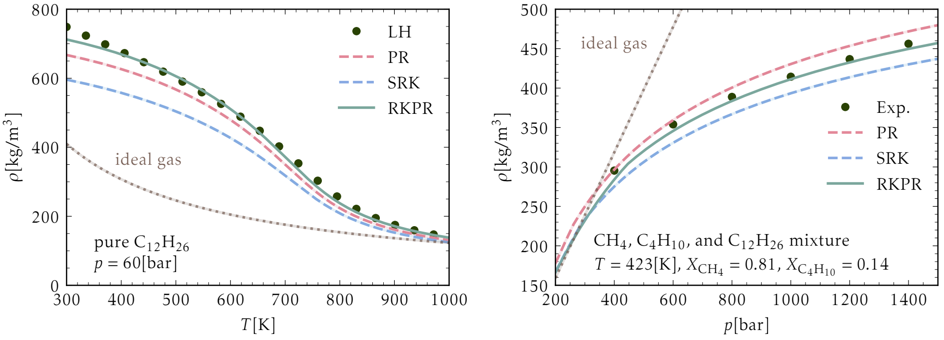

Figure 4.3.: Density prediction of PR, SRK, and RKPR EOSs for pure n-dodecane against the reference work of Lemmon and Huber [97] (left), and a ternary mixture of methane, n-butane, and n-dodecane against experimental measurements of Regueira *et al.* [119] (right).

The caloric EOS for real fluids can be derived using the departure function formalism. For the general form of cubic EOS, the molar-specific internal energy of the fluid mixture is expressed as:

$$\bar{e} = \sum_{k=1}^{N} X_k \bar{h}_k^\circ - \mathcal{R}T + (a - T\partial a/\partial T) / \left[(\delta_2 - \delta_1)\, b\right] \ln\left[\left(\bar{\vartheta} + \delta_1 b\right) / \left(\bar{\vartheta} + \delta_2 b\right)\right] \ . \quad (4.12)$$

The molar specific enthalpy $\bar{h}_k^\circ$ of the pure species k at the standard pressure (including the enthalpy of formation) is calculated via so-called NASA polynomials [100]:

$$\begin{aligned} \bar{h}_k^\circ / \mathcal{R} = &-a_{k,1} T^{-1} + a_{k,2} \ln T + a_{k,3} T + a_{k,4} T^2/2 \dots \\ &+ a_{k,5} T^3/3 + a_{k,6} T^4/4 + a_{i,7} T^5/5 + a_{k,8} \ , \end{aligned} \quad (4.13)$$

where $a_{k,1..8}$ are polynomial coefficients of the species k, and their values are tabulated in the reference paper [100]. In the following, the formulations required for the computation of the thermodynamic properties using the aforementioned kinetic and caloric state equations are elaborated.

SINGLE-PHASE REAL-FLUID THERMODYNAMICS

This subsection summarizes the required formulations for evaluating the thermodynamic properties of a stable single-phase multi-component fluid mixture. It includes the equations necessary to calculate mole fractions, density, thermal expansion coefficient, constant-pressure heat capacity, and partial volume and enthalpy of the species for given temperature, pressure, and species mass fractions.

Mole fractions are computed from known mass fractions via

$$X_k = W Y_k / W_k \ , \tag{4.14}$$

where $W = 1/\sum_{k=1}^{N} Y_k/W_k$ is the mean molar mass of the mixture and W_k is the molar mass of the species k. The molar-specific volume is determined by rewriting the cubic EOS as follows:

$$\bar{\vartheta}^3 + \varrho_2 \bar{\vartheta}^2 + \varrho_1 \bar{\vartheta} + \varrho_0 = 0 \tag{4.15}$$

with

$$\begin{aligned} \varrho_0 &= -ab/p - (b + \mathcal{R}T/p)\, \delta_1 \delta_2 b^2 \ , \\ \varrho_1 &= \delta_1 \delta_2 b^2 + a/p - (\delta_1 + \delta_2)\, b\, (b + \mathcal{R}T/p) \ , \\ \varrho_2 &= (\delta_1 + \delta_2 - 1)\, b - \mathcal{R}T/p \ . \end{aligned} \tag{4.16}$$

Cardano's algorithm is typically used to determine the roots of Eq. (4.15). In case of more than one real root, the root associated with the lowest Gibbs free energy should be selected [63]. The density is eventually calculated using $\rho = W/\bar{\vartheta}$.

The partial volume of species $\vartheta_k = \bar{\vartheta}_k / W_k$ is computed from the partial molar volume $\bar{\vartheta}_k \equiv (\partial \bar{\vartheta} / \partial X_k)|_{T,P,X_{j \neq k}}$. The partial derivative is evaluated by assuming that δ_1 and δ_2 are composition independent. For the general form of cubic EOS one obtains:

$$\bar{\vartheta}_k = -\{\mathcal{R}T/[(\bar{\vartheta} - b) + (\bar{\vartheta} - b)^2/\hat{b}_k] - (\partial a/\partial X_k)\,/[(\bar{\vartheta} + \delta_1 b)(\bar{\vartheta} + \delta_2 b)] \ldots \tag{4.17}$$

$$+\, a\hat{b}_k[2b\delta_1\delta_2 + \bar{\vartheta}(\delta_1 + \delta_2)]/[(\bar{\vartheta} + \delta_1 b)(\bar{\vartheta} + \delta_2 b)]^2\}/(\partial p/\partial \bar{\vartheta})|_{T,X_k} \ , \tag{4.18}$$

in which $(\partial p/\partial \bar{\vartheta})|_{T,X_k}$ is

$$(\partial p/\partial \bar{\vartheta})|_{T,X_k} = -\mathcal{R}T/(\bar{\vartheta} - b)^2 + a\left[2\bar{\vartheta} + (\delta_1 + \delta_2)\, b\right]/[(\bar{\vartheta} + \delta_1 b)(\bar{\vartheta} + \delta_2 b)]^2 \ . \tag{4.19}$$

The volumetric thermal expansion coefficient can be computed using the thermodynamic relation

$$\alpha_p = -\left(1/\bar{\vartheta}\right)\left(\partial p/\partial T\right)|_{\bar{\vartheta},X_k} \left(\partial p/\partial \bar{\vartheta}\right)^{-1}|_{T,X_k} \tag{4.20}$$

with

$$\left(\partial p/\partial T\right)|_{\bar{\vartheta},X_k} = \mathcal{R}/(\bar{\vartheta} - b) - \left(\partial a/\partial T\right)/\left[(\bar{\vartheta} + \delta_1)(\bar{\vartheta} + \delta_2)\right] \ . \tag{4.21}$$

The heat capacity of the mixture can be computed via $c_p = \bar{c}_p/W$ with the following thermodynamic relation for its molar specific value,

$$\bar{c}_p = \bar{c}_v - T(\partial p/\partial T)^2|_{\bar{\vartheta},X_k}(\partial p/\partial\bar{\vartheta})^{-1}|_{T,X_k} \ , \tag{4.22}$$

where $\bar{c}_v \equiv (\partial\bar{e}/\partial T)\,|_{\bar{\vartheta},X_k}$ is the molar specific heat capacity of the mixture at constant volume, and can be obtained from the caloric EOS as:

$$\bar{c}_v = \sum_{k=1}^{N} X_k\bar{c}^{\circ}_{p,k} - \mathcal{R} - (T\partial^2 a/\partial T^2)/\left[(\delta_2-\delta_1)\,b\right]\ln\left[\left(\bar{\vartheta}+\delta_1 b\right)/\left(\bar{\vartheta}+\delta_2 b\right)\right] \ . \tag{4.23}$$

with $\bar{c}^{\circ}_{p,k} \equiv \mathrm{d}\bar{h}^{\circ}_k(T)/\mathrm{d}T$ being the molar specific heat capacity of the pure component k at standard pressure, which is the temperature derivative of Eq. (4.13).

The partial enthalpy of species k is defined as

$$h_k = (\bar{e}_k + p\bar{\vartheta}_k)/W_k \ , \tag{4.24}$$

in which the molar partial internal energy of the species $\bar{e}_k \equiv (\partial\bar{e}/\partial X_k)\,|_{T,P,X_{j\neq k}}$ is

$$\begin{aligned}\bar{e}_k = \bar{h}^{\circ}_k - \mathcal{R}T &+ (\bar{\vartheta}_k - \bar{\vartheta}\hat{b}_k/b)(a - T\,(\partial a/\partial T))/[(\bar{\vartheta}+\delta_1 b)(\bar{\vartheta}+\delta_2 b)]\ldots\\ &+ \{b[(\partial a/\partial X_k) - T\left(\partial^2 a/\partial T\partial X_k\right)] - \hat{b}_k[a - T\,(\partial a/\partial T)]\}\ldots\\ &\times\ \ln\left[(\bar{\vartheta}+\delta_1 b)/(\bar{\vartheta}+\delta_2 b)\right]/[(\delta_2-\delta_1)\,b^2]\ .\end{aligned} \tag{4.25}$$

for the general cubic EOS.

Multi-Phase Real-Fluid Thermodynamics

When the boundary of the two-phase region is crossed during the mixing at transcritical operating conditions, the fluid becomes thermodynamically unstable in a single phase. That is, its Gibbs free energy is not a minimum for the given temperature, pressure, and composition, and thus it splits into vapor and liquid phases with different compositions to lower the Gibbs free energy.

Phase-splitting (flash) calculations must be performed to determine the equilibrium amount and compositions of the saturated vapor and liquid mixtures. In this study, we use the rapid isothermal-isobaric flash (PT-flash) calculation method of Fathi and Hickel [51], which is formulated for general cubic EOS. For a comprehensive review and practical implementation guidelines, the readers are referred to Ref. [51].

Once the vapor fraction and the molar composition of the liquid and vapor phases are determined, the aforementioned single-phase thermodynamic correlations are used to separately evaluate all properties of interest for each phase. The combined total properties of the two-phase mixture are obtained as follows: The total value of a mole-specific quantity $\bar{\varphi}$ in the multiphase region is

$$\bar{\varphi} = (1-\theta)\bar{\varphi}^L + \theta\bar{\varphi}^V \ , \tag{4.26}$$

with θ being the vapor mole fraction, and superscript L and V refer to the value in the liquid and vapor phases. The mixture value of a molar partial quantity $\bar{\varphi}_k$ is

$$\bar{\varphi}_k = (1-\theta)\bar{\varphi}_k^L X_k^L / X_k + \theta \bar{\varphi}_k^V X_k^V / X_k \ , \tag{4.27}$$

where X_k^L and X_k^V denote the mole fraction of species k in the liquid and vapor phase and $X_k = (1-\theta)X_k^L + \theta X_k^V$.

4.3.2. TRANSPORT PROPERTIES

VISCOSITY AND CONDUCTIVITY

We first review Chung's method for single-phase multi-component mixtures and afterwards discuss how the overall transport properties can be effectively determined when the mixture is thermodynamically unstable. Following Chung *et al.* [116], and neglecting the effect of molecular polarity, the dynamic viscosity with the unit [Pa s] is modelled as

$$\mu = 36.344 \times 10^{-7} \mu_* (W T_c)^{1/2} \bar{\vartheta}_c^{-2/3} \ , \tag{4.28}$$

in which W [g mol^{-1}], T_c [K], and $\bar{\vartheta}_c$ [cm^3/mol] are the molar mass, critical temperature, and critical molar specific volume. The factor μ_* is

$$\begin{aligned} \mu_* &= T_*^{1/2} \Omega_v^{-1} \mathrm{F}_c (\mathrm{G}_2^{-1} + \mathrm{E}_6 Y_*) \ldots \\ &+ \mathrm{E}_7 Y_*^2 \mathrm{G}_2 \exp(\mathrm{E}_8 + \mathrm{E}_9 T_*^{-1} + \mathrm{E}_{10} T_*^{-2}) \ , \end{aligned} \tag{4.29}$$

with $T_* = 1.2593 T/T_c$ and $Y_* = \bar{\vartheta}_c/(6\bar{\vartheta})$ are the effective reduced temperature and density, respectively. The correction factor $\mathrm{F}_c = 1 - 0.276\omega$ is computed using ω as the representative acentric factor, and the other parameters are

$$\begin{aligned} \Omega_v &= 1.161 T_*^{-0.149} + 0.525 \mathrm{e}^{-0.773 T_*} + 2.162 \mathrm{e}^{-2.438 T_*} \ , \\ \mathrm{G}_2 &= \left[\mathrm{E}_1 / Y_* (1 - \mathrm{e}^{-\mathrm{E}_4 Y_*}) + \mathrm{E}_2 \mathrm{G}_1 \mathrm{e}^{\mathrm{E}_5 Y_*} + \mathrm{E}_3 \mathrm{G}_1\right] / \left(\mathrm{E}_1 \mathrm{E}_4 + \mathrm{E}_2 + \mathrm{E}_3\right) \ , \\ \mathrm{G}_1 &= (1 - 0.5 Y_*)/(1 - Y_*)^3 \ . \end{aligned}$$

The coefficients $\mathrm{E_i} = \mathrm{a_i} + \mathrm{b_i}\omega$ depends on the calibrated parameters $\mathrm{a_i}$ and $\mathrm{b_i}$ available in the original paper [116].

The thermal conductivity with the unit [W m^{-1} K^{-1}] is approximated as

$$\lambda = 31.2 \times 10^3 \mathrm{G}_4 (\mathrm{G}_3^{-1} + \mathrm{B}_6 Y_*) \mu^0 / W + \mathrm{G}_5 \mathrm{B}_7 Y_*^2 (T/T_c)^{1/2} \mathrm{G}_3 \ , \tag{4.30}$$

where μ^0 with unit [Pa s] is the low-pressure (or ideal-gas) viscosity of the mixture. The latter is estimated as

$$\mu^0 = 40.785 \times 10^{-7} F_c (W T)^{1/2} / (\bar{\vartheta}_c^{2/3} \Omega_v) \ , \tag{4.31}$$

and the remaining parameters are

$$\begin{aligned}
\mathrm{G}_5 &= 0.1134(T_c/W)^{1/2}\bar{\vartheta}_c^{-2/3} \ , \\
\mathrm{G}_4 &= 1+\alpha(0.215+0.283\alpha-1.061\beta+0.267\gamma)/(0.637+\beta\gamma+1.061\alpha\beta) \ , \\
\mathrm{G}_3 &= \left[(\mathrm{B}_1/Y_*)\left(1-e^{-\mathrm{B}_4 Y_*}\right)+\mathrm{B}_2\mathrm{G}_1 e^{\mathrm{B}_5 Y_*}+\mathrm{B}_3\mathrm{G}_1\right]/\left(\mathrm{B}_1\mathrm{B}_4+\mathrm{B}_2+\mathrm{B}_3\right) \ ,
\end{aligned}$$

with $\alpha = \bar{c}_p^0/\mathcal{R} - 2.5$, $\beta = 0.786 - 0.711\omega + 1.317\omega^2$, $\gamma = 2 + 10.5(T/T_c)^2$, and $\mathrm{B}_\mathrm{i} = \mathrm{c}_\mathrm{i} + \mathrm{d}_\mathrm{i}\omega$. The calibrated values of the parameters c_i and d_i are available in the original paper [116]. All fluid-specific inputs required by this model can be obtained from readily available data of individual stable components, such as the molar mass, critical temperature, critical molar specific volume, and acentric factor.

To estimate the overall transport properties of unstable mixtures, we first determine the composition of the saturated vapor and liquid phases and compute the transport properties of those (stable) mixtures via the aforementioned equations separately. Afterward, we combine these values to find the overall transport properties of the fluid. To this end, we recommend the use of the effective medium theory (EMT) model [120], which was initially proposed for the evaluation of conductivity in heterogeneous materials [121]. This model assumes a random distribution of all participants in a heterogeneous environment, which is assumed to be similar to the distribution of vapor and liquid phases in a transcritical environment, where very small local variations can cause phase separation and recombination.

With the EMT model, the overall dynamic viscosity and thermal conductivity of the unstable multi-component mixture are calculated from their values in the saturated liquid and vapor phase as

$$(1-\Theta)\frac{\mu^L-\mu}{\mu^L+2\mu}+\Theta\frac{\mu^V-\mu}{\mu^V+2\mu}=0 \ , \tag{4.32}$$

$$(1-\Theta)\frac{\lambda^L-\lambda}{\lambda^L+2\lambda}+\Theta\frac{\lambda^V-\lambda}{\lambda^V+2\lambda}=0 \ , \tag{4.33}$$

where Θ is the fraction of the total volume occupied by the vapor phase and can be obtained from the vapor mole fraction θ available from flash calculations as

$$\Theta = \theta\bar{\vartheta}^V/[\theta\bar{\vartheta}^V + (1-\theta)\bar{\vartheta}^L] \ . \tag{4.34}$$

Figure 4.4 compares predictions of two approaches for the evaluations of thermal conductivity and dynamic viscosity of the mixtures in the context of MT. We see that a naive application of Chung's method using total fluid composition leads to spurious oscillations of the conductivity and a too-low dynamic viscosity in the two-phase region. Considering phase separation with an appropriate mixing rule, like the proposed EMT model, provides the expected monotonous variation of the transport properties in the two-phase region. Note that there exists no exact reference data, as the effective mixture viscosity and conductivity depend on the exact geometry of the phase interfaces, which is generally unavailable.

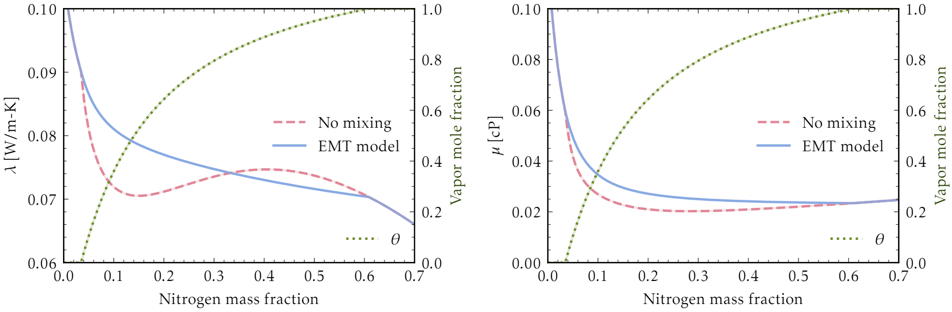

Figure 4.4.: Thermal conductivity (left) and dynamic viscosity (right) of n-dodecane and nitrogen mixtures at 60 bar and 600 K computed with the EMT model using RKPR EOS coupled with VLE and Chung correlations, compared to predictions neglecting phase separation.

DIFFUSION MASS FLUX

For real-fluid multi-component mixtures, the diffusive species mass flux due to the composition inhomogeneities can be computed using the Dixon-Lewis formulation in the generalized form of Fick's law

$$\mathcal{J}_k = -\rho(W_k/W)\mathcal{D}_{kN} \sum_{j=1}^{N-1} c_{kj} d_j \ , \tag{4.35}$$

in which $\mathcal{D}_{kj}$ is the Stefan-Maxwell diffusion coefficient of the species pair k, j and c_{kj} is the dimensionless multi-component diffusion factor matrix

$$c_{kj} = (\mathcal{I} + \mathcal{A})^{-1}_{kj} \ . \tag{4.36}$$

The matrix $\mathcal{A}$ is constructed from the mole fractions and the Stefan-Maxwell binary diffusion coefficients

$$\mathcal{A}_{kj} = \sum_{l=1}^{N-1} X_l \left(\frac{\mathcal{D}_{lN}}{\mathcal{D}_{lk}} - 1 \right) \delta_{lj} + X_k \left(\frac{W_j}{W_N} - \frac{\mathcal{D}_{kN}}{\mathcal{D}_{kj}} \right) \frac{\mathcal{D}_{jN}}{\mathcal{D}_{kN}} \ , \tag{4.37}$$

with δ_{lk} being the Kronecker delta, and $\mathcal{I}$ is the identity matrix. The diffusion driving force vector d_j is usually approximated by the gradient of the species mole fractions. For the present study, we include the so-called thermodynamic factor matrix Γ to represent high-pressure effects [122] as

$$d_j = \sum_{k=1}^{N-1} \Gamma_{jk} \left(\partial X_k / \partial x \right) \ , \tag{4.38}$$

where

$$\Gamma_{jk} = X_j \left(\partial \ln f_j / \partial X_k \right) |_{P,T,X_{i \neq k}} \ . \tag{4.39}$$

However, instead of using the above definition of Γ directly, we express the fugacity f_j of species j as

$$f_j = X_j \mathcal{R} T / \psi_j \ , \tag{4.40}$$

based on the specific volume function ψ_j of Fathi and Hickel [51], which is for the general cubic EOS given by

$$\begin{aligned} \ln \psi_j = {} & \ln\left(\bar{\vartheta} - b\right) - \hat{b}_j / \left(\bar{\vartheta} - b\right) + \bar{\vartheta} a \hat{b}_j / \left[(b\mathcal{R}T)(\bar{\vartheta} + \delta_1 b)(\bar{\vartheta} + \delta_2 b)\right] \dots \\ & - \left[a\hat{b}_j - b\left(\partial a / \partial X_j\right)\right] / \left[(\delta_1 - \delta_2) b^2 \mathcal{R} T\right] \ln\left[\left(\bar{\vartheta} + \delta_1 b\right) / \left(\bar{\vartheta} + \delta_2 b\right)\right] \ . \end{aligned} \tag{4.41}$$

Substituting Eq. (4.40) into Eq. (4.39), the thermodynamic correction matrix can be written as the sum of an ideal and non-ideal contribution:

$$\Gamma_{jk} = \delta_{jk} - X_j \left(\partial \ln \psi_j / \partial X_k\right)|_{P,T,X_{j \neq k}} \ . \tag{4.42}$$

The second term represents the deviation from the ideal driving force for real-fluid mixtures. The fact that it is derived analytically and only the second term is zero when the mole fraction of the species j is negligible shows that this formulation is free from the singularity problem of alternative formulations that was addressed by Giovangigli, Matuszewski, and Gaillard [123].

In order to determine the Stefan-Maxwell binary diffusion coefficient of real fluids, we generally recommend the correction method of Leahy-Dios and Firoozabadi [124]. When the system pressure is under 100 bar, computations can be significantly accelerated by simply correcting the ideal binary diffusion coefficient with the mixture's compressibility factor, that is,

$$\mathcal{D}_{ij} = z \mathcal{D}_{ij}^0 \ , \tag{4.43}$$

where z is the compressibility factor of the mixture, and $\mathcal{D}_{ij}^0$ is the molecular diffusion coefficients of component i infinitely diluted in component j at negligible pressure. We use the Chapman-Enskog theory [see, [95], e.g.] for the evaluation of $\mathcal{D}_{ij}^0$.

The computation of the dimensionless multi-component diffusion factors from the inversion of the matrix given by Eq. (4.36) is very expensive. One common remedy is known as the mixture-averaged method. Using this approximation, the molar diffusion velocity of species i in the mixture is calculated by assuming the equality of the molar diffusion velocity of all other species. Although the results of the mixture-averaged model are typically quite close to the full Dixon-Lewis approach, specifically when there is a large amount of an inert gas like nitrogen in the environment, considerable differences may be observed in cases that include a very diffusive species like hydrogen or light radicals.

Recently, Naud and Arias-Zugasti [125] introduced a novel numerical framework with the main idea of using no approximation for the $(1 + M)$ most abundant species and applying truncated power series expansion models for the other species with negligible concentrations. They could reproduce the diffusion mass flux within the accuracy of the Dixon-Lewis approach at a computational cost always lower than the mixture-averaged method. The model of Naud and Arias-Zugasti can be rewritten as follows:

$$\mathcal{J}_i = \begin{cases} -\rho W_i/W\mathcal{D}_{iN}\sum_{j=1}^{N-1} c_{ij}d_j & , \ i \leq M \ , \\ -\rho W_i/W\mathcal{D}_{iN}c_{ii}d_i & , \ M < i < N \ , \\ -\sum_{j=1}^{N-1}\mathcal{J}_j & , \ i = N \ , \end{cases} \tag{4.44}$$

where c_{ij} is computed with the method explained in the original work [125].

In the two-phase region, we approximate the effective non-ideal diffusion driving force using Eq. (4.26) with $\bar{\varphi}$ being the amount of deviation from the ideal driving force for the liquid and vapor phases. Figure 4.5 highlights one important effect of the MT formulation on the non-ideal driving force at transcritical conditions on the example of the diffusion mass fluxes of n-dodecane (left) and oxygen (right), which were computed at a constant temperature of 500 K and constant pressure 60 bar using a predefined profile for the mixture fraction of pure n-dodecane fuel and an oxidizer consisting of oxygen, nitrogen, carbon dioxide, and water. The MT framework predicts the expected mixing of fuel and oxidizer, whereas the application of a single-phase DG approach combined with the accurate model for the non-ideal diffusion driving force leads to an anti-diffusion in the diffusional spinodal of the two-phase region. These results demonstrate the importance of consistent models; if meso-scale phase separation is ignored (single-phase DG), then an accurate fugacity-based diffusion model will demix an unstable mixture and thereby establish phase separation on the macro scale. This spurious demixing intercepts the fueling of the flame, and might result in flame extinction or a wrong ignition delay time in actual simulations.

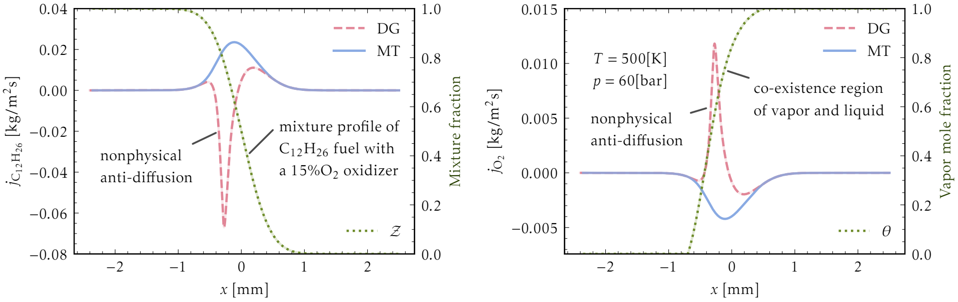

Figure 4.5.: Diffusion mass flux for n-dodecane (left) and oxygen (right) computed at 60 bar and 500 K for a predefined mixture fraction distribution using the non-ideal driving force formulations within a single-phase (DG) and multiphase (MT) model.

4.3.3. CHEMICAL PROPERTIES

According to the mass action law, the species' net mass production rates are

$$\dot{\omega}_i = M_i \sum_{r=1}^{N_r}(\nu_{ir}^{\mathcal{P}} - \nu_{ir}^{\mathcal{R}})\mathcal{Q}_r \ , \tag{4.45}$$

where N_r is the total number of reactions, and $\nu_{ir}^{\mathcal{P}}$ and $\nu_{ir}^{\mathcal{R}}$ are the stoichiometric coefficients of species i on the right and left side of the reaction r. The reaction rate $\mathcal{Q}_r$ is a function of the concentrations of the reactants through

$$\mathcal{Q}_r = k_{f,r} \prod\nolimits_{j=1}^{N} \mathcal{C}_j^{\nu_{jr}^{\mathcal{R}}} - k_{b,r} \prod\nolimits_{j=1}^{N} \mathcal{C}_j^{\nu_{jr}^{\mathcal{P}}} . \tag{4.46}$$

The forward and backward rate coefficients k_f and k_b are commonly computed by the Arrhenius law.

Following the real-fluid finite-rate chemistry model of Fathi, Hickel, and Roekaerts [75], the required concentrations of the species in Eq. (4.45) can be calculated in a thermodynamically consistent way from the fugacity of the species in the mixture or from the specific volume function defined in Eq. (4.40) as follows:

$$\mathcal{C}_j \simeq f_j/(\mathcal{R}T) = X_j/\psi_j \ . \tag{4.47}$$

When the reaction rates are expressed in terms of the fugacity or the specific volume function, the backward rates can be calculated from the equilibrium constant

$$K_{\mathrm{c},r} = [p^\circ/(\mathcal{R}T)]^{\nu_r} \exp[\Delta S_r^\circ/\mathcal{R} - \Delta H_r^\circ/(\mathcal{R}T)] \ , \tag{4.48}$$

where $\nu_r = \sum_{i=1}^{N} (\nu_{ir}^{\mathcal{P}} - \nu_{ir}^{\mathcal{R}})$ is the net change in the number of species in the reaction, and ΔH_r° and ΔS_r° are the net change in reaction enthalpy and entropy at the standard pressure $p^\circ = 1\,\mathrm{atm}$.

The present fugacity-based approach for real-fluid chemistry is conceptually aligned with the earlier non-ideal model of Giovangigli and co-workers [126, 127] which is used recently by Monnier, Ribert, and Duhem-Duvilla [128] for the high-fidelity simulations of the oxy-combustion of methane in the context of liquid rocket engines. While the Giovangigli's formulation leverages the activity to account for the non-idealities effects for the evaluation of the concentrations, the current model utilizes the equivalent concept via the specific volume function.

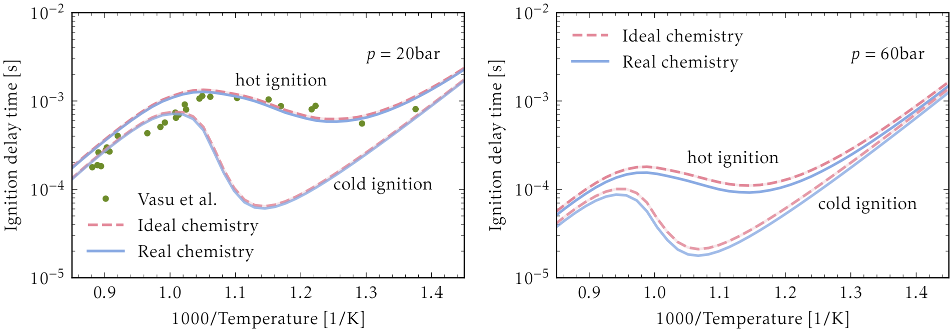

Figure 4.6.: Real gas effects on first and second ignition delay time as a function of inverse temperature for stoichiometric mixtures of n-dodecane and air at two different pressures. For the pressure of 20 bar, symbols denote experimental data of Vasu *et al.* [129].

Figure 4.6 quantifies real-gas effects on the prediction of the ignition delay time for stoichiometric mixtures of pure n-dodecane and air at two different pressures of 20 and 60 bar. Here we use a reduced chemical mechanism calibrated following the methodology presented by Lapointe, Zhang, and McNenly [130]. The mechanism consists of 65 species and 363 reactions, and yields predictions in very good agreement with the experimental data of Vasu *et al.* [129], as shown in the figure. The first (cold) ignition time is defined as the point in time when the temperature rapidly ascends a few degrees during the first stage of combustion, and the second (hot) ignition time is defined as the elapsed time until the initial temperature of the mixture increased by 400 K. We observe that real-gas effects are noticeable but small at 20 bar and become significant at the higher pressure of 60 bar. Note that the ignition delay time is plotted on a logarithmic scale.

4.4. NUMERICAL IMPLEMENTATION

4.4.1. SPATIAL DISCRETIZATION

The governing equations are discretized on a one-dimensional grid with a non-uniform distribution. All variables are stored at grid points $\{x_i\}$ and the method of lines is followed to separate the space and time derivatives.

Viscous terms are discretized using the central difference scheme:

$$\frac{\partial}{\partial x}\left(\eta\frac{\partial\varphi}{\partial x}\right)\bigg|_i = 2\frac{\eta_{i+1/2}\ell_{i-1}(\varphi_{i+1}-\varphi_i)-\eta_{i-1/2}\ell_i(\varphi_i-\varphi_{i-1})}{\ell_i\ell_{i-1}(\ell_i+\ell_{i-1})}\ , \tag{4.49}$$

here written for a generic variable φ and the corresponding generic viscosity η ; where $\eta_{i\pm1/2}$ is the interpolated viscosity coefficient at $x_{i\pm1/2}=(x_i+x_{i\pm1})/2$, and $\ell_i = x_{i+1}-x_i$ is the grid spacing. This formula is employed for the viscous terms in the stretch rate, temperature, mixture fraction, and progress variable equations. For the species equations, the first-order derivative of the diffusion flux is discretized in a conservative way as follows:

$$\frac{\partial \mathcal{J}_k}{\partial x}\bigg|_i = 2\frac{\mathcal{J}_k|_{i+1/2}-\mathcal{J}_k|_{i-1/2}}{\ell_i+\ell_{i+1}}\ , \tag{4.50}$$

using Eq. (4.44) to compute the value of species diffusion mass flux $\mathcal{J}_k|_{i\pm1/2}$ based on the interpolated solution at $x_{i\pm1/2}$. The corresponding enthalpy transport in the energy equation is

$$\left(\mathcal{J}_k\frac{\partial h_k}{\partial x}\right)\bigg|_i = 2\frac{h_{k,i+1/2}\mathcal{J}_k|_{i+1/2}-h_{k,i-1/2}\mathcal{J}_k|_{i-1/2}}{\ell_i+\ell_{i-1}} - h_{k,i}\frac{\partial \mathcal{J}_k}{\partial x}\bigg|_i\ , \tag{4.51}$$

where the partial enthalpies at locations $i\pm1/2$ are estimated by averaging their values at the adjacent grid points. Note that the first term on the right-hand side stands for the inter-diffusion heat flux of species k, and the second term exists due to writing the energy equation based on the temperature instead of enthalpy.

Convective terms are discretized using the QUICK-FD method [131] with the following formulation derived for the stretched grid:

$$\left.\frac{\partial\varphi}{\partial x}\right|_i = \begin{cases} \varsigma_1\varphi_{i-2} + \varsigma_2\varphi_{i-1} + \varsigma_3\varphi_i + \varsigma_4\varphi_{i+1} & , \quad u_i > 0 \\ \varsigma_5\varphi_{i-1} + \varsigma_6\varphi_i + \varsigma_7\varphi_{i+1} + \varsigma_8\varphi_{i+2} & , \quad u_i < 0 \end{cases} \tag{4.52}$$

with

$$\begin{aligned}
\varsigma_1 &= \ell_i\ell_{i-1}/[(\ell_{i-2}+\ell_{i-1})(\ell_{i-2}+\ell_i+\ell_{i-1})\ell_{i-2}] \ , \\
\varsigma_2 &= -(\ell_{i-2}+\ell_{i-1})\ell_i/[\ell_{i-2}\ell_{i-1}(\ell_i+\ell_{i-1})] \ , \\
\varsigma_3 &= [-\ell_{i-1}^2 + (2\ell_i-\ell_{i-2})\ell_{i-1} + \ell_i\ell_{i-2}]/[(\ell_{i-2}+\ell_{i-1})\ell_i\ell_{i-1}] \ , \\
\varsigma_4 &= \ell_{i-1}(\ell_{i-2}+\ell_{i-1})/[(\ell_{i-2}+\ell_i+\ell_{i-1})(\ell_i+\ell_{i-1})\ell_i] \ , \\
\varsigma_5 &= -\ell_i(\ell_i+\ell_{i+1})/[(\ell_i+\ell_{i-1}+\ell_{i+1})\ell_{i-1}(\ell_i+\ell_{i-1})] \ , \\
\varsigma_6 &= [\ell_i^2 + (\ell_{i+1}-2\ell_{i-1})\ell_i - \ell_{i-1}\ell_{i+1}]/[(\ell_i+\ell_{i+1})\ell_i\ell_{i-1}] \ , \\
\varsigma_7 &= (\ell_i+\ell_{i+1})\ell_{i-1}/[\ell_{i+1}(\ell_i+\ell_{i-1}]\ell_i) \ , \\
\varsigma_8 &= -\ell_i\ell_{i-1}/[(\ell_i+\ell_{i+1})(\ell_i+\ell_{i-1}+\ell_{i+1})\ell_{i+1}] \ .
\end{aligned}$$

4.4.2. TIME INTEGRATION

The spatial semi-discretization yields a system of ordinary differential equations (ODE) that can be written as

$$\mathrm{d}_t\boldsymbol{\mathcal{U}} = \mathrm{T}(\boldsymbol{\mathcal{U}}) + \mathrm{R}(\boldsymbol{\mathcal{U}}) \ , \tag{4.53}$$

where $\boldsymbol{\mathcal{U}} = [Y_{1:N}, \mathcal{K}, T, \mathcal{Z}]^\top$ is the vector of primary variables. All other variables, such as the axial velocity u and fluid properties, can be computed from $\boldsymbol{\mathcal{U}}$. The two vectors on the right hand side of Eq. (4.53) denote the rates of change due to the transport processes $\mathrm{T}(\boldsymbol{\mathcal{U}})$ and chemical reactions $\mathrm{R}(\boldsymbol{\mathcal{U}})$. The latter stiffly couples the system of equations and would require very small time steps with explicit time marching methods. We, therefore, use a suitable operator splitting method in which the stiff reaction part is separated from the transport process. As shown in the analysis of Speth *et al.* [132], the operators should be regrouped by adding and subtracting a balancing term $\mathbf{c}_n$ that is kept constant during all splitting sub-steps of time step n in order to guarantee that steady-state solutions are independent of the time step size. In this study, we use the second-order balanced splitting method of Wu, Ma, and Ihme [49], which can be written in semi-discrete form as:

$$\begin{aligned}
\mathbf{c}_n &= -\mathrm{T}(\boldsymbol{\mathcal{U}}_n) \\
\mathrm{d}_t\boldsymbol{\mathcal{U}}^{(1)} &= \mathrm{R}(\boldsymbol{\mathcal{U}}^{(1)}) - \mathbf{c}_n \ , \ \text{with } \boldsymbol{\mathcal{U}}^{(1)}(t_n) = \boldsymbol{\mathcal{U}}_n \\
\mathrm{d}_t\boldsymbol{\mathcal{U}}^{(2)} &= \mathrm{T}(\boldsymbol{\mathcal{U}}^{(2)}) + \mathbf{c}_n \ , \ \text{with } \boldsymbol{\mathcal{U}}^{(2)}(t_n+\Delta t/2) = \boldsymbol{\mathcal{U}}^{(1)}(t_n+\Delta t) \\
\boldsymbol{\mathcal{U}}_{n+1} &= \boldsymbol{\mathcal{U}}^{(2)}(t_n+\Delta t) \ .
\end{aligned} \tag{4.54}$$

The balancing term $\mathbf{c}_n = -\mathrm{T}(\boldsymbol{\mathcal{U}}_n)$ is computed at the beginning of each time step. The stiff reaction step, which is now a local system of ODEs for the specific heat release and mass rates, is integrated by a variable-coefficient ODE solver using a fifth-order backward differentiation scheme [105] over two half-time steps with an update of the thermodynamic properties in between. For the non-stiff transport step, we use a Lie-Trotter splitting of the diffusion terms and the remaining terms.

For the implicit time integration of the diffusion terms, we use the trapezoidal rule with second-order backward difference formula (TR-BDF2) [133]. A third-order strong stability preserving explicit Runge-Kutta (RK) method [134] is used for the remainder, in which the axial velocity and the thermo-transport properties are updated each sub-step.

4.4.3. INITIAL AND BOUNDARY CONDITIONS

Dirichlet boundary conditions are imposed for temperature and species mass fractions on both inlets. The stretch rate is set equal to the specified strain rate on one side and a Neumann boundary condition is used on the other side. The mixture fraction is 1 in the fuel stream and 0 in the oxidizer stream. In this study, we put the stagnation point (point of zero axial velocity) at the origin of the axial direction, which is in the middle of the computational domain.

All primary variables in the solution vector $\boldsymbol{\mathcal{U}}$ can be initialized based on a prescribed distribution of the mixture fraction in the computational domain. For simplicity, we use a step profile around the stagnation point so that the mixture fraction is 1 on the fuel side and is 0 on the oxidizer side and at the stagnation point. Subsequently, the mass fractions are obtained via a linear combination of their values at the boundaries and the local mixture fraction. Given the local composition, the temperature can be computed with the assumption of adiabatic mixing based on the enthalpy at the inlets and the local mixture fraction. The stretch rate is computed using the density of the fluid at each point via

$$\mathcal{K}(x) = \sqrt{-\Lambda/\rho(x)}\ , \tag{4.55}$$

with Λ obtained from the boundary conditions, see Eqn. (4.6). For unsteady igniting flames, initialization could also be based on the steady-state solution of the inert case. However, to remove any case-dependency of initialization effects on the transient results, we decided to use the initialization with a step profile also for unsteady calculations.

4.5. RESULTS

In this section, simulation results are reported and analyzed for three flames. First, supercritical gaseous hydrogen-oxygen flames are simulated for validation purposes. Next, counterflow diffusion problems at parameters that match the ECN Spray-A flame are considered, and the effects of different sub-models and model assumptions are analysed in detail. Finally, the model is applied to study dual-fuel combustion at high-pressure conditions.

4.5.1. SUPERCRITICAL FLAMES

We validate our solver against the results of Ribert *et al.* [135] for hydrogen-oxygen counter-flow diffusion flames at supercritical conditions. The selected test case has opposite streams of pure oxygen and hydrogen, both with an inlet temperature of 300 K. A strain rate of 2000 s^{-1} is applied to the fuel stream. For this test case, numerical results for different pressures ranging from 25 bar to 250 bar are reported by Ribert *et al.* [135]. We use a DG approach consistent with the reference; however, it should be noted that there are some differences between the supercritical flame modeling used in the current work and the models used by Ribert *et al.* [135], which are listed in Table 4.1. We have performed a grid-sensitivity study and all results presented in the following are grid-converged.

Table 4.1.: Differences between the present study and work of Ribert *et al.* [135] in the high-pressure combustion modeling of the hydrogen-oxygen benchmark test.

	Present work	*Ribert* et al. *[135]*
Equation of state	RKPR [92]	SRK [86]
Reaction mechanism	O Conaire *et al.* [136]	Li *et al.* [137]
Diffusion correction	Leahy-Firoozabadi	Takahashi
Diffusion driving force	non-ideal	ideal
Grid generation	locally refined	gradient-based locally refined
Numerical scheme	balanced splitting [49]	Newton marching [138]

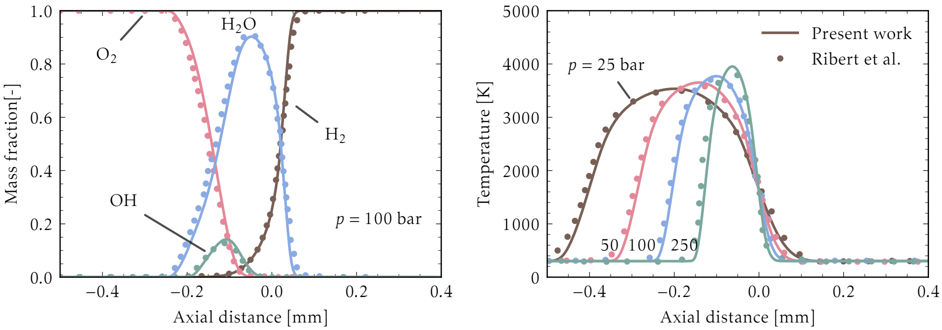

Figure 4.7.: Validation of the high-pressure combustion modeling with the detailed numerical simulations of Ribert *et al.* [135] for hydrogen-oxygen counterflow diffusion flames with inlet temperature 300 K and strain rate 2000 s^{-1}. Left: mass fraction profiles of major species at 100 bar; right: temperature profiles at different pressures.

The results obtained with the present solver and data of Ribert *et al.* [135] are shown in Fig. 4.7. The mass fraction profiles of major species at supercritical pressure of 100 bar are depicted on the left side. On the right side, temperature profiles for different pressures in the range 25 − 250 bar are shown. As reported in Ref. [135], pressure increase leads to a narrower flame with a higher peak temperature for this moderate strain rate. The current method captures this flame response very well and all results are in good agreement with the reference data.

4.5.2. TRANSCRITICAL FLAMES

The operating conditions of the ECN Spray-A setup are selected to study the unsteady behavior of transcritical flames and to scrutinize the importance of including real-fluid thermochemical and transport properties in simulations of this spray and similar setups. At a transcritical pressure of 60 bar, Spray-A injects liquid n-dodecane at a low temperature of 363 K into a preheated oxidizer at high temperature of 900 K with a molar composition of 15 $\%O_2$, 6.23 $\%CO_2$, 3.62 $\%H_2O$, and 75.15 $\%N_2$.

Unless otherwise stated, the CDF strain rate is set to $500\,s^{-1}$ at the oxidizer side. The hybrid reaction mechanism [130], which was already used for the IDT study of a stoichiometric mixture of n-dodecane and air in Section 4.3.3, is used here again. The initial conditions are prescribed as a step profile. We note that the steady-state solution of the corresponding inert flow is not a suitable initial condition for the study of the effects of the proposed thermochemistry and transport modeling on the unsteady flame behavior because differences between models would already be present in the initial conditions.

All simulations are conducted in the domain [-3 mm,+3 mm]. The grid is refined towards the center and consists of 444 points in total. A uniform grid spacing of 0.002 mm is used for the center region between −0.01 mm and 0.02 mm. Outside of this region, the grid is gradually stretched to the maximum spacing of 0.1 mm at both ends of the domain.

REAL-FLUID THERMODYNAMICS

The high-pressure effects and the possible coexistence of vapor and liquid for certain compositions of the mixture can play an essential role in inert or reacting counterflow problems under the operating conditions considered. It is expected that the models utilized for the thermo-transport properties of the working fluid can significantly affect the predictions. To analyze these effects, we performed simulations with different fluid models and otherwise identical setups.

Table 4.2.: Models for the transcritical n-dodecane flame: effects of real-fluid thermodynamics.

Label	*State equation*	*Transport properties*	*Diffusion modeling*	*Diffusion driving force*	*Chemistry modeling*
IG	ideal gas	Chung	Dixon-Lewis	ideal	ideal
DG	RKPR	Chung	Dixon-Lewis	ideal	ideal
MT	RKPR+VLE	Chung+EMT	Dixon-Lewis	ideal	ideal

In this section, the effects of the equation of state and the multiphase mixture model for inert and reacting CDF are evaluated using the models summarized in Table 4.2. The only difference between the DG and IG methods is the applied EOS. We used RKPR EOS for the DG method. The MT method is also based on the RKPR EOS and additionally includes VLE calculations in the two-phase region and EMT mixing rules.

Figure 4.8 shows steady-state results for the non-reacting case. It is clear that using ideal gas (IG) volumetric and caloric EOS results in significant errors in the thermo-transport properties at high pressure. Even accurate state equations, such as the utilized RKPR, result in large errors in the two-phase region if phase separation is neglected (DG). For instance, the density is strongly over-predicted in the coexistence region, and the temperature and thermal conductivity profiles

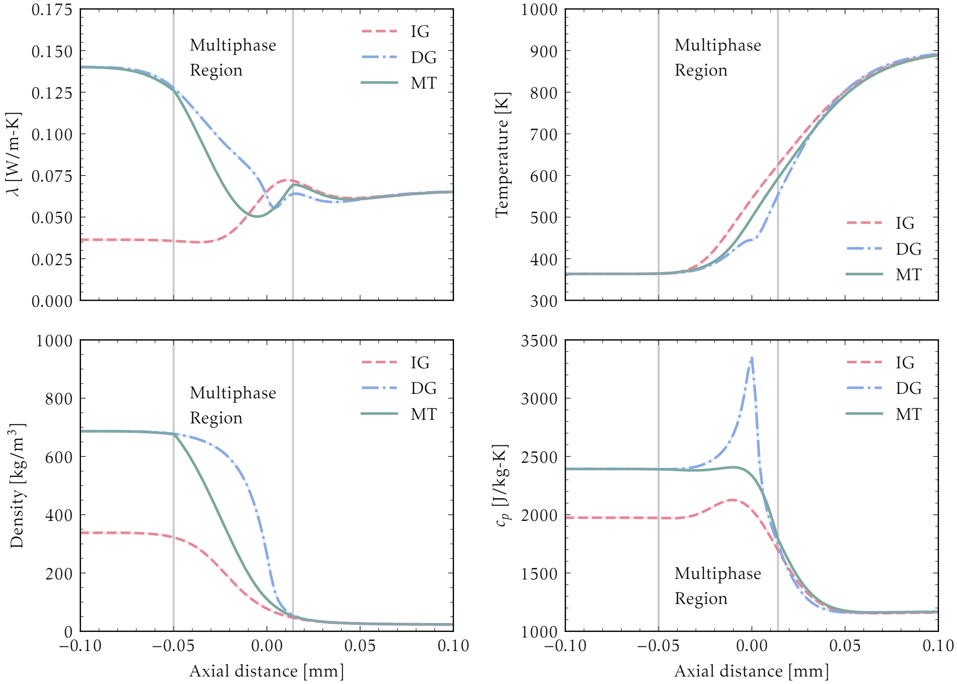

Figure 4.8.: Profiles of thermo-transport properties obtained with the proposed MT method and the conventional DG and IG approaches for steady-state inert counterflow of n-dodecane fuel in the transcritical Spray-A environment.

show a strange behavior that is mainly caused by the non-physical peak in the heat capacity. By including phase-splitting calculations (MT), we obtain results that are free of such artifacts.

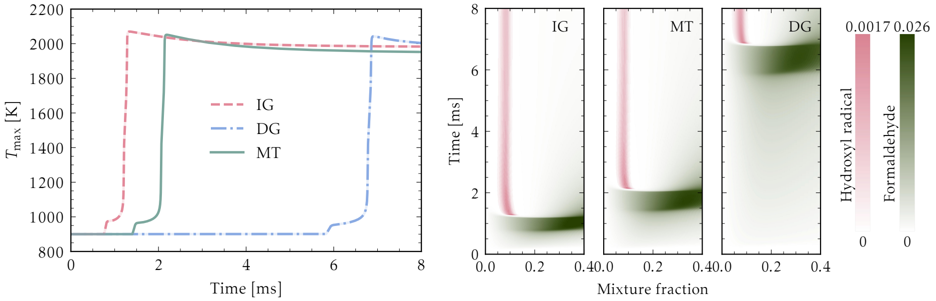

Figure 4.9.: Time evolution of maximum temperature (left) and mole fraction contours for formaldehyde and hydroxyl radicals (right) obtained with the proposed MT method and the conventional DG and IG approaches for the unsteady counterflow diffusion flame in the transcritical Spray-A environment.

Figure 4.9 shows results for the unsteady reacting case. The left panels show the temporal evolution of the maximum temperature T_{max}, from which the ignition delay time (IDT) can be deduced. The right panels show the mole fraction contours for formaldehyde (CH_2O) and hydroxyl (OH) for the three methods in mixture fraction – time coordinates. Formaldehyde is representative of radical formation during the cold ignition phase, which can also be clearly distinguished in the T_{max} diagram, and hydroxyl is used to visualize the hot reaction zone.

We observe large differences between the three models, which are mainly due to severe discrepancies in the IDT predictions with the IG and DG methods. Neglecting high-pressure effects with the IG approach results in a 50% under-prediction of the IDT. This is expected because the IG method yields too low values for fuel density and heat capacity, cf. Fig. 4.8, which results in an accelerated initial heat-up process and a faster ignition. The opposite observations are made for the DG approach, which shows a strong peak in heat capacity and overestimates the density of the mixture in the transcritical vaporization region. This hinders the heat-up process and results in a severe delay in the development of the cold flame and the subsequent hot ignition.

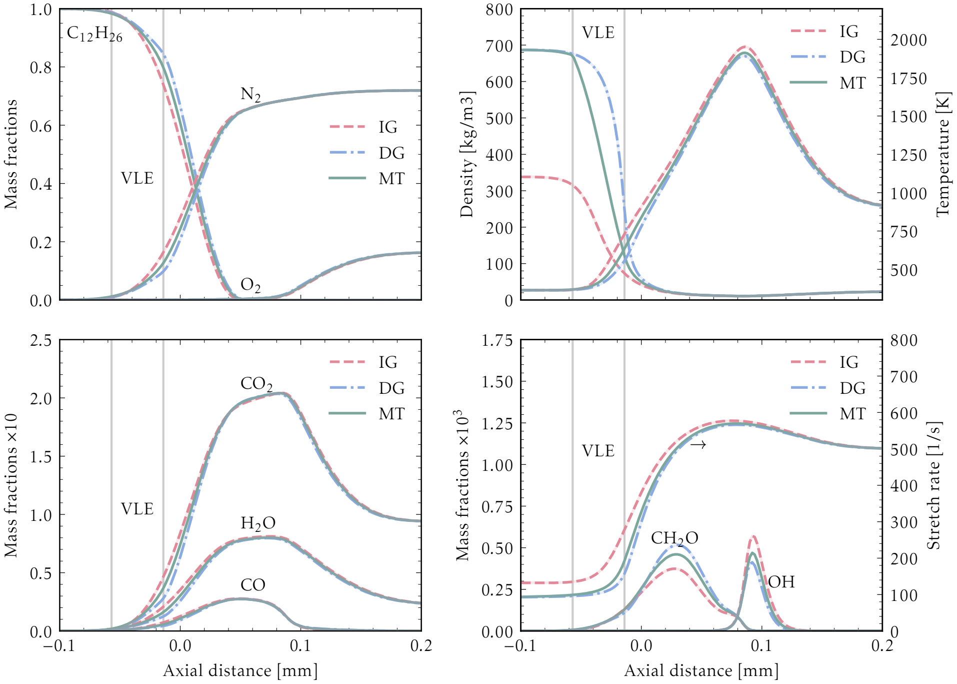

Figure 4.10.: Steady-state profiles of temperature, stretch rate, and mass fraction of major species and the formaldehyde and hydroxyl radicals obtained with the proposed MT method and the conventional DG and IG approaches for the unsteady counterflow diffusion flame in the transcritical Spray-A environment.

The differences between the IG, DG, and MT methods are reduced once the exothermic chemical reactions have sufficiently heated the fluid within the flame. This is expected because the cubic EOS is asymptotically consistent with ideal-gas EOS in the high-temperature limit. Figure 4.10 shows the fully developed steady-state results for the reacting case. The MT method can differentiate liquid, co-existence, dense-gas, and dilute-gas regions, see density and temperature profiles in the top-right panel. The IG method is accurate only in the latter region, and the DG method over-predicts the density in the co-existence region. The temperature profiles agree well within the hot flame and the oxidizer stream, however, the peak temperature is over-predicted by about 50 K with the IG model. Larger temperature differences are observed in the co-existence and dense-gas regions. Similar to the temperature profile, the species mass fraction profiles of the major species, see left panels, show the largest discrepancies in the two-phase and dense-gas regions, whereas the minor species are stronger affected around their peak concentrations. Overall, deviations from the ideal-gas conditions are much smaller for steady-state conditions than for the transient ignition. Nevertheless, one should keep in mind that incorrect predictions of the ignition delay time may have potentially large effects on the combustor dynamics, and an over-prediction of the peak temperature by 50 K can have significant effects on unwanted emissions.

REAL-FLUID DIFFUSION

Table 4.3.: Models for the transcritical n-dodecane flame: effects of non-ideal mass diffusion.

Label	*State equation*	*Transport properties*	*Diffusion modeling*	*Diffusion driving force*	*Chemistry modeling*
UL	RKPR+VLE	Chung+EMT	unitary Lewis	ideal	ideal
MC	RKPR+VLE	Chung+EMT	Dixon-Lewis	ideal	ideal
RMC	RKPR+VLE	Chung+EMT	Dixon-Lewis	non-ideal	ideal

During mixing and reaction, heavy and light species diffuse at different rates. In the following, we study the effect of non-ideal mass diffusion on our transcritical benchmark's inert mixing and reacting cases. Table 4.3 summarizes the models considered. A unitary Lewis (UL) model is studied due to its popularity in the combustion community. The standard Dixon-Lewis multi-component (MC) model uses ideal-gas approximations for the diffusion driving force, whereas high-pressure real-fluid effects are included in the RMC model through the thermodynamic correction matrix. All simulations have been conducted in the context of the MT approach.

Profiles of mass fractions and mass diffusive fluxes for the steady-state inert test case are shown in Fig. 4.11. There is no significant difference between the steady-state results of MC and RMC at the considered transcritical pressure of 60 bar. However, assuming a unitary Lewis number results in strongly increased diffusion towards the oxidizer stream.

Figure 4.12 shows the results for the unstable reaction case, which reveals the importance of accurate molecular diffusion models for ignition and flame evolution. MT simulations using UL lead to a significantly shorter IDT compared

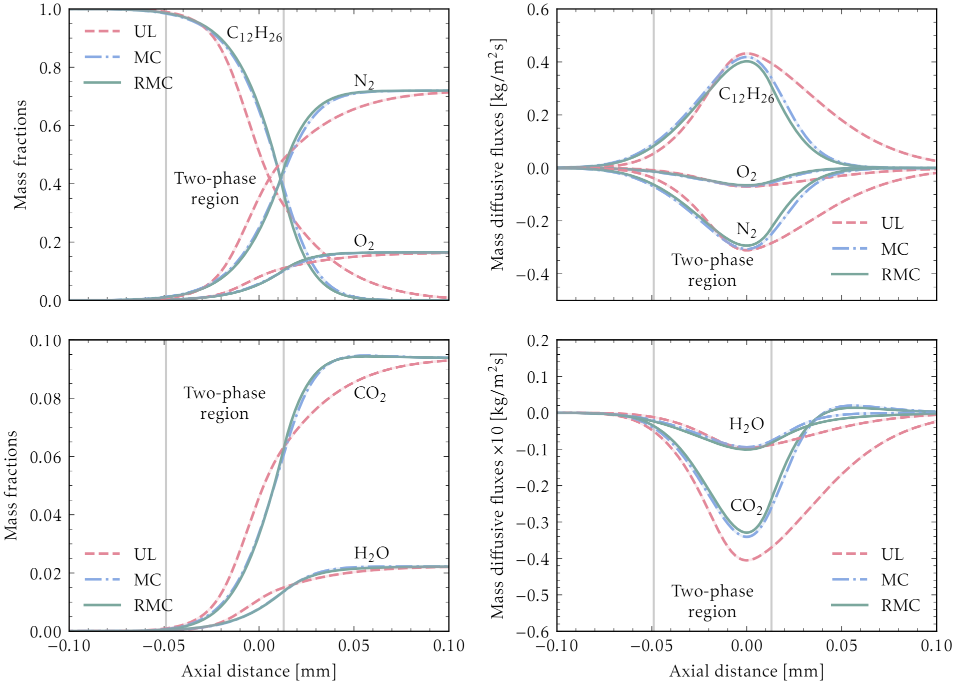

Figure 4.11.: Profiles of species mass fraction and diffusion flux computed based on the proposed MT method with unitary Lewis assumption (UL), multi-component method with ideal driving force (MC), and multi-component method with thermodynamic correction (RMC). Results show steady-state inert counterflow of n-dodecane fuel in the transcritical Spray-A environment.

to the more accurate MC and RMC models. The difference between MC and RMC results is significant and demonstrates that accurate modeling of not only the diffusivity coefficients but also the diffusion driving force is essential. The maximum temperature is also sensitive to diffusion modeling via the inter-species heat flux. This net heat flux is zero with a UL approximation; consequently, the maximum temperature remains constant after ignition. The MC and RMC results show that there is about 100 K reduction within 2 ms after ignition. The mole fraction contours of formaldehyde and OH visualize the cold and hot flames. The elapsed time between these two flames predicted using the Dixon-Lewis formula is shorter than that obtained with the UL assumption. In addition, the hot flame predicted with the UL method appears in the stoichiometric mixture fraction, and its location does not change over time. However, for the MC and RMC methods, the hot flame first appears in a fuel-rich location and then moves toward the stoichiometric mixture fraction.

Fig. 4.13 compares the steady-state results for the different diffusion models. Similar to the conclusions for the inert test case, there is no significant difference between the MC and RMC results. However, the unitary Lewis (UL) assumption

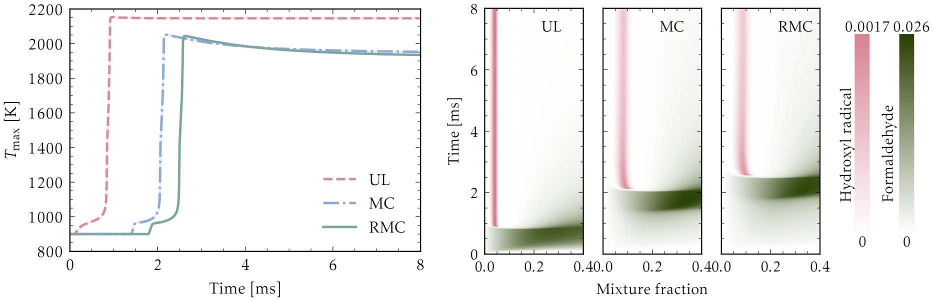

Figure 4.12.: Time evolution of maximum temperature (left) and mole fraction of formaldehyde and hydroxyl radical (right) computed based on the proposed MT method with unitary Lewis assumption (UL), multi-component method with ideal driving force (MC), and multi-component method with thermodynamic correction (RMC), for the unsteady reacting counterflow simulation of n-dodecane fuel in transcritical Spray-A environment.

leads to hugely different species profiles and changes the flame location.

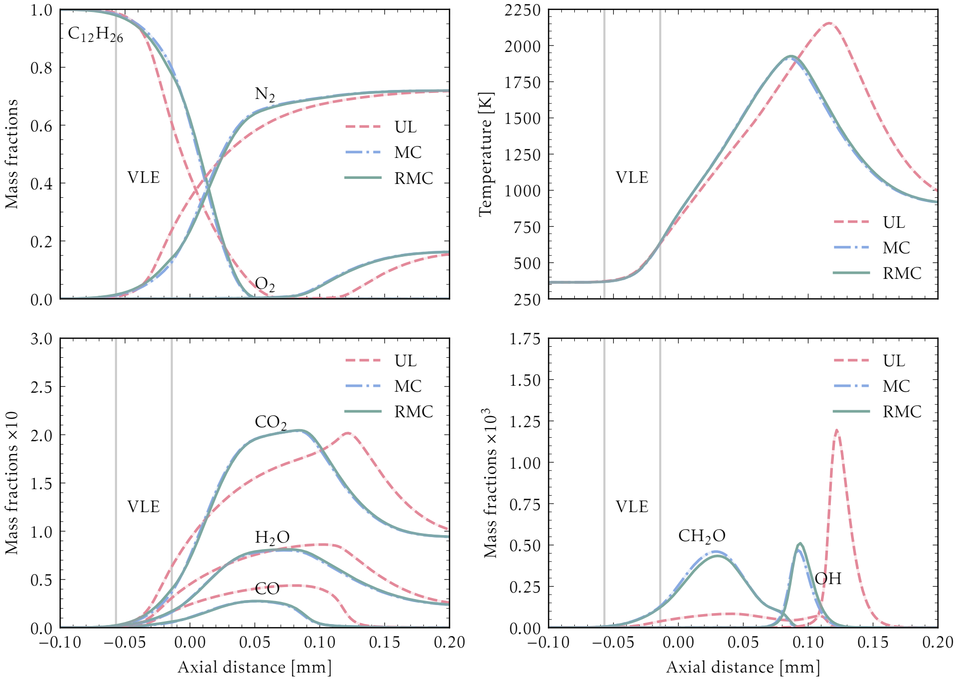

Figure 4.13.: Steady-state temperature and mass fractions profiles computed based on the proposed MT method with unitary Lewis assumption (UL), multi-component method with ideal driving force (MC), and multi-component method with thermodynamic correction (RMC), for the reacting counterflow simulation of n-dodecane fuel in transcritical Spray-A environment.

REAL-FLUID CHEMISTRY

The effect of high pressure on the heat reaction rates is studied. Table 4.4 shows two numerical modeling sets with differences in the evaluation of chemical source terms. The real-fluid chemistry model uses fugacity-based chemical source terms, as discussed above.

Table 4.4.: Models for the transcritical n-dodecane flame: effects of real-fluid chemistry.

Label	*State equation*	*Transport properties*	*Diffusion modeling*	*Diffusion driving force*	*Chemistry modeling*
Ideal Chem.	RKPR+VLE	Chung+EMT	Dixon-Lewis	non-ideal	ideal
Real Chem.	RKPR+VLE	Chung+EMT	Dixon-Lewis	non-ideal	non-ideal

Fig. 4.14 shows the effects of real-fluid chemistry models on the temporal variations of the maximum temperature and the mole fraction of the formaldehyde and hydroxyl radicals. The temperature plot shows that the use of a real-fluid chemistry model results in a shorter IDT. The contour of formaldehyde shows that this is mainly caused by the earlier creation of the cold flame.

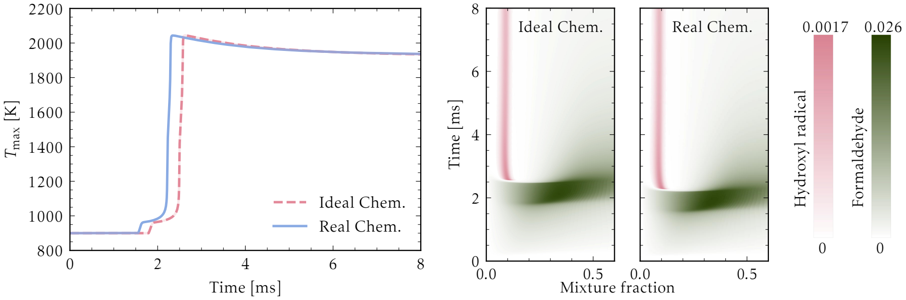

Figure 4.14.: Time evolution of maximum temperature (left) and mole fraction of formaldehyde and hydroxyl radical (right) computed based on the proposed MT with RMC methods with ideal and real chemistry models, for the reacting counterflow simulation of n-dodecane fuel in transcritical Spray-A environment.

4.5.3. ALTERNATIVE FUELS

A possible remedy to reduce the formation of soot in a diesel engine is the use of oxygenated fuels without a carbon-carbon bond in their molecular structure. Oxymethylene ether-3 (OME3), a soot-free high-cetane number fuel with properties close to those of diesel fuel, is one of the most promising candidates among such fuels. Additionally, a dual-fuel configuration burning a light hydrocarbon such as methane along with the main heavy hydrocarbon fuel can reduce the net amount of the engine's emissions. In dual-fuel engines, a low-reactive fuel like methane is premixed with the oxidizer and combustion occurs by auto-ignition via transcritical injection of diesel (or OME_3) into this compressed lean fuel-air mixture. In this section, we apply our model framework to compare the combustion of OME_3 versus n-dodecane in a diesel-like environment in single and dual-fuel configurations.

Similar to the previous sections, a liquid fuel mixture with a temperature of 363 K is injected into a preheated oxidizer at a high temperature of 900 K. A strain rate of 500 s^{-1} is also applied on the oxidizer side. The operating pressure is 60 bar, which is above the critical pressure of both fuels.

In the single-fuel case, the oxidizer has the same molar composition as the ECN Spray-A benchmark with 15 %O_2. As a dual-fuel example, we use a lean mixture for the oxidizer stream with a molar composition of 15 %O_2, 5.955 %CO_2, 3.460 %H_2O, 3.750 %CH_4, and 71.835 %N_2. This oxidizer mixture has a methane-based equivalence ratio of 0 5. The concentrations are calibrated so that 15 % O_2 is maintained in the oxidizer stream.

The hybrid reaction mechanism of Lapointe, Zhang, and McNenly [130] is used again for the combustion of n-dodecane, and the reduced mechanism of Lin *et al.* [139] is chosen for the combustion of OME_3. Transcritical real-fluid effects on the thermochemical and transport properties are included using the RKPR EOS coupled with a rapid VLE calculator, Chung correlations with the EMT mixing rule, Dixon-Lewis diffusion formula with the thermodynamic correction factor, and fugacity-based evaluation of the chemical source terms. The grid is the same as used in the previous section for the n-dodecane CDF studies.

Figure 4.15 compares the unsteady flame behavior of transcritical n-dodecane and OME_3 fuels for single-fuel (without methane in the oxidizer) and dual-fuel configurations. The evolution of the maximum temperature shows that OME_3 ignites faster than n-dodecane. Dual fueling retards ignition for both fuels, but the delay is greater for n-dodecane. The presence of methane burning along with the primary fuel increases the maximum temperature of the flame. The temporal contours of formaldehyde in single- and dual-fuel environments confirm the retardation of ignition and show a slight change in the cold-flame structure. The OH concentration is higher in the dual-fuel environment, consistent with a higher heat release. The dual-fuel hot flames stabilize at a richer mixture fraction compared to the single-fuel case.

Figure 4.16 shows the steady-state profiles of the mass fraction of acetylene and temperature for the single and dual fuel cases. Acetylene is selected because it is a primary soot precursor at elevated pressures. As expected, OME_3 combustion produces negligible amounts of acetylene (note the different scaling of the axis for n-dodecane). In general, the response of the OME_3 flame structure to dual fueling is similar to that of the n-dodecane flame. For both fuels, we find that adding methane to the environment increases the peak of acetylene and the flame temperature, and the flame becomes thicker. The former effect is stronger for n-dodecane. The vertical dotted lines indicate the VLE region, which is narrower and is more on the left for OME_3. That is, OME_3 evaporates faster than n-dodecane.

One of the advantages of OME_3 is that it can be mixed with other standard fuels such as diesel and benzine. In the following, we study the effects of blending OME_3 with different portions of octane in a setup similar to that used for the previous single-fuel transcritical test case. The reduced mechanism of Lin *et al.* [140] is chosen for the combustion of the binary mixture of OME_3 and octane.

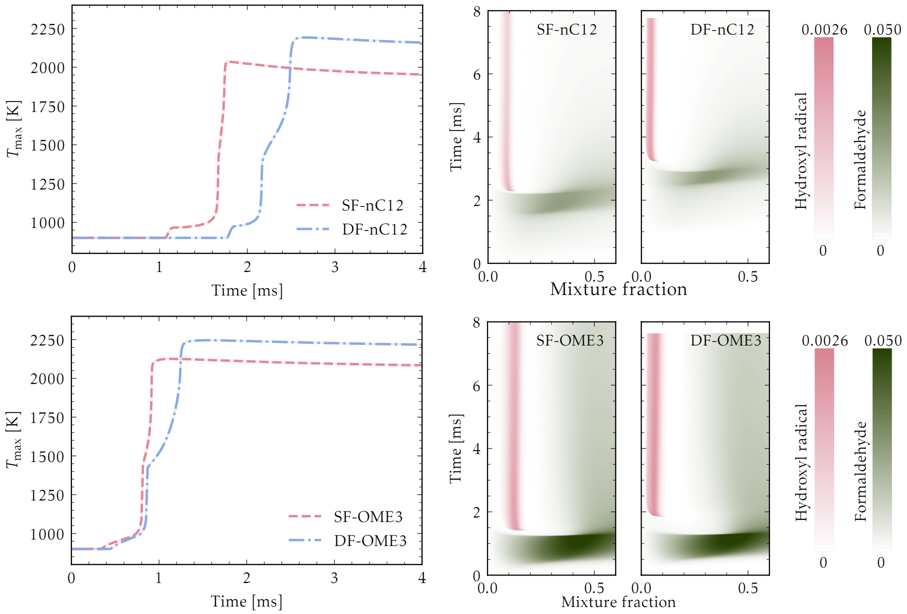

Figure 4.15.: Time evolution of maximum temperature (left) and mole fraction of formaldehyde and hydroxyl radical (right) for the unsteady counterflow simulation of n-dodecane (nC12) and oxymethylene ether-3 (OME3) fuels in single-fuel (SF) and double-fuel (DF) environments.

Figure 4.17 compares the unsteady flame behavior of transcritical OME_3-based fuels with various molar percentages of iso-octane. Tracking the maximum temperature shows that adding octane to OME_3 delays ignition, which is an expected result. The temporal contours of formaldehyde confirm the retardation of the cold-flame ignition and show a noticeable change in the structure of the cold flame. The peak and steady-state temperatures are similar for all fuel blends considered, whereas the peak OH concentrations shift slightly to lower mixture fractions when octane is added.

Figure 4.18 shows the steady-state profiles of the temperature and mass fraction of acetylene for various fuel blends with iso-octane. Adding octane to the OME_3 fuel increases the peak of acetylene, while the thermal shape of the flame remains almost unchanged. The amount of acetylene is still meager compared with the n-dodecane flame shown previously for the same conditions.

Figure 4.19 compares mole-fraction profiles for OME_3 and octane in the saturated vapor and liquid phases. The mole fractions of OME_3 and octane in the saturated liquid composition are reduced during mixing and vaporization. This reduction indicates that combustion products diffuse into the liquid phase.

APPLICATION IN MULTI-DIMENSIONAL SIMULATIONS

To demonstrate the application of the multiphase laminar flamelet model in multi-dimensional computational fluid dynamics simulations at transcritical pressure, we

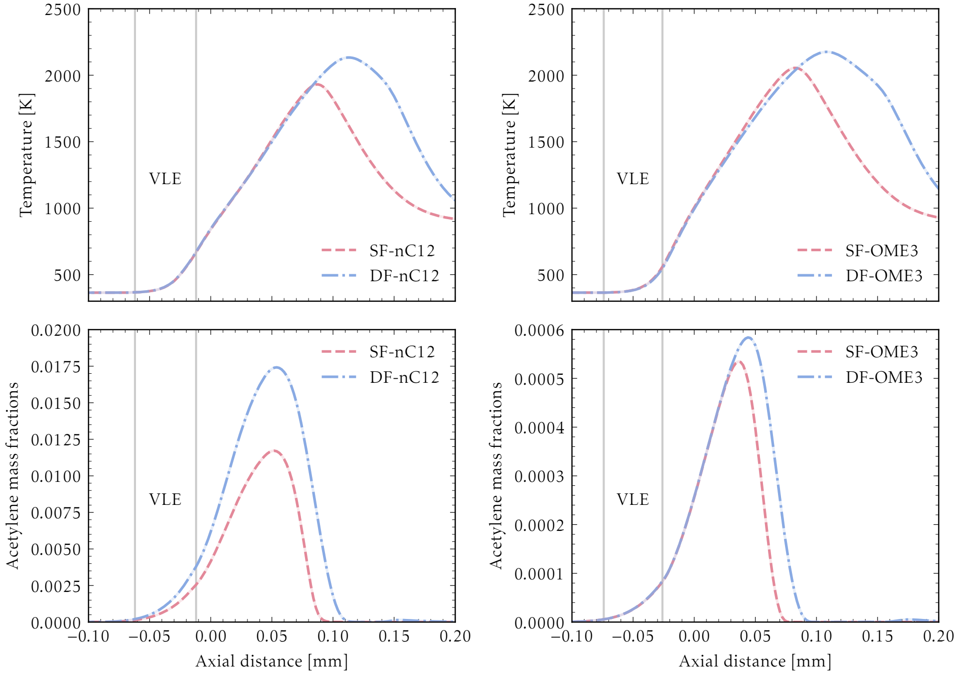

Figure 4.16.: Temperature and acetylene mass fraction profiles for the steady-state CDF simulation of n-dodecane (nC12) and oxymethylene ether-3 (OME3) fuels in single-fuel (SF) and double-fuel (DF) environments.

present and analyze results for a reacting shear flow using a fuel stream sandwiched between two oxidizer streams with a relatively high difference in velocities. The computational domain is two-dimensional; therefore, a fully realistic structure of turbulent-flow features cannot be expected. However, the selected configuration can represent the multiphase reacting behavior of real fluid mixtures and the important role of the presented CDF for such complex simulations.

The cold and liquid fuel stream consists of pure OME_3. The hot and gaseous oxidizer streams have the same composition as used for the dual-fuel counter-flow diffusion-flame study with 15% oxygen and a methane-based equivalence ratio of 0.5. The operating pressure is set at 60 bar, and the cold and hot temperatures are set at 365 K and 900 K, reproducing the operating conditions of the transcritical ECN Spray-A injector. The momentum shear layer is characterized by a relative velocity difference of $50\,\mathrm{m\,s^{-1}}$ and initialized using a tangent hyperbolic function. The Kelvin-Helmholtz instability is initiated by adding random perturbations with a turbulence intensity of 5% to the velocity field.

Periodic boundary conditions are applied for all directions. The mesh is uniform and consists of 336×336 cells in a square domain of length $L = 10\,\mathrm{mm}$. The initial thickness of the fuel stream is $L/10$, similar to the work of Tekgul *et al.* [27]. The CFL number is set to 1.0, and no subgrid-scale model is utilized for

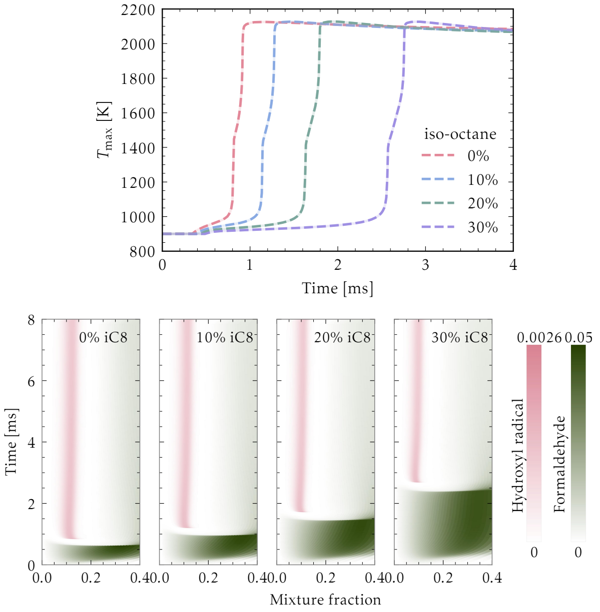

Figure 4.17.: Time evolution of $T_{\max}$ (top) and mole fraction of formaldehyde and hydroxyl radical (bottom) computed for OME_3 fuel blended with different molar percentages of iso-octane.

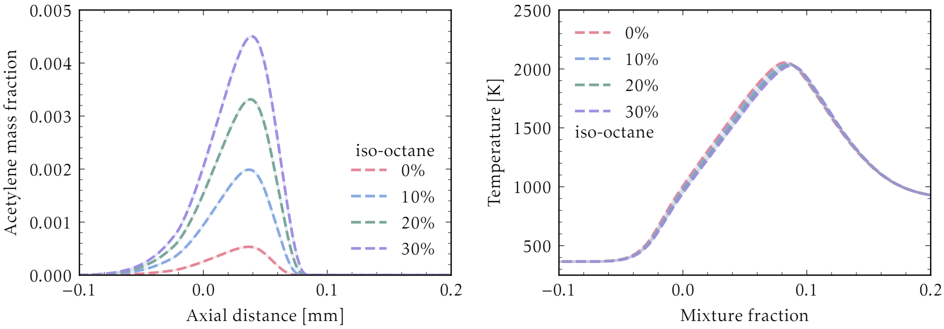

Figure 4.18.: Temperature and acetylene mass fraction profiles for the steady-state reacting counterflow simulation of OME_3 fuel blended with different molar percentages of iso-octane.

these 2-D simulations. The simulation is performed using the INCA flow solver (`http://inca.cfd`). For the purpose of this demonstration, a fast-chemistry assumption is a reasonable choice [27]. Therefore, we solved a transport equation for the mixture fraction under the assumption of fast combustion with an efficient one-dimensional lookup table for the composition, which was constructed based on the steady-state results of the laminar CDF.

Figure 4.20 shows a snapshot of the solution at 0.8 ms. The locations of hot and cold flames are highlighted using the mass fraction contours of OH and CH_2O.

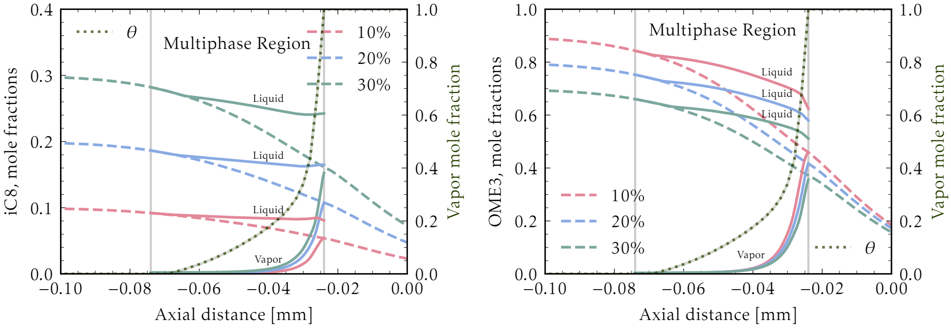

Figure 4.19.: Mole fraction profiles of the fuel components in the steady-state reacting counterflow simulation of OME3 blended with different molar percentages of iso-octane. Dashed lines indicate the total mole fraction, and solid lines indicate the concentration in vapor and liquid. The background shows the variation of the vapor mole fraction.

On the right, the background shows the temperature variations. The contour is superimposed with the vapor mole fraction to indicate the transcritical two-phase region for this test case.

4.6. CONCLUSIONS

We have presented a comprehensive framework of models for the efficient and accurate simulation of real-fluid transcritical flames, developed using multiphase thermodynamics and real-fluid finite-rate chemistry, and applied these models in parametric studies that contribute to the in-depth understanding of the properties of transcritical diffusion flames.

The framework includes novel strategies for the accurate evaluation of transport properties in two-phase regions and addresses the computation of thermodynamic correction factors using real-fluid EOS coupled with the rapid VLE solver of the multiphase thermodynamic approach. All equations and numerical schemes required for unsteady simulations of multiphase counterflow flames at trans/supercritical pressures have been presented in detail. The application as a promising sub-model for flamelet-based CFD simulations of turbulent combustion was briefly demonstrated.

The effects of transcritical mixing and evaporation have been studied for a series of steady and unsteady simulations of inert and reacting counter flows of transcritical n-dodecane and an oxidizer stream corresponding to the ECN Spray-A benchmark, which is too close to operating conditions of internal combustion engines and gas turbines. From these studies, the following main conclusions are drawn:

- Using a suitable EOS coupled with VLE calculations is essential for the accurate prediction of the unsteady behavior of flames at transcritical pressures. A single-phase model neglecting phase separation over-predicts

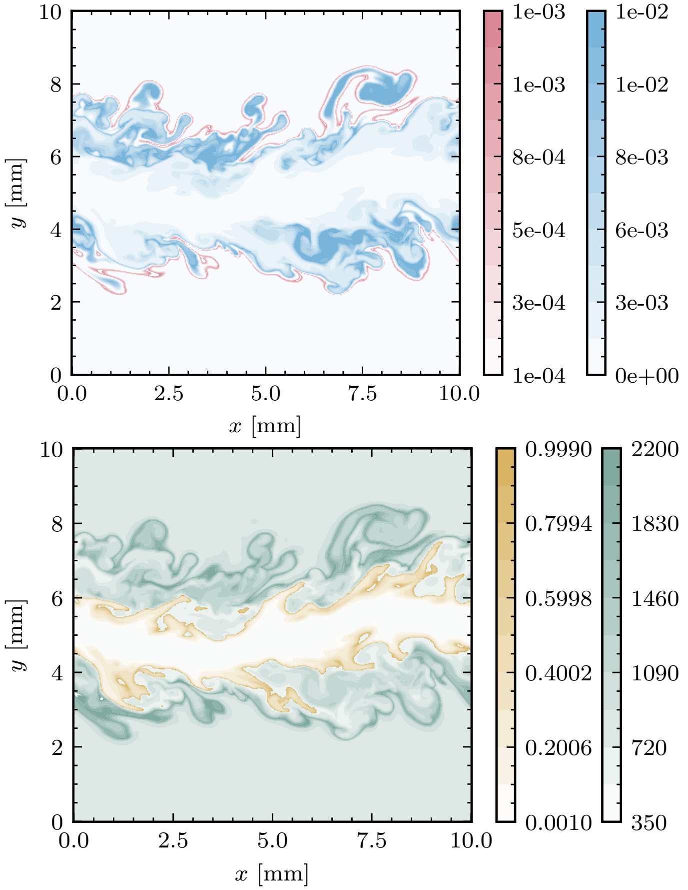

Figure 4.20.: Top: mass fraction contours of OH (red) and CH_2O (blue) for the reacting shear flow simulation at 0.8 ms. The background features CH_2O contours, overlaid with OH contours, and color bars represent the varying mass fractions. Bottom: temperature contours (green) in the background of the snapshot. Vapor mole fraction contours (brown) are superimposed to indicate the locations of vapor-liquid coexistence.

the heat capacity and density in the two-phase region, and thereby causes a significant delay of the ignition. On the other hand, ideal-gas approximations underestimate those key properties and shorten the ignition delay time.

- The unitary-Lewis assumption, which is very common in combustion modeling, changes the flame temperature and structure and should not be made at transcritical pressures. A unitary species fugacity approximation for modeling the mass diffusion driving force only affects the transient flame behavior but not the steady state solution.
- Real-fluid effects on combustion kinetics can be modeled effectively with the proposed fugacity-based finite-rate chemistry model. Real-fluid chemistry

accelerates the cold-flame formation and thereby reduces the ignition delay time.

We have also studied OME_3 as a promising soot-free alternative to diesel fuels in single- and dual-fuel configurations. The computational results confirm that OME_3 reduces the soot precursor acetylene by 97% compared to n-dodecane. In general, although OME_3 ignites a bit faster than n-dodecane, the flame structure is similar. Dual fueling with methane retards the ignition of both fuels, but this delay is relatively minor for OME_3 compared to n-dodecane.

5

Transcritical Combustion using Tabulated Chemistry

This chapter integrates the real-fluid transcritical flame results from Chapter 4 into an effective compressible flamlet approach to simulate full reacting sprays with detailed combustion while maintaining computational efficiency. This Flamelet Progress Variable (FPV) method is coupled with the LES-MT solver. For completeness, the chapter provides a concise overview of certain material that was discussed earlier, ensuring that all essential elements are available in a self-contained form. The framework is validated for both conventional and alternative fuels, including OME_3*, n-dodecane, and their blends. Results highlight how* OME_3*, for example, changes ignition characteristics and reduces soot formation.*

The content of this chapter has been published as *Large Eddy Simulations of Transcritical e-Fuel Sprays Using Real-Fluid Multiphase Flamelet-based Modeling* in Combustion and Flame **275** (2024) [141].

5.1. INTRODUCTION

Polyoxymethylene dimethyl ethers (OMEs) are carbon-neutral e-fuels with a significant amount of oxygen in their molecular structure. The absence of C-C bonds in the chemical structure of OMEs leads to a significantly reduced soot formation and makes them practically soot-free during combustion. In addition, their high oxygen content enhances combustion efficiency and reduces carbon monoxide and particulate matter emissions [142–145]. Although previous studies have focused predominantly on OME_1 due to synthesis challenges, recent research is moving toward higher OMEs due to their favorable properties, such as boiling point, lubricity, and viscosity, which are similar to diesel [146]. This similarity allows higher OMEs to be effectively blended with conventional fuels. Investigating the combustion properties of these green synfuels, particularly under transcritical high-pressure conditions, requires advanced simulation techniques to predict not only their emission profile using a detailed chemistry but also the complex interactions in mixed fuel systems.

Flamelet-based combustion modeling is commonly used to simulate reacting flows with detailed chemistry. Flamelet methods are very effective at high pressures, where the flame becomes thinner and the Kolmogorov eddies cannot change the inner laminar structure of the flame [44]. Flamelet models provide an accurate representation of the actual flame through a pre-tabulating database of one-dimensional flamelets using a few controlling parameters. This can be achieved using the flamelet-generated manifold (FGM) method, which effectively incorporates transport effects into the generation of tabulated chemistry [147]. As the main combustion mode in transcritical engines is non-premixed and autoignition is inherently transient, the flamelet database is typically generated based on the results of unsteady counterflow diffusion flames (CDF) [26, 46, 47].

As shown in Chapter 4, the ignition of CDFs is significantly influenced by the methods used to model the thermodynamic and transport properties. In transcritical settings, ignoring the real-fluid effects or the two-phase region would yield an incorrect transient result. Unlike classical flamelet models based on ideal-gas assumptions, recent studies [148–151] have sought to include real-gas effects in their tabulated chemistry. The first step to consider phase separation in transcritical flamelets was taken by Traxinger, Zips, and Pfitzner [38] to study transcritical combustion under rocket engine conditions. They used VLE calculations along with flamelet equations expressed in the mixture fraction space using the unitary Lewis assumption with an approximate scalar dissipation rate profile. The approach used in the present chapter constructs a flamelet-based library solving governing equations for the igniting CDF expressed in the physical space. The present model does not make a unitary Lewis assumption; instead, it utilizes detailed fugacity-based diffusion and chemistry models. It accurately captures the effects of both the two-phase region and the real-fluid properties in the flamelet database.

A remaining modeling problem to be addressed is the representation of the influence of subgrid scale (SGS) fluctuations on the resolved chemical source term. In the present work, this influence is neglected by evaluating the source term directly from the resolved composition (species concentrations and temperature) via the laminar kinetic rate expressions often called the well-stirred reactor (WSR) model in literature. This choice aligns with a substantial body of prior LES studies. As summarized by Hadadpour *et al.* [152], a broad range of turbulence-chemistry interaction (TCI) closures has been employed in 21 LES investigations of ECN Spray A and Spray H configurations, also listing the minimum cell size. It shows that a wide range of models has been used, divided as follows: WSR (8 studies), Partially Stirred Reactor (PaSR) (4), Conditional Moment Closure (CMC)(1), Flamelet (1), FGM (3) and Transported PDF (4). Because these studies also differ in the adopted chemical mechanisms, no definitive conclusion can be drawn regarding the relative performance of the different TCI strategies. Notably, the smallest LES cell sizes-down to 62.5 µm-have been used in combination with the WSR model, whereas other closures typically rely on grids up to eight times coarser. This agrees with the fact that in explicit LES modeling, where the LES filtering is controlled by the computational mesh, the accuracy of the WSR approach is expected to increase with grid refinement, because the assumption of homogeneity becomes more plausible.

This chapter presents a novel numerical framework to efficiently include real-fluid multiphase thermo-transport effects within an MT-based and tabulated reacting flow solver, allowing high-fidelity simulation of high-pressure transcritical fuel sprays with detailed chemistry. The transcritical flamelet library is generated using unsteady simulations of multiphase counterflow flames at transcritical pressures, including the effects of real fluids and subcritical vaporization. The fluid flow solver uses the RKPR EOS coupled with the rapid VLE solver of Fathi and Hickel [51] and employs the adaptive local deconvolution method (ALDM) for LES-based turbulence modeling [148].

In gas turbines and diesel engines, the air-fuel mixture can easily traverse the metastable region and enter the physically forbidden (unstable) area of the two-phase dome [5]. Hence, the proposed method is first validated by comparing numerical results with the available experimental measurements for the transcritical n-dodecane Spray-A of the engine combustion network (ECN) [110, 153]. To expand our understanding of the combustion characteristics of OMEs, we additionally performed Spray-A simulations using OME_3 and a mixture of OME_3 and nC_{12}, providing novel insights into the dynamics of evaporation, ignition behavior, and soot formation in different fuel configurations.

For completeness and to maintain a self-contained presentation, this chapter includes an outline of selected material introduced in earlier sections. This allows the reader to follow the developments without referring back to previous chapters.

5.2. TRANSCRITICAL SPRAYS

The representative benchmark case of ECN Spray-A has been selected because it considers transcritical conditions typically encountered in modern internal combustion engines. The standard experimental setup involves a fuel jet at a temperature of 363 K, which is injected at a speed of approximately 600 $\mathrm{m\,s^{-1}}$

over a duration of 1.5 ms. This is achieved by a rail pressure of 1500 bar and injection through a single-hole nozzle with a nominal diameter of $D = 0.09$mm into a preheated oxidizer chamber at a temperature of 1000 K and a pressure of 60 bar. The chamber has a molar composition of 15 %O_2, 6.23 %CO_2, 3.62 %H_2O, and 75.15 %N_2. The present study focuses on three different fuel types: pure n-dodecane (nC_{12}), pure polyoxymethylene dimethyl ether 3 (OME_3), and a mixture of both with a molar composition of 50% nC_{12} and 50% OME_3.

Table 5.1.: Critical properties and acentric factors of major species

Species	T_c [K]	p_c [bar]	Z_c	Ω
OME_3	621.5	30.20	0.247	0.507
nC_{12}	658.0	18.20	0.251	0.576
O_2	154.6	50.43	0.288	0.022
N_2	126.2	34.00	0.289	0.038

The Spray-A operating pressure is much higher than the critical pressure of the individual fuel species, see Table 5.1. For all three cases, the liquid fuel experiences transcritical vaporization as it blends with the hot pressurized oxidizer. Spray-A with the diesel-like fuel nC_{12} has been extensively examined in the past. More recently, experimental data have been reported for Spray-A with OME_3 fuel. To our knowledge, no experimental or numerical studies have been conducted for the blended case.

5.3. NUMERICAL MODELS

The numerical models for MT-LES of transcritical fuel sprays with tabulated real-fluid multiphase chemistry are detailed in this section.

5.3.1. GOVERNING EQUATIONS

Using the standard notation, the governing equations describing the conservation of mass, momentum, and total (absolute) energy for a single-fluid compressible flow can be written as

$$\partial_t \rho + \boldsymbol{\nabla} \cdot (\rho \mathbf{u}) = 0, \tag{5.1}$$

$$\partial_t \rho \mathbf{u} + \boldsymbol{\nabla} \cdot (\rho \mathbf{u}\mathbf{u} + p\mathbf{I}) = \boldsymbol{\nabla} \cdot \boldsymbol{\tau}, \tag{5.2}$$

$$\partial_t \rho e_t + \boldsymbol{\nabla} \cdot [(\rho e_t + p)\mathbf{u}] = \boldsymbol{\nabla} \cdot (\mathbf{u} \cdot \boldsymbol{\tau} + \lambda \nabla T). \tag{5.3}$$

where ρ is the density, $\mathbf{u}$ is the velocity vector, p is the thermodynamic pressure, T is the temperature, and e_t is the total specific energy which includes the internal (absolute) energy e as well as the kinetic energy of the flow. There is no source term in the energy conservation equation, as the internal energy includes the heat of formation. λ denotes the thermal conductivity. $\boldsymbol{\tau}$ is the viscous stress tensor that is estimated using molecular viscosity μ as follows:

$$\boldsymbol{\tau} = \mu\left(\boldsymbol{\nabla}\mathbf{u} + (\boldsymbol{\nabla}\mathbf{u})^T\right) - 2/3\mu(\boldsymbol{\nabla}\cdot\mathbf{u})\mathbf{I}. \tag{5.4}$$

To identify the thermodynamic state (p,T) and transport properties (λ,μ) of the working fluid, we need to know the composition in addition to the internal energy and mass density of the mixture. To avoid solving a very large number of species transport equations, the composition of the mixture is determined through a look-up table constructed based on the mixture fraction $\mathcal{Z}$ and the progress variable $\mathcal{C}$ as controlling parameters. The solved transport equations for the mixture fraction and the progress variable are

$$\partial_t\rho\mathcal{Z} + \boldsymbol{\nabla}\cdot(\rho\mathbf{u}\mathcal{Z}) = \boldsymbol{\nabla}\cdot(\lambda/c_p\nabla\mathcal{Z})/\mathrm{Le}_{\mathcal{Z}}, \tag{5.5}$$

$$\partial_t\rho\mathcal{C} + \boldsymbol{\nabla}\cdot(\rho\mathbf{u}\mathcal{C}) = \boldsymbol{\nabla}\cdot(\lambda/c_p\nabla\mathcal{C})/\mathrm{Le}_{\mathcal{C}} + \dot{\omega}_{\mathcal{C}}. \tag{5.6}$$

The source term of the progress variable, $\dot{\omega}_{\mathcal{C}}$, is also obtained from the look-up table. The Lewis numbers $\mathrm{Le}_{\mathcal{Z}}$ and $\mathrm{Le}_{\mathcal{C}}$ of the mixture fraction and the progress variable are set to those used for the auxiliary equations in the generation of the flamelet database; see Ref. [118] for a discussion of the differential equations for $\mathcal{Z}$ and $\mathcal{C}$ in the presence of preferential diffusion.

5

In the appendix A.2, we explain the rationale for employing the fully conservative form of the compressible Navier-Stokes equations instead of using pressure-based solvers with the low-Mach assumption.

5.3.2. MULTIPHASE THERMODYNAMICS

The unique characteristic of the high-pressure transcritical environment is that the working fluid can cross the two-phase region and become thermodynamically unstable. Following the MT approach for modeling the real-fluid transcritical phase separation, in addition to using suitable real-gas caloric and volumetric EOSs, rapid and robust phase-splitting or flash calculations are required to account for the transcritical formation of the vapor-liquid interphase.

SINGLE-PHASE CALCULATIONS

A cubic EOS is often chosen as a practical balance between precision, intricacy, and computational expenses; the general form of cubic EOSs is

$$p = \mathcal{R}T/(\bar{\vartheta} - b) - a/[(\bar{\vartheta} + \delta_1 b)(\bar{\vartheta} + \delta_2 b)]. \tag{5.7}$$

The symbol $\mathcal{R}$ represents the universal gas constant and $\bar{\vartheta} \equiv W/\rho$ is the molar specific volume of the mixture. δ_1 and δ_2 are volume parameters. a and b are energy parameters that account for non-ideal behavior caused by attractive and repulsive forces between molecules. For real-fluid mixtures, these parameters can be determined using the van der Waals mixing rule, which can be expressed as

$$a = \sum_{i=1}^{N} \sum_{j=1}^{N} X_i X_j (1 - k_{ij}) \sqrt{a_i a_j}, \tag{5.8}$$

$$b = \sum_{i=1}^{N} X_i b_i, \tag{5.9}$$

where X_i is the mole fraction of species i. The values of a_i and b_i are determined for the pure species i, and k_{ij} represents the binary interaction coefficient between species i and j. For two-parameter cubic EOS such as SRK and PR, a_i and b_i are expressed as a general function of the acentric factor, the critical temperature, and the critical pressure of the species along with constant values for δ_1 and δ_2. The latter results in a single universal compressibility factor at the critical point and implies a systematic error in predicting the specific volume (or density) when conditions are close to the critical point. To solve this problem, Cismondi and Mollerup [92] proposed RKPR as a three-parameter EOS, in which $\delta_2 = (1 - \delta_1)/(1 + \delta_1)$ and δ_1 is a function of the compressibility factor. Using the van der Waals mixing rule, we can determine δ_1 by the following expression:

$$\delta_1 = \sum_{i=1}^{N} X_i \delta_{1,i}(\hat{Z}_i), \tag{5.10}$$

with $\hat{Z}_i = 1.168 Z_{c,i}$ where $Z_{c,i}$ is the critical compressibility factor of species i. We consider RKPR the most promising three-parameter cubic EOS and use it throughout this study. Phase diagrams computed using the RKPR EOS for the considered nC_{12} and OME_3 fuels are shown in Fig. 5.1. The two-phase dome is highlighted using vapor mole fraction (VMF) contours, explained in the next section. The figure shows an insignificant difference between the prediction of saturated vapor and liquid density for RKPR EOS and the highly accurate EOS of Lemmon and Huber [97] and the results of the molecular simulation of Kulkarni *et al.* [154].

Moreover, RKPR EOS has shown reliable performance for blend system predictions. Tassin, Mascietti, and Cismondi [155] showed that RKPR significantly improves the phase equilibrium predictions for hydrocarbon mixtures, particularly those with highly asymmetric molecules. Kim, Choi, and Kim [93] further highlighted RKPR's robustness in reacting flow environments, including kerosene/LOx combustion.

Using Eq. 5.7, the thermodynamic pressure of the single-phase mixture can be calculated directly when the temperature of the mixture is known. Determining the temperature requires a caloric EOS. The caloric EOS for the single-phase real fluids can be obtained by employing the departure function formalism consistent

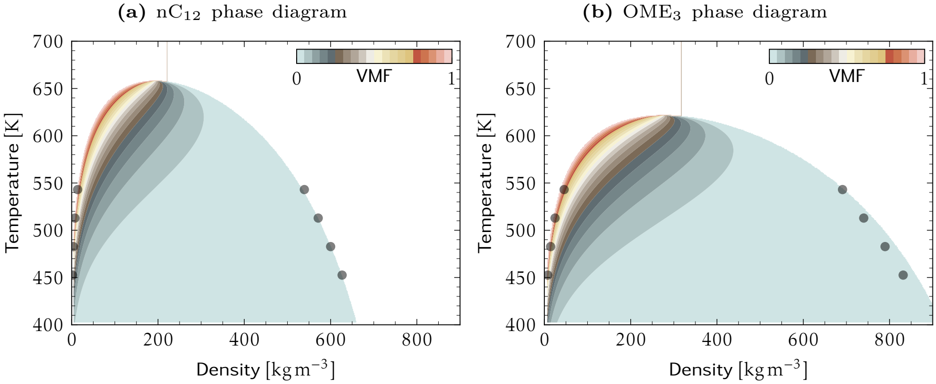

Figure 5.1.: Fuel phase diagrams using RKPR EOS showing vapor mole fraction (VMF) contours. The symbols show accurate reference data from Lemmon and Huber [97] for nC_{12} and from Kulkarni *et al.* [154] for OME_3.

with the utilized volumetric EOS as follows:

$$\bar{e} = \sum_{i=1}^{N} X_i \bar{h}_i^\circ - \mathcal{R}T + (a - T\partial a/\partial T)/[(\delta_2 - \delta_1)b] \ln[(\bar{\vartheta} + \delta_1 b)/(\bar{\vartheta} + \delta_2 b)], \quad (5.11)$$

with $\bar{e} \equiv e/W$ being the molar specific internal energy. The first two terms account for the absolute internal energy of the mixture at the actual temperature but at the (low) standard pressure, and the last term accounts for the internal energy change along an isothermal thermodynamic path from the standard reference pressure to the actual pressure. The molar specific enthalpy $\bar{h}_i^\circ$ of pure species i at the standard pressure (including the formation enthalpy) can be calculated using so-called NASA polynomials:

$$\begin{aligned} \bar{h}_i^\circ/\mathcal{R} = & - a_{i,1}T^{-1} + a_{i,2}\ln T + a_{i,3}T + a_{i,4}T^2/2 \dots \\ & + a_{i,5}T^3/3 + a_{i,6}T^4/4 + a_{i,7}T^5/5 + a_{i,8}, \end{aligned} \quad (5.12)$$

where $a_{i,1..8}$ are polynomial coefficients of the species i, and their values for the most common species are tabulated in Ref. [100].

TWO-PHASE CALCULATIONS

In two-phase regions, the molar composition of the liquid and vapor phases is typically calculated using the vector of K factors, which is defined as the ratio of the mole fractions in the vapor phase (X^V) to the liquid phase (X^L), such that:

$$X_i^L = X_i/[1 + \theta\,(K_i - 1)], \quad (5.13)$$

$$X_i^V = X_i^L K_i, \quad (5.14)$$

X_i is the overall mole fraction of component i in the mixture. The vapor mole fraction θ is determined by the Rachford-Rice equation

$$\sum_{i=1}^{N} X_i(K_i - 1)/[1 + \theta(K_i - 1)] = 0 \ , \tag{5.15}$$

The natural logarithm of the K-factors are a complicated function of the composition itself. One possible approach to estimate it initially is by using Wilson's equation, and then iteratively updating it via

$$\ln K_i = \ln \psi_i^V - \ln \psi_i^L, \tag{5.16}$$

where ψ is the specific volume function and can be calculated for the general cubic EOS as

$$\begin{aligned}\ln \psi_i = \ln(\bar{\vartheta} - b) - b_i/(\bar{\vartheta} - b) + a\bar{\vartheta}b_i/[(b\mathcal{R}T)(\bar{\vartheta} + \delta_1 b)(\bar{\vartheta} + \delta_2 b)] \ldots \\ - (ab_i - 2b\varsigma_i)/[(\delta_1 - \delta_2)b^2\mathcal{R}T] \ln[(\bar{\vartheta} + \delta_1 b)/(\bar{\vartheta} + \delta_2 b)],\end{aligned} \tag{5.17}$$

with $\varsigma_i \equiv \sum_{j=1}^{N} X_j(1 - k_{ij})\sqrt{a_i a_j}$. In addition to the thermal and mechanical phase equilibrium conditions, two more constraints are required for the unique determination of T and $\bar{\vartheta}$ of each phase. As we solve the fully conservative form of the compressible Navier-Stokes equations, that is, transport equations for energy and density, isoenergetic-isochoric phase-splitting calculations, also known as UV-flash calculations, must be performed. The two additional constraints for UV-flash calculations are

$$\bar{\vartheta} = (1 - \theta)\bar{\vartheta}^L + \theta\bar{\vartheta}^V, \tag{5.18}$$

$$\bar{e} = (1 - \theta)\bar{e}^L + \theta\bar{e}^V. \tag{5.19}$$

To iteratively solve the phase-splitting equations outlined above, we utilize the method of Fathi and Hickel [51], which performs rapid UV-flash calculations robustly via Newton iterations with the exact Jacobian based on an effective reduction method. We note that tabulation methods are a suitable alternative for non-reacting flows. However, when the number of species is large, both memory requirements and table query time grow unfavorably, while the cost of the Fathi-Hickel reduction method remains low and essentially independent of the number of species. For a comprehensive review and practical implementation guidelines, the readers are referred to the original article [51].

5.3.3. MULTIPHASE TRANSPORT PROPERTIES

Thermal conductivity and dynamic viscosity of liquid and gaseous fluids at high pressures can be estimated using the correlations of Chung *et al.* [116]. Based on the Chung method, a transport property $\phi \in \{\lambda, \mu\}$ is a complex function of temperature, specific molar volume, molecular weight, acentric factor ω, critical molar specific volume, and critical temperature:

$$\phi = f(T, \bar{\vartheta}, W, T_c, \bar{\vartheta}_c, \Omega). \tag{5.20}$$

Chung *et al.* [116] also explain how to estimate the molecular weight, critical temperature, critical molar specific volume, and acentric factor for a mixture with a certain composition. Here, it is important to emphasize that the fundamental assumption in this context is that the mixture constitutes a solitary (stable) phase. Hence, it would be questionable to calculate the transport properties of a two-phase mixture using these correlations directly [120].

A structural model can be used to calculate the transport property of a mixture comprising two phases. As described in Ref. [120], this can be achieved by performing separate Chung calculations for the saturated liquid and vapor phases. Assuming that the vapor and liquid phases are randomly distributed within the finite-volume cells, the transport property of the mixture are computed using the effective medium theory (EMT) model [121]

$$(1-\Theta)(\phi^L - \phi)/(\phi^L + 2\phi) + \Theta(\phi^V - \phi)/(\phi^V + 2\phi) = 0, \tag{5.21}$$

with $\Theta \equiv \theta\bar{\vartheta}^V/[\theta\bar{\vartheta}^V + (1-\theta)\bar{\vartheta}^L]$ being the volume fraction of the vapor phase. The EMT model can evaluate transport properties without nonphysical oscillations or underestimations for thermal conductivity or dynamic viscosity.

5.3.4. COMBUSTION MODELING

Although there are many reaction mechanisms for the combustion of pure OME_3 or pure nC_{12} with air, no suitable reduced mechanism is available for their mixture. This section explains how we have developed a reduced mechanism through a decoupling methodology to cover this gap. Then, we describe our novel transcritical combustion model using MT-based real-fluid flamelet simulations in the context of the transient counterflow model (TCM).

REACTION MECHANISM

Since comprehensive reaction mechanisms of heavy fuels are usually inaccessible or too complex for direct application, the use of a suitable reduced reaction mechanism is inevitable. For our flamelet calculations in this study, we derived a reduced chemical mechanism through a decoupling methodology in which the main oxidation path of the fuels is integrated with an effective reduced C_2-C_3 mechanism and a detailed $H_2/CO/C_1$ mechanism. For the pressurized environment of internal combustion engines, Lapointe, Zhang, and McNenly [130] used this methodology and proposed an optimized reduced mechanism consisting of 65 species and 363 reactions for the oxidation of pure nC_{12}. To study blended fuels, we have added the main OME_3 oxidation pathway of Lin *et al.* [139] to the original Lapointe mechanism. The final hybrid mechanism used here in this study consists of 76 species and 380 reactions. The mechanism is provided as supplementary material with this article in both Cantera and Chemkin formats.

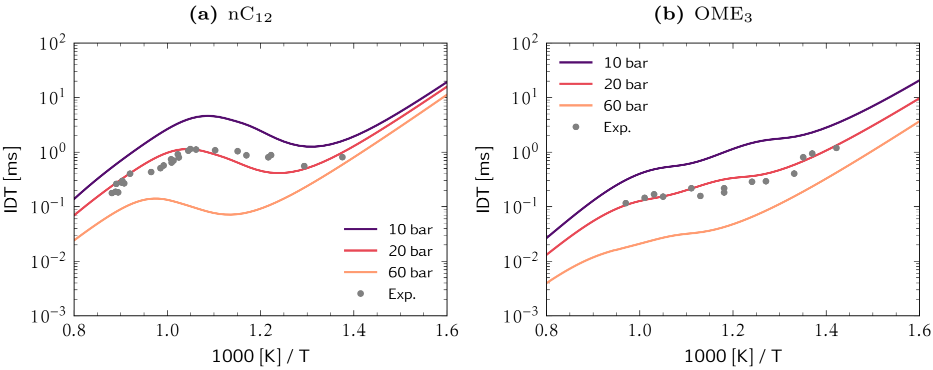

Figure 5.2.: Comparison of ignition delay time (IDT) of the stoichiometric air-fuel mixture calculated using the proposed hybrid mechanism (solid line) at various pressures with experimental measurements (scatter) at 20 bar [129, 156].

Figure 5.2 illustrates the prediction of the ignition delay time (IDT) for the stoichiometric mixture of nC_{12} and OME_3 with air as the oxidizer via the proposed reaction mechanism. Here, the IDT is defined as the time at which the combustible mixture experiences a temperature rise of 400 K. The predictions based on the hybrid mechanism agree very well with those reported for experiments at a pressure of 20 bar [129, 156]. For both fuels, the figure additionally shows the decrease in IDT due to the increase in pressure.

Transient Counterflow Model

The main idea behind any flamelet-based combustion model is that turbulent eddies only distort the shape of the flame, while the inner structure of the flame remains laminar. This means that we can solve a set of laminar cases separately with detailed chemistry under conditions similar to those under the target flame and retrieve the required thermochemistry data of the main (turbulent) reacting flow using a tabulation method. To look up data, one can use a few controlling parameters representing the simulated laminar flame behavior. Typically, the control parameters that construct the manifold are a mixture fraction, indicating the state of mixing between fuel and oxidizer streams, and a progress variable that represents the degree of conversion to final products [157, 158].

Counterflow flames are widely used to generate the flamelet database. For transcritical pressures, the configuration involves the injection of a liquid- or liquid-like fuel and a gaseous- or gaseous-like oxidizer in opposite directions, resulting in the formation of a reaction zone near the stagnation plane. The governing equations of unsteady transcritical counterflow flames along the axis of symmetry can be expressed as:

$$\partial_t \rho + \partial_x(\rho u) = -2\rho\mathcal{K}, \tag{5.22}$$

$$\rho\partial_t Y_k + \rho u \partial_x Y_k = -\partial_x \mathcal{J}_k + \dot{\omega}_k, \tag{5.23}$$

$$\rho\partial_t \mathcal{K} + \rho u \partial_x \mathcal{K} = \partial_x(\mu \partial_x \mathcal{K}) - \rho\mathcal{K}^2 + \rho_\infty a_\infty^2, \tag{5.24}$$

$$\rho c_p \partial_t T + \rho u c_p \partial_x T = \partial_x(\lambda \partial_x T) - \mathcal{J}_k \partial_x h_k - h_k \dot{\omega}_k. \tag{5.25}$$

where c_p is the heat capacity of the mixture. Y_k, h_k, $\mathcal{J}_k$, and $\dot{\omega}_k$ are the mass fraction, the partial enthalpy, the diffusion mass flux, and the net production rate of the species $k = 1, 2, \dots, N$ with N being the total number of species. In the equation of the stretch rate $\mathcal{K}$, the subscript ∞ denotes the reference boundary used to evaluate the pressure curvature $\rho_\infty a_\infty^2$ where a_∞ is the applied strain rate. To solve these stiffly coupled equations, we use our in-house unsteady real-fluid flamelet solver, developed specifically for this purpose; further details are previously presented in Chapter 3.

The unsteady counterflow configuration required for the TCM of the target sprays is as follows. The operating pressure is 60 bar. The fuel stream at 363 K and the oxidizer stream at 1000 K are injected into a computational domain from opposite directions. This domain is initialized using the steady-state solution of the corresponding inert case. The computational domain extends from −3 mm to 3 mm and is discretized into 444 points. A uniform grid spacing of 0.002 mm is applied primarily in the center region between −0.01 mm and 0.01 mm. Outside of the central region, the grid spacing gradually increases to 0.1 mm at both ends of the domain.

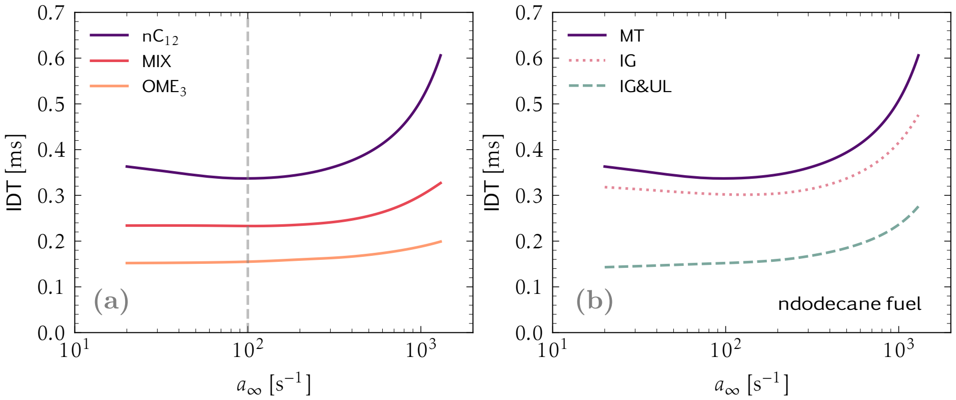

Figure 5.3.: Ignition delay time (IDT) as a function of applied strain rate at the oxidizer side a_∞ obtained from unsteady transcritical flamelet calculations using the proposed hybrid mechanism.

Figure 5.3a examines the effect of the strain rate on the IDT for three different fuels using MT-based TCM calculations. The results suggest that a strain rate of $100\,\mathrm{s}^{-1}$, which is very close to the one corresponding to the minimum IDT, is a suitable choice to accurately capture the initial stages of combustion in the target sprays. Although accounting for varying strain rates in generating the flamelet database would be more accurate, using a single representative strain rate is deemed acceptable for practical simulation purposes [159].

To accurately predict the autoignition transition, it is essential to include real-fluid thermochemical and transport effects in transcritical TCM computations. Figure 5.3b shows IDT variations of n-dodecane against the applied strain rate at the oxidizer side in the TCM using different models: MT (real-gas effects with transcritical phase separation), IG (ideal-gas assumption), and IG&UL (IG with unitary Lewis number). The results strongly suggest that the unitary Lewis assumption should be avoided because of its significant impact on IDT predictions. While both MT and IG models show a similar trend, the ideal gas model clearly underestimates the ignition time.

To obtain the low-dimensional manifold, we solve Eqs. (5.22)-(5.25) along with the two transport equations 5.5 and 5.6 for the mixture fraction and the reaction progress variable. In this study, Lewis numbers of the control parameters are set to $\mathrm{Le}_{\mathcal{Z}} = 1$ and $\mathrm{Le}_{\mathcal{C}} = 2$. The source term of the progress variable $\dot{\omega}_{\mathcal{C}}$ is calculated according to the oxidizer-based progress variable definition of Hadadpour *et al.* [46]:

$$\mathcal{C} = Y_{\mathrm{N}_2}(Y^0_{\mathrm{O}_2}/Y^0_{\mathrm{N}_2}) - Y_{\mathrm{O}_2}. \tag{5.26}$$

This equation subtracts the actual amount of oxygen from that in case there is no reaction. In this way, we can determine how much oxygen has been consumed locally and thus how much progress has been made in the reaction. With the mechanism used in this study, N_2 is an inert gas. Therefore, the source term of the progress variable is simply the oxygen consumption $-\dot{\omega}_{\mathrm{O}_2}$.

Due to the strong effects of differential diffusion, the governing equation for the mixture fraction, computed by tracking the elements of the fuel composition using Bilger's definition [160], becomes very complex. To effectively resolve this issue, we solved an additional transport equation along with our flamelet governing equations for the mixture fraction [161]. The utilized mixture fraction equals the Bilger mixture fraction only when all species have unitary Lewis numbers. The amount of difference between them shows the strength of the differential diffusion effect.

Figure 5.4 shows the difference between the mixture fraction based on the transport equation utilized in this study and the one computed through post-processing based on Bilger's definition for the target sprays. Due to the unsteady nature of the ignition process, the profiles are not constant, and the shaded area highlights this variation. The deviation is significant from the initial steady-state inert mixing condition to the final ignited flame, underscoring the important role of differential diffusion at transcritical pressures. It should be emphasized that the stoichiometric value of the utilized conserved scalar mixture fraction is not constant nor equal to the Bilger value.

When using unsteady flamelets to build the FGM, the selected progress variable must have a monotonic variation over time from the unburned to the burned

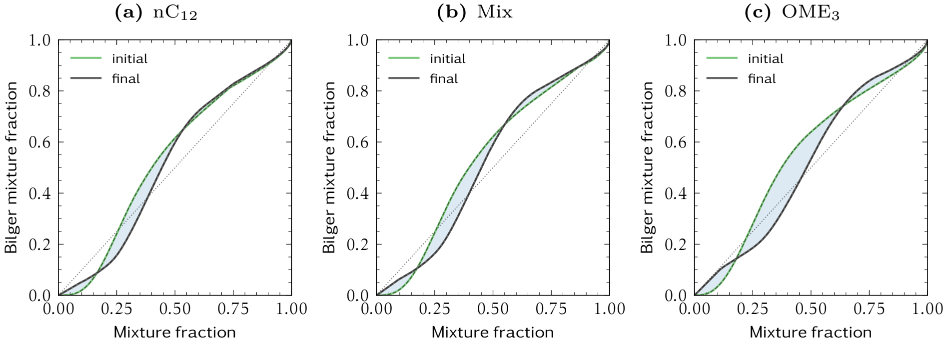

Figure 5.4.: Deviation of the mixture fraction from Bilger's definition for the unsteady transcritical flamelet calculation (strain rate $100\,\mathrm{s}^{-1}$). The shaded region illustrates the temporal variations from the initial to the final states.

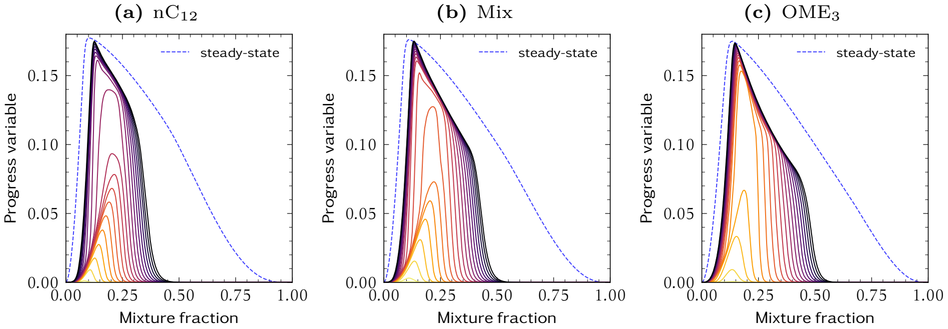

Figure 5.5.: Temporal evolution of the progress variable as a function of mixture fraction from the unsteady transcritical flamelet calculation (strain rate $100\,\mathrm{s}^{-1}$). The blue dashed line marks the steady-state condition. Solid lines of the same color represent transient profiles at the same time.

states [162]. This results in a one-to-one mapping of each unique point in the (x, t) domain to a unique point in the 2D output codomain $(\mathcal{Z}, \mathcal{C})$, with no two different points in the domain mapping to the same point in the codomain. Figure 5.5 demonstrates the monotonic characteristic for our oxidizer-based progress variable by showing the temporal profiles of $\mathcal{C}$ for three fuel types used to study transcritical spray-A. In all cases, there is a monotonic increase in $\mathcal{C}$ with time, which means that it is suitable to be used directly without further optimization [163].

Figure 5.6 presents the temporal evolution of the temperature profile in the mixture fraction space for different fuels. The colored lines are plotted based on a constant time interval. The figure illustrates that the most reactive mixture fraction indicated by the peak temperature follows a similar trend for different fuels. It initially shifts toward the rich side before returning to the steady-state value. However, the rate of temperature change increases when OME_3 is added

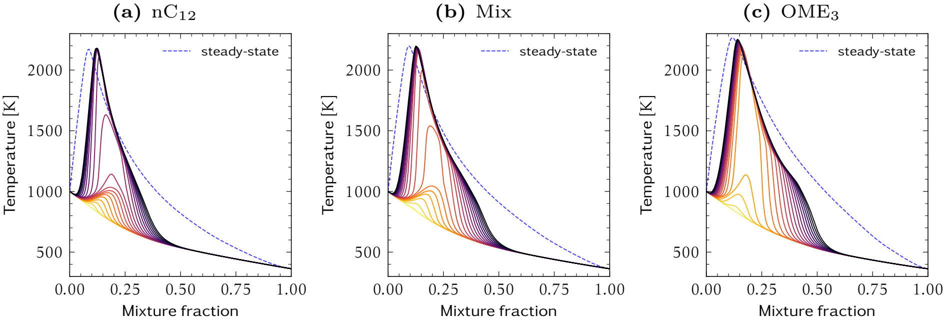

Figure 5.6.: Temporal evolution of the temperature as a function of mixture fraction from the unsteady transcritical flamelet calculation (strain rate $100\,\mathrm{s}^{-1}$). The blue dashed line marks the steady-state condition. Solid lines of the same color represent transient profiles at the same time.

to nC_{12} fuel. Furthermore, as indicated by the steady-state dashed lines, adding OME_3 causes an increase in maximum temperature. The latter indicates a higher heat release rate for OME_3 than for the other fuels.

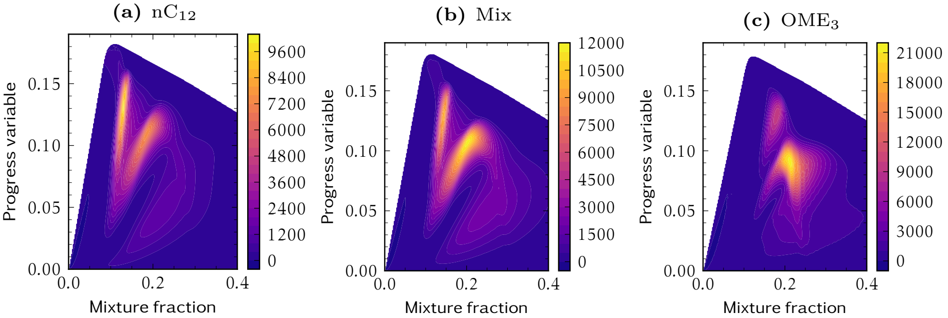

Figure 5.7.: Progress variable source term $\dot{\omega}_C$ as a function of the mixture fraction and progress variable generated based on the transient counterflow model.

Figure 5.7 shows the source term of the progress variable in the mapped space of the mixture fraction and the progress variable. The source term of the progress variable, which directly influences the increase in the progress variable, plays a critical role in determining the predicted ignition delay in the LES of spray combustion. This figure displays a significant increase in the source term with higher concentrations of OME_3, suggesting an earlier and more rapid ignition, consistent with the previous trends observed in flamelet IDTs.

Figure 5.8 presents the compressibility factor as a function of the mixture fraction, illustrating the deviation from the ideal gas law from the initial point of inert mixing to the steady-state burnt condition. As shown in the figure, the deviation from ideal gas behavior is evident from the initial to the final stage. This

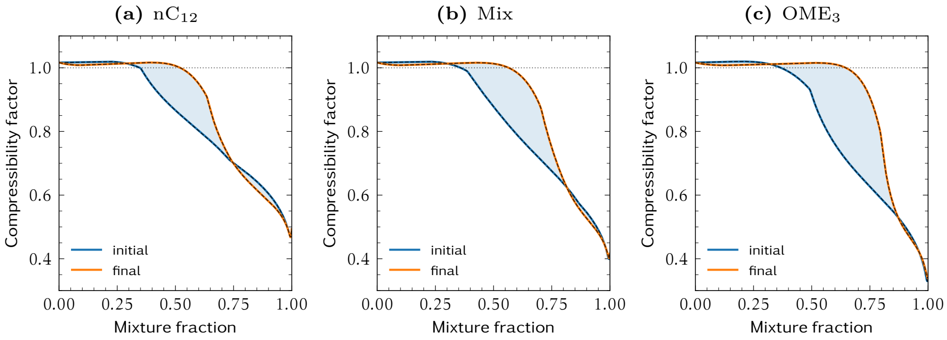

Figure 5.8.: Compressibility factor as a function of the mixture fraction computed for the unsteady transcritical flamelet calculation (strain rate $100\,\mathrm{s}^{-1}$). The shaded region illustrates the temporal variations from the initial to the final states.

deviation is more pronounced for the OME_3 fuel than for nC_{12}.

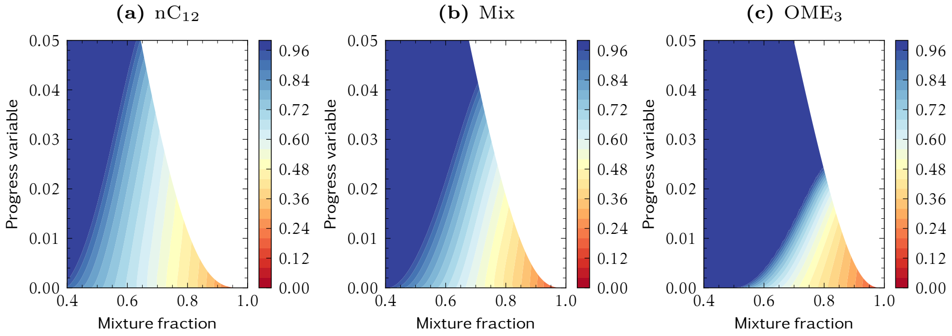

Figure 5.9.: Vapor mole fraction (VMF) θ as a function of the mixture fraction and progress variable generated based on the transient counterflow model.

Figure 5.9 highlights the importance of modeling transcritical phase separation in flamelet calculations. In this figure, the two-phase region is depicted using the contours of the vapor mole fraction (VMF) for all three cases. We can see that the two-phase region in the mixture fraction – progress variable space is smaller for the OME_3 fuel compared to nC_{12}. Although in the target LES simulations, we only use the mass fractions from these flamelets and perform multiphase thermodynamics calculations based on the density and internal energy of the flow to determine whether the mixture is in a two-phase or single-phase state, the tabulated VLE information from flamelets can significantly accelerate the iterative thermodynamic calculations by providing a suitable initial guess.

5.3.5. FLOW-TURBULENCE INTERACTIONS

Large eddy simulation (LES) offers a detailed representation of the large scales of fluid motion that dominate the mechanical energy of turbulent flows. These large scales are governed by a coarse-grained or low-pass-filtered form of the Navier–Stokes equations in which the effects of the interactions between represented and unrepresented scales are included through appropriate subgrid-scale (SGS) modeling. In a finite-volume framework, the need for SGS modeling directly originates in the residual of the non-linear fluxes, that is, in the limited ability to represent the exact flux across cell faces with discrete reconstruction operators. Thus, turbulence modeling and numerical discretization are intrinsically linked. We use the LES method of Hickel, Egerer, and Larsson [94], which is based on a nonlinear, solution-adaptive flux reconstruction method and spectral turbulence theory. The method is well suited for applications across all Mach numbers and has been extensively verified and validated for reacting and non-reacting transcritical fuel injectors [72]. For simplicity of the computations and following common practice, we neglect SGS terms that arise from low-pass filtering the non-linear equations used to evaluate the properties of real fluids [35]. Furthermore, the interactions between SGS turbulence and combustion can be neglected in the context of ALDM with sufficiently fine spatial and temporal resolution, as shown in Ref. [75]. Since the same grid resolutions and turbulence modeling are used in this study, we opted not to include the variances of the progress variable and the mixture fraction, see Eguz *et al.* [45] for a detailed analysis of the effects of the turbulence-combustion interaction in the diesel spray context.

5.4. SIMULATION SETUP

5.4.1. MULTI-BLOCK STRUCTURED GRID

All simulations have been carried out using a multi-block structured grid generated in a rectangular cubic domain with a size of 84 × 42 × 42 mm. We utilize the INCA flow solver (`https://inca.cfd`) with static zonal mesh refinement within a user-defined region of interest [75]. This region is defined as a 10° cone encompassing the injected jet. The level of refinement within this cone is strategically determined by the distance from the injector nozzle, with specific resolution steps at axial locations 60, 37, 23, 14, 9 and 5.5mm from the injector nozzle. The resulting multi-block structured grid comprises 2864 blocks and 12.7×10^6 cells distributed in seven resolution levels (L1 to L7). Approximately 40 % of the cells are concentrated on the finest level L7, with $\Delta y_{\min} = \Delta z_{\min} \simeq 10.25\,\mu\text{m}$ and $\Delta x_{\min} = 2\Delta y_{\min}$ near the nozzle region.

5.4.2. BOUNDARY CONDITIONS

A transient inflow velocity boundary condition is implemented in the exit plane of the fuel injector. For all types of fuel cases, the inflow velocity is calculated to provide the same amount of momentum as in the standard case of ECN Spray-A. Similar to our previous study [113], we first calculated the mass flow rate using the clean mobility and thermofluids (CMT) virtual injection rate generator (`https://www.cmt.upv.es`), with input parameters that match the experimental conditions and fuel densities calculated using the RKPR EOS at the injection pressure and temperature of 60 bar and 363 K. Then, we computed the required inflow velocity using the fuel density. Figure 5.10 illustrates the transient injection velocity generated for all fuel cases. The transient velocity profile is used in a subsonic inlet boundary condition without adding any artificial turbulent fluctuations. Fluctuations induced by shear and hydrodynamic pressure are expected to be strong enough to create turbulence almost instantaneously.

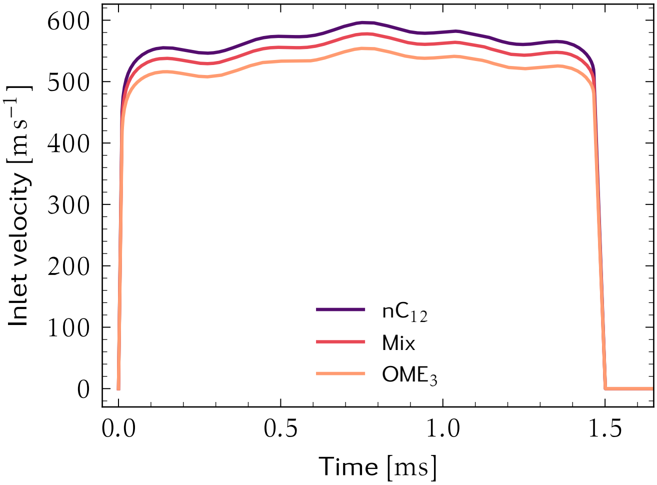

Figure 5.10.: Transient injection velocity profile for Spray-A test cases using RKPR EOS.

Subsonic outflow boundary conditions are imposed on the opposite end of the domain, where a consistent static pressure of 60 bar is specified as the Dirichlet condition, and the remaining flow variables are extrapolated from the internal domain. Adiabatic no-slip conditions are enforced on all other boundaries of the computation domain.

5.4.3. Tabulated Chemistry

In the present combustion model, the mass fractions of the species are determined by the mixture fraction and the progress variable. For this purpose, a two-dimensional manifold is created for each fuel, using 256 x 1024 points to represent the table space based on the mixture fraction and the dimensionless progress variable. The dimensionless progress variable is computed via $\mathcal{C}_s \equiv \mathcal{C}/\mathcal{C}_b(\mathcal{Z})$. The subscript b denotes the values obtained from the final burnt state. The blue dotted line in Fig. 5.5, shows the mixture fraction functionality of $\mathcal{C}_b(\mathcal{Z})$.

5.4.4. FLOW SOLVER

All numerical models are implemented in our INCA flow solver (`https://inca.cfd`) with the same discretization techniques used in our previous work [75]. The governing equations are spatially discretized using a conservative finite-volume scheme. A second-order central difference method is utilized for viscous terms and ALDM for inviscid fluxes [94]. The van Albada limiter prevents spurious oscillations at sharp density gradients for mass- and energy-flux reconstruction.

A second-order Strang splitting method separates the chemical reactions from the advection and diffusion processes. This separation is required because the VLE calculations are only valid for non-reacting mixtures. The splitting approach comprises three main stages: Initially, the solution is advanced by incorporating solely the source term of the progress variable in a half-time step. For this step, we used the explicit sixth-order Runge-Kutta technique developed by Verner [164]. Subsequently, the updated solution is set as the initial state for the progress variable, which is used to determine the new composition from the lookup table and update the necessary thermo-transport properties for a complete advection and diffusion time step. For the non-reacting step, we utilized the explicit third-order strong stability-preserving Runge-Kutta method proposed by Gottlieb, Shu, and Tadmor [134]. Finally, the solution is further advanced with the second half of the time step similar to the initial one. The time-step size is dynamically adjusted by the Courant-Friedrichs-Lewy stability criterion with a unitary CFL number.

5.5. NUMERICAL RESULTS

This section addresses two primary objectives. First, it aims to validate the proposed multiphase flamelet-based solver for accurately modeling transcritical combustion processes, emphasizing its capacity to capture key spray characteristics, including vaporization behavior and ignition dynamics. Second, we present a comprehensive comparison of the spray-A performance for pure nC_{12}, pure OME_3, and their mixture under identical transcritical conditions. The analysis includes a detailed examination of transcritical vaporization phenomena, highlighting the differential evaporation rates of fuel components and the interaction between the liquid fuel and the surrounding environment. We also investigate ignition characteristics, focusing on ignition times and penetration lengths, as well as the evolution of various combustion zones, including two-phase, cool-flame, and high-temperature regions. Finally, the study evaluates the formation of soot using acetylene (C_2H_2) as a key precursor, offering insight into the impact of fuel composition on emissions.

5.5.1. OVERVIEW AND TEMPORAL EVOLUTION

The temporal evolution of the reacting Spray-A with three different fuels is illustrated in Fig. 5.11, displaying instantaneous snapshots of the solution. Here, the two-phase region is represented by the liquid volume fraction (LVF) contours, shown in green, which also indicate the predicted distribution of the liquid injectant in the transcritical combustion chamber. With regard to ignition delay time (IDT),

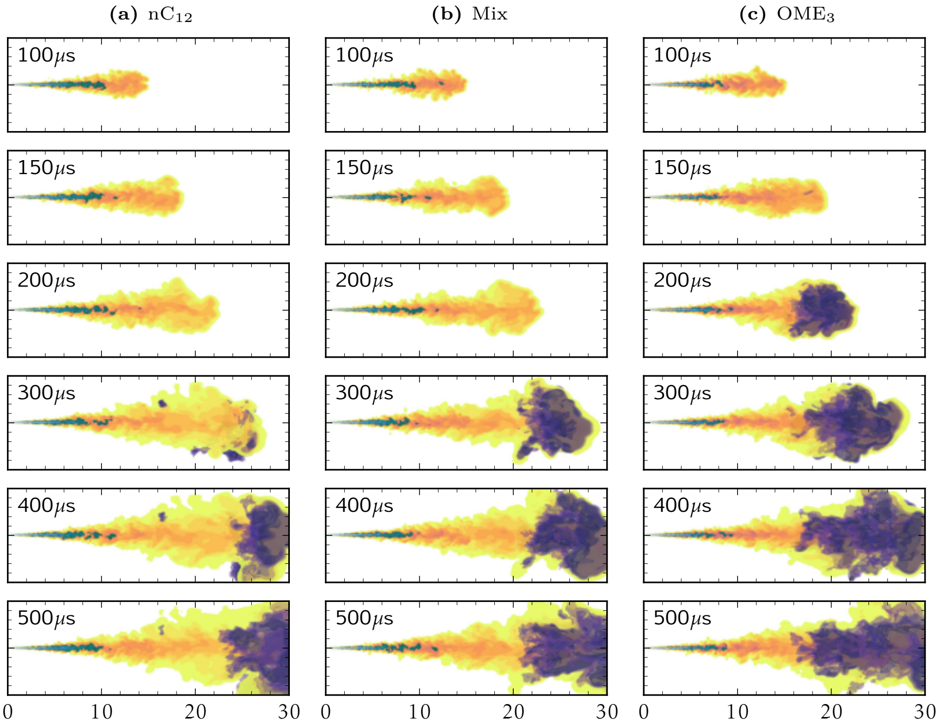

Figure 5.11.: Time sequence snapshots of reacting spray-A with different fuels. The light background contours display the mixture fraction, overlaid with the green contours of liquid volume fraction in the two-phase region. The deep purple area shows the temperature isosurface at 1800 K.

a good agreement is observed between the available experimental data from Pastor *et al.* [153] (CMT) and the results of LES in the current work, using the reduced hybrid reaction mechanism within the flamelet modeling framework based on MT. These ignition times are summarized in Table 5.2 and are defined based on a temperature increase of 400 K above the initial ambient temperature.

The ignition process across all fuel cases shows similar behavior, where around the ignition time, low-temperature reactions are activated in a substantial portion of the vaporized fuel. The iso-temperature surface at 1800 K is used to highlight the most reactive regions (Fig. 5.11, deep purple). The transition to high-temperature ignition is characterized by a rapid, volumetric expansion, with an abrupt radial spread of the reacting jet observed in proximity to the flame front.

Figure 5.12 presents the temporal evolution of the liquid penetration length (LPL) and the vapor penetration length (VPL) for the present simulations alongside the experimental measurements [153]. For our LES, LPL and VPL are defined as the maximum axial positions where the liquid volume fraction (LVF) is 5% and the mixture fraction is 1%, respectively. The results demonstrate excellent

Table 5.2.: Ignition delay time predicted by the available experiments [153] and current work simulations.

	nC_{12}	Mix	OME_3
IDT (LES)	242µs	214µs	149µs
IDT (EXP)	294µs	-	194µs

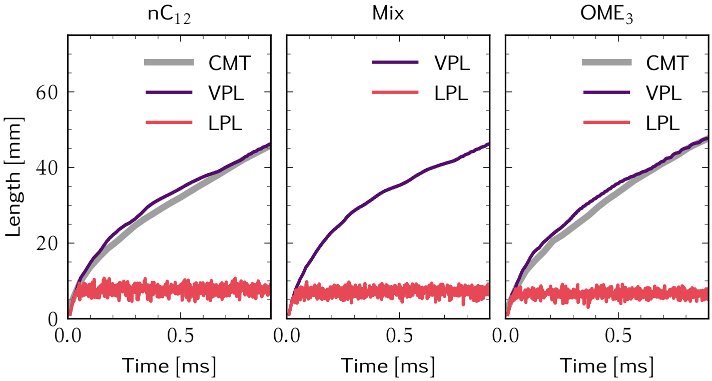

Figure 5.12.: Comparison between CMT experiments [153] and current LES for the vapor penetration length (VPL) and liquid penetration length (LPL) for all fuels. The uncertainty of the measurements is expressed by the line thickness.

agreement between the LES and the experimental data for both LPL and VPL. It should be noted that experimental data for the mixed fuel case are not available and for pure OME_3, data from OMEx, a mixture of OME_3 and OME_4, were used as reference. The LPL values, which are listed in Table 5.3, show close agreement with Sandia experimental data reported for the nC_{12} case. In line with the comparative study of Xuan *et al.* [165], our results demonstrate that the liquid penetration length is indeed shorter for OME_3 than for nC_{12}. This supports the conclusion that OME_3's lower boiling point is more influential on the vaporization length than its higher latent heat of vaporization or density.

Table 5.3.: Liquid penetration length predicted by the available experiment [110] and current work simulations. The unit of numbers is mm.

	nC_{12}	Mix	OME_3
LPL (LES)	9.8	8.8	7.9
LPL (EXP)	9.4	-	-

5.5.2. IGNITION ZONES

Figure 5.13 illustrates the three main zones in transcritical reacting sprays: (1) the two-phase region, influenced by fuel properties and injection conditions, (2) the cool flame region marked by CH_2O formation, indicating low-temperature reactions

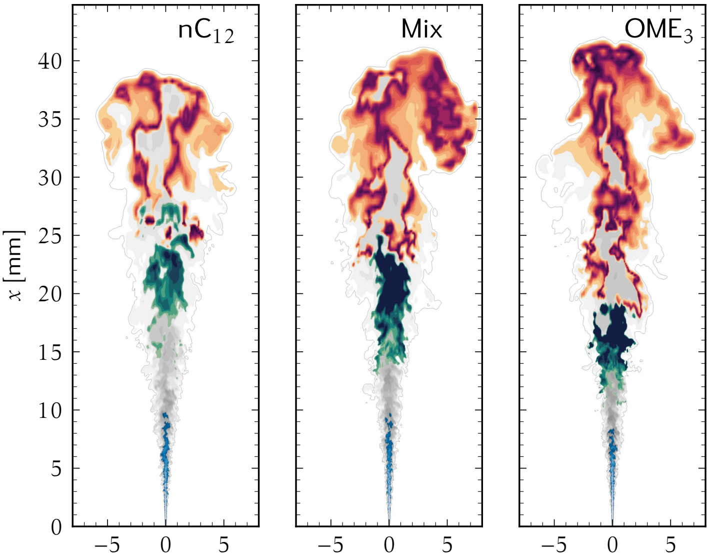

Figure 5.13.: Comparison of two-phase region (in blue), hot and cold flame regions marked by OH (in red) and CH_2O (in green) distribution for different fuels at 670 µs after the fuel injection.

and first-stage ignition, and (3) the high-temperature reaction zone, highlighted by OH radicals, representing second-stage ignition and complete combustion.

In general, the addition of OME_3 to the n-dodecane fuel results in several significant changes in the three characteristic zones. The length of the two-phase region is reduced. The lift-off length of the cool flame also decreases, which indicates a shorter distance from the nozzle where ignition initiates. Moreover, the overall length of the cool flame region also decreases, leading to the formation of the hot flame in closer proximity to the nozzle, with an extended flame length; see Table 5.4. Another notable effect of adding OME_3 is the disappearance of the overlap between the cool flame and hot flame regions, which can be attributed to differences in their stoichiometric and most ignitable mixture fraction. These findings align with experimental results reported by Pastor *et al.* [153] regarding the lift-off length (LOL) of Spray-A under similar conditions. They observed a 20 % reduction in LOL for oxygenated fuel OMEx compared to n-dodecane. The measured LOL values were 13.7 mm for OMEx and 16.6 mm for n-dodecane, respectively.

Table 5.4.: Lift-off length of hot and cold spray flames. Numbers are in mm

	nC_{12}	Mix	OME_3
LOL (Hot Flame)	24.6	22.3	16.1
LOL (Cold Flame)	15.2	13.3	10.4

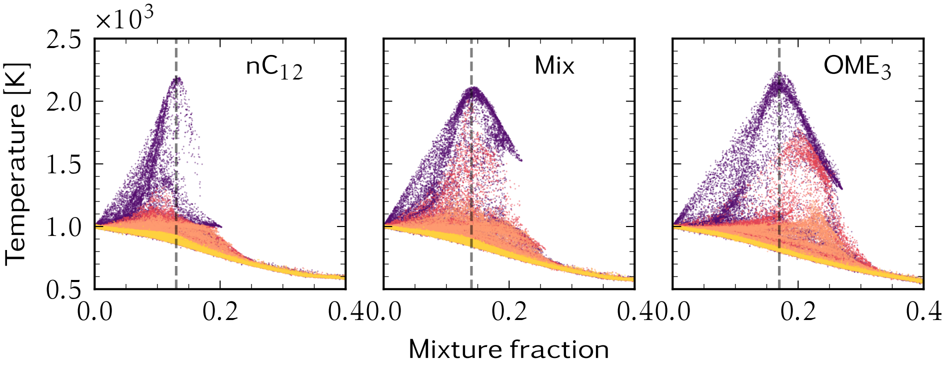

Figure 5.14.: Mixture fraction-temperature map for different fuel sprays at 0.5 (yellow), 1.0 (orange), 1.1 (red), and 1.5 (purple) times of the ignition time.

The auto-ignition process is depicted in Fig. 5.14 through global scatter plots of temperature within mixture fraction space at various time instants (0.5, 1.0, 1.1, and 1.5 times the ignition time). The figure illustrates that the first and second stages of the ignition for pure OME$_3$ fuel start at regions with lower oxygen concentration (i.e., higher mixture fraction) compared to pure n-dodecane. In the case of mixed fuel, the behavior falls between the two pure fuel cases, reflecting characteristics of both fuels during the ignition process.

5.5.3. TRANSCRITICAL VAPORIZATION

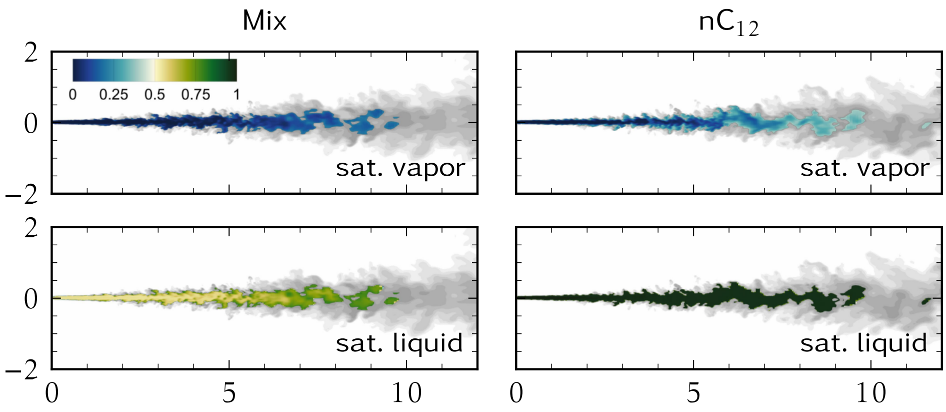

Figure 5.15.: Comparison of transcritical evaporation of n-dodecane for pure nC$_{12}$ and mixed fuel (nC$_{12}$/OME$_3$) cases. Contours show mass fraction of n-dodecane in the two-phase region for the saturated vapor and the saturated liquid.

Figure 5.15 compares the transcritical evaporation of n-dodecane for pure n-dodecane and mixed fuel scenarios. In both cases, the saturated vapor of n-dodecane becomes progressively richer as it travels through the combustion chamber, driven by the increased evaporation of the liquid phase. For pure n-dodecane, the saturated liquid jet undergoes a negligible dissolution of the surrounding ambient gases (less than 3%), resulting in a relatively constant composition from the inlet to the tip of the liquid jet. In contrast, for the mixed fuel scenario, the n-dodecane mass fraction within the liquid jet increases from the initial 50% at the inlet to about 75% at the jet tip. This behavior is directly attributed to the differential evaporation rates of OME_3 and nC_{12} species. OME_3 has a higher volatility than nC_{12}, resulting in the enrichment of the saturated liquid phase in n-dodecane as the jet advances.

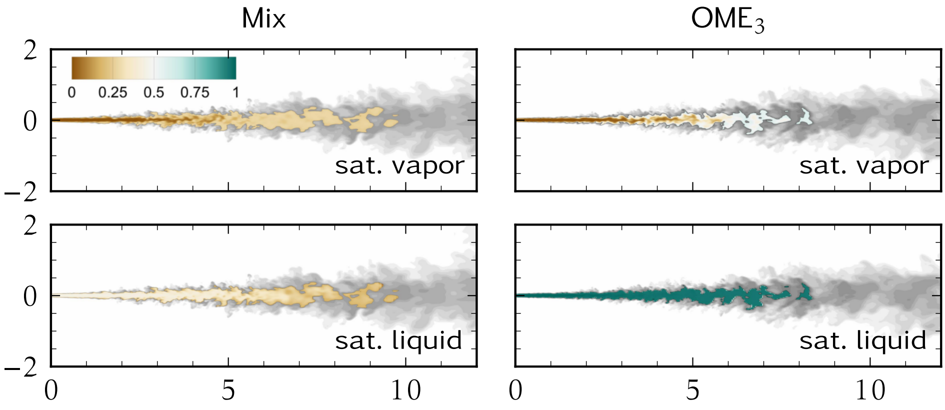

Figure 5.16.: Comparison of transcritical evaporation of OME_3 for pure OME_3 and mixed fuel (nC_{12}/OME_3) cases. Contours show mass fraction of OME_3 in the two-phase region for the saturated vapor and the saturated liquid.

Figure 5.16 illustrates the transcritical evaporation of OME_3 for two scenarios: a mixed fuel (n-dodecane/OME_3) and pure OME_3. In both cases, the saturated vapor becomes progressively enriched in OME_3 as it penetrates further into the chamber due to the heat absorption from the surroundings that drives the phase change from liquid to vapor. For pure OME_3, the liquid jet composition changes insignificantly from the nozzle to the jet tip, indicating that a negligible amount of ambient gas (less than 5%) dissolves into the liquid. However, in the mixed fuel case, the mass fraction of OME_3 in the liquid phase decreases from the initial 50% at the nozzle to about 25% at the jet tip, suggesting that OME_3 evaporates more rapidly compared to n-dodecane.

5.5.4. Soot formation

The present simulations do not include detailed models for the formation of soot particles; however, they represent key precursors in the formation of soot that directly contribute to the growth of soot particles during combustion. Figure 5.17 presents the contours of C_2H_2 (acetylene) for the developed flame at a distance

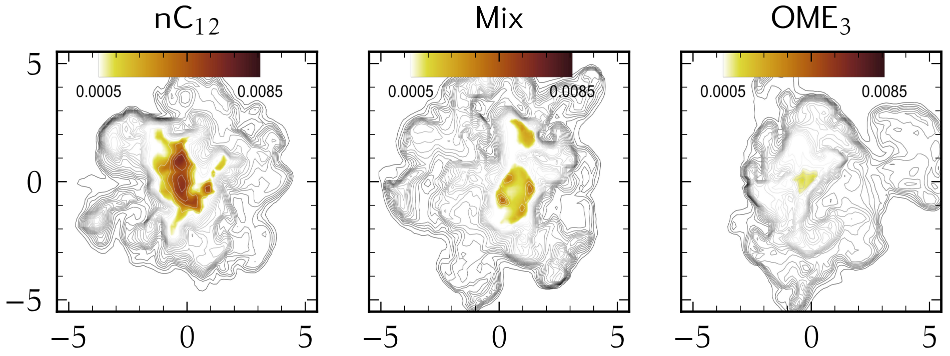

Figure 5.17.: Acetylene mass fraction contours on a plane normal to the axial direction at $x = 30\text{mm}$ and 670 µs after the start of the injection. The background shows temperature contour lines.

larger than the lift-off length (LOL) for all fuel cases. Due to the absence of C-C bonds, OME_3 burns almost soot-free, while the nC_{12} and Mix fuel cases show considerable concentrations of C_2H_2 within the core flame region, indicating a higher propensity to soot formation. As anticipated, the addition of OME_3 to nC_{12} can reduce the C_2H_2 levels; the maximum acetylene concentration observed for the mixed fuel is less than half of that for pure dodecane in this snapshot section.

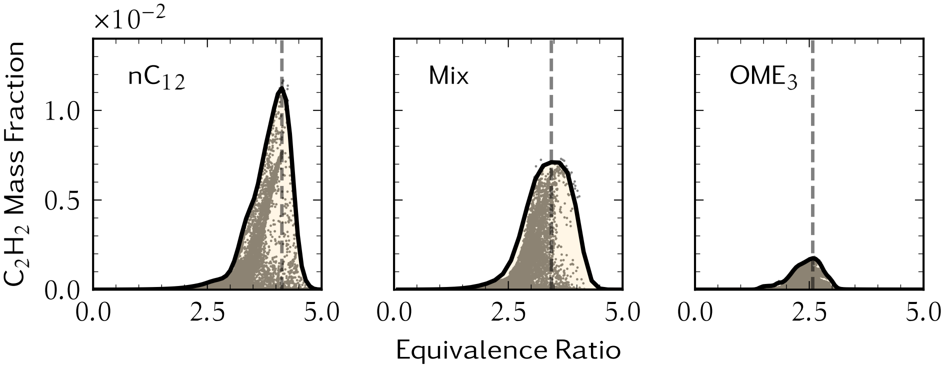

Figure 5.18.: Equivalence ratio-acetylene map for sprays with different fuels. The scatter points show data at 670 µs after the start of the injection. The solid lines show a Gaussian curve fit through the upper points. The dashed lines show the location of the peak of the fitted curves.

Figure 5.18 illustrates the global C_2H_2 mass fraction versus the local equivalence ratio for the three sprays. The LES results show that acetylene forms in equivalence ratios between 2.5 and 5.0 for the n-dodecane fuel. Pastor *et al.* [153] reported an upper limit of 5.5 in a similar context. For mixed fuel, acetylene forms between 2.0 and 4.5 and for OME_3, between 2.0 and 3.0. Peak values are marked with dashed lines in Fig. 5.18. The lower ϕ for peak values for the Mix and OME_3 cases are mainly related to their lower stoichiometric air-fuel ratios, which are 15.59 and 8.59, respectively, compared to 21.18 for nC_{12}. The figure confirms that the OME_3 spray flame can be expected to be nearly soot-free, but the two other flames create a noticeable amount of C_2H_2. For Spray-A with nC_{12} fuel, the amount of acetylene produced, $\int \rho Y_{C_2H_2} \mathrm{d}V$, is approximately 1.76×10^{-9} kg at 1000 µs after the start of the injection. This amount decreases by about 25 % for the mixed fuel, reaching approximately 1.29×10^{-9} kg at the same time. This modest reduction can be explained by considering the effect of the faster evaporation rate of OME_3, resulting in a rapid depletion of OME_3 in the fuel mixture and an initial enrichment of the remaining nC_{12}. This procedure shifts the combustion of n-dodecane to occur in a more fuel-rich environment, especially in regions with a higher mixture fraction, thereby lowering the local oxygen concentration available during the ignition phase. Lower oxygen availability at the start of combustion leads to increased production of C_2H_2. Lastly, we note that the same bulk strain is used in the generation of all chemistry tables. Consequently, the observed reduction is not related to flame straining, as presented by Bao *et al.* [159]; rather, it is directly a result of changes in fuel composition.

5.6. CONCLUSIONS

We have presented a new method for high-fidelity simulations of transcritical combustion using a real-fluid multiphase thermo-transport solver based on the LES-MT framework with a transcritical flamelet library. This model effectively combines detailed chemical kinetics with multiphase interactions in complex fuel sprays. Validation against experimental data for Spray-A with n-dodecane fueling confirms the accuracy of the LES-MT approach in predicting ignition delay time, vapor penetration length, and liquid penetration length under transcritical conditions.

LES-MT results indicate distinct differences in the behaviors of transcritical evaporation, ignition, and soot formation between the injection of pure n-dodecane, pure OME_3, and a nC_{12}– OME_3 fuel mixture. Adding OME_3 to nC_{12} shortens the two-phase region and reduces the lift-off length of the cool flame, resulting in earlier ignition. Although OME_3 shows an advantage in being nearly soot-free, the mixed fuel case shows a surprisingly modest reduction of soot formation due to fuel-rich conditions and reduced oxygen availability, driven by OME_3's faster evaporation. These findings, based on the proposed reduced hybrid reaction mechanism, underscore the need for further studies to fully understand the complex interactions in mixed fuels under varying conditions.

6

Conclusions

This dissertation set out to formulate accurate numerical models for high-fidelity simulations of transcritical combustion. Operating modern propulsion systems like rocket engines, gas turbines, and diesel engines under transcritical conditions offers opportunities for improved fuel efficiency and engine performance, but the complex physical phenomena, particularly the non-ideal behavior of fuel sprays under extreme pressures and the interaction between turbulent mixing, transritical phase-change, and chemical reactions, were poorly understood and hard to predict. Addressing this gap required developing advanced physical and numerical models that precisely account for the non-idealities of fluid mixtures and the challenges of transcritical vaporization and combustion. To achieve this, the research focused on four key objectives:

1. Developing a Robust and Rapid VLE Solver

Computationally efficient and reliable phase-splitting calculations aka vapor-liquid equilibrium (VLE) calculations are crucial for simulating transcritical multiphase flows, where millions of such calculations are needed at each time step. Chapter 2 introduced a new family of VLE algorithms for isothermal and non-isothermal conditions that formulate phase-equilibrium conditions in an effectively reduced space, independent of the number of components. These new algorithms are computationally efficient, robust, and fault-tolerant, offering quadratic convergence even near complex phase boundaries, significantly outperforming conventional techniques. This development provides an essential foundation for feasible high-fidelity simulations.

2. Extending the LES-MT Method to Reacting Flows

Building upon the established Multiphase Thermodynamics (MT) approach for non-reacting flows, Chapter 3 extended this framework to include reacting systems. The LES-MT method, which uses a diffuse interface approach with real-fluid equations of state and VLE calculations, was successfully applied to simulate reacting and non-reacting transcritical fuel sprays. Validation against experimental data for the ECN Spray-A benchmark showed excellent agreement for liquid and vapor penetration lengths, ignition delay time, and flame lift-off length. This method demonstrated superiority over traditional Lagrangian Particle Tracking (LPT) and Eulerian single-phase Dense-Gas (DG) approaches by accurately capturing transcritical phase separation and real-fluid effects like the high solubility of ambient gas in liquid fuel.

3. DEVELOPING A REAL-FLUID MULTIPHASE FLAMELET SOLVER

A detailed understanding of transcritical flames requires accurate simulation of laminar flame structures under relevant high-pressure, multiphase conditions. Chapter 4 presented a comprehensive numerical framework for unsteady flamelet calculations that includes precise modeling of real-fluid thermo-transport and chemical properties. This involved using the RKPR EOS coupled with VLE for thermodynamic properties, the Chung method with an Effective Medium Theory (EMT) mixing rule for transport properties in two-phase regions, and the Dixon-Lewis diffusion formula with a thermodynamic correction factor (derived consistently with the EOS and extended for multiphase regions) for diffusion driving forces. Simulations of transcritical counterflow diffusion flames highlighted the essential role of accurate real-fluid models; neglecting phase separation or using ideal-gas assumptions led to significant errors in predicting unsteady ignition behavior. The framework provides a tool for detailed analysis of transcritical flame physics.

4. USING THE LES-MT METHOD WITH TABULATED CHEMISTRY

To incorporate detailed chemical kinetics into computationally feasible large-scale simulations, Chapter 5 integrated the MT-based LES approach with a transcritical flamelet library generated the real-fluid multiphase flamelet solver. This framework was validated against ECN Spray-A experiments, confirming its ability to accurately predict key spray characteristics. Application to alternative fuels, such as OME_3 and its mixtures with n-dodecane, provided novel insights into the differences in evaporation dynamics, ignition characteristics, and soot formation under transcritical conditions. The results showed that adding OME_3 shortens the two-phase region and cool flame lift-off, accelerating ignition, but also revealed complex interactions like differential evaporation influencing local composition and potentially limiting soot reduction in blends.

The final outcome of this work can then be summarized as follows: addressing critical challenges in VLE calculations, extending LES-MT to reacting flows, developing detailed real-fluid flamelet models, and integrating them through tabulated chemistry, this work provides unprecedented insights into high-pressure transcritical injection and combustion phenomena. The successful validation against experimental data and the detailed analysis of fundamental processes and alternative fuels underscore the potential of this approach to become a powerful tool for designing cleaner and more fuel-efficient engines in the future. While significant advancements have been made, future work could explore further refinements, such as incorporating detailed turbulence-combustion interaction models, implementing dynamic load balancing for improved parallel performance, and conducting more extensive studies on a wider range of new fuels and operating conditions.

Bibliography

[1] M. Fathi, D. Roekaerts, and S. Hickel. “Transcritical Real-Fluid Effects on Dual-Fuel Combustion of Methane and N-Dodecane”. In: *Appl. Energy Combust. Sci.* 24 (2025). Publisher: Elsevier, p. 100398. ISSN: 2666-352X. DOI: `10.1016/j.jaecs.2025.100398`.

[2] A. L. Sanchez, J. Urzay, and A. Liñan. “The role of separation of scales in the description of spray combustion”. In: *Proc. Combust. Inst.* 35.2 (2015). Publisher: Elsevier, pp. 1549–1577. DOI: `10.1016/j.proci.2014.08.018`.

[3] T. C. Klima, A. Peter, S. Riess, M. Wensing, and A. S. Braeuer. “Quantification of mixture composition, liquid-phase fraction and-temperature in transcritical sprays”. In: *The Journal of Supercritical Fluids* 159 (2020). Publisher: Elsevier, p. 104777. DOI: `10.1016/j.supflu.2020.104777`.

[4] L. Jofre and J. Urzay. “Transcritical diffuse-interface hydrodynamics of propellants in high-pressure combustors of chemical propulsion systems”. In: *Prog. Energ. Combust.* 82 (2021). Publisher: Elsevier, p. 100877. ISSN: 0360-1285. DOI: `10.1016/j.pecs.2020.100877`.

[5] P. C. Ma, H. Wu, D. T. Banuti, and M. Ihme. “On the numerical behavior of diffuse-interface methods for transcritical real-fluids simulations”. In: *Int. J. Multiphas. Flow* 113 (2019). Publisher: Elsevier, pp. 231–249. ISSN: 0301-9322. DOI: `10.1016/j.ijmultiphaseflow.2019.01.015`.

[6] W. O. H. Mayer, B. Ivancic, A. Schik, and U. Hornung. “Propellant Atomization and Ignition Phenomena in Liquid Oxygen/Gaseous Hydrogen Rocket Combustors”. In: *J. Propul. Power* 17.4 (2001). Publisher: American Institute of Aeronautics and Astronautics (AIAA), pp. 794–799. ISSN: 1533-3876. DOI: `10.2514/2.5835`.

[7] A. Firoozabadi. *Thermodynamics of hydrocarbon reservoirs.* McGraw-Hill, 1999.

[8] J. Bellan. “Theory, modeling and analysis of turbulent supercritical mixing”. In: *Combustion science and technology* 178.1 (2006). Publisher: Taylor & Francis, pp. 253–281. DOI: `10.1080/00102200500292241`.

[9] S. C. Tucker. “Solvent density inhomogeneities in supercritical fluids”. In: *Chem. Rev.* 99.2 (1999). Publisher: ACS Publications, pp. 391–418. DOI: `10.1021/cr9700437`.

[10] J. C. Oefelein. "Mixing and combustion of cryogenic oxygen-hydrogen shear-coaxial jet flames at supercritical pressure". In: *Combust. Sci. Technol.* 178.1 (2006). Publisher: Taylor & Francis, pp. 229–252. DOI: 10.1080/00102200500325322.

[11] S. Candel, M. Juniper, G. Singla, P. Scouflaire, and C. Rolon. "Structure And Dynamics Of Cryogenic Flames At Supercritical Pressure". In: *Combust. Sci. Technol.* 178.1 (2006). Publisher: Informa UK Limited, pp. 161–192. ISSN: 1563-521x. DOI: 10.1080/00102200500292530.

[12] I. H. Bell, J. Wronski, S. Quoilin, and V. Lemort. "CoolProp: Open-source thermophysical property library". In: *Ind. Eng. Chem. Res.* 53.6 (2014), pp. 2498–2508. DOI: 10.1021/ie4033999.

[13] F. Gorelli, M. Santoro, T. Scopigno, M. Krisch, and G. Ruocco. "Liquidlike behavior of supercritical fluids". In: *Physical review letters* 97.24 (2006). Publisher: APS _eprint: cond-mat/0611044, p. 245702. DOI: 10.48550/arxiv.cond-mat/0611044.

[14] G. G. Simeoni, T. Bryk, F. A. Gorelli, M. Krisch, G. Ruocco, M. Santoro, and T. Scopigno. "The Widom line as the crossover between liquid-like and gas-like behaviour in supercritical fluids". In: *Nat. Phys.* 6.7 (2010). Publisher: Nature Publishing Group UK London, pp. 503–507. DOI: 10.1038/nphys1683.

[15] D. Banuti, M. Raju, P. C. Ma, M. Ihme, and J.-P. Hickey. "Seven questions about supercritical fluids-towards a new fluid state diagram". In: *55th AIAA Aerospace Sciences Meeting*. 2017, p. 1106. DOI: 10.2514/6.2017-1106.

[16] D. Banuti. "Crossing the Widom-line–supercritical pseudo-boiling". In: *J. Supercrit. Fluids.* 98 (2015), pp. 12–16. DOI: 10.1016/j.supflu.2014.12.019.

[17] D. T. Banuti, M. Raju, and M. Ihme. "Between supercritical liquids and gases–reconciling dynamic and thermodynamic state transitions". In: *J. Supercrit. Fluids.* 165 (2020), p. 104895. DOI: 10.1016/j.supflu.2020.104895.

[18] V. Brazhkin, Y. D. Fomin, A. Lyapin, V. Ryzhov, and K. Trachenko. "Two liquid states of matter: A dynamic line on a phase diagram". In: *Physical Review E—Statistical, Nonlinear, and Soft Matter Physics* 85.3 (2012), p. 031203. DOI: 10.1103/PhysRevE.85.031203.

[19] B. Chehroudi, D. Talley, and E. Coy. "Initial growth rate and visual characteristics of a round jet into a sub-to supercritical environment of relevance to rocket, gas turbine, and diesel engines". In: *37th aerospace sciences meeting and exhibit*. 1999, p. 206. DOI: 10.2514/6.1999-206.

[20] R. D. Reitz and F. Bracco. *On the dependence of spray angle and other spray parameters on nozzle design and operating conditions*. SAE technical paper, 1979. DOI: 10.4271/790494.

[21] B. Chehroudi. “Recent Experimental Efforts on High-Pressure Supercritical Injection for Liquid Rockets and Their Implications”. In: *International Journal of Aerospace Engineering* 2012.1 (2012). Publisher: Wiley Online Library, p. 121802. DOI: 10.1155/2012/121802.

[22] A. Roy and C. Segal. “Experimental study of subcritical to supercritical jet mixing”. In: *47th AIAA Aerospace Sciences Meeting including The New Horizons Forum and Aerospace Exposition*. 2009, p. 809. DOI: 10.2514/6.2009-809.

[23] R. Woodward and D. Talley. “Raman imaging of transcritical cryogenic propellants”. In: *34th Aerospace Sciences Meeting and Exhibit*. 1996, p. 468. DOI: 10.2514/6.1996-468.

[24] P. Van Konynenburg and R. Scott. “Critical lines and phase equilibria in binary van der Waals mixtures”. In: *Philosophical Transactions of the Royal Society of London. Series A, Mathematical and Physical Sciences* 298.1442 (1980). Publisher: The Royal Society London, pp. 495–540.

[25] L. Qiu and R. D. Reitz. “An investigation of thermodynamic states during high-pressure fuel injection using equilibrium thermodynamics”. In: *Int. J. Multiphas. Flow* 72 (2015). Publisher: Elsevier, pp. 24–38. ISSN: 0301-9322. DOI: 10.1016/j.ijmultiphaseflow.2015.01.011.

[26] A. Wehrfritz, O. Kaario, V. Vuorinen, and B. Somers. “Large eddy simulation of n-dodecane spray flames using flamelet generated manifolds”. In: *Combust. Flame* 167 (2016). Publisher: Elsevier, pp. 113–131. ISSN: 0010-2180. DOI: 10.1016/j.combustflame.2016.02.019.

[27] B. Tekgul, H. Kahila, O. Kaario, and V. Vuorinen. “Large-eddy simulation of dual-fuel spray ignition at different ambient temperatures”. In: *Combust. Flame* 215 (2020). Publisher: Elsevier Inc., pp. 51–65. ISSN: 1556-2921. DOI: 10.1016/j.combustflame.2020.01.017.

[28] S. Karimkashi, M. Gadalla, J. Kannan, B. Tekgul, O. Kaario, and V. Vuorinen. “Large-eddy simulation of diesel pilot spray ignition in lean methane-air and methanol-air mixtures at different ambient temperatures”. In: *Int. J. Engine Res.* 24 (2023). Publisher: SAGE Publications Ltd, pp. 965–981. ISSN: 2041-3149. DOI: 10.1177/14680874211070368.

[29] G. Lacaze, A. Misdariis, A. Ruiz, and J. C. Oefelein. “Analysis of high-pressure Diesel fuel injection processes using LES with real-fluid thermodynamics and transport”. In: *Proc. Combust. Inst.* 35.2 (2015). Publisher: Elsevier, pp. 1603–1611. ISSN: 1540-7489. DOI: 10.1016/j.proci.2014.06.072.

[30] J. Matheis and S. Hickel. *Multi-component vapor-liquid equilibrium model for LES and application to ECN Spray A*. _eprint: 1609.08533. 2016. DOI: 10.48550/arxiv.1609.08533.

[31] H. Muller, C. A. Niedermeier, J. Matheis, M. Pfitzner, and S. Hickel. "Large-eddy simulation of nitrogen injection at trans- and supercritical conditions". In: *Phys. Fluids* 28.1 (2016). Publisher: AIP Publishing. ISSN: 1089-7666. DOI: 10.1063/1.4937948.

[32] H. Muller, M. Pfitzner, J. Matheis, and S. Hickel. "Large-Eddy Simulation of Coaxial LN2/GH2 Injection at Trans- and Supercritical Conditions". In: *J. Propul. Power* 32.1 (2016). Publisher: American Institute of Aeronautics and Astronautics (AIAA), pp. 46–56. ISSN: 1533-3876. DOI: 10.2514/1.b35827.

[33] B. Balaji, V. Raghavan, K. Ramamurthi, and G. Gogos. "A numerical study of evaporation characteristics of spherical n-dodecane droplets in high pressure nitrogen environment". In: *Phys. Fluids* 23.6 (2011). Publisher: AIP Publishing. DOI: 10.1063/1.3599700.

[34] L. M. Ricart, R. D. Reltz, and J. E. Dec. "Comparisons of Diesel Spray Liquid Penetration and Vapor Fuel Distributions With In-Cylinder Optical Measurements". In: *J. Eng. Gas Turbines Power* 122.4 (1999). Publisher: ASME International, pp. 588–595. ISSN: 1528-8919. DOI: 10.1115/1.1290591.

[35] J. Matheis and S. Hickel. "Multi-component vapor-liquid equilibrium model for LES of high-pressure fuel injection and application to ECN Spray A". In: *Int. J. Multiphas. Flow* 99 (2018). Publisher: Elsevier, pp. 294–311. ISSN: 0301-9322. DOI: 10.1016/j.ijmultiphaseflow.2017.11.001.

[36] P. Tudisco and S. Menon. "Numerical investigations of phase-separation during multi-component mixing at super-critical conditions". In: *Flow Turbul. Combust.* 104.2 (2020). Publisher: Springer, pp. 693–724.

[37] J. Matheis, H. Mller, S. Hickel, and M. Pfitzner. "Large-Eddy Simulation of Cryogenic Jet Injection at Supercritical Pressures". In: *High-Pressure Flows for Propulsion Applications*. Ed. by J. Bellan. Progress in Astronautics and Aeronautics. American Institute of Aeronautics and Astronautics, Inc., 2020, pp. 531–570. ISBN: 978-1-62410-581-4. DOI: 10.2514/5.9781624105814.0531.0570.

[38] C. Traxinger, J. Zips, and M. Pfitzner. "Single-Phase Instability in Non-Premixed Flames Under Liquid Rocket Engine Relevant Conditions". In: *J. Propul. Power* 35.4 (2019). Publisher: American Institute of Aeronautics and Astronautics (AIAA), pp. 675–689. ISSN: 1533-3876. DOI: 10.2514/1.b37395.

[39] S. Yang, P. Yi, and C. Habchi. "Real-fluid injection modeling and LES simulation of the ECN Spray A injector using a fully compressible two-phase flow approach". In: *Int. J. Multiphas. Flow* 122 (2020). Publisher: Elsevier, p. 103145. ISSN: 0301-9322. DOI: 10.1016/j.ijmultiphaseflow.2019.103145.

[40] S. Jafari, H. Gaballa, C. Habchi, and J. C. de Hemptinne. "Towards understanding the structure of subcritical and transcritical liquid–gas interfaces using a tabulated real fluid modeling approach". In: *Energies* 14 (18 Sept. 2021). ISSN: 19961073. DOI: 10.3390/en14185621.

[41] P. Koukouvinis, A. Vidal-Roncero, C. Rodriguez, M. Gavaises, and L. Pickett. "High pressure/high temperature multiphase simulations of dodecane injection to nitrogen: Application on ECN Spray-A". In: *Fuel* 275 (2020). Publisher: Elsevier, p. 117871. ISSN: 0016-2361. DOI: 10.1016/j.fuel.2020.117871.

[42] H. Gaballa, C. Habchi, and J. C. de Hemptinne. "Modeling and LES of high-pressure liquid injection under evaporating and non-evaporating conditions by a real fluid model and surface density approach". In: *Int. J. Multiph. Flow* 160 (Mar. 2023). ISSN: 03019322. DOI: 10.1016/j.ijmultiphaseflow.2022.104372.

[43] A. Doehring, T. Trummler, M. Pfitzner, and M. Klein. "Two-dimensional direct numerical simulation study of multicomponent mixing with phase transition in a transcritical shear layer". In: *Phys. Fluids* 36.6 (2024). Publisher: AIP Publishing. DOI: 10.1063/5.0211029.

[44] F. V. Bracco. "Structure of Flames in Premixed-Charge IC Engines". In: *Combust. Sci. Technol.* 58.1 (1988). Publisher: Informa UK Limited, pp. 209–230. ISSN: 1563-521x. DOI: 10.1080/00102208808923964.

[45] U. Eguz, S. Ayyapureddi, C. Bekdemir, B. Somers, and P. de Goey. "Manifold resolution study of the FGM method for an igniting diesel spray". In: *Fuel* 113 (2013). Publisher: Elsevier, pp. 228–238. DOI: 10.1016/j.fuel.2013.05.090.

[46] A. Hadadpour, S. Xu, Y. Zhang, X.-S. Bai, and M. Jangi. "An extended FGM model with transported PDF for LES of spray combustion". In: *Proc. Combust. Inst.* 39.4 (2023). Publisher: Elsevier, pp. 4889–4898. ISSN: 1540-7489. DOI: 10.1016/j.proci.2022.09.014.

[47] C. Sula, H. Grosshans, and M. V. Papalexandris. "Numerical study of spray combustion of a biodiesel surrogate fuel using the LES-FGM approach". In: *Combust. Flame* 249 (2023). Publisher: Elsevier, p. 112611. ISSN: 0010-2180. DOI: 10.1016/j.combustflame.2022.112611.

[48] L. Hakim, G. Lacaze, M. Khalil, H. N. Najm, and J. C. Oefelein. "Modeling Auto-Ignition Transients in Reacting Diesel Jets". In: *J. Eng. Gas Turbines Power* 138.11 (2016). Publisher: ASME International. ISSN: 1528-8919. DOI: 10.1115/1.4033502.

[49] H. Wu, P. C. Ma, and M. Ihme. "Efficient time-stepping techniques for simulating turbulent reactive flows with stiff chemistry". In: *Comput. Phys. Commun.* 243 (2019). Publisher: Elsevier, pp. 81–96. ISSN: 0010-4655. DOI: 10.1016/j.cpc.2019.04.016.

[50] W. T. Chung, P. Ma, and M. Ihme. "Examination of diesel spray combustion in supercritical ambient fluid using large-eddy simulations". In: *Int. J. Engine Res.* 21.1 (2020). Publisher: SAGE Publications, pp. 122–133. ISSN: 2041-3149. DOI: 10.1177/1468087419868388.

[51] M. Fathi and S. Hickel. "Rapid Multi-Component Phase-Split Calculations Using Volume Functions and Reduction Methods". In: *AIChE J.* 67.6 (2021). Publisher: Wiley _eprint: 2001.06285, e17174. ISSN: 1547-5905. DOI: 10.1002/aic.17174.

[52] A. S. Abhvani and D. N. Beaumont. "Development of an Efficient Algorithm for the Calculation of Two-Phase Flash Equilibria". In: *SPE Reservoir Engineering* 2.4 (1987). Publisher: Society of Petroleum Engineers (SPE), pp. 695–702. ISSN: 2469-9683. DOI: 10.2118/13951-pa.

[53] M. L. Michelsen. "The isothermal flash problem. Part I. Stability". In: *Fluid Phase Equilibr.* 9.1 (1982). Publisher: Elsevier, pp. 1–19. ISSN: 0378-3812. DOI: 10.1016/0378-3812(82)85001-2.

[54] M. L. Michelsen. "State function based flash specifications". In: *Fluid Phase Equilibr.* 158–160 (1999). Publisher: Elsevier, pp. 617–626. ISSN: 0378-3812. DOI: 10.1016/s0378-3812(99)00092-8.

[55] M. L. Michelsen. "Simplified flash calculations for Cubic Equations of State". In: *Industrial & Engineering Chemistry Process Design and Development* 25.1 (1986). Publisher: American Chemical Society (ACS), pp. 184–188. ISSN: 1541-5716. DOI: 10.1021/i200032a029.

[56] M. Petitfrere and D. V. Nichita. "A comparison of conventional and reduction approaches for phase equilibrium calculations". In: *Fluid Phase Equilibr.* 386 (2015). Publisher: Elsevier, pp. 30–46. ISSN: 0378-3812. DOI: 10.1016/j.fluid.2014.11.017.

[57] E. Hendriks and A. van Bergen. "Application of a reduction method to phase equilibria calculations". In: *Fluid Phase Equilibr.* 74 (1992). Publisher: Elsevier, pp. 17–34. ISSN: 0378-3812. DOI: 10.1016/0378-3812(92)85050-i.

[58] D. V. Nichita and A. Graciaa. "A new reduction method for phase equilibrium calculations". In: *Fluid Phase Equilibr.* 302.1 (2011). Publisher: Elsevier, pp. 226–233. ISSN: 0378-3812. DOI: 10.1016/j.fluid.2010.11.007.

[59] J. Mikyska and A. Firoozabadi. "A new thermodynamic function for phase-splitting at constant temperature, moles, and volume". In: *AIChE J.* 57.7 (2011). Publisher: Wiley Online Library, pp. 1897–1904.

[60] T. Jindrova and J. Mikyska. "General algorithm for multiphase equilibria calculation at given volume, temperature, and moles". In: *Fluid Phase Equilibr.* 393 (2015). Publisher: Elsevier, pp. 7–25. ISSN: 0378-3812. DOI: 10.1016/j.fluid.2015.02.013.

[61] D. V. Nichita. "New unconstrained minimization methods for robust flash calculations at temperature, volume and moles specifications". In: *Fluid Phase Equilibr.* 466 (2018). Publisher: Elsevier, pp. 31–47. ISSN: 0378-3812. DOI: `10.1016/j.fluid.2018.03.012`.

[62] M. Cismondi, P. M. Ndiaye, and F. W. Tavares. "A new simple and efficient flash algorithm for T-v specifications". In: *Fluid Phase Equilibr.* 464 (2018). Publisher: Elsevier, pp. 32–39. ISSN: 0378-3812. DOI: `10.1016/j.fluid.2018.02.019`.

[63] A. Firoozabadi. *Thermodynamics and Applications of Hydrocarbons Energy Production.* McGraw-Hill Professional, 2015.

[64] M. L. Michelsen and J. Mollerup. *Thermodynamic Models: Fundamentals and Computational Aspects.* Tie-Line Publications, 2007.

[65] D. V. Nichita and M. Petitfrere. "Phase stability analysis using a reduction method". In: *Fluid Phase Equilibr.* 358 (2013). Publisher: Elsevier, pp. 27–39. ISSN: 0378-3812. DOI: `10.1016/j.fluid.2013.08.006`.

[66] E. Goos, A. Burcat, and B. Ruscic. "Third millennium ideal gas and condensed phase thermochemical database for combustion". In: *URL: http://garfield.chem.elte.hu/Burcat/burcat.html* (2009).

[67] D. V. Nichita. "Fast and robust phase stability testing at isothermal-isochoric conditions". In: *Fluid Phase Equilibr.* 447 (2017). Publisher: Elsevier, pp. 107–124. ISSN: 0378-3812. DOI: `10.1016/j.fluid.2017.05.022`.

[68] D. V. Nichita and C. F. Leibovici. "A rapid and robust method for solving the Rachford–Rice equation using convex transformations". In: *Fluid Phase Equilibr.* 353 (2013). Publisher: Elsevier, pp. 38–49. ISSN: 0378-3812. DOI: `10.1016/j.fluid.2013.05.030`.

[69] L. Yarborough. "Vapor-liquid equilibrium data for multicomponent mixtures containing hydrocarbon and nonhydrocarbon components". In: *Journal of Chemical & Engineering Data* 17.2 (1972). Publisher: American Chemical Society (ACS), pp. 129–133. ISSN: 1520-5134. DOI: `10.1021/je60053a027`.

[70] R. Metcalfe and L. Yarborough. "The Effect of Phase Equilibria on the CO2 Displacement Mechanism". In: *Soc. Petrol. Eng. J.* 19.4 (1979). Publisher: Society of Petroleum Engineers (SPE), pp. 242–252. ISSN: 0197-7520. DOI: `10.2118/7061-pa`.

[71] A. Firoozabadi and H. Pan. "Fast and Robust Algorithm for Compositional Modeling: Part I–Stability Analysis Testing". In: *SPE Journal* 7.1 (2002). Publisher: Society of Petroleum Engineers (SPE), pp. 78–89. ISSN: 1930-0220. DOI: `10.2118/77299-pa`.

[72] J. Matheis. "Numerical simulation of fuel injection and turbulent mixing under high-pressure conditions". PhD thesis. Technische Universität Munchen, 2018.

[73] W. B. Kay. “Liquid-Vapor Phase Equilibrium Relations in the Ethane-n-Heptane System”. In: *Industrial & Engineering Chemistry* 30.4 (1938). Publisher: American Chemical Society (ACS), pp. 459–465. ISSN: 1541-5724. DOI: `10.1021/ie50340a023`.

[74] V. S. Mehra and G. Thodos. “Vapor-Liquid Equilibrium in the Ethane-n-Heptane System.” In: *Journal of Chemical & Engineering Data* 10.3 (1965). Publisher: American Chemical Society (ACS), pp. 211–214. ISSN: 1520-5134. DOI: `10.1021/je60026a001`.

[75] M. Fathi, S. Hickel, and D. Roekaerts. “Large Eddy Simulations of Reacting and Non-Reacting Transcritical Fuel Sprays Using Multiphase Thermodynamics”. In: *Phys. Fluids* 34.8 (2022). Publisher: AIP Publishing _eprint: 2205.07504, p. 085131. ISSN: 1089-7666. DOI: `10.1063/5.0099154`.

[76] W. O. H. Mayer, A. H. A. Schik, B. Vielle, C. Chauveau, I. Gokalp, D. G. Talley, and R. D. Woodward. “Atomization and Breakup of Cryogenic Propellants Under High-Pressure Subcritical and Supercritical Conditions”. In: *J. Propul. Power* 14.5 (1998). Publisher: American Institute of Aeronautics and Astronautics (AIAA), pp. 835–842. ISSN: 1533-3876. DOI: `10.2514/2.5348`.

[77] G. Singla, P. Scouflaire, C. Rolon, and S. Candel. “Transcritical oxygen/transcritical or supercritical methane combustion”. In: *Proc. Combust. Inst.* 30.2 (2005). Publisher: Elsevier, pp. 2921–2928. ISSN: 1540-7489. DOI: `10.1016/j.proci.2004.08.063`.

[78] J. Gimeno, G. Bracho, P. Marti-Aldaravi, and J. E. Peraza. “Experimental study of the injection conditions influence over n-dodecane and diesel sprays with two ECN single-hole nozzles. Part I: Inert atmosphere”. In: *Energ. Convers. Manage.* 126 (2016). Publisher: Elsevier, pp. 1146–1156. ISSN: 0196-8904. DOI: `10.1016/j.enconman.2016.07.077`.

[79] R. Payri, F. Salvador, J. Gimeno, and J. E. Peraza. “Experimental study of the injection conditions influence over n-dodecane and diesel sprays with two ECN single-hole nozzles. Part II: Reactive atmosphere”. In: *Energ. Convers. Manage.* 126 (2016). Publisher: Elsevier, pp. 1157–1167. ISSN: 0196-8904. DOI: `10.1016/j.enconman.2016.07.079`.

[80] Y. Pei, S. Som, E. Pomraning, P. K. Senecal, S. A. Skeen, J. Manin, and L. M. Pickett. “Large eddy simulation of a reacting spray flame with multiple realizations under compression ignition engine conditions”. In: *Combust. Flame* 162.12 (2015). Publisher: Elsevier, pp. 4442–4455. ISSN: 0010-2180. DOI: `10.1016/j.combustflame.2015.08.010`.

[81] H. Kahila, A. Wehrfritz, O. Kaario, M. Ghaderi Masouleh, N. Maes, B. Somers, and V. Vuorinen. “Large-eddy simulation on the influence of injection pressure in reacting Spray A”. In: *Combust. Flame* 191 (2018). Publisher: Elsevier, pp. 142–159. ISSN: 0010-2180. DOI: `10.1016/j.combustflame.2018.01.004`.

[82] M. Gadalla, J. Kannan, B. Tekgul, S. Karimkashi, O. Kaario, and V. Vuorinen. “Large-Eddy Simulation of ECN Spray A: Sensitivity Study on Modeling Assumptions”. In: *Energies* 13.13 (2020). Publisher: Mdpi Ag, p. 3360. ISSN: 1996-1073. DOI: 10.3390/en13133360.

[83] L. Hakim, G. Lacaze, and J. Oefelein. “Large Eddy Simulation of Autoignition Transients in a Model Diesel Injector Configuration”. In: *SAE Int. J. Fuels Lubr.* 9.1 (2016). Publisher: SAE International, pp. 165–176. ISSN: 1946-3960. DOI: 10.4271/2016-01-0872.

[84] L. Hakim, G. Lacaze, M. Khalil, K. Sargsyan, H. Najm, and J. Oefelein. “Probabilistic parameter estimation in a 2-step chemical kinetics model for n-dodecane jet autoignition”. In: *Combust. Theor. Model.* 22.3 (2018). Publisher: Taylor & Francis, pp. 446–466.

[85] G. Kogekar, C. Karakaya, G. J. Liskovich, M. A. Oehlschlaeger, S. C. DeCaluwe, and R. J. Kee. “Impact of non-ideal behavior on ignition delay and chemical kinetics in high-pressure shock tube reactors”. In: *Combust. Flame* 189 (2018). Publisher: Elsevier, pp. 1–11. ISSN: 0010-2180. DOI: 10.1016/j.combustflame.2017.10.014.

[86] G. Soave. “Equilibrium constants from a modified Redlich-Kwong equation of state”. In: *Chem. Eng. Sci.* 27.6 (1972). Publisher: Elsevier, pp. 1197–1203. ISSN: 0009-2509. DOI: 10.1016/0009-2509(72)80096-4.

[87] D.-Y. Peng and D. B. Robinson. “A New Two-Constant Equation of State”. In: *Ind. Eng. Chem. Fund.* 15.1 (1976). Publisher: American Chemical Society (ACS), pp. 59–64. ISSN: 1541-4833. DOI: 10.1021/i160057a011.

[88] P. Ma, L. Bravo, and M. Ihme. “Supercritical and transcritical real-fluid mixing in diesel engine applications”. In: *Proceedings of the Center for Turbulence Research 2014 Summer Program.* Stanford University, 2014, p. 99.

[89] J. Matheis, H. Muller, C. Lenz, M. Pfitzner, and S. Hickel. “Volume translation methods for real-gas computational fluid dynamics simulations”. In: *J. Supercrit. Fluid.* 107 (2016). Publisher: Elsevier, pp. 422–432. ISSN: 0896-8446. DOI: 10.1016/j.supflu.2015.10.004.

[90] J. Bellan. “Direct numerical simulation of a high-pressure turbulent reacting temporal mixing layer”. In: *Combust. Flame* 176 (2017). Publisher: Elsevier, pp. 245–262. ISSN: 0010-2180. DOI: 10.1016/j.combustflame.2016.09.026.

[91] X. Wang, H. Huo, U. Unnikrishnan, and V. Yang. “A systematic approach to high-fidelity modeling and efficient simulation of supercritical fluid mixing and combustion”. In: *Combust. Flame* 195 (2018). Publisher: Elsevier, pp. 203–215. ISSN: 0010-2180. DOI: 10.1016/j.combustflame.2018.04.030.

[92] M. Cismondi and J. Mollerup. “Development and application of a three-parameter RK-PR equation of state”. In: *Fluid Phase Equilibr.* 232.1 (2005). Publisher: Elsevier, pp. 74–89. ISSN: 0378-3812. DOI: 10.1016/j.fluid.2005.03.020.

[93] S.-K. Kim, H.-S. Choi, and Y. Kim. “Thermodynamic modeling based on a generalized cubic equation of state for kerosene/LOx rocket combustion”. In: *Combust. Flame* 159.3 (2012). Publisher: Elsevier, pp. 1351–1365. ISSN: 0010-2180. DOI: `10.1016/j.combustflame.2011.10.008`.

[94] S. Hickel, C. P. Egerer, and J. Larsson. “Subgrid-scale modeling for implicit large eddy simulation of compressible flows and shock-turbulence interaction”. In: *Phys. Fluids* 26.10 (2014). Publisher: AIP Publishing, p. 106101. ISSN: 1089-7666. DOI: `10.1063/1.4898641`.

[95] B. Poling, J. Prausnitz, and J. O’Connell. *The Properties of Gases and Liquids*. McGraw-Hill Companies, 2001. ISBN: 0-07-149999-7. DOI: `10.1036/0070116822`.

[96] R. Krishna and J. M. van Baten. “Describing diffusion in fluid mixtures at elevated pressures by combining the Maxwell–Stefan formulation with an equation of state”. In: *Chem. Eng. Sci.* 153 (2016). Publisher: Elsevier, pp. 174–187. ISSN: 0009-2509. DOI: `10.1016/j.ces.2016.07.025`.

[97] E. W. Lemmon and M. L. Huber. “Thermodynamic properties of n-dodecane”. In: *Energy & fuels* 18.4 (2004). Publisher: ACS Publications, pp. 960–967.

[98] J. Gross and G. Sadowski. “Perturbed-Chain SAFT: An Equation of State Based on a Perturbation Theory for Chain Molecules”. In: *Industrial & Engineering Chemistry Research* 40.4 (2001). Publisher: American Chemical Society (ACS), pp. 1244–1260. ISSN: 1520-5045. DOI: `10.1021/ie0003887`.

[99] S. A. Martinez and K. R. Hall. “Thermodynamic Properties of Light Synthetic Natural Gas Mixtures Using the RK-PR Cubic Equation of State”. In: *Industrial & Engineering Chemistry Research* 45.10 (2006). Publisher: American Chemical Society (ACS), pp. 3684–3692. ISSN: 1520-5045. DOI: `10.1021/ie051241o`.

[100] A. Burcat, B. Ruscic, and Chemistry. *Third millenium ideal gas and condensed phase thermochemical database for combustion (with update from active thermochemical tables)*. Office of Scientific and Technical Information (OSTI), 2005. DOI: `10.2172/925269`.

[101] J. Gmehling, M. Kleiber, B. Kolbe, and J. Rarey. *Chemical Thermodynamics for Process Simulation*. Wiley, 2019. ISBN: 978-3-527-80947-9. DOI: `10.1002/9783527809479`.

[102] F. Diegelmann, S. Hickel, and N. A. Adams. “Shock Mach number influence on reaction wave types and mixing in reactive shock–bubble interaction”. In: *Combust. Flame* 174 (2016). Publisher: Elsevier, pp. 85–99. ISSN: 0010-2180. DOI: `10.1016/j.combustflame.2016.09.014`.

[103] S. Hickel, N. A. Adams, and J. A. Domaradzki. “An adaptive local deconvolution method for implicit LES”. In: *J. Comput. Phys.* 213.1 (2006). Publisher: Elsevier, pp. 413–436. ISSN: 0021-9991. DOI: `10.1016/j.jcp.2005.08.017`.

[104] G. D. van Albada, B. van Leer, and W. W. Roberts. “A Comparative Study of Computational Methods in Cosmic Gas Dynamics”. In: *Upwind and High-Resolution Schemes*. Springer Berlin Heidelberg, 1997, pp. 95–103. ISBN: 978-3-642-60543-7. DOI: `10.1007/978-3-642-60543-7_6`.

[105] P. N. Brown, G. D. Byrne, and A. C. Hindmarsh. “VODE: A Variable-Coefficient ODE Solver”. In: *SIAM J. Sci. Stat. Comput* 10.5 (1989). Publisher: Society for Industrial & Applied Mathematics (SIAM), pp. 1038–1051. ISSN: 2168-3417. DOI: `10.1137/0910062`.

[106] S. Gottlieb and C.-W. Shu. “Total variation diminishing Runge-Kutta schemes”. In: *Math. Comput.* 67.221 (1998). Publisher: American Mathematical Society (AMS), pp. 73–85. ISSN: 1088-6842. DOI: `10.1090/s0025-5718-98-00913-2`.

[107] L. M. Pickett, C. L. Genzale, G. Bruneaux, L.-M. Malbec, L. Hermant, C. Christiansen, and J. Schramm. “Comparison of Diesel Spray Combustion in Different High-Temperature, High-Pressure Facilities”. In: *SAE Int. J. Engines* 3.2 (2010). Publisher: SAE International, pp. 156–181. ISSN: 1946-3944. DOI: `10.4271/2010-01-2106`.

[108] K. Narayanaswamy, P. Pepiot, and H. Pitsch. “A chemical mechanism for low to high temperature oxidation of n-dodecane as a component of transportation fuel surrogates”. In: *Combust. Flame* 161.4 (2014). Publisher: Elsevier, pp. 866–884. ISSN: 0010-2180. DOI: `10.1016/j.combustflame.2013.10.012`.

[109] S. A. Skeen, J. Manin, and L. M. Pickett. “Simultaneous formaldehyde PLIF and high-speed schlieren imaging for ignition visualization in high-pressure spray flames”. In: *Proc. Combust. Inst.* 35.3 (2015). Publisher: Elsevier, pp. 3167–3174. ISSN: 1540-7489. DOI: `10.1016/j.proci.2014.06.040`.

[110] L. M. Pickett and J. Abraham. “Computed And Measured Fuel Vapor Distribution In A Diesel Spray”. In: *Atomization Spray.* 20.3 (2010). Publisher: Begell House, pp. 241–250. ISSN: 1044-5110. DOI: `10.1615/atomizspr.v20.i3.50`.

[111] L. M. Pickett, J. Manin, C. L. Genzale, D. L. Siebers, M. P. B. Musculus, and C. A. Idicheria. “Relationship Between Diesel Fuel Spray Vapor Penetration/Dispersion and Local Fuel Mixture Fraction”. In: *SAE Int. J. Engines* 4.1 (2011). Publisher: SAE International, pp. 764–799. ISSN: 1946-3944. DOI: `10.4271/2011-01-0686`.

[112] U. Unnikrishnan, J. C. Oefelein, and V. Yang. “Subgrid modeling of the filtered equation of state with application to real-fluid turbulent mixing at supercritical pressures”. In: *Phys. Fluids* 34.6 (2022). Publisher: AIP Publishing. ISSN: 1089-7666. DOI: `10.1063/5.0088074`.

[113] M. Fathi, D. Roekaerts, and S. Hickel. “Numerical Simulation of Transcritical Multiphase Combustion Using Real-Fluid Thermochemical and Transport Properties”. In: *Combust. Flame* 275 (2024). Publisher: Elsevier, p. 114055. DOI: `10.1016/j.combustflame.2025.114055`.

[114] D. L. Siebers. “Scaling Liquid-Phase Fuel Penetration in Diesel Sprays Based on Mixing-Limited Vaporization”. In: *SAE Technical Paper Series*. Annual. ISSN: 0148-7191 Journal Abbreviation: SAE TRANSACTIONS. SAE International, 1999, pp. 703–728. DOI: 10.4271/1999-01-0528.

[115] U. Guven and G. Ribert. “Impact of non-ideal transport modeling on supercritical flow simulation”. In: *Proc. Combust. Inst.* 37.3 (2019). Publisher: Elsevier, pp. 3255–3262. ISSN: 1540-7489. DOI: 10.1016/j.proci.2018.05.013.

[116] T. H. Chung, M. Ajlan, L. L. Lee, and K. E. Starling. “Generalized multiparameter correlation for nonpolar and polar fluid transport properties”. In: *Industrial & Engineering Chemistry Research* 27.4 (1988). Publisher: American Chemical Society (ACS), pp. 671–679. ISSN: 1520-5045. DOI: 10.1021/ie00076a024.

[117] A. C. ZAMBON and H. K. CHELLIAH. “Self-sustained acoustic-wave interactions with counterflow flames”. In: *J. Fluid Mech.* 560 (2006). Publisher: Cambridge University Press (CUP), p. 249. ISSN: 1469-7645. DOI: 10.1017/s0022112006000498.

[118] N. Mukundakumar, D. Efimov, N. Beishuizen, and J. van Oijen. “A new preferential diffusion model applied to FGM simulations of hydrogen flames”. In: *Combust. Theor. Model.* 25.7 (2021). Publisher: Informa UK Limited, pp. 1245–1267. ISSN: 1741-3559. DOI: 10.1080/13647830.2021.1970232.

[119] T. Regueira, M.-L. Glykioti, E. H. Stenby, and W. Yan. “Density and Compressibility of Multicomponent n-Alkane Mixtures up to 463 K and 140 MPa”. In: *J. Chem. Eng. Data* 63.4 (2017). Publisher: ACS Publications, pp. 1072–1080.

[120] M. Fathi, S. Hickel, and D. Roekaerts. “Numerical Simulations of Real-Fluid Reacting Sprays at Transcritical Pressures Using Multiphase Thermodynamics”. In: *Proceedings of the 4th International Seminar on Non-Ideal Compressible Fluid Dynamics for Propulsion and Power.* Publisher: Springer Nature Switzerland. 2023, pp. 169–177. ISBN: 978-3-031-30936-6. DOI: 10.1007/978-3-031-30936-6_17.

[121] J. Wang, J. K. Carson, M. F. North, and D. J. Cleland. “A new approach to modelling the effective thermal conductivity of heterogeneous materials”. In: *Int. J. Heat Mass Tran.* 49.17 (2006). Publisher: Elsevier, pp. 3075–3083. ISSN: 0017-9310. DOI: 10.1016/j.ijheatmasstransfer.2006.02.007.

[122] K. Ghorayeb and A. Firoozabadi. “Modeling Multicomponent Diffusion and Convection in Porous Media”. In: *SPE Journal* 5.2 (2000). Publisher: Society of Petroleum Engineers (SPE), pp. 158–171. ISSN: 1930-0220. DOI: 10.2118/62168-pa.

[123] V. Giovangigli, L. Matuszewski, and P. Gaillard. “High pressure flames with multicomponent transport J. Bellan (Ed.), High pressure flows for propulsion applications, Progress in Astronautics and Aeronautics”. In: *American Institute of Aeronautics and Astronautics* (2019). Publisher: American Institute of Aeronautics and Astronautics.

[124] A. Leahy-Dios and A. Firoozabadi. “Unified model for nonideal multicomponent molecular diffusion coefficients”. In: *AlChE J.* 53.11 (2007). Publisher: Wiley, pp. 2932–2939. ISSN: 1547-5905. DOI: 10.1002/aic.11279.

[125] B. Naud and M. Arias-Zugasti. “Accurate multicomponent Fick diffusion at a lower cost than mixture-averaged approximation: Validation in steady and unsteady counterflow flamelets”. In: *Combust. Flame* 219 (2020). Publisher: Elsevier, pp. 120–128. ISSN: 0010-2180. DOI: 10.1016/j.combustflame.2020.05.003.

[126] V. Giovangigli, L. Matuszewski, and F. Dupoirieux. “Detailed modeling of planar transcritical H2–O2–N2 flames”. In: *Combust. Theor. Model.* 15.2 (2011), pp. 141–182. DOI: 10.1080/13647830.2010.527016.

[127] V. Giovangigli and L. Matuszewski. “Numerical simulation of transcritical strained laminar flames”. In: *Combust. Flame* 159.9 (2012), pp. 2829–2840. DOI: 10.1016/j.combustflame.2012.05.011.

[128] F. Monnier, G. Ribert, and L. Duhem-Duvilla. “CH4/O2 supercritical flame structure and simulation”. In: *Proc. Combust. Inst.* 40.1-4 (2024), p. 105514. DOI: 10.1016/j.proci.2024.105514.

[129] S. Vasu, D. Davidson, Z. Hong, V. Vasudevan, and R. Hanson. “n-Dodecane oxidation at high-pressures: Measurements of ignition delay times and OH concentration time-histories”. In: *Proc. Combust. Inst.* 32.1 (2009). Publisher: Elsevier, pp. 173–180. ISSN: 1540-7489. DOI: 10.1016/j.proci.2008.05.006.

[130] S. Lapointe, K. Zhang, and M. McNenly. “Reduced chemical model for low and high-temperature oxidation of fuel blends relevant to internal combustion engines”. In: *Proc. Combust. Inst.* 37.1 (2019). Publisher: Elsevier, pp. 789–796. ISSN: 1540-7489. DOI: 10.1016/j.proci.2018.06.139.

[131] R. W. Johnson and R. J. MacKinnon. “Equivalent versions of the quick scheme for finite-difference and finite-volume numerical methods”. In: *Commun. Appl. Numer. M.* 8.12 (1992). Publisher: Wiley, pp. 841–847. ISSN: 1555-2047. DOI: 10.1002/cnm.1630081202.

[132] R. L. Speth, W. H. Green, S. MacNamara, and G. Strang. “Balanced Splitting and Rebalanced Splitting”. In: *SIAM J. Numer. Anal.* 51.6 (2013). Publisher: Society for Industrial & Applied Mathematics (SIAM), pp. 3084–3105. ISSN: 1095-7170. DOI: 10.1137/120878641.

[133] S. Dharmaraja. “An analysis of the TR-BDF2 integration scheme”. Master’s Thesis. Massachusetts Institute of Technology, 2007. 31–35.

[134] S. Gottlieb, C.-W. Shu, and E. Tadmor. “Strong Stability-Preserving High-Order Time Discretization Methods”. In: *SIAM Rev.* 43.1 (2001). Publisher: Society for Industrial & Applied Mathematics (SIAM), pp. 89–112. ISSN: 1095-7200. DOI: `10.1137/s003614450036757x`.

[135] G. Ribert, N. Zong, V. Yang, L. Pons, N. Darabiha, and S. Candel. “Counterflow diffusion flames of general fluids: Oxygen/hydrogen mixtures”. In: *Combust. Flame* 154.3 (2008). Publisher: Elsevier, pp. 319–330. ISSN: 0010-2180. DOI: `10.1016/j.combustflame.2008.04.023`.

[136] M. O Conaire, H. J. Curran, J. M. Simmie, W. J. Pitz, and C. K. Westbrook. “A comprehensive modeling study of hydrogen oxidation”. In: *Int. J. Chem. Kinet.* 36.11 (2004). Publisher: Wiley, pp. 603–622. ISSN: 1097-4601. DOI: `10.1002/kin.20036`.

[137] J. Li, Z. Zhao, A. Kazakov, and F. L. Dryer. “An updated comprehensive kinetic model of hydrogen combustion”. In: *Int. J. Chem. Kinet.* 36.10 (2004). Publisher: Wiley, pp. 566–575. ISSN: 1097-4601. DOI: `10.1002/kin.20026`.

[138] N. Darabiha, S. M. Candel, V. Giovangigli, and M. D. Smooke. “Extinction of Strained Premixed Propane-air Flames with Complex Chemistry”. In: *Combust. Sci. Technol.* 60.4 (1988). Publisher: Informa UK Limited, pp. 267–285. ISSN: 1563-521x. DOI: `10.1080/00102208808923988`.

[139] Q. Lin, K. L. Tay, D. Zhou, and W. Yang. “Development of a compact and robust Polyoxymethylene Dimethyl Ether 3 reaction mechanism for internal combustion engines”. In: *Energ. Convers. Manage.* 185 (2019). Publisher: Elsevier, pp. 35–43. ISSN: 0196-8904. DOI: `10.1016/j.enconman.2019.02.007`.

[140] Q. Lin, K. L. Tay, F. Zhao, and W. Yang. “Enabling robust simulation of polyoxymethylene dimethyl ether 3 (PODE3) combustion in engines”. In: *Int. J. Engine Res.* 23 (2022). Publisher: SAGE Publications Sage UK: London, England, pp. 1522–1542.

[141] M. Fathi, S. Hickel, and D. Roekaerts. “Large Eddy Simulations of Transcritical E-Fuel Sprays Using Real-Fluid Multiphase Flamelet-Based Modeling”. In: *Combust. Flame* 281 (2025). Publisher: Elsevier, p. 114360. ISSN: 0010-2180. DOI: `10.1016/j.combustflame.2025.114360`.

[142] J. Liu, H. Wang, Y. Li, Z. Zheng, Z. Xue, H. Shang, and M. Yao. “Effects of diesel/PODE (polyoxymethylene dimethyl ethers) blends on combustion and emission characteristics in a heavy duty diesel engine”. In: *Fuel* 177 (2016). Publisher: Elsevier, pp. 206–216. ISSN: 0016-2361. DOI: `10.1016/j.fuel.2016.03.019`.

[143] R. Novella, G. Bracho, J. Gomez-Soriano, C. S. Fernandes, and T. Lucchini. “Combustion system optimization for the integration of e-fuels (Oxymethylene Ether) in compression ignition engines”. In: *Fuel* 305 (2021). Publisher: Elsevier, p. 121580. ISSN: 0016-2361. DOI: `10.1016/j.fuel.2021.121580`.

[144] F. Ferraro, C. Russo, R. Schmitz, C. Hasse, and M. Sirignano. “Experimental and numerical study on the effect of oxymethylene ether-3 (OME3) on soot particle formation”. In: *Fuel* 286 (2021). Publisher: Elsevier _eprint: 2104.12873, p. 119353. ISSN: 0016-2361. DOI: `10.1016/j.fuel.2020.119353`.

[145] R. Schmitz, C. Russo, F. Ferraro, B. Apicella, C. Hasse, and M. Sirignano. “Effect of oxymethylene ether-2-3-4 (OME2-4) on soot particle formation and chemical features”. In: *Fuel* 324 (2022). Publisher: Elsevier, p. 124617. ISSN: 0016-2361. DOI: `10.1016/j.fuel.2022.124617`.

[146] H. Pitsch, D. Goeb, L. Cai, and W. Willems. “Potential of oxymethylene ethers as renewable diesel substitute”. In: *Prog. Energ. Combust.* 104 (2024). Publisher: Elsevier, p. 101173. ISSN: 0360-1285. DOI: `10.1016/j.pecs.2024.101173`.

[147] J. van Oijen, A. Donini, R. Bastiaans, J. ten Thije Boonkkamp, and L. de Goey. “State-of-the-art in premixed combustion modeling using flamelet generated manifolds”. In: *Prog. Energ. Combust.* 57 (2016). Publisher: Elsevier, pp. 30–74. ISSN: 0360-1285. DOI: `10.1016/j.pecs.2016.07.001`.

[148] J.-P. Hickey and M. Ihme. “Large Eddy Simulation of Supercritical Mixing and Combustion for Rocket Applications”. In: *52nd Aerospace Sciences Meeting*. American Institute of Aeronautics and Astronautics, 2014, p. 0138. DOI: `10.2514/6.2014-0138`.

[149] H. Muller and M. Pfitzner. “A flamelet model for transcritical LOx/GCH4 flames”. In: *J. Phys. Conf. Ser.* 821.1 (2017). Publisher: IOP Publishing, p. 012010.

[150] J. Zips, H. Muller, and M. Pfitzner. “Efficient thermo-chemistry tabulation for non-premixed combustion at high-pressure conditions”. In: *Flow Turbul. Combust.* 101 (2018). Publisher: Springer, pp. 821–850. DOI: `10.1007/s10494-018-9932-4`.

[151] Z. Gao, H. Wang, C. Song, K. Luo, and J. Fan. “Large-eddy simulation of hydrothermal flames using extended flamelet/progress variable approach”. In: *The Journal of Supercritical Fluids* 163 (2020). Publisher: Elsevier, p. 104843. ISSN: 0896-8446. DOI: `10.1016/j.supflu.2020.104843`.

[152] A. Hadadpour, S. Xu, K. M. Pang, X. S. Bai, and M. Jangi. “Effects of pre-injection on ignition, combustion and emissions of spray under engine-like conditions”. In: *Combust. Flame* 241 (2022). ISSN: 15562921. DOI: `10.1016/j.combustflame.2022.112082`.

[153] J. V. Pastor, J. M. Garcia-Oliver, C. Mico, and A. A. Garcia-Carrero. “An experimental study with renewable fuels using ECN Spray A and D nozzles”. In: *Int. J. Engine Res.* 23.10 (2021). Publisher: SAGE Publications, pp. 1748–1759. ISSN: 2041-3149. DOI: `10.1177/14680874211031200`.

[154] A. Kulkarni, E. J. Garcia, A. Damone, M. Schappals, S. Stephan, M. Kohns, and H. Hasse. “A Force Field for Poly(oxymethylene) Dimethyl Ethers (OMEn)”. In: *J. Chem. Theory Comput.* 16 (2021). Publisher: Center for Open Science, pp. 2517–2528. DOI: `10.31219/osf.io/nm26c`.

[155] N. Tassin, V. Mascietti, and M. Cismondi. “Phase behavior of multicomponent alkane mixtures and evaluation of predictive capacity for the PR and RKPR EoSś”. In: *Fluid Phase Equilibr.* 480 (2019). Publisher: Elsevier, pp. 53–65. DOI: 10.1016/j.fluid.2018.10.005.

[156] L. Cai, S. Jacobs, R. Langer, F. vom Lehn, K. A. Heufer, and H. Pitsch. “Auto-ignition of oxymethylene ethers (OMEn, n = 2–4) as promising synthetic e-fuels from renewable electricity: shock tube experiments and automatic mechanism generation”. In: *Fuel* 264 (2020). Publisher: Elsevier, p. 116711. ISSN: 0016-2361. DOI: 10.1016/j.fuel.2019.116711.

[157] J. V. OIJEN and L. D. GOEY. “Modelling of Premixed Laminar Flames using Flamelet-Generated Manifolds”. In: *Combust. Sci. Technol.* 161.1 (2000). Publisher: Informa UK Limited, pp. 113–137. ISSN: 1563-521x. DOI: 10.1080/00102200008935814.

[158] O. Gicquel, N. Darabiha, and D. Thevenin. “Liminar premixed hydrogen/air counterflow flame simulations using flame prolongation of ILDM with differential diffusion”. In: *Proc. Combust. Inst.* 28.2 (2000). Publisher: Elsevier, pp. 1901–1908. ISSN: 1540-7489. DOI: 10.1016/s0082-0784(00)80594-9.

[159] H. Bao, H. Y. Akargun, D. Roekaerts, and B. Somers. “The inclusion of scalar dissipation rate in modeling of an n-dodecane spray flame using flamelet generated manifold”. In: *Combust. Flame* 249 (2023), p. 112610. ISSN: 0010-2180.

[160] R. Bilger, S. Starner, and R. Kee. “On reduced mechanisms for methane-air combustion in nonpremixed flames”. In: *Combust. Flame* 80.2 (1990). Publisher: Elsevier, pp. 135–149. ISSN: 0010-2180. DOI: 10.1016/0010-2180(90)90122-8.

[161] H. Pitsch and N. Peters. “A Consistent Flamelet Formulation for Non-Premixed Combustion Considering Differential Diffusion Effects”. In: *Combust. Flame* 114.1 (1998). Publisher: Elsevier, pp. 26–40. ISSN: 0010-2180. DOI: 10.1016/s0010-2180(97)00278-2.

[162] M. Ihme, L. Shunn, and J. Zhang. “Regularization of reaction progress variable for application to flamelet-based combustion models”. In: *J. Comput. Phys.* 231.23 (2012). Publisher: Elsevier, pp. 7715–7721. ISSN: 0021-9991. DOI: 10.1016/j.jcp.2012.06.029.

[163] P. Rahnama, A. Maghbouli, H. Bao, A. Vasavan, R. Novella, and B. Somers. “Generalizing progress variable definition in CFD simulation of combustion systems using tabulated chemistry models”. In: *Applications in Energy and Combustion Science* 14 (2023). Publisher: Elsevier, p. 100132. ISSN: 2666-352x. DOI: 10.1016/j.jaecs.2023.100132.

[164] J. H. Verner. “Some Runge–Kutta Formula Pairs”. In: *SIAM J. Numer. Anal.* 28.2 (1991). Publisher: Society for Industrial & Applied Mathematics (SIAM), pp. 496–511. ISSN: 1095-7170. DOI: 10.1137/0728027.

[165] T. Xuan, H. Li, Y. Wang, Y. Chang, M. Jia, Z. He, Q. Wang, J. Cao, and R. Payri. “A conceptual model of polyoxymethylene dimethyl ether 3 (PODE3) spray combustion under compression ignition engine-like conditions”. In: *Combust. Flame* 261 (2024). Publisher: Elsevier, p. 113296. DOI: `10.1016/j.combustflame.2024.113296`.

[166] A. Saghafian, V. Terrapon, and H. Pitsch. “An efficient flamelet-based combustion model for compressible flows”. In: *Combust. Flame* 162 (2015). Publisher: Elsevier, pp. 652–667. DOI: `10.1016/j.combustflame.2014.08.007`.

[167] G. van den Oord, V. Azizi, M. Fathi, and S. Hickel. “Dynamic Multilevel Load Balancing for Scalable Simulations of Reacting Multiphase Flows”. In: *Int. J. High Perform. Comput. Appl* (2025). Publisher: SAGE Publications Sage UK: London, England, p. 10943420251329199. DOI: `10.1177/10943420251329199`.

A

Appendices

A.1. Sensitivity to Grid Resolutions

To evaluate the grid sensitivity of the numerical results presented, a grid convergence study is conducted by refining and coarsening the base grid. The finest grid has the minimum spacing of 6.84 µm, while the coarsest has 20.50 µm. Applying the same local grid refinement procedure as used for the base grid (with 12.7×10^6 cells), we obtain a total cell number of approximately 1.2×10^6 for the coarse grid and 36.1×10^6 for the finest grid.

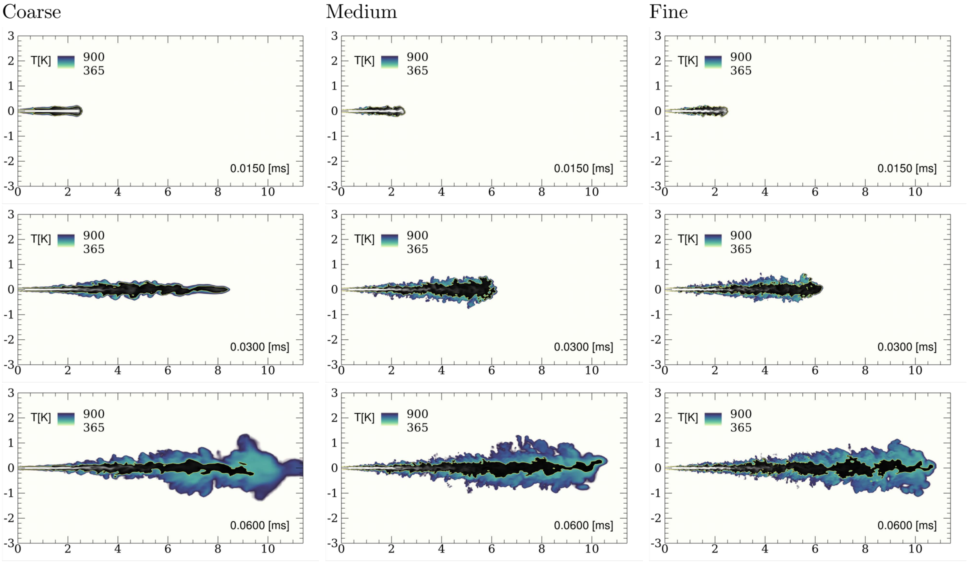
Coarse

Medium

Fine

Figure A.1.: Grid sensitivity of the temporal evolution of the temperature field superimposed by the LVF distribution from 1 to 0 printed white to black colors.

Figure A.1 visualizes the temporal evolution of the jet on the three grids.

The results obtained on the medium and fine grids are almost indistinguishable, whereas too rapid penetration and a different jet break-up topology are observed for the coarsest grid. Such a rapid nonphysical penetration was also reported for too coarse meshes [35]. The main reason for this error is an insufficient number of cells in the radial direction, resulting in extra momentum in the axial direction. The corresponding liquid and vapor penetration trajectories are shown in Fig. A.2. Only negligible differences can be observed between the results obtained on the medium and fine grids.

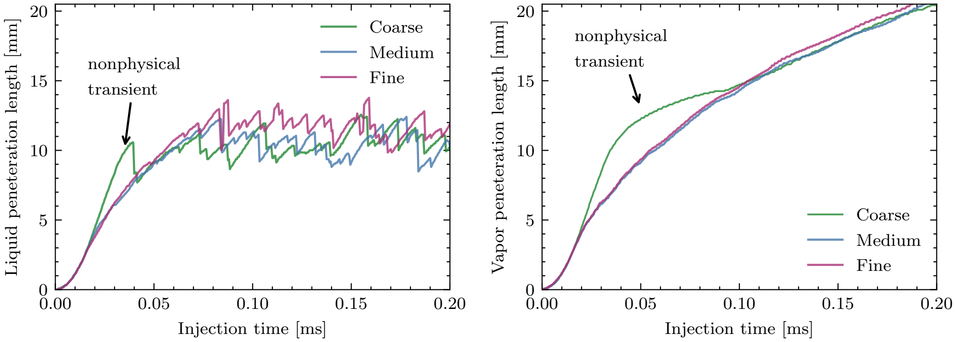

Figure A.2.: Grid sensitivity of the liquid and vapor penetration trajectories.

A.2. COMPRESSIBLE FORMULATION

Although pressure-based solvers that operate under low-Mach assumptions can be suitable in some cases, like those used by Traxinger, Zips, and Pfitzner [38], they are not ideal for test cases such as the ECN Spray-A configuration. In the Spray-A setup, the sound speed of the liquid phase is approximately $900\,\mathrm{m\,s^{-1}}$, but it can decrease to values lower than $300\,\mathrm{m\,s^{-1}}$ in the vaporized regions. With injection velocities close to $600\,\mathrm{m\,s^{-1}}$, local Mach numbers often exceed unity, as illustrated in Fig. A.3.

Solving the fully conservative compressible Navier-Stokes equations is essential to accurately simulate these regimes and capture dynamic pressure changes, shock waves, and phase transitions [35]. Manifold retrieval techniques, which separate pressure from thermodynamic states, fall short in such dynamic settings. In contrast, the on-the-fly UV-flash method, updating internal energy and volume in real time, maintains a tight coupling of thermodynamic and pressure fields in all flow regions. For this reason, in our studies, instead of manifold retrieval, we use on-the-fly UV flash calculations, like the compressible flamelet approach proposed by Saghafian, Terrapon, and Pitsch [166].

The UV-flash method [51] is optimized for computational efficiency and remains efficient regardless of the number of chemical species monitored. This makes it suitable for LES of multi-component fuels in high-pressure, turbulent spray environments. However, the intricate nature of such modeling can significantly

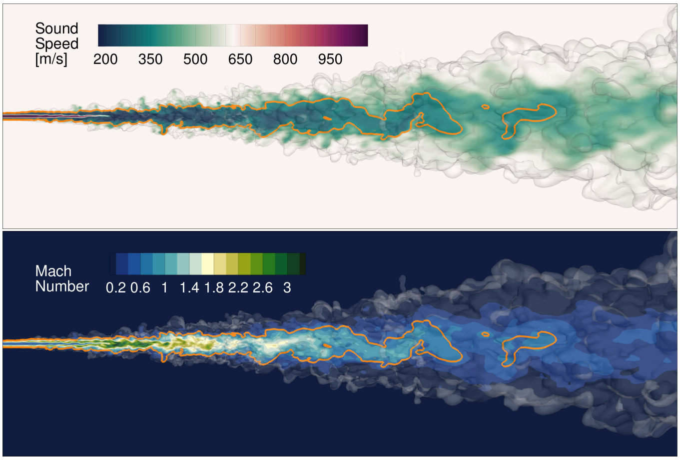

Figure A.3.: Mid-plane contours of speed of sound and Mach number along with a 3D rendering of mixture fraction iso-surface of 0.001. The orange line shows the edge of the vaporizing region.

increase local computational expenses, often causing an uneven distribution of workload with a traditional domain decomposition. Thus, employing dynamic load balancing strategies [167] is crucial to maintain parallel scalability of simulations that feature detailed spray flame modeling.

Epilogue

The models and frameworks presented here represent significant steps forward in our ability to accurately predict the behavior of transcritical fuel sprays. By confronting the challenges of real-fluid thermodynamics, robust phase equilibrium calculations, and the nuances of high-pressure reaction kinetics, we have provided unprecedented insights into these critical processes. Looking back, the complexity of these phenomena underscores the necessity of the detailed, first-principles-based approaches pursued. Looking forward, this research provides a powerful tool for the continued development of cleaner and more fuel-efficient engines, enabling the exploration of novel fuels like OMEs. The journey of discovery in transcritical combustion is far from complete, but the foundations laid here offer a promising path towards unlocking its full potential for the future of propulsion systems.

Mohamad Fathi
Rotterdam, June 2025

Acknowledgements

Looking back on these years, I realize that the true essence of this journey is found not only in the research completed or the results presented here, but in the people, experiences, and transformations that shaped me along the way. I am sincerely grateful to everyone who has been part of this unforgettable chapter of my life.

My deepest professional gratitude goes to my wonderful promotors and supervisors.

To Stefan Hickel: thank you for your unwavering trust, guidance, and support. This journey began with your trust in me and the insightful vision through which you conceived the foundations of this great project. Implementing complex models in INCA–the countless hours of coding, debugging, and our long, patient afternoon sessions–were among the most enjoyable and formative experiences of these years. I am deeply grateful for your openness and flexibility, which allowed me to explore and contribute in my own way. Your continued support into my postdoc has been invaluable, giving me yet another rewarding chapter at TU Delft.

To Dirk Roekaerts: I truly feel fortunate to have the opportunity to learn directly from you. Becoming your last PhD student is something I will always carry with pride. Our meetings where you patiently revisited the fundamentals of reactive flows with me step by step, were unforgettable. Your guidance sharpened my thinking, helped me face complexity clearly, and showed me the value of deep understanding. Thank you for providing an environment where I could pursue this work with genuine passion.

A special thanks to Colette Russo, whose efficiency, kindness, and reliability made every administrative matter remarkably smooth. I would like to extend my thanks to our colleagues at the e-Science Center: Victor Azizi and Gijs van den Oord. Our weekly virtual meetings during the pandemic, and the unforgettable news of the paper's acceptance on the first working day of the new year, are memories I will always cherish. Gijs, you truly embodied the Dutch spirit of "de aanhouder wint".

My heartfelt appreciation goes to my fellow PhD students and friends–this journey would not have been the same without you. To those who have already graduated: Alberto, Alessandro, Alexander, Christoph, Constantin, Edoardo, Gabriel, Jordi, Kushal, Tiago, Luis, Weibo, Martin, Sagar, Tiago, Varun, Wouter, Yi, Xiaodong, Ming, Yu, and Kaisheng and to those who are on the way: Haris, Ata, and Babak: thank you for all our conversations during lectures, workshops, and conferences, and for the moments we shared over lunches and coffee breaks. A special thanks to Tiago, Luis, and Weibo whose support during my initial months was indispensable. You welcomed me from day one, shared your experience, taught me INCA, and guided me through the many stages of this journey.

To my wonderful Iranian friends: Arash Norouzi, Hamed Abdullahi, Mostafa Saket, Faezeh Shams, Rezvan Sarkhosh, Sara Marzban, Mahya Ganjian, Said Hussaini, Zahra Shams, Hamidreza Heydarian, Iman Atayi, Ali Eidi, Abbas Daliri, and Hassan Nemati. Thank you for the warmth, friendship, and sense of home you brought into our lives here.

Above all, my deepest gratitude belongs to my family. To my parents: your unwavering confidence in me has been a constant wellspring of strength since my childhood. Your unconditional support means more to me than I can express. I hope this work makes you proud. To my sister: your kindness and the love you share with your two adorable kids, Delnia and Daniar, have always brought me comfort. I am truly lucky to have you in my life.

I would also like to thank my wife's family for their kindness and support–especially my brother-in-law, Alireza, who, since moving to Germany, has never hesitated to take a train to Rotterdam whenever we needed a helping hand.

And finally, to my wife to whom this thesis is dedicated: Narges, you are the heart of this journey. You have always believed in me, encouraged me, and supported me through various challenges. I am endlessly grateful to have you as my wife, my best friend, and as an extraordinary mother to our little princesses, Nilda and Anida, whose love inspires me every day to contribute, in whatever way I can, to a sustainable future filled with hope, peace, and endless possibilities. They say hardship sweetens achievement. Completing this journey while raising our kids has multiplied that joy immeasurably. Thank you, azizam, for making this path not only possible, but profoundly meaningful and filled with light.

Mohamad Fathi
Rotterdam, December 2025

Publications

1. M. Fathi and S. Hickel. “Rapid Multi-Component Phase-Split Calculations Using Volume Functions and Reduction Methods”. In: *AIChE J.* 67.6 (2021). Publisher: Wiley _eprint: 2001.06285, e17174. ISSN: 1547-5905. DOI: `10.1002/aic.17174`
2. M. Fathi, S. Hickel, and D. Roekaerts. “Large Eddy Simulations of Reacting and Non-Reacting Transcritical Fuel Sprays Using Multiphase Thermodynamics”. In: *Phys. Fluids* 34.8 (2022). Publisher: AIP Publishing _eprint: 2205.07504, p. 085131. ISSN: 1089-7666. DOI: `10.1063/5.0099154`
3. M. Fathi, S. Hickel, and D. Roekaerts. “Numerical Simulations of Real-Fluid Reacting Sprays at Transcritical Pressures Using Multiphase Thermodynamics”. In: *Proceedings of the 4th International Seminar on Non-Ideal Compressible Fluid Dynamics for Propulsion and Power.* Publisher: Springer Nature Switzerland. 2023, pp. 169–177. ISBN: 978-3-031-30936-6. DOI: `10.1007/978-3-031-30936-6_17`
4. M. Fathi, D. Roekaerts, and S. Hickel. “Numerical Simulation of Transcritical Multiphase Combustion Using Real-Fluid Thermochemical and Transport Properties”. In: *Combust. Flame* 275 (2024). Publisher: Elsevier, p. 114055. DOI: `10.1016/j.combustflame.2025.114055`
5. G. van den Oord, V. Azizi, M. Fathi, and S. Hickel. “Dynamic Multi-level Load Balancing for Scalable Simulations of Reacting Multiphase Flows”. In: *Int. J. High Perform. Comput. Appl* (2025). Publisher: SAGE Publications Sage UK: London, England, p. 10943420251329199. DOI: `10.1177/10943420251329199`
6. M. Fathi, S. Hickel, and D. Roekaerts. “Large Eddy Simulations of Transcritical E-Fuel Sprays Using Real-Fluid Multiphase Flamelet-Based Modeling”. In: *Combust. Flame* 281 (2025). Publisher: Elsevier, p. 114360. ISSN: 0010-2180. DOI: `10.1016/j.combustflame.2025.114360`
7. M. Fathi, D. Roekaerts, and S. Hickel. “Transcritical Real-Fluid Effects on Dual-Fuel Combustion of Methane and N-Dodecane”. In: *Appl. Energy Combust. Sci.* 24 (2025). Publisher: Elsevier, p. 100398. ISSN: 2666-352X. DOI: `10.1016/j.jaecs.2025.100398`

Multimedia

Scan to watch

LES of Transcritical Fuel Sprays

A short scientific animation based on the results of this PhD dissertation, awarded *Best Animation* at the *Art of Scientific Computing Symposium* during the grand opening of the DelftBlue supercomputer.

Watch the animation:
`https://rb.gy/sm770w`

Scan to read

High-Pressure Combustion Simulations

A short scientific *TU Delft Story* based on the results of this PhD dissertation, introducing complexities related to high-pressure simulations of internal combustion in simple words.

Read the full story:
`https://rb.gy/59hjxw`

TU Delft

ISBN 978-94-6384-889-3